



**HAL**  
open science

# Ultra-wide band gap semiconductors $\beta$ -Ga<sub>2</sub>O<sub>3</sub> and ZnGa<sub>2</sub>O<sub>4</sub> electronic properties

Zeyu Chi

► **To cite this version:**

Zeyu Chi. Ultra-wide band gap semiconductors  $\beta$ -Ga<sub>2</sub>O<sub>3</sub> and ZnGa<sub>2</sub>O<sub>4</sub> electronic properties. Materials Science [cond-mat.mtrl-sci]. Université Paris-Saclay, 2023. English. NNT : 2023UPAST095 . tel-04268510

**HAL Id: tel-04268510**

**<https://theses.hal.science/tel-04268510v1>**

Submitted on 2 Nov 2023

**HAL** is a multi-disciplinary open access archive for the deposit and dissemination of scientific research documents, whether they are published or not. The documents may come from teaching and research institutions in France or abroad, or from public or private research centers.

L'archive ouverte pluridisciplinaire **HAL**, est destinée au dépôt et à la diffusion de documents scientifiques de niveau recherche, publiés ou non, émanant des établissements d'enseignement et de recherche français ou étrangers, des laboratoires publics ou privés.

# Ultra-wide band gap semiconductors $\beta$ -Ga<sub>2</sub>O<sub>3</sub> and ZnGa<sub>2</sub>O<sub>4</sub> electronic properties

*Propriétés électroniques des semi-conducteurs à ultra-large bande interdite  $\beta$ -Ga<sub>2</sub>O<sub>3</sub> et ZnGa<sub>2</sub>O<sub>4</sub>*

## Thèse de doctorat de l'université Paris-Saclay

École doctorale n° 573, Interfaces : matériaux, systèmes, usages (INTERFACES)  
Spécialité de doctorat : Physique  
Graduate School : Sciences de l'ingénierie et des systèmes.  
Référent : Université de Versailles-Saint-Quentin-en-Yvelines

Thèse préparée dans l'unité de recherche **GEMAC** (Université Paris-Saclay, UVSQ, CNRS), sous la direction d'**Yves DUMONT**, professeur des universités, et le co-encadrement d'**Ekaterine CHIKOIDZE**, ingénieure de recherche CNRS

Thèse soutenue à Versailles, le 11 Juillet 2023, par

**Zeyu CHI**

### Composition du Jury

Membres du jury avec voix délibérative

<b>Anne-Marie GONCALVES</b> Professeure des universités, UVSQ, Univ. Paris-Saclay	Présidente
<b>Etienne GHEERAERT</b> Professeur des universités, Univ. Grenoble Alpes	Rapporteur & Examineur
<b>Andrej KUZNETSOV</b> Professeur, Univ. d'Oslo, Norvège	Rapporteur & Examineur
<b>Laurent BINET</b> Professeur des universités, Chimie ParisTech – PSL	Examineur
<b>Vanya DARAKCHIEVA</b> Professeure, Univ. de Lund, Suède	Examinatrice

**Title:** Ultra-wide band gap semiconductors  $\beta$ -Ga<sub>2</sub>O<sub>3</sub> and ZnGa<sub>2</sub>O<sub>4</sub> electronic properties

**Keywords:** Semiconductor; Oxide, Ultra-wide band gap; Electronic properties;  $\beta$ -Ga<sub>2</sub>O<sub>3</sub>; ZnGa<sub>2</sub>O<sub>4</sub>

**Abstract:** Improving energy efficiency and reducing power consumption is important for accelerating climate saving. To this end, efficient power electronics devices based on new generations of wide and ultra-wide band gap (UWBG) semiconductors are an ultimate solution. Last several years, Gallia ( $\beta$ -Ga<sub>2</sub>O<sub>3</sub>) and Zinc gallate (ZnGa<sub>2</sub>O<sub>4</sub>) have attracted much attention due to their UWBG ( $E_g > 4.5$  eV) and realizable high  $n$ -type electrical conductivity. Though, to fully realize the functionality of these two materials, power devices based on bipolar structure ( $p$ - $n$ , or  $p$ - $i$ - $n$ ) are required. However,  $p$ -type doping is a challenge for both materials:  $\beta$ -Ga<sub>2</sub>O<sub>3</sub> and ZnGa<sub>2</sub>O<sub>4</sub>.

The objective of this PhD work is to investigate the electronic properties of  $\beta$ -Ga<sub>2</sub>O<sub>3</sub> and ZnGa<sub>2</sub>O<sub>4</sub> materials to disclose their potential for applications in power electronics.

The first part of the thesis describes the realization of native defect related hole conductivity in undoped  $\beta$ -Ga<sub>2</sub>O<sub>3</sub>. According to thermodynamic analysis, the realization of hole conductivity in  $\beta$ -Ga<sub>2</sub>O<sub>3</sub> is possible thanks to the comparatively high enthalpy of compensating donor creation. Indeed,  $p$ -type conductivity ( $p = 2 \times 10^{14}$  cm<sup>-3</sup> and mobility  $\mu = 9$  cm<sup>2</sup>/(V·s) at 800 K) in MOCVD grown  $\beta$ -Ga<sub>2</sub>O<sub>3</sub> thin film has been experimentally demonstrated. The origin of the conductivity is attributed to native defect gallium vacancies ( $V_{Ga}$ ) with an ionization energy  $E_i = 1.2$  eV. To further increase the hole conductivity, Zn doping was studied. Based on thermodynamic analysis, Zn can take substitutional or interstitial site, and act as an acceptor or a donor dopant in  $\beta$ -Ga<sub>2</sub>O<sub>3</sub>. Then, I studied Zn-doped  $\beta$ -Ga<sub>2</sub>O<sub>3</sub>//Al<sub>2</sub>O<sub>3</sub> thin films with incorporated Zn concentration in  $10^{16} - 10^{19}$  cm<sup>-3</sup> range. Compared to undoped film,  $p$ -type conductivity was enhanced when  $[Zn] = 10^{16}$  cm<sup>-3</sup>. The origin is  $Zn_{Ga}$  defect, its ionization energy was estimated to be  $E_i = 0.77$  eV by Hall effect measurement. With increasing Zn doping level ( $> 10^{18}$  cm<sup>-3</sup>), the “auto-compensation” effect takes place, i.e., acceptor  $Zn_{Ga}$

and donor  $Zn_i$  defects start to compensate each other, resulting in the decrease of hole concentration by more than one order of magnitude. Though, the “auto-compensation” effect has been used as a positive phenomenon for increasing the critical electrical field ( $E_{CR}$ ) of  $\beta$ -Ga<sub>2</sub>O<sub>3</sub>, which was experimentally estimated to be  $E_{CR} = 13.2$  MV/cm.

With the further increasing ( $> 6.85\%$ ) incorporated Zn concentration in  $\beta$ -Ga<sub>2</sub>O<sub>3</sub>, cubic spinel ZnGa<sub>2</sub>O<sub>4</sub> starts to form during MOCVD growth. I have studied the electronic properties of ZnGa<sub>2</sub>O<sub>4</sub>//Al<sub>2</sub>O<sub>3</sub> thin films. Comparative analysis of structural, chemical, optical, and electrical transport measurements demonstrated that both semi-insulating  $p$ -type (by  $Zn_{Ga}$ ) and conducting  $n$ -ZnGa<sub>2</sub>O<sub>4</sub> thin films were achieved by tuning the growth conditions, with the native defect conductivity controlled up to 10 orders of magnitude thanks to “self-doping” effect. It is suggested that the native high electron concentration was achieved due to the hybridization of the Zn-O orbitals resulting in a “self-impurity” band where the  $Zn_i$  hopping occurs. The important influence of oxygen on electrical properties can be clearly seen and shown. The critical electric field  $E_{CR} > 5.3$  MV/cm was estimated for the first time.

Finally, a preliminary study of electrical metal contacts to  $p$ -Ga<sub>2</sub>O<sub>3</sub> is discussed, by looking at the perspective of the use of  $p$ -Ga<sub>2</sub>O<sub>3</sub> in power device structures. Pt and Ti/Pt/Au was identified to form Schottky and quasi-Ohmic contacts in the measurement temperature range to  $p$ -Ga<sub>2</sub>O<sub>3</sub>, respectively. CTLM methodology to evaluate the corresponding specific contact resistance was developed with photolithographic masks.

**Titre :** Propriétés électroniques des semi-conducteurs à ultra-large bande interdite  $\beta$ -Ga<sub>2</sub>O<sub>3</sub> et ZnGa<sub>2</sub>O<sub>4</sub>.

**Mots clés :** Semi-conducteur ; Ultra-large bande interdite ; Propriétés électroniques ;  $\beta$ -Ga<sub>2</sub>O<sub>3</sub> ; ZnGa<sub>2</sub>O<sub>4</sub>

**Résumé :** L'amélioration de l'efficacité énergétique et la réduction de la consommation d'énergie sont importantes pour accélérer la préservation du climat. Pour cela, des dispositifs d'électronique de puissance basés sur des semi-conducteurs à ultra-large bande interdite (UWBG) de nouvelle génération sont une solution ultime. Ces dernières années,  $\beta$ -Ga<sub>2</sub>O<sub>3</sub> et ZnGa<sub>2</sub>O<sub>4</sub> ont attiré beaucoup d'attention grâce à leur ultra-large bande interdite ( $E_g > 4,5$  eV) et d'un très fort dopage contrôlé de type  $n$ . Cependant, pour réaliser pleinement les fonctionnalités des deux matériaux, des dispositifs de puissance basés sur une structure bipolaire ( $p$ - $n$  ou  $p$ - $i$ - $n$ ) sont nécessaires. Néanmoins, le dopage de type  $p$  est un défi pour ces deux oxydes UWBG.

L'objectif de ce travail est d'étudier expérimentalement les propriétés électroniques des matériaux  $\beta$ -Ga<sub>2</sub>O<sub>3</sub> et ZnGa<sub>2</sub>O<sub>4</sub> en films minces pour évaluer leur potentiel pour des applications en électronique de puissance.

La première partie de la thèse étudie la conductivité de type  $p$  liée aux défauts intrinsèques dans  $\beta$ -Ga<sub>2</sub>O<sub>3</sub> non dopé. Selon l'analyse thermodynamique,  $\beta$ -Ga<sub>2</sub>O<sub>3</sub> du type  $p$  est réalisable grâce à une enthalpie relativement élevée de création de donneur. En effet, le type  $p$  ( $p = 2 \times 10^{14}$  cm<sup>-3</sup> et mobilité  $\mu = 9$  cm<sup>2</sup>/(V·s) à 800 K) dans la couche mince de  $\beta$ -Ga<sub>2</sub>O<sub>3</sub> élaborée par MOCVD a été démontrée expérimentalement. L'origine de la conductivité est attribuée à la lacune de gallium ( $V_{Ga}$ ) avec une énergie d'ionisation  $E_i = 1,2$  eV. Pour augmenter la conductivité du type  $p$ , un dopage du Zn a été étudié. Par une analyse thermodynamique, Zn peut prendre un site de substitution ou interstitiel et agir comme un accepteur ou un donneur dans le  $\beta$ -Ga<sub>2</sub>O<sub>3</sub>. Ensuite, j'ai étudié des films minces de  $\beta$ -Ga<sub>2</sub>O<sub>3</sub>//Al<sub>2</sub>O<sub>3</sub> dopés au Zn avec une concentration de Zn incorporée dans la gamme  $10^{16} - 10^{19}$  cm<sup>-3</sup>. Par rapport au film non dopé, la conductivité de type  $p$  augmente avec  $[Zn] = 10^{16}$  cm<sup>-3</sup>. L'origine est le défaut Zn<sub>Ga</sub>, son énergie d'ionisation a été estimée à  $E_i = 0,77$  eV par mesure d'effet Hall. Avec l'augmentation du niveau de dopage en

Zn ( $> 10^{18}$  cm<sup>-3</sup>), l'effet "auto-compensation" se produit, les défauts accepteur Zn<sub>Ga</sub> et donneur Zn<sub>i</sub> commencent à se compenser, provoquant la diminution de la concentration en trous de plus d'un ordre de grandeur. Cependant, cet effet a été utilisé comme un phénomène positif qui a permis d'augmenter le champ électrique critique ( $E_{CR}$ ) de  $\beta$ -Ga<sub>2</sub>O<sub>3</sub>, avec une valeur expérimentale estimée à  $E_{CR} = 13,2$  MV/cm.

Avec l'augmentation de la concentration de Zn incorporé ( $> 6,85\%$ ) dans le  $\beta$ -Ga<sub>2</sub>O<sub>3</sub>, la spinelle cubique ZnGa<sub>2</sub>O<sub>4</sub> commence à cristalliser durant la croissance du MOCVD. J'ai étudié les propriétés électroniques de films minces de ZnGa<sub>2</sub>O<sub>4</sub>//Al<sub>2</sub>O<sub>3</sub>. L'analyse comparative des mesures structurales, chimiques, optiques et de transport électrique a démontré que les couches minces semi-isolantes de type  $p$  (par Zn<sub>Ga</sub>) et conductrices  $n$ -ZnGa<sub>2</sub>O<sub>4</sub> ont été réalisées en ajustant les conditions de croissance, la conductivité du défaut intrinsèque étant contrôlée jusqu'à 10 ordres de grandeur grâce à l'effet "auto-dopage". Il est suggéré que la concentration élevée d'électrons intrinsèque a été obtenue par l'hybridation des orbitales Zn-O résultant en une bande « d'auto-impuretés », où le saut entre zinks interstitiels (Zn<sub>i</sub>) se produit. L'influence importante de l'oxygène sur les propriétés électriques est démontrée. Un champ électrique critique  $E_{CR} > 5,3$  MV/cm a été estimé expérimentalement, pour la première fois.

Enfin, une étude préliminaire des contacts métalliques électriques au  $p$ -Ga<sub>2</sub>O<sub>3</sub> est discutée, cette problématique est abordée en regardant la perspective d'utilisation du  $p$ -Ga<sub>2</sub>O<sub>3</sub> dans les structures de dispositifs de puissance. Pt et Ti/Pt/Au ont été identifiés comme formant des contacts Schottky et quasi-ohmiques avec  $p$ -Ga<sub>2</sub>O<sub>3</sub>, respectivement. La méthodologie CTLM pour évaluer la résistance de contact spécifique correspondante a été développée avec des masques photo-lithographiques.

---

## Résumé substantiel :

Ce travail de recherche en science des matériaux se situe dans le contexte de réduction de l'utilisation des énergies fossiles et de la lutte contre le dérèglement climatique. En effet, de près d'un siècle, la production d'énergie a été principalement basée sur la consommation de ressources fossiles, qui d'une part ne sont pas inépuisables, et d'autre part produisent une pollution énorme. Ce sont l'amélioration de l'efficacité de conversion énergétique et la réduction de la consommation d'énergie au global, qui apporteront des accélérations dans la préservation du climat. Pour cela, des dispositifs d'électronique de puissance basés sur des semi-conducteurs à ultra-large bande interdite (UWBG) de nouvelle génération sont une solution ultime. Ces dernières années,  $\beta$ -Ga<sub>2</sub>O<sub>3</sub> et ses dérivés, dont le ZnGa<sub>2</sub>O<sub>4</sub>, ont attiré beaucoup d'attention grâce à leur bande interdite ultra-large ( $E_g > 4,5$  eV) et de la capacité à les doper très fortement et de manière contrôlée de type  $n$ , comme de nombreux semiconducteurs oxydes. Cependant, pour réaliser pleinement les fonctionnalités des deux matériaux  $\beta$ -Ga<sub>2</sub>O<sub>3</sub> et ZnGa<sub>2</sub>O<sub>4</sub>, des dispositifs de puissance basés sur une structure bipolaire de type jonction  $p-n$  ou  $p-i-n$  sont nécessaires. Néanmoins, le dopage de type  $p$  est un défi matériau et propriétés pour ces deux oxydes UWBG.

L'objectif de ce travail de doctorat est d'étudier expérimentalement les propriétés électroniques des matériaux  $\beta$ -Ga<sub>2</sub>O<sub>3</sub> et ZnGa<sub>2</sub>O<sub>4</sub> en films minces pour qualifier leur potentiel pour des applications en électronique de puissance.

La première partie de la thèse étudie la conductivité de type  $p$  liée aux défauts intrinsèques dans  $\beta$ -Ga<sub>2</sub>O<sub>3</sub> non dopé. Selon l'analyse thermodynamique pour les défauts ponctuels,  $\beta$ -Ga<sub>2</sub>O<sub>3</sub> du type  $p$  est réalisable grâce à une enthalpie relativement élevée de création des donneurs. En effet, le type  $p$  ( $p = 2 \times 10^{14}$  cm<sup>-3</sup> et mobilité  $\mu = 9$  cm<sup>2</sup>V<sup>-1</sup>s<sup>-1</sup> à 800 K) dans la couche mince de  $\beta$ -Ga<sub>2</sub>O<sub>3</sub> élaborée par la technique de dépôt chimique par précurseurs métal-organique (MOCVD), fonctionnant à l'équilibre, a été démontrée expérimentalement. L'origine de la conductivité est attribuée à la lacune de gallium ( $V_{Ga}$ ) avec une énergie d'ionisation  $E_i \sim 1,2$  eV d'après la littérature. La couche présente une bande interdite très large à 4.7 eV, comme espérée. Ces réalisations ouvrent la voie à une nouvelle amélioration de la conductivité des trous par dopage accepteur. L'influence de la température de croissance est brièvement présentée : l'augmentation de la température de croissance de 775 à 825 °C, diminue la concentration du donneur intrinsèque compensatoire, et donc augmente la concentration de l'accepteur intrinsèque majoritaire.

---

Afin d'augmenter la conductivité du type  $p$ , l'élément Zn du groupe II a été choisi, et l'effet du dopage de Zn a été étudié. Par une analyse thermodynamique pour les défauts ponctuels, Zn pourrait prendre un site de substitution ou interstitiel et agir comme un accepteur ( $Zn_{Ga}$ ) ou/et un donneur ( $Zn_i$ ) dans le  $\beta$ -Ga<sub>2</sub>O<sub>3</sub>, suivant les conditions de croissance (température, pression dans la chambre de croissance, et surtout concentration en dopant Zn extrinsèque). Ensuite, j'ai étudié des films minces de  $\beta$ -Ga<sub>2</sub>O<sub>3</sub> déposés sur substrats Al<sub>2</sub>O<sub>3</sub>(0001), dopés au Zn avec une concentration de Zn incorporée dans la gamme  $10^{16} - 10^{19} \text{ cm}^{-3}$ . La symétrie cristalline de phase  $\beta$  est conservée avec le dopage, selon l'analyse de diffraction par rayons X. Par rapport au film non dopé, la conductivité de type  $p$  augmente ( $p = 1 \times 10^{15} \text{ cm}^{-3}$  à 800 K) avec  $[Zn] = 10^{16} \text{ cm}^{-3}$ . L'origine est identifiée comme le défaut  $Zn_{Ga}$ , dont l'énergie d'ionisation a été estimée à  $E_i = 0,77 \text{ eV}$  par mesure d'effet Hall. Avec l'augmentation du niveau de dopage en Zn ( $> 10^{18} \text{ cm}^{-3}$ ), « l'auto-compensation » se produit, les défauts accepteur zinc en site de gallium  $Zn_{Ga}$  et donneur zinc interstitiel  $Zn_i$  commencent à se compenser, provoquant la diminution de la concentration en trous mobiles de plus d'un ordre de grandeur. Cependant, cet effet a été exploité positivement pour augmenter le champ électrique critique ( $E_{CR}$ ) de  $\beta$ -Ga<sub>2</sub>O<sub>3</sub>, avec une valeur expérimentale évaluée à  $E_{CR} = 13,2 \text{ MV/cm}$ .

Avec l'augmentation de la concentration de Zn incorporé ( $> 6,85\%$ ) dans le  $\beta$ -Ga<sub>2</sub>O<sub>3</sub>, la spinelle cubique ZnGa<sub>2</sub>O<sub>4</sub> commence à cristalliser durant la croissance par MOCVD. Lorsque l'incorporation du Zn dépasse 13%, la couche devient pure spinelle ZnGa<sub>2</sub>O<sub>4</sub>, selon la diffraction des rayons X et des électrons. Ensuite, j'ai étudié les propriétés électroniques de films minces de ZnGa<sub>2</sub>O<sub>4</sub> sur substrats Al<sub>2</sub>O<sub>3</sub> : l'analyse comparative des mesures structurales, chimiques, optiques et de transport électrique a démontré que les couches minces semi-isolantes de type  $p$  (via la substitution  $Zn_{Ga}$ ) et conductrices  $n$ -ZnGa<sub>2</sub>O<sub>4</sub> ont été réalisées en ajustant les conditions de croissance, la conductivité associée au défaut intrinsèque étant contrôlée jusqu'à 10 ordres de grandeur grâce à l'effet d'« auto-dopage ». Il est suggéré que la concentration intrinsèque élevée d'électrons mobiles a été obtenue par l'hybridation des orbitales Zn-O formant une bande « d'auto-impuretés ». Le mécanisme de conduction est alors de type « sauts » entre zincs interstitiels ( $Zn_i$ ). L'influence importante de l'oxygène sur les propriétés électriques est démontrée. Un champ électrique critique  $E_{CR} > 5,3 \text{ MV/cm}$  a été estimé expérimentalement, pour la première fois pour la spinelle ZnGa<sub>2</sub>O<sub>4</sub>.

---

Enfin, une étude préliminaire des contacts métalliques électriques au  $p\text{-Ga}_2\text{O}_3$  est discutée, cette problématique est abordée en regardant la perspective d'utilisation du  $p\text{-Ga}_2\text{O}_3$  dans les structures de dispositifs de puissance. Pt et Ti/Pt/Au ont été identifiés comme formant : des contacts Schottky et quasi-ohmiques avec  $p\text{-Ga}_2\text{O}_3$ , respectivement. La méthodologie CTLM pour évaluer la résistance de contact spécifique correspondante a été développée avec des masques photo-lithographiques.

---

## Acknowledgement

At this point, I would like to express my deepest gratitude and appreciation to all those who have supported and guided me throughout my PhD journey. Without their valuable contributions, this thesis would not have been possible.

First and foremost, I am immensely grateful to my supervisors, Dr. Ekaterine Chikoidze and Prof. Yves Dumont, for the discussion together we had, the infinite patience they showed, for their unwavering support, invaluable guidance, and continuous encouragement. Their expertise, knowledge, and dedication have been instrumental in shaping my growth in research and academic.

I am thankful to my colleagues in GEMaC for providing the necessary support, sharing their knowledge. I would like to acknowledge Dr. Corinne Sartel and Dr. Vincent Sallet for our fruitful discussions related to the MOCVD growth of thin films, M. Guillaume Bouchez, for his help and explanations on the optical characterizations, Dr. Bruno Berini for doping numbers of metal depositions by RF sputtering. I would like to thank Dr. Thierry Kociniowski, Dr. Gaëlle Amiri, and Dr. Christèle Vilar, for providing me with training in the operation of experimental equipment. I also want to thank M. Sébastien Colinot and M. Stéphane Denise, our mechanical experts, for their assistance in the design and development of our measurement equipment. I would like to thank Prof. Julien Barjon and Prof. Jean-Michel Chauveau for giving me the opportunity to teach physics experiments courses.

I am deeply grateful to our various collaborators. I would like to thank Dr. Amador Pérez-Tomás in Institut Català de Nanociència i Nanotecnologia (ICN2), Spain; Prof. Tamar Tchelidze in Ivane Javakhishvili Tbilisi State University, Georgia; our neighbour Dr. Mathieu Frégnaux in Institut Lavoisier (ILV) in Versailles, France; Dr. Jurgen Von Bardeleben and Dr. Yunlin Zheng in Institut des Nanosciences de Paris (INSP), Sorbonne Université, France; Prof. Georges Bremond, Prof. Jean-Marie Bluet, Prof. Gérard Guillot in Institut National des Sciences Appliquées de Lyon (INSA Lyon), France; Prof. Mike Jennings and his PhD student Jacob Asher in Swansea University, UK, for their valuable contributions, necessary support for my works, insightful discussions on various topics, and for generously sharing their knowledge and experience with me.

I would like to express my sincere appreciation to my lab mates Ismail, Sumit, Nour, Hamid, Mohamed, Clarisse, ... and my office mates Yoan, Subodh, Sébastien, Trang, ...

---

who have been there for me, not only for fruitful discussions, but also for offering support, laughter, and small breaks during everyday life.

While it is impossible to name everyone individually, I am grateful to all those who have contributed in various ways, whether big or small, to the completion of this thesis. Your support and encouragement have meant the world to me. Thank you all once again for being an integral part of my PhD journey and for your invaluable contributions.

*To my family, my wife Yangkexin Gao (高杨可馨), my mother Li Xing (邢莉) and my father Qingwang Chi (池清旺)*

---

# Table of content

<b>Abstract.....</b>	<b>II</b>
<b>Résumé substantiel.....</b>	<b>IV</b>
<b>Acknowledgement.....</b>	<b>VII</b>
<b>Table of content .....</b>	<b>IX</b>
<b>Introduction.....</b>	<b>- 1 -</b>
<b>1. <math>\beta</math>-Ga<sub>2</sub>O<sub>3</sub> and ZnGa<sub>2</sub>O<sub>4</sub> – Overview of Properties.....</b>	<b>- 7 -</b>
1.1 $\beta$ -Ga <sub>2</sub> O <sub>3</sub> .....	- 7 -
1.1.1 Fundamental properties of $\beta$ -Ga <sub>2</sub> O <sub>3</sub> .....	- 7 -
1.1.2 Bulk and thin films growth techniques.....	- 9 -
1.1.3 Point defects studies and doping issues.....	- 11 -
1.2 ZnGa <sub>2</sub> O <sub>4</sub> .....	- 16 -
1.2.1 Fundamental properties .....	- 17 -
1.2.2 Bulk and thin film growth techniques .....	- 18 -
1.2.3 Point defects and self-doping effect .....	- 20 -
1.3 Summary.....	- 21 -
<b>2. Experimental Techniques and Methods.....</b>	<b>- 23 -</b>
2.1 Metal organic chemical vapor deposition (MOCVD) .....	- 23 -
2.2 Structural, morphological, and chemical characterizations .....	- 24 -
2.2.1 X-ray diffraction (XRD).....	- 24 -
2.2.2 Scanning electron microscopy (SEM):.....	- 25 -
2.2.3 Transmission electron microscopy (TEM):.....	- 25 -
2.2.4 Secondary ion mass spectrometry (SIMS): .....	- 26 -
2.2.5 Raman spectroscopy .....	- 26 -
2.2.6 X-ray photoelectron spectroscopy (XPS) .....	- 27 -
2.3 Optical characterization .....	- 28 -
2.3.1 Transmittance and reflectance spectroscopy .....	- 28 -
2.3.2 Photoluminescence spectroscopy .....	- 29 -
2.4 Electrical transport characterization .....	- 30 -
2.4.1 Electrical contact preparation .....	- 30 -
2.4.2 Current-voltage characteristics and photocurrent test .....	- 30 -
2.4.3 Hall effect measurements .....	- 31 -
2.4.4 Physical property measurement system (PPMS).....	- 39 -
2.4.5 Seebeck effect measurements.....	- 40 -

---

<b>3.</b>	<b><math>\beta</math>-Ga<sub>2</sub>O<sub>3</sub>: Experimental Results and Discussion</b>	<b>- 41 -</b>
3.1	Undoped $\beta$ -Ga <sub>2</sub> O <sub>3</sub> thin films	- 41 -
3.1.1	Structural characterizations	- 42 -
3.1.2	Electrical transport properties	- 44 -
3.1.3	Optical band gap and photoluminescence	- 48 -
3.1.4	XPS valence band tail states	- 50 -
3.1.5	Influence of the growth temperature on electrical properties	- 51 -
3.2	Zn doping in $\beta$ -Ga <sub>2</sub> O <sub>3</sub>	- 54 -
3.2.1	State of the art for Zn doping in $\beta$ -Ga <sub>2</sub> O <sub>3</sub>	- 54 -
3.2.2	Thermodynamic analysis of point defects for Zn:Ga <sub>2</sub> O <sub>3</sub> system	- 56 -
3.3	Zn doped $\beta$ -Ga <sub>2</sub> O <sub>3</sub> thin films: experimental results	- 60 -
3.3.1	Structural and morphological characterizations	- 61 -
3.3.2	Optical properties	- 63 -
3.3.3	Electrical transport properties	- 65 -
3.3.4	Critical electric field	- 68 -
3.3.5	Summary	- 74 -
<b>4.</b>	<b>ZnGa<sub>2</sub>O<sub>4</sub>: Experimental Results and Discussion</b>	<b>- 77 -</b>
4.1	From $\beta$ -Ga <sub>2</sub> O <sub>3</sub> to ZnGa <sub>2</sub> O <sub>4</sub> : structural characterizations	- 77 -
4.2	Bipolar self-doping in ultra-wide band gap spinel ZnGa <sub>2</sub> O <sub>4</sub>	- 80 -
4.2.1	Structural studies of <i>n</i> -type and <i>p</i> -type ZnGa <sub>2</sub> O <sub>4</sub> thin films	- 82 -
4.2.2	Electronic properties of <i>n</i> -type and <i>p</i> -type ZnGa <sub>2</sub> O <sub>4</sub> thin films	- 83 -
4.2.3	Valence Band and Optical Band gap of <i>n</i> - and <i>p</i> -ZnGa <sub>2</sub> O <sub>4</sub> layers	- 87 -
4.2.4	Electrical Transport properties of <i>n</i> - and <i>p</i> -ZnGa <sub>2</sub> O <sub>4</sub> layers	- 90 -
4.2.5	Summary	- 95 -
4.3	Influence of the oxygen content on the electrical properties	- 96 -
4.3.1	Structural characterization	- 96 -
4.3.2	Electrical transport properties	- 98 -
4.3.3	Optical transmittance	- 99 -
4.3.4	Electronic properties	- 100 -
4.3.5	Photo-sensibility test	- 102 -
4.4	Estimation of the critical electric field for ZnGa <sub>2</sub> O <sub>4</sub>	- 103 -
4.4.1	Structural characterization for ZnGa <sub>2</sub> O <sub>4</sub> /Si	- 103 -
4.4.2	Electrical transport properties of ZnGa <sub>2</sub> O <sub>4</sub> // <i>c</i> -Al <sub>2</sub> O <sub>3</sub>	- 104 -
4.4.3	Critical electric field of ZnGa <sub>2</sub> O <sub>4</sub>	- 106 -
4.5	Summary	- 107 -
<b>5.</b>	<b>Electrical Contacts to <i>p</i>-type <math>\beta</math>-Ga<sub>2</sub>O<sub>3</sub></b>	<b>- 109 -</b>
5.1	State of the art	- 109 -
5.2	Experimental methods	- 112 -

---

---

5.2.1	Circular transmission line model (CTLTM) method .....	- 112 -
5.2.2	Photolithography and metal deposition process .....	- 114 -
5.2.3	Calculation and measurement methods .....	- 119 -
5.3	Experimental results and discussion .....	- 122 -
5.4	Summary and next steps .....	- 126 -
<b>6.</b>	<b>Conclusion and Perspectives .....</b>	<b>- 129 -</b>
	<b>References.....</b>	<b>- 133 -</b>
<b>A.</b>	<b>List of Publications and Presentations .....</b>	<b>- 163 -</b>
<b>B.</b>	<b>List of Figures .....</b>	<b>- 165 -</b>
<b>C.</b>	<b>List of Tables.....</b>	<b>- 172 -</b>

## Introduction

At the global level, energy production has mainly been based on the consumption of fossil resources, this not only consumes excess fossil energy, which is limited but also leads to pollution. The Paris Conference (COP 21) led to a new international climate agreement, applicable to all countries, aimed at keeping global warming to 1.5 – 2 °C, in accordance with the recommendations of the Intergovernmental Panel of Experts on climate change (IPCC) (Ministère de l'Europe et des Affaires, 2015). The COP 26 summit held in Glasgow brought parties together to accelerate action towards the goals of the Paris Agreement and the UN Framework Convention on Climate Change (COP26 Webpage, 2021). Two separate developments are needed to secure stable energy supplies soon: widespread adoption of revolutionary sustainable generation technologies and efficient energy use. The one very concrete way to reach the target of energy efficiency is to turn to more efficient power electronics, which is the application of solid-state electronics to the control and conversion of electric power, it plays a crucial role in achieving the goal of reduced power consumption.

Power semiconductor electronics is the application of electronics to the control and conversion of electric power. Power electronics based on silicon has already been widely used in industrial, commercial, and transportation systems (Bose, 2017). However, it has low operating temperature and low breakdown voltage, which makes its applications limited. Consequently, a clear transition to more electric energy and efficient systems is still mandatory (Steimer, 2010). Indeed, for the time being, different semiconductor materials such as 4H-SiC, GaN, diamond, AlN, and  $\beta$ -Ga<sub>2</sub>O<sub>3</sub>, etc. are competing to be the next choice for highly efficient power electronics. Among wide and ultra-wide band gap (UWBG) semiconductors, monoclinic  $\beta$ -Ga<sub>2</sub>O<sub>3</sub> has attracted much attention for power electronics applications recently.

$\beta$ -Ga<sub>2</sub>O<sub>3</sub> has an ultra-wide band gap of up to 5 eV, high critical electrical field compared to wide band gap semiconductors SiC and GaN (**Figure 1-1**), and the successful growth and availability of 6-inch wafers from bulk single crystals on the market (Novel Crystal Technology, Japan). The targeted power electronic devices are high voltage rectifiers, aiming to reduce energy consumption, achieve compact designs, and expand the voltage and temperature range of applications (**Figure 1-2**). For the time being, high electron concentration (up to 10<sup>20</sup> cm<sup>-3</sup>) in  $\beta$ -Ga<sub>2</sub>O<sub>3</sub> can be achieved usually by Sn, Si, and Ge dopants.

Currently,  $\beta$ -Ga<sub>2</sub>O<sub>3</sub> based power electronic devices made are all unipolar (i.e., fabricated with  $n$ -type  $\beta$ -Ga<sub>2</sub>O<sub>3</sub>): field effect transistors (Higashiwaki et al., 2016a; Lv et al., 2020), Schottky barrier diode (Hu et al., 2020; Wang et al., 2016),  $p$ -NiO/ $n$ -Ga<sub>2</sub>O<sub>3</sub> diode (Gong et al., 2021; Zhang et al., 2022), etc have been demonstrated recently. The breakdown voltage can reach 8.32 kV for a  $p$ -NiO/ $n$ -Ga<sub>2</sub>O<sub>3</sub> diode (Zhang et al., 2022).

However, the vertical bipolar (i.e.  $p$ - $n$  or  $p$ - $i$ - $n$  structure) power electronic devices are required to sustain ultra-high ( $> 10$  kV) reverse voltage. The  $p$ -type conductivity of UWBG oxides is well-known to be very challenging, due to large hole effective mass, and thus low hole mobility, and the compensation by donor defects such as oxygen vacancies  $V_O$  (Zhang et al., 2020). The first reported hole concentration of undoped  $p$ -type  $\beta$ -Ga<sub>2</sub>O<sub>3</sub> at room temperature is as low as  $2 \times 10^{13} \text{ cm}^{-3}$  (Chikoidze et al., 2017a), which is far to be enough for the requirement of device operation.

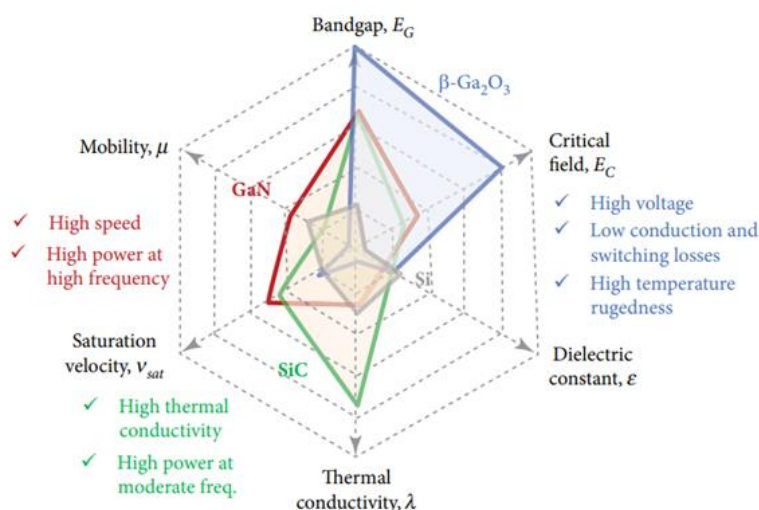


Figure 1-1. Comparison of semiconductor material parameters (Speck and Esmat, 2023).

Similar to  $\beta$ -Ga<sub>2</sub>O<sub>3</sub>, cubic spinel oxide zinc gallate (ZnGa<sub>2</sub>O<sub>4</sub>) also has an ultra-wide band gap of up to 5 eV. The existing reports related to ZnGa<sub>2</sub>O<sub>4</sub> are mainly focused on its application in photonic and opto-electronic devices. Consequently, the optical properties are largely studied, while the research on the electrical properties is very limited, though ZnGa<sub>2</sub>O<sub>4</sub> based metal oxide semiconductor field effect transistor (MOSFET) (L.-C. Cheng et al., 2018; Shen et al., 2017), thin film transistor (TFT) (Cheng et al., 2019; Jang et al., 2020), deep ultra-violet phototransistors (Y.-C. Shen et al., 2019) have already been

demonstrated. However, further deep studies of  $\text{ZnGa}_2\text{O}_4$  electrical conductivity and point defects is still clearly required.

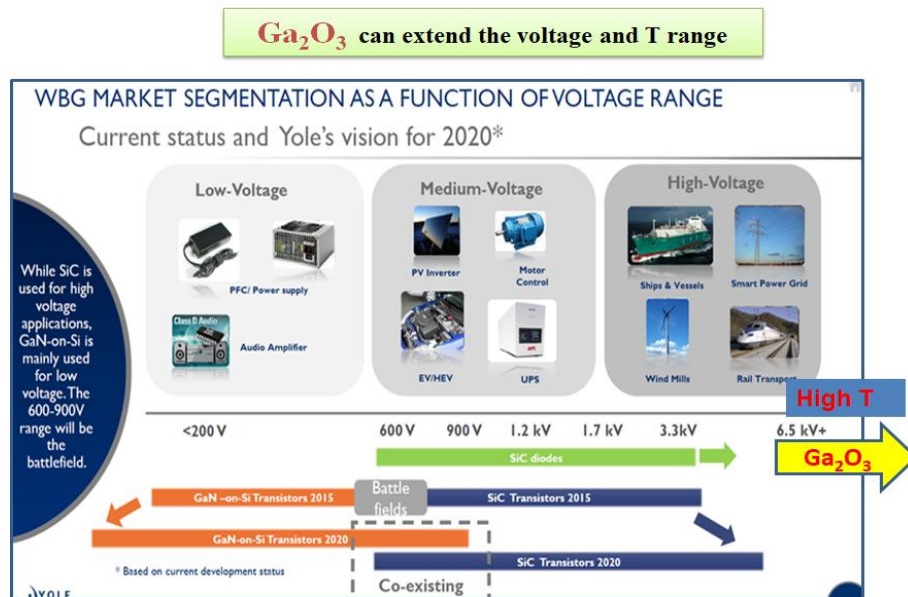


Figure 1-2. Targeted applications of wide bandgap semiconductors (GaN and SiC) and  $\text{Ga}_2\text{O}_3$ .  $\text{Ga}_2\text{O}_3$  has potential application in both medium and high-voltage range.

Overall, it is clear that the study and the understanding of the electronic properties of  $\text{ZnGa}_2\text{O}_4$  and  $\beta\text{-Ga}_2\text{O}_3$  are of great importance for the application of these materials in various electronic devices.

**The objective of my work** is to study the electronic properties of the metal organic chemical vapor deposition (MOCVD) grown *p*-type  $\beta\text{-Ga}_2\text{O}_3$  and both *n*-type and *p*-type  $\text{ZnGa}_2\text{O}_4$  thin films. The manuscript is arranged as follows:

Chapter 1 (State of the Art) provides an overview of the fundamental properties, recent theoretical and experimental reports on the point defects, and electronic properties for  $\beta\text{-Ga}_2\text{O}_3$  and  $\text{ZnGa}_2\text{O}_4$ .

Chapter 2 (Experimental Techniques and Methods) describes the experimental methods, techniques, and facilities used to carry out presented works, including thin films growth technique, characterization methods and set-ups. Detailed descriptions are given for the electrical transport properties measurements (both set-ups and methods).

In Chapter 3 ( $\beta\text{-Ga}_2\text{O}_3$ : Experimental Results and Discussion), the electronic properties of MOCVD grown  $\beta\text{-Ga}_2\text{O}_3$  layers are discussed. The first objective is, to get an undoped highly compensated semi-insulating *p*-type  $\beta\text{-Ga}_2\text{O}_3$  layer, suitable for further *p*-type doping

---

trials. As a II group element, Zn is expected to substitute Ga and become an effective dopant in  $\beta$ -Ga<sub>2</sub>O<sub>3</sub>. Thus, Zn was selected as a dopant, in order to improve the hole conductivity in  $\beta$ -Ga<sub>2</sub>O<sub>3</sub>. My objective was to study the influence of Zn dopant on electrical and optical properties in  $\beta$ -Ga<sub>2</sub>O<sub>3</sub>. The investigation of Zn-doped  $\beta$ -Ga<sub>2</sub>O<sub>3</sub> is started with the thermodynamic study of point defects in the  $\beta$ -Ga<sub>2</sub>O<sub>3</sub>:Zn system. Then, the experimental results of  $\beta$ -Ga<sub>2</sub>O<sub>3</sub>:Zn thin films grown by MOCVD, with different Zn doping levels ( $10^{16} - 2 \times 10^{19} \text{ cm}^{-3}$ ), are presented. According to both of the experimental facts and thermodynamic calculations, we observed the amphoteric nature of Zn in  $\beta$ -Ga<sub>2</sub>O<sub>3</sub>, Zn can take both interstitial and gallium sites, being donor Zn<sub>i</sub> and acceptor Zn<sub>Ga</sub> centres depending on the doping concentration, which is the so-called impurity “auto-compensation” effect. Taking advantage of this effect, by further lowering the hole concentration, we aimed to further increase the critical electric field of  $\beta$ -Ga<sub>2</sub>O<sub>3</sub>. Therefore, the critical electric field of undoped and Zn ( $2 \times 10^{19} \text{ cm}^{-3}$ ) doped  $\beta$ -Ga<sub>2</sub>O<sub>3</sub> thin films is experimentally estimated.

In Chapter 4 (ZnGa<sub>2</sub>O<sub>4</sub>: Experimental Results and Discussion), the experimental results for the MOCVD-grown ZnGa<sub>2</sub>O<sub>4</sub> layers are presented. With the further incorporated Zn concentration in  $\beta$ -Ga<sub>2</sub>O<sub>3</sub>, the ternary semiconductor ZnGa<sub>2</sub>O<sub>4</sub> started to form on the sapphire substrates. I first showed the transformation from pure monoclinic  $\beta$ -Ga<sub>2</sub>O<sub>3</sub> to pure cubic spinel ZnGa<sub>2</sub>O<sub>4</sub>. As a ternary compound, ZnGa<sub>2</sub>O<sub>4</sub> has a higher flexibility of doping than binary semiconductors. A bunch of theoretical works reported the “self-doping” effect (De Vos et al., 2016; Paudel et al., 2011b; Shi et al., 2014; Stoica and S Lo, 2014) in ZnGa<sub>2</sub>O<sub>4</sub>, which generally refers to the creation of cross-substitution of the cations on the tetrahedral and octahedral sites, leading to variations in the electrical, optical properties and offering opportunities for tailoring the electronic behavior of spinel oxide compounds. Besides, though the room-temperature conducting ( $\sim 10^2 \text{ S/cm}$ ) intrinsic *n*-type ZnGa<sub>2</sub>O<sub>4</sub> thin films with electron concentration  $n > 2 \times 10^{19} \text{ cm}^{-3}$  have already been achieved (L.-C. Cheng et al., 2018; Cheng et al., 2019; Look et al., 2020), while the origin of conductivity and the conduction mechanism are still open questions. Therefore, I aimed to address these open questions by conducting a comprehensive investigation of the electronic properties and carrier transport mechanisms. Additionally, further experimental evidence of the “self-doping” effect of ZnGa<sub>2</sub>O<sub>4</sub> is shown by a comparative study of the structural, optical, and electronic properties between intrinsic semi-insulating *p*-type and conducting *n*-type ZnGa<sub>2</sub>O<sub>4</sub> layers. Since the study on the electrical properties of ZnGa<sub>2</sub>O<sub>4</sub> is still very limited, we aimed to gain a deeper understanding of the growth parameters influencing the

conductivity in the  $\text{ZnGa}_2\text{O}_4$  films. Thus, the influence of the oxygen content in MOCVD-grown  $\text{ZnGa}_2\text{O}_4$  layers is investigated. At the end of this chapter, the first experimental investigation of the critical electric field of  $\text{ZnGa}_2\text{O}_4$  is reported.

Chapter 5 (Electrical Contacts to  $p$ -type  $\beta\text{-Ga}_2\text{O}_3$ ) presents my preliminary study of electrical metal contacts to  $p$ -type  $\beta\text{-Ga}_2\text{O}_3$ , in perspective of higher current conditions for future power-electronic applications under high voltages. The objective was to first establish a protocol for electrical contact preparation by photolithography, and identify the electrical contact types among the metals selected (Ag, Pt, Ti/Pt/Au) and  $p$ -type  $\beta\text{-Ga}_2\text{O}_3$ . The related experimental methods, including the photolithography process, metal deposition, and  $I$ - $V$  characterization methods, are presented in this chapter.

Chapter 6 (Conclusion and Perspectives) summarizes the results in this manuscript and discusses future works.

---

---

# 1. $\beta$ -Ga<sub>2</sub>O<sub>3</sub> and ZnGa<sub>2</sub>O<sub>4</sub> – Overview of Properties

## 1.1 $\beta$ -Ga<sub>2</sub>O<sub>3</sub>

Gallium oxide (Ga<sub>2</sub>O<sub>3</sub>) has, at least, six crystalized polymorphs of which only the monoclinic  $\beta$  phase is thermodynamically stable at high temperatures, while the others are metastable and tend to convert to  $\beta$  upon high-temperature treatments including the phases: corundum  $\alpha$ , cubic  $\delta$ , hexagonal  $\varepsilon$ , defective-spinel  $\gamma$ , and orthorhombic  $\kappa$  polymorph (Spaziani and Lu, 2018). Early crystallographic studies for single crystals (Geller, 1960) together with diverse luminescence studies of doped  $\beta$ -Ga<sub>2</sub>O<sub>3</sub> were reported as early as the 1960s (Blasse and Bril, 1970). Lorenz et al. (Lorenz et al., 1967) reported in 1966 that  $n$ -type Ga<sub>2</sub>O<sub>3</sub> exhibits mobilities in the range of 100 cm<sup>2</sup>/(V·s) and an adequate device doping of 10<sup>18</sup> cm<sup>-3</sup> can be achieved just by controlling the native oxygen vacancies' density. Its deep-ultraviolet intrinsic bandgap of around 4.5 – 5 eV and excellent photoconductivity are also well-known from early contemporary studies (Tippins, 1965). It was not until this decade that the research on  $\beta$ -Ga<sub>2</sub>O<sub>3</sub> was rejuvenated due to the limitations of silicon-based electronic devices (low operation temperature and breakdown voltage).  $\beta$ -Ga<sub>2</sub>O<sub>3</sub> itself is also a potential candidate for next-generation power devices because of: (i) its fundamental properties (Section 1.1.1). (ii) the further availability of large-area single crystals by melt growth, and functional epitaxial layers (Section 1.1.2). (iii) easy  $n$ -type doping. However, to fully realize the functionality of  $\beta$ -Ga<sub>2</sub>O<sub>3</sub> in electronics, it requires further development on  $p$ -type conductivity, thus the control of point defects is a central issue. a state of the art for the current study on defects in  $\beta$ -Ga<sub>2</sub>O<sub>3</sub> and progress in the achievement of  $p$ -type is presented in Section 1.1.3.

### 1.1.1 Fundamental properties of $\beta$ -Ga<sub>2</sub>O<sub>3</sub>

**Structure:** The monoclinic structure of  $\beta$ -Ga<sub>2</sub>O<sub>3</sub> belongs to the space group  $C2/m$  as shown in **Figure 1-1** (Mastro et al., 2020). The lattice parameters are  $a = 12.23$  Å,  $b = 3.04$  Å,  $c = 5.80$  Å, and  $\alpha = \gamma = 90^\circ$ ,  $\beta = 103.83^\circ$ . Each unit consists of two inequivalent Ga cations and three inequivalent O ions. Ga (I) in the tetrahedral site bonds to four O ions and Ga (II)

in the octahedral site bonds to six O ions. O (I) bonds to two Ga (II) ions and one Ga (I) ion, O (II) bonds to one Ga (II) ion and two Ga (I) ions, while O (III) bonds to three Ga (II) ions and one Ga (I) ion. The crystallographically inequivalent sites of different coordination in the unit cell lead to strong orientation dependence and anisotropy of several physical properties (e.g., anisotropic effective mass, impact ionization parameters (Ghosh and Singiseti, 2018a, 2018b, 2017), optical absorption (Ricci et al., 2016)), and possible device development opportunities (e.g., different electrical contact performance depending on the  $\beta$ -Ga<sub>2</sub>O<sub>3</sub> single crystal orientation (Lee et al., 2022a)).

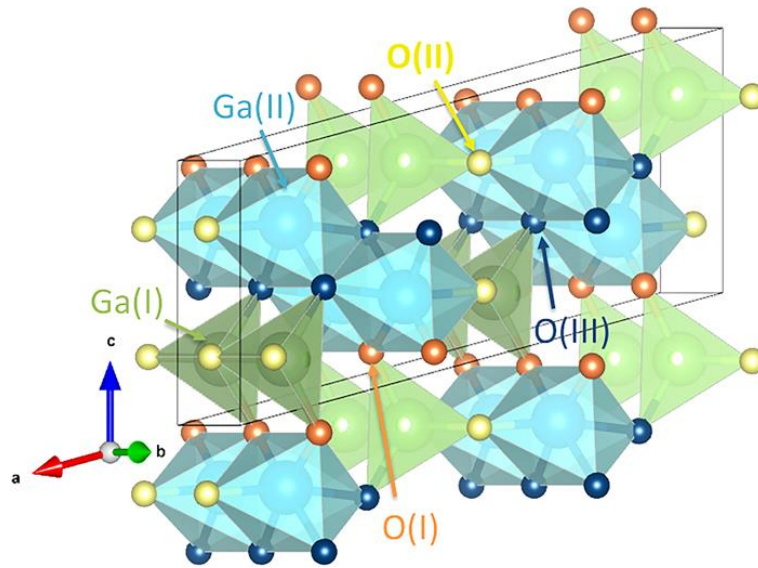


Figure 1-1. Unit cell of  $\beta$ -Ga<sub>2</sub>O<sub>3</sub> (Mastro et al., 2020).

**Band structure:** The electronic structure of  $\beta$ -Ga<sub>2</sub>O<sub>3</sub> has been studied using the density functional theory (DFT) and photoemission spectroscopy measurements, the general consensus is that,  $\beta$ -Ga<sub>2</sub>O<sub>3</sub> has a direct band gap of  $\sim 4.88$  eV for the vertical  $\Gamma$ - $\Gamma$  transition, although there is a much weaker  $\Gamma$ - $M$  transition leads to an indirect band gap of with only a few tens of meV less (He et al., 2006; Janowitz et al., 2011; Mock et al., 2017; Peelaers and Van de Walle, 2015; Varley et al., 2010).

**Thermal conductivity:**  $\beta$ -Ga<sub>2</sub>O<sub>3</sub> has a poor thermal conductivity of  $\sim 10 - 27$  W/(m·K) at room temperature, which is also anisotropic and dependent on the direction of planes (Galazka et al., 2014; Guo et al., 2015; Jiang et al., 2018; Santia et al., 2015), though the highest value was found along the [010] direction up to  $27 \pm 2$  W/(m·K). However, several solutions have been proposed to address the thermal dissipation difficulty for actual device

applications. Oda *et al.* (Oda et al., 2016) lifted off the  $\alpha$ -Ga<sub>2</sub>O<sub>3</sub> epilayer from the sapphire substrate to fabricate the Schottky barrier diode. Hetero-growth of  $\beta$ -Ga<sub>2</sub>O<sub>3</sub> on GaN (Cao et al., 2018; Lyu and Pasquarello, 2020; Muhammed et al., 2014) or AlN (Lyu and Pasquarello, 2020; Sun et al., 2017) substrates was also studied, the in-plane mismatch between the (-201)  $\beta$ -Ga<sub>2</sub>O<sub>3</sub> and (0002) AlN was found to be as low as 2.4% (Sun et al., 2017). Additionally, flip-chip technology was employed for the thermal management at the device level (Chatterjee et al., 2019).

**Other parameters:** The melting point of  $\beta$ -Ga<sub>2</sub>O<sub>3</sub> is  $\sim 1800$  °C, which allows the melt-growth at high temperatures (Galazka et al., 2010). All the other polymorphs will transform into the beta phase within  $\sim 750 - 950$  °C. Ghosh and Singiseti (Ghosh and Singiseti, 2017) calculated the drift velocity of electrons of  $\beta$ -Ga<sub>2</sub>O<sub>3</sub> and found that, an average peak velocity at an electric field of 200 kV/cm can reach  $\sim 2 \times 10^7$  cm/s. The critical electric field was first proposed to be as high as 8 MV/cm (Higashiwaki et al., 2012) by extrapolation. Experimentally, a high critical field of 5.2 MV/cm was demonstrated (Yan et al., 2018), and up to 13.2 MV/cm for Zn doped *p*-type  $\beta$ -Ga<sub>2</sub>O<sub>3</sub> (Chikoidze et al., 2020b). Experimental works demonstrated the electron mobility  $\mu_n \sim 200$  cm<sup>2</sup>/(V·s) of  $\beta$ -Ga<sub>2</sub>O<sub>3</sub> (Feng et al., 2020; Rajapitamahuni et al., 2022).

### 1.1.2 Bulk and thin films growth techniques

To explore the structural, electrical, and optical characteristics of  $\beta$ -Ga<sub>2</sub>O<sub>3</sub> and develop devices, it is crucial to begin with high-quality bulk crystals and thin films. Commonly used growth techniques of **bulk  $\beta$ -Ga<sub>2</sub>O<sub>3</sub> crystal** are: Verneuil method (Chase, 1964; Harwig and Schoonman, 1978; Lorenz et al., 1967), Czochralski (CZ) method (Galazka, 2018; Galazka et al., 2021, 2020b, 2020a, 2016; Irmscher et al., 2011; Saleh et al., 2020), floating-zone (FZ) method (Cui et al., 2019; Hossain et al., 2019; Suzuki et al., 2007; Tomioka et al., 2019; Villora et al., 2004; W. Zhou et al., 2017), edge-defined film fed (EFG) method (Higashiwaki et al., 2016b; Kuramata et al., 2018, 2016; Yao et al., 2020), Bridgman (horizontal or vertical, HB and VB) method (Hoshikawa et al., 2020b, 2020a, 2016). **Table 1-1** summarizes the basic features of melt growth methods reported so far. It is worth noting that the largest wafer size of 6-inch width was achieved by EFG growth (Kuramata et al., 2016).

Table 1-1. Outcome of  $\beta$ -Ga<sub>2</sub>O<sub>3</sub> bulk crystal growth methods. Remarks (a) and (b) refer to: a) in diameter, b) in width.

Method	Verneuil	FZ	CZ	EFG	VB
Bulk size	3/8-inch <sup>a</sup> 1-inch <sup>b</sup>	1-inch <sup>a</sup>	2-inch <sup>a</sup>	6-inch <sup>b</sup> 4-inch <sup>a</sup>	2-inch <sup>a</sup>
Growth rate [mm/h]	10	20 - 40	2	15	5
FWMH [arcsec]	-	22	22 – 50	17	10 – 50
Dislocation density [cm <sup>-2</sup> ]	-	-	~10 <sup>3</sup>	10 <sup>3</sup>	10 <sup>2</sup> – 2×10 <sup>3</sup>
Residual impurity [cm <sup>-3</sup> ]	2×10 <sup>18</sup>	~10 <sup>17</sup> (Si, Sn)	~10 <sup>16</sup> (Si)	~10 <sup>17</sup> (Si)	~several tens wt.ppm (Rh)
Intentional doping [cm <sup>-3</sup> ]	~10 <sup>19</sup> (Mg) ~10 <sup>21</sup> (Zr) 900°C	~10 <sup>19</sup> (Nb, Ta)	~10 <sup>19</sup> (Sn, Si, Hf)	6-7×10 <sup>18</sup> (Si, Sn)	3.6×10 <sup>18</sup> (Sn)

For epitaxial thin film growth of  $\beta$ -Ga<sub>2</sub>O<sub>3</sub>, various methods have been used, such as Molecular Beam Epitaxy (MBE), metal organic chemical vapor deposition (MOCVD), mist-CVD, pulsed laser deposition (PLD), halide vapor phase epitaxy (HVPE), atomic layer deposition (ALD), and so on. Here, I will focus on recent progress of the properties of the MOCVD-grown layers, since our thin films are grown by this technique.

The **MOCVD technique** has demonstrated its ability to generate high-quality epitaxial films with a rapid growth rate and consistent, controllable doping. It is highly scalable, thereby suitable for large-scale production.  $\beta$ -Ga<sub>2</sub>O<sub>3</sub> thin films grown by the MOCVD technique uses Ga-based organic material such as Trimethylgallium (TMGa) and Triethylgallium (TEGa) as metal precursors, and N<sub>2</sub>O or pure O<sub>2</sub> gas as the source of oxygen. TMGa is cheaper than TEGa and provides a higher growth rate of up to 10  $\mu$ m/hour (Alema et al., 2017b), due to a shorter pyrolysis pathway of 2 steps vs. 3 steps for TEGa (Baldini et al., 2016), and high vapor pressure that allows the large concentration introduced during the growth (Seryogin et al., 2020). Seryogin *et al.* (Seryogin et al., 2020) demonstrated that the growth rate is almost linearly proportional to the TMGa flow during the MOCVD growth, which can be as high as 5.8  $\mu$ m/hour, with 580  $\mu$ mol/min TMGa. The highest growth rate to date is 4  $\mu$ m/hour using TEGa (Tadjer et al., 2020). However, TEGa allows a relatively less contamination of carbon and hydrogen than TMGa, while it is process dependent (e.g., high O<sub>2</sub>/TMGa ratio can reduce carbon contamination (Seryogin et al., 2020)). The use of N<sub>2</sub>O as

the source of oxygen can lead to a high resistivity of the film, which is attributed to the incorporation of N (substituting O becoming acceptor impurity N<sub>O</sub>) compensating donors (Tadjer et al., 2018; Wong et al., 2018). Besides, high quality  $\beta$ -Ga<sub>2</sub>O<sub>3</sub> epilayers can be achieved by this technique, Li *et al.* (Z. Li et al., 2020) reported a homoepitaxially grown film with FWMH and surface roughness of 21.6 arcsec, and 0.68 nm, respectively. The highest mobility achieved using MOCVD was 194 cm<sup>2</sup>/(V·s) (Feng et al., 2020). This technique is also available for both *n*- and *p*-type dopability (Alema et al., 2019; Chikoidze et al., 2020c).

### 1.1.3 Point defects studies and doping issues

A number of experiments and calculations-based studies provide the electronic behaviors of intrinsic and extrinsic defects, and interactions between intrinsic and dopants in  $\beta$ -Ga<sub>2</sub>O<sub>3</sub>. Here, I will focus on the studies on the intrinsic defects, including oxygen interstitials (O<sub>i</sub>), oxygen vacancies (V<sub>O</sub>), gallium vacancies (V<sub>Ga</sub>), gallium interstitials (Ga<sub>i</sub>), divacancy complex (V<sub>O</sub> – V<sub>Ga</sub>), and interstitial – divacancy (2 V<sub>Ga</sub> – Ga<sub>i</sub>) complex.

**Oxygen vacancies** were considered as the source of the *n*-type conductivity in  $\beta$ -Ga<sub>2</sub>O<sub>3</sub> according to the experimental observations that the electrical conductivity is inversely dependent on the oxygen partial pressure (Aubay and Gourier, 1993; Hajnal et al., 1999; Ueda et al., 1997; Yamaga et al., 2003). Based on the electron paramagnetic resonance (EPR) study, V<sub>O</sub> was proposed as a shallow donor (Aubay and Gourier, 1993; Yamaga et al., 2003). However, DFT and *ab initio* calculations (Deák et al., 2017; Ingebrigtsen et al., 2019a; Usseinov et al., 2021, 2022; Varley et al., 2010) proposed that V<sub>O</sub> is too deep (transition energy is more than 1 eV) to be responsible for the *n*-type conductivity, its formation energy is also very high in oxygen-rich condition (Deák et al., 2017; Ingebrigtsen et al., 2019a; Matsubara et al., 2017; Usseinov et al., 2022; Varley et al., 2010; Zacherle et al., 2013). Experimentally, the V<sub>O</sub> was also correlated with blue luminescence by the comparison of the intensity between pure and doped  $\beta$ -Ga<sub>2</sub>O<sub>3</sub> (Onuma et al., 2013; Q. Shi et al., 2019; Shimamura et al., 2008). Besides, only neutral state V<sub>O</sub> and double charged state V<sub>O</sub><sup>2+</sup> are predicted to be stable in  $\beta$ -Ga<sub>2</sub>O<sub>3</sub> (Akiyama et al., 2023; Varley et al., 2010), and was speculated by EPR results (Bhandari and Zvanut, 2021). Instead of causing *n*-type conductivity, they may compensate acceptors (Dong et al., 2017; McCluskey, 2020). The

observed *n*-type conductivity in unintentionally doped  $\beta$ -Ga<sub>2</sub>O<sub>3</sub> single crystals were explained by the unintentionally incorporated shallow impurities such as H, Sn, etc. (Varley et al., 2010).

**Gallium vacancies** are generally recognized as common deep acceptors in  $\beta$ -Ga<sub>2</sub>O<sub>3</sub>, it has low formation energy in oxygen-rich condition, and high ( $-2/-3$ ) transition energy of 0.7 – 2.5 eV depending on the sites, calculation methods (Deák et al., 2017; Ingebrigtsen et al., 2019a; Peelaers et al., 2019; Varley et al., 2011). It is suggested that it may act as self-trapped holes (STHs) and contribute to the so-called polaron behavior of hole conductivity. Tetrahedrally coordinated  $V_{\text{Ga}}$  (I) has a lower formation energy than octahedrally coordinated  $V_{\text{Ga}}$  (II) (Varley et al., 2011). Based on infra-red (IR) absorption spectra, the concentration of  $V_{\text{Ga}}$  (II) in a Czochralski-grown sample was estimated to be 2 – 3 orders of magnitude lower than that of  $V_{\text{Ga}}$  (I) (Portoff et al., 2023). Gallium vacancies was also studied by several experimental methods such as EPR and positron annihilation. In an *n*-type conducting  $\beta$ -Ga<sub>2</sub>O<sub>3</sub> sample, the gallium vacancy is expected to be diamagnetic in the fully occupied state with a charge  $q = -3$  acting as compensating acceptor (He et al., 2022). In this case, there is no EPR signal as the electrons are paired. However, irradiation can create vacancy and lower the Fermi energy below the ( $-2/-3$ ) transition level, leading to  $V_{\text{Ga}}^{2-}$  with one unpaired spin. Then the monovacancy  $V_{\text{Ga}}$  was observed (Bhandari and Zvanut, 2021; Kananen et al., 2017; von Bardeleben et al., 2019). Positron annihilation experiments have confirmed that  $V_{\text{Ga}}$  can form efficiently and act as compensating acceptor in Si-doped *n*-type  $\beta$ -Ga<sub>2</sub>O<sub>3</sub> (Korhonen et al., 2015). Besides, the ionization energy  $E_i = \sim 1.2$  eV (Chikoidze et al., 2017a; Ekaterine Chikoidze et al., 2019) was determined for the free holes in the intrinsic *p*-type  $\beta$ -Ga<sub>2</sub>O<sub>3</sub>, which was attributed to gallium vacancies. In deep level transient spectroscopy (DLTS) measurements, a hole trap peak at  $E_{\text{v}} + \sim 1.2$  eV (H2) has also been observed (Polyakov et al., 2018).

There are limited studies on the interstitial defects in  $\beta$ -Ga<sub>2</sub>O<sub>3</sub>.

**Oxygen interstitials** exhibit different site preferences and electronic behavior depending on the Fermi level (Ingebrigtsen et al., 2019a). It can act as either a deep donor (split-interstitial  $\text{O}_{\text{Si}}$  configurations on the O (I) site) or a deep acceptor (other interstitial configurations in *n*-type) depending on the Fermi levels (Deák et al., 2017; Ingebrigtsen et al., 2019a). It is proposed that the  $\text{O}_{\text{i}}$  is electrically inactive and acts as a hole trap (Deák et

al., 2017) in *n*-type  $\beta$ -Ga<sub>2</sub>O<sub>3</sub>. Also, both O<sub>i</sub> and O<sub>si</sub> configurations have low formation energy in oxygen-rich condition (Deák et al., 2017; Ingebrigtsen et al., 2019a; Zacherle et al., 2013). Ho *et al.* (Ho et al., 2018) assigned the green luminescence to O<sub>i</sub> defect centre.

**Gallium interstitial** was indirectly presumed to be responsible for the *n*-type conductivity in a  $\beta$ -Ga<sub>2</sub>O<sub>3</sub> single crystal (Irmscher et al., 2011) and predicted as an alternative source with respect to V<sub>O</sub> for the electron conductivity. However, it is suggested that Ga<sub>i</sub> is highly mobile and has a high formation energy at extreme oxygen-poor growth conditions (Deák et al., 2017; Ma et al., 2017; Zacherle et al., 2013), making it less likely to be present.

Additional to the single defects, complex defects can also be created due to the interactions between intrinsic or/and extrinsic defects (Binet et al., 1994; Ingebrigtsen et al., 2019a; Varley et al., 2011), and also play crucial roles in  $\beta$ -Ga<sub>2</sub>O<sub>3</sub>. I will focus on the intrinsic complex defects here.

**Divacancy pair (V<sub>Ga</sub> – V<sub>O</sub>)** in  $\beta$ -Ga<sub>2</sub>O<sub>3</sub> has a long history. According to Vasiltsiv *et al.* (Vasiltsiv et al., 1988), the vacancies pair V<sub>Ga</sub>-V<sub>O</sub> are charge-active centers that, together with single Ga vacancies, can act as acceptors, and might be responsible for the blue luminescence. Binet and Gourier (Binet and Gourier, 1998) studied the temperature dependent blue luminescence, and proposed that, a trapped exciton is formed by the capture of an electron in a donor cluster (V<sub>O</sub>) via tunnel transfer by acceptor level (pair of charged V<sub>O</sub> + V<sub>Ga</sub>), resulting in the formation of a donor band, this radiative recombination emits a blue photon. The ionization energy of this acceptor level was speculated to be  $E_V + \sim 0.42$  eV. Similar propositions have also been made by later photoluminescence experiments (Nie et al., 2022; Onuma et al., 2018, 2013; Shimamura et al., 2008; Zhu et al., 2022). Very recently, Zhu *et al.* (Zhu et al., 2022) proposed that the native V<sub>Ga</sub>-V<sub>O</sub> divacancy defects level can be at 4.42 eV from the conduction band ( $E_V + 0.27$  eV in their undoped  $\beta$ -Ga<sub>2</sub>O<sub>3</sub> single crystal) by photoluminescence. Furthermore, abundant gallium and oxygen vacancy complexes were identified by positron-electron annihilation signals irrespective of the conductivity of  $\beta$ -Ga<sub>2</sub>O<sub>3</sub> single crystals (Karjalainen et al., 2021). Theoretically, in oxygen-rich condition, this defect complex was predicted to have comparable or even lower formation energy than single vacancies in oxygen-rich conditions based on *ab initio* and DFT calculations (Frodason et al., 2021; Usseinov et al., 2022). The role and the charge state transition of this defect depend on the Fermi level position (Frodason et al., 2021;

Ingebrigtsen et al., 2019a). As calculated in the ref. (Frodason et al., 2021), the (+2/+1) transition of ( $V_{\text{Ga(II)}} - V_{\text{O(II)}}$ ) is about  $E_V + 0.4$  eV (to clarify, the notations of Ga and O sites are the same as Section 1.1.1), while other configurations such as ( $V_{\text{Ga(I)}} - V_{\text{O(II)}}$ ) or ( $V_{\text{Ga(II)}} - V_{\text{O(I)}}$ ) in *n*-type condition might be correlated with the  $E_2^*$  trap at  $E_C - 0.75$  eV observed by DLTS (McGlone et al., 2019; Wang et al., 2022).

**Divacancy – interstitial complex ( $V_{\text{Ga(I)}} - \text{Ga}_i - V_{\text{Ga(I)}}$ )** was first discovered by Varley *et al.* (Varley et al., 2011), it is suggested that the  $V_{\text{Ga(I)}}$  is metastable, and its presence induces a nearby Ga atom to leave its tetrahedral site, leading to the creation of a second vacancy and the movement of the Ga atom (a migration barrier of 0.53 eV) towards an interstitial site located between the two vacancies. As a result, a divacancy – interstitial complex ( $V_{\text{Ga(I)}} - \text{Ga}_i - V_{\text{Ga(I)}}$ ) complex is formed, which is lower in energy than the isolated vacancy and acts as a deep acceptor. It was then confirmed by scanning transmission electron microscopy (STEM) (Johnson et al., 2019). Besides, Bardeleben *et al.* (von Bardeleben et al., 2019) also proposed that the model of such a complex defect is the most plausible for the one of the EPR center observed in their proton irradiated  $\beta$ -Ga<sub>2</sub>O<sub>3</sub> single crystals.

$\beta$ -Ga<sub>2</sub>O<sub>3</sub> has very good ***n*-type dopability** up to the degenerate state, *n*-type doped  $\beta$ -Ga<sub>2</sub>O<sub>3</sub> with carrier concentration from  $10^{16}$  to  $10^{20}$  cm<sup>-3</sup> (Chikoidze et al., 2016; Guo et al., 2019) has been achieved by Sn and Ge doping by MBE, Si and Sn doping by MOVPE, and Sn doping by MOCVD (Leedy et al., 2017). A high electron mobility at room temperature of 145 – 194 cm<sup>2</sup>/(V·s) (Feng et al., 2020, 2019; Goto et al., 2018; Zhang et al., 2018) has been reached by Si doping, and even till 10<sup>4</sup> cm<sup>2</sup>/(V·s) at 46 K (Alema et al., 2019).

**On the contrary, there is a lack of high hole conductivity in  $\beta$ -Ga<sub>2</sub>O<sub>3</sub>.** And consequently, it is probably the main limitation of emerging gallium oxide technology for power and UV diode electronics.

**Native *p*-type conductivity:** Interestingly, based on thermodynamic calculations for point defects, gallium oxide has been shown that for a growth at 500° C,  $P \approx 1.33 \times 10^{-2}$  atm, a hole concentration around  $p \approx 10^{15}$  cm<sup>-3</sup> can be achieved (Chikoidze et al., 2017a). Experimentally, the native hole conductivity was reported in undoped  $\beta$ -Ga<sub>2</sub>O<sub>3</sub> thin film

grown on *c*-sapphire substrates by pulsed laser deposition (PLD) elaborated by Nanovation (SME, France), with  $\rho = 1.8 \times 10^2 \Omega \cdot \text{cm}$  resistivity, and  $p = 2 \times 10^{13} \text{ cm}^{-3}$  and  $4.2 \text{ cm}^2/(\text{V} \cdot \text{s})$ , hole concentration and hole mobility respectively (Chikoidze et al., 2017a). The determination of conductivity mechanism showed that Ga vacancies act as deep level acceptors with the activation energy of 0.56 eV in the low compensated sample, having ionization energy of 1.2 eV. Later it was shown the improvement of native *p*-type conductivity by post-annealing in an oxygen atmosphere for  $\beta$ -Ga<sub>2</sub>O<sub>3</sub> thin film grown on *c*-sapphire substrates by MOCVD (Ekaterine Chikoidze et al., 2019). After oxygen annealing, the hole concentration increased from  $5.6 \times 10^{14} \text{ cm}^{-3}$  to  $5.6 \times 10^{17} \text{ cm}^{-3}$  at 850 K. The authors claimed that the annealing effect is related to the formation of  $V_{\text{Ga}}^- - V_{\text{O}}^{++}$  complexes as a shallow acceptor center with  $E_a = 0.17 \text{ eV}$  activation energy.

For device application, higher room temperature hole concentration is required, which could be probably achieved by external acceptor impurity incorporation.

There are already extensive **theoretical studies** (Goyal et al., 2021; Kyrtos et al., 2018; Lyons, 2018; Sun et al., 2019; Varley et al., 2012) (standard density functional theory such as DFT and DFT with GGA+U) of acceptor impurity doping of  $\beta$ -Ga<sub>2</sub>O<sub>3</sub> in order to identify efficient *p*-type dopant. Zn, Mg, N can introduce acceptor level but relatively deep (more than 1 eV). Besides, **co-doping** (doping by two elements) has been predicted by DFT, which showed a promising method to get *p*-type  $\beta$ -Ga<sub>2</sub>O<sub>3</sub>, as it can break the solubility limit of mono-doping and improves the photoelectric properties of semiconductor materials. Consequently, conductivity can be increased (L. Li et al., 2020; Ma et al., 2020; Sabino et al., 2019; Zhang et al., 2012a). The impurity level can be as shallow as 0.149 eV above the VBM (Zhang et al., 2012a). More details of theoretical and co-doping can be found in ref. (Chi et al., 2022).

Zn has been predicted to be an effective dopant in  $\beta$ -Ga<sub>2</sub>O<sub>3</sub> and was widely studied, the related state-of-the-art will be presented in Section 3.2 (Zn doping in  $\beta$ -Ga<sub>2</sub>O<sub>3</sub>) together with my experimental results of Zn doping effect in  $\beta$ -Ga<sub>2</sub>O<sub>3</sub>.

Besides, there are limited **experimental works** reported regarding *p*-type doping of gallium oxide. Mg-doped  $\beta$ -Ga<sub>2</sub>O<sub>3</sub> has been studied by Qian *et al.* (Qian et al., 2017) for the photo-blind detector, and the  $\beta$ -Ga<sub>2</sub>O<sub>3</sub> containing 4.92 at. % Mg has shown an acceptor level by XPS. A variation of band gap has also been reported (Tao et al., 2019; Yue et al., 2012).

Islam *et al.* (Islam et al., 2020) reported that hydrogen annealing could vastly reduce the resistivity and reach a remarkable hole density of  $\sim 10^{15} \text{ cm}^{-3}$  at room temperature. The ionization energy of acceptor is as low as 42 meV by incorporation of hydrogen in the lattice. This improvement is related to hydrogen decorated gallium vacancies  $V_{\text{Ga-H}}$ .

Nitrogen-doped  $p$ -Ga<sub>2</sub>O<sub>3</sub> has been experimentally achieved by non-conventional growth technique. Wu *et al.* (Wu et al., 2021) demonstrated a multi-step structural phase transition growth (oxidation of GaN substrate to GaN<sub>x</sub>O<sub>3(1-x)/2</sub>, total transformation to  $\beta$ -Ga<sub>2</sub>O<sub>3</sub>, finally to N-doped  $\beta$ -Ga<sub>2</sub>O<sub>3</sub>), with the acceptor ionization energy of 0.165 eV. The resistivity, hole concentration and hole mobility are 17.0  $\Omega \cdot \text{cm}$ ,  $1.56 \times 10^{16} \text{ cm}^{-3}$ , and 23.6  $\text{cm}^2/(\text{V} \cdot \text{s})$ , respectively, by employing the Hall effect measurements. This method was also used for the fabrication of metal-semiconductor-metal solar-blind photodetectors (Jiang et al., 2020). The sizable mobility was attributed to the increase of the elastic constant, enhancement of Valence Band dispersion (the decrease of the hole effective mass) using the DFT calculation (Ma et al., 2022). Luan *et al.* (Luan et al., 2020) fabricated N doped  $\beta$ -Ga<sub>2</sub>O<sub>3</sub> by N implantation, the decrease in carrier concentration (1 – 2 orders of magnitude) further proved that the N can introduce acceptor impurity in  $\beta$ -Ga<sub>2</sub>O<sub>3</sub>.

Additionally, dilute alloying was proposed theoretically using Bi (Cai et al., 2021), and experimentally using NiO (Ezeh et al., 2023), Ir ( $\alpha$ -Ga<sub>2</sub>O<sub>3</sub>) (Kaneko et al., 2021) and Se (Bai et al., 2022). It provides an alternative way to get  $p$ -type conductivity. A significant decrease in band gap of  $\sim 1$  eV or even more is envisaged.

Overall, achieving high room temperature  $p$ -type conductivity remains a priority challenge, further experimental studies for identification/creation of shallow acceptor defects are required. This is part of my motivation for this PhD work.

## 1.2 ZnGa<sub>2</sub>O<sub>4</sub>

Spinel structure materials were first discovered in 1915 by Bragg (Bragg, 1915), with the formulation of AB<sub>2</sub>X<sub>4</sub>, where A and B are either II-valent and III-valent or IV-valent and II-valent metal cations, respectively, and X being the O, S, Se, or Te (Hill et al., 1979). There are about 1000 known spinels including  $\sim 130$  oxides. Among these oxides, zinc gallate ZnGa<sub>2</sub>O<sub>4</sub>, which is almost the stoichiometric mixture of binary semiconductor oxides Ga<sub>2</sub>O<sub>3</sub> and ZnO, has an ultra-wide band gap. The research on optical and Raman spectra of ZnGa<sub>2</sub>O<sub>4</sub>

(Cr doped) was started from 1970s, for the interest to magnetic insulators, that were used as the substrate of magnetic spinel ferrites (Kahan and Macfarlane, 2003; Van der Straten et al., 1978; Van Gorkom et al., 1973). We need to wait until 1994 for Omata *et al.* (Omata et al., 1994) proposition that spinel ZnGa<sub>2</sub>O<sub>4</sub> is a new ultraviolet-transparent electroconductive oxide. Only very recently, ZnGa<sub>2</sub>O<sub>4</sub> has shown potential in power electronics applications as the high electron concentration ( $n > 10^{19} \text{ m}^{-3}$ ) and mobility ( $\mu = 107 \text{ cm}^2/(\text{V}\cdot\text{s})$ ) have been achieved in ZnGa<sub>2</sub>O<sub>4</sub> single crystal (Boy et al., 2020; Cheng et al., 2019; Galazka et al., 2019; Look et al., 2020). For example, the ZnGa<sub>2</sub>O<sub>4</sub> based power thin-film-transistors (PTFTs) have been demonstrated (L. C. Cheng et al., 2018; Shen et al., 2017). However, its main battlefield is optoelectronics applications for the time being. It has been recently investigated for photonics (phosphors (Luchechko et al., 2019; Maldiney et al., 2014), deep-ultraviolet photodetectors (Tsai et al., 2019), phototransistors (Huang et al., 2020; Y. C. Shen et al., 2019; Y.-C. Shen et al., 2020)). Besides, a few works studied ZnGa<sub>2</sub>O<sub>4</sub> based gas sensors for Liquid-petroleum-gas (LPG), NO<sub>2</sub>, and NO (C. Chen et al., 2015; Satyanarayana et al., 1998; Tung et al., 2020).

### 1.2.1 Fundamental properties

**Structure:** Spinel oxides generally refer to the compound with the formulation of AB<sub>2</sub>O<sub>4</sub>. Arranging a close-packed face-centred cubic crystal structure (Fd-3m), in an ordered-normal phase, the oxygen ions in such AB<sub>2</sub>O<sub>4</sub> materials form tetrahedral (T<sub>d</sub>) sites where 1/8 occupied by all A cations, whereas the entire B cations reside in one-half of octahedral (O<sub>h</sub>) sites. **Figure 1-2** shows the cubic spinel structure of ZnGa<sub>2</sub>O<sub>4</sub>, displaying the tetrahedrally coordinated Zn atoms and octahedrally coordinated Ga atoms (W.-K. Wang et al., 2019b).

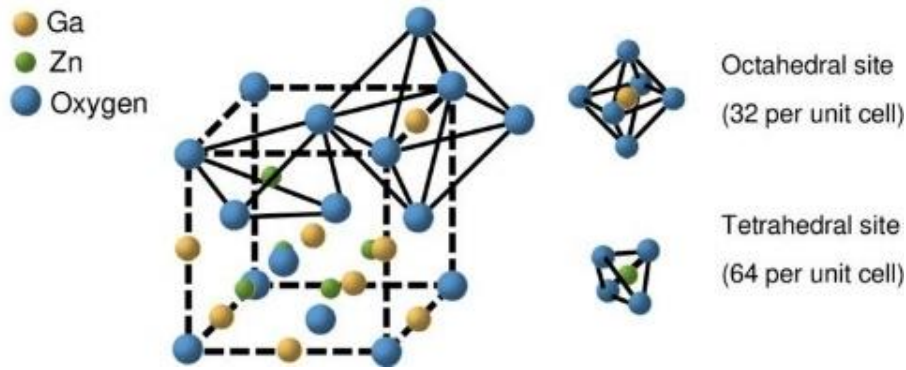


Figure 1-2. Spinel structure of ZnGa<sub>2</sub>O<sub>4</sub> (W.-K. Wang et al., 2019b).

**Band structure:** Band structure calculations based on density functional theory (DFT), *ab initio*, and first principles provided evidence of the indirect transition  $K$ - $\Gamma$ , of 2.7 – 4.7 eV (Brik, 2010; Dixit et al., 2011; Karazhanov and Ravindran, 2010; López-Moreno et al., 2011; Pisani et al., 2006; Zerarga et al., 2011; Zhang et al., 2011). While experimentally, the indirect band gap has not yet been evidenced to the best of my knowledge. Galazka *et al.* (Galazka et al., 2019) estimated the band gaps 4.59 eV (direct), or 4.33 eV (indirect) by different plot methods (absorption coefficient  $\alpha$  in power 2 for direct, while in power 1/2 for indirect) for the bulk crystal. General experimental band gap values estimated are in the range of 4.0 – 5.0 eV depending on the growth methods and conditions (Bairagi et al., 2022; Boy et al., 2020; Brik, 2010; Galazka et al., 2019; Krishna et al., 2005).

**Other parameters:** The high melting point at  $1900 \pm 20$  °C and poor thermal conductivity of 22.1 W/(m·K) of ZnGa<sub>2</sub>O<sub>4</sub> single crystal have been reported by Galazka *et al.* (Galazka et al., 2019), one of the pioneers in the field of this material.

## 1.2.2 Bulk and thin film growth techniques

At the early stage, ZnGa<sub>2</sub>O<sub>4</sub> was grown by flux growth technique, while the important contamination of Pb from PbO-PbF<sub>2</sub>-B<sub>2</sub>O<sub>3</sub> flux results in poor quality of the bulk crystal (Van der Straten et al., 1978; Yan and Takei, 1997). Some other methods such as solid state (Can et al., 2013), and laser heat pedestal growth (LHPG) (Gazit and Feigelson, 1988) have been used as well. Recently, Galazka *et al.* (Galazka et al., 2019) synthesized the ZnGa<sub>2</sub>O<sub>4</sub> single crystal by CZ and VGF methods (**Figure 1-3**). Colors (light blue, blue, dark blue) depend on the growth conditions, and can be attributed to the free carrier absorption. As-

grown crystals can be annealed in an oxidizing atmosphere (air or O<sub>2</sub>) at  $T > 700$  °C to become colorless and electrically insulating, while annealing in the presence of hydrogen can turn them into a semiconducting state with lower electron mobility. Large single crystals can be easily fabricated into wafers with high structural quality and cubic shape.

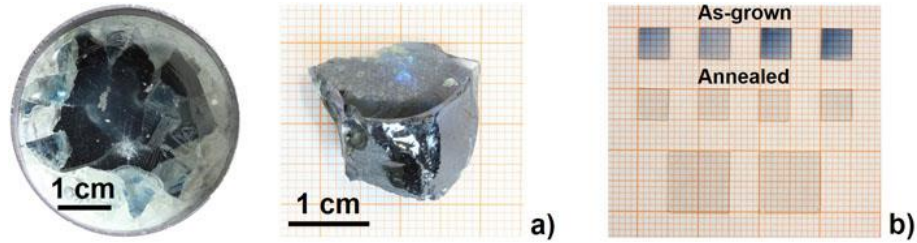


Figure 1-3. (a) Bulk ZnGa<sub>2</sub>O<sub>4</sub> single crystals synthesized using the VGF/Bridgman method. (b) (100)-oriented wafers prepared from the as-grown and annealed bulk crystals (Galazka et al., 2019).

Similar to  $\beta$ -Ga<sub>2</sub>O<sub>3</sub>, spinel ZnGa<sub>2</sub>O<sub>4</sub> thin films can also be easily and directly grown epitaxially on cheap sapphire substrates, using several techniques such as PLD, radio frequency (RF) magnetron sputtering, and CVD. Here, I will briefly introduce the outcomes of the MOCVD-grown layers, since ZnGa<sub>2</sub>O<sub>4</sub> thin films presented in this manuscript were all grown using MOCVD technique.

Metal organic precursors TEGa, TMGa are usually used for the source of Ga as in Section 1.1.2, while diethylzinc (DEZn) is used as the source of Zn. Though investigation on the growth itself is still limited, it is evident that this ternary spinel oxide has a much higher doping flexibility than binary semiconductors by tuning the growth conditions. The electron concentration in undoped ZnGa<sub>2</sub>O<sub>4</sub> thin films can be tuned from  $1.9 \times 10^{14}$  to  $2 \times 10^{20}$  cm<sup>-3</sup>, and electron mobility  $\mu_n = 2 - 20$  cm<sup>2</sup>/(V·s) at room temperature using different DEZn precursors flow rate, growth time, growth temperature, etc (Cheng et al., 2019; Horng et al., 2017; Look et al., 2020). The semi-insulating *p*-type thin film has also been demonstrated (Chikoidze et al., 2020a). Though oxygen vacancies are well-known deep donors (Paudel et al., 2011b; Shi et al., 2014), the impact of oxygen on the electronic properties has been evidenced (L.-C. Cheng et al., 2018; Horng et al., 2021; H. Shen et al., 2020).

### 1.2.3 Point defects and self-doping effect

Though works have been carried out on the optical properties in (Cr, Mn, Eu doped) ZnGa<sub>2</sub>O<sub>4</sub> for the interest of (persistent) luminescence and phosphor related applications, the study on the intrinsic defects in ZnGa<sub>2</sub>O<sub>4</sub> is limited.

In an ordered-normal system of spinel AB<sub>2</sub>O<sub>4</sub>, i.e., atoms A and B take their own sites (T<sub>d</sub> and O<sub>h</sub> sites, respectively), a stable octet, so-called closed-shell, is made up of the system, it then leads to an electrical insulator behavior (Paudel et al., 2011b). However, the distribution of cations in T<sub>d</sub> and O<sub>h</sub> sites is dependent on several factors, such as impurities (Dazai et al., 2020; Lu et al., 2017) and preparation methods (Li, 2010; Srinivas Reddy et al., 2020). Therefore, the disorder distribution of cations could result in additional routes for **self-doping effects**. According to a number of theoretical works, spinel oxides are well-known to have the inverted distribution of cations caused by antisite defects (e.g., in the case of ZnGa<sub>2</sub>O<sub>4</sub> as illustrated in **Figure 1-4**) (De Vos et al., 2016; Paudel et al., 2011a; Seko et al., 2010; Shi et al., 2014; Stoica and S Lo, 2014), which is an usual self-doping defect and could improve materials' conductivity (Paudel et al., 2011b; Perkins et al., 2011; Shi et al., 2014; Zakutayev et al., 2012; Zhang and Wei, 2002). For example, when the cation Ga remains at its high valent moving from its home-base octahedral site in normal ZnGa<sub>2</sub>O<sub>4</sub>, then such cross-substitution to the tetrahedral site would lead to a donor level, capable of releasing electrons.

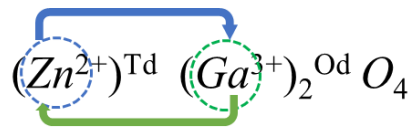


Figure 1-4. Illustration of cations inversion in spinel ZnGa<sub>2</sub>O<sub>4</sub>.

As mentioned above, both room-temperature conducting *n*-type (up to conductivity  $\sigma = 1.78 \times 10^2$  S/cm) and semi-insulating *p*-type ZnGa<sub>2</sub>O<sub>4</sub> thin films without any intentional doping have been reported. This self-doping effect may release us from the doping difficulty which is often very challenging in binary wide-bandgap oxides. According to theoretical works (Paudel et al., 2011b; Sabino et al., 2022; Shi et al., 2014), a *n*-type conductivity can be expected when the Ga content is more than the stoichiometric scenario (Zn/Ga < 1/2 in ZnGa<sub>2</sub>O<sub>4</sub>), or vice versa.

Due to the higher formation energy of other intrinsic defects (vacancies ( $V_O$ ,  $V_{Zn}$ , and  $V_{Ga}$ ), antisites ( $Ga_O$ ,  $Zn_O$ ,  $O_{Zn}$ , and  $O_{Ga}$ ), and interstitials ( $Zn_i$ ,  $Ga_i$  and  $O_i$ )) than  $Zn_{Ga}$  and  $Ga_{Zn}$ , the study on these defects in ZnGa<sub>2</sub>O<sub>4</sub> is very limited to date. Photoluminescence measurements suggested that the blue luminescence may be assigned to the oxygen vacancies (Jeong et al., 1998; Sambandam et al., 2015; Satya Kamal et al., 2017). DFT-based calculations suggested that, in oxygen-rich condition,  $V_{Zn}$ ,  $V_{Ga}$  and  $Zn_{Ga}$  are stable and act as acceptors in the  $n$ -type case (Fermi level in the upper band gap), which makes the effective  $n$ -type conductivity difficult to be realized due to the compensation. On the other hand, acceptor defects have much higher formation energy than donors  $Ga_{Zn}$ ,  $Ga_i$ ,  $Zn_i$  and  $V_O$  in the region near the valence band in oxygen-poor condition, which makes  $p$ -type conductivity difficult to be achieved (Sabino et al., 2022; Y.-P. Wang et al., 2019).

Different from the antisite defect  $Zn_{Ga}$  induced  $p$ -type conductivity predicted previously (Paudel et al., 2011b; Shi et al., 2014), Sabino *et al.* (Sabino et al., 2022) recently proposed that the excess of Zn may lead to a creation of polaronic band resulting in small polaron hopping conduction. In any case, outstanding prospects due to the high degree of freedom for doping in this ternary oxide has been demonstrated.

### 1.3 Summary

Overall, both  $\beta$ -Ga<sub>2</sub>O<sub>3</sub> and ZnGa<sub>2</sub>O<sub>4</sub>, show promise, while  $\beta$ -Ga<sub>2</sub>O<sub>3</sub> is more developed than ZnGa<sub>2</sub>O<sub>4</sub>, having commercially available 6-inch wafer from bulk crystals, while ZnGa<sub>2</sub>O<sub>4</sub> single crystal elaboration from melt growth was just started in an academic laboratory level. However, ZnGa<sub>2</sub>O<sub>4</sub> has been long time targeted for applications in optoelectronics and photonics in particular. Its cubic structure is easier for thin film growth, and point defects creation than  $\beta$ -Ga<sub>2</sub>O<sub>3</sub>, and as a spinel, it has higher doping flexibility, though both compounds have poor thermal conductivity (for comparison, that of 4H-SiC is 490 W/(m·K)). **Table 1-2** summarizes some parameters and research outcomes for  $\beta$ -Ga<sub>2</sub>O<sub>3</sub> and ZnGa<sub>2</sub>O<sub>4</sub>. it should be underlined that the study of point defects and electronic structure in both semiconductors is still strongly required.

Table 1-2. Summary of main parameters and research outcomes for  $\beta$ -Ga<sub>2</sub>O<sub>3</sub> and ZnGa<sub>2</sub>O<sub>4</sub>. Remarks (a-e) refer to: a) common value from literature, b) experimental result, c) results will be presented in this manuscript, d) values of epilayers, e) values of bulk crystals.

	$\beta$ -Ga <sub>2</sub> O <sub>3</sub>	ZnGa <sub>2</sub> O <sub>4</sub>
Crystal structural, space group	Monoclinic, $C2/m$ (low symmetry)	Cubic spinel, $Fd-3m$ (high symmetry)
Research status	More advanced	Less developed
Direct band gap, $E_g$ [eV]	4.6 – 5.0	4.0 – 5.0
Dielectric constant, $\epsilon$	~ 10	~ 10
Melting point, $T$ [°C]	~1800	~1900
Thermal conductivity, $\lambda$ [W/m·K]	10 – 30 (Anisotropic)	22
Saturation velocity, $v_s$ [cm/s]	$2 \times 10^7$	-
Max. size of single crystal wafer	6-inch, commercially available (Tamura inc., Japan)	2-cm width not yet commercial wafer
Critical electric field, $E_{CR}$ [MV/cm]	8 <sup>a</sup> , 5.2 <sup>b</sup> , 13.2 <sup>c</sup>	5.3 <sup>c</sup>
Max. electron mobility, $\mu_n$ [cm <sup>2</sup> /(V·s)]	~200 <sup>d</sup> , 100 – 150 <sup>e</sup> ~10 <sup>19-20</sup> cm <sup>-3</sup> d,e	20 <sup>d</sup> , 107 <sup>e</sup> ~10 <sup>19-20</sup> cm <sup>-3</sup> d,e
Max. electron concentration, $n$ [cm <sup>-3</sup> ]	(Si, Sn, Ge doped)	(undoped)
Max. hole mobility, $\mu_p$ [cm <sup>2</sup> /(V·s)]	~10 <sup>d</sup> (800 K)	~10 <sup>d</sup> (800 K)
Max. hole concentration, $p$ [cm <sup>-3</sup> ]	~10 <sup>16</sup> cm <sup>-3</sup> d (300 K, N doped)	~10 <sup>15</sup> cm <sup>-3</sup> d (800 K, undoped)

## 2. Experimental Techniques and Methods

In this chapter, I will describe the experimental facilities and methods used during my work.

### 2.1 Metal organic chemical vapor deposition (MOCVD)

The  $\beta$ -Ga<sub>2</sub>O<sub>3</sub> and ZnGa<sub>2</sub>O<sub>4</sub> layers investigated in this manuscript were all grown on c-sapphire substrates by the metal organic chemical vapor deposition (MOCVD) technique. In GEMaC laboratory, we use a radio frequency (RF) heated horizontal MOCVD reactor (MR Semicon, 1992) with separate inlets of precursors with their own mass flow controllers (**Figure 2-1**). The pressure can be tuned from 30 Torr to ambient, the temperature range is 20 – 1000 °C, the maximum substrate size is 2 inches.

The sources of gallium and oxygen were trimethylgallium (TMGa) and pure O<sub>2</sub> gas, respectively. The diethylzinc (DEZn) was used as the precursor for Zn for the growth of Zn-doped  $\beta$ -Ga<sub>2</sub>O<sub>3</sub> and ZnGa<sub>2</sub>O<sub>4</sub> layers. Pure Ar gas was used as vector gas. In GEMaC, the growth of  $\beta$ -Ga<sub>2</sub>O<sub>3</sub> and ZnGa<sub>2</sub>O<sub>4</sub> is carried out by Dr. Corinne Sartel.

Studied *n*-type ZnGa<sub>2</sub>O<sub>4</sub> layers (that will be shown in Chapter 4) were grown by colleagues Dr. Fu-Gow Tarntair, and Prof. Ray-Hua Horng in National Yang Ming Chiao Tung University (NYCU). The used metal organic precursors, the oxygen source as well as the vector gas were DEZn, TEGa, pure O<sub>2</sub>, and pure Ar.



Figure 2-1. MOCVD machine and reactor in GEMaC.

---

## 2.2 Structural, morphological, and chemical characterizations

### 2.2.1 X-ray diffraction (XRD)

X-ray diffraction (XRD) measurements were used to identify the crystalline structure and crystallinity of the deposited thin films.

The dominant effect that occurs when an incident beam of X-rays interacts with a target material is the scattering of those X-rays from atoms within the target material (Cullity, 1956). In materials with regular structure (i.e. crystalline), the interaction of the incident beam with the refracted beam produces constructive interference (and a diffracted ray) when conditions satisfy Bragg's Law:

$$n\lambda = 2d\sin\theta \quad (2 - 1)$$

Where  $n$ ,  $\lambda$ ,  $d$ ,  $\theta$  are the order of reflection, the wavelength of the incident beam, interplanar spacing of the crystal, and angle between incidence beam and reticular plane, respectively.



Figure 2-2. Photograph of X-ray diffractometer Bruker-Siemens D5000, in Bragg-Brentano configuration, in GEMaC.

I performed  $\theta$ - $2\theta$  scans for samples in GEMaC using a Bruker-Siemens XRD diffractometer D5000 (**Figure 2-2**). The XRD diffractometer D5000 consists of a conventional copper X-ray source with a nickel filter, giving a working wavelength ( $\lambda$ ) Cu- $K_{\alpha}$  of 1.54 Å, and a detector (scintillation photomultiplier). X-rays are generated from a copper tube with a voltage of 30 kV and a current of 20 mA. While the rocking curves ( $\omega$  scan) and in-plane measurements for  $\beta$ -Ga<sub>2</sub>O<sub>3</sub> were carried out using the diffractometer

Rigaku SmartLab with monochromatized Cu-K $\alpha$  radiation from a rotating anode, by Dr. Yunling Zheng in Institut des NanoSciences de Paris (INSP), Sorbonne University.

### **2.2.2 Scanning electron microscopy (SEM):**

Scanning electron microscopy (SEM) measurements were used to characterize the surface morphology of samples, and to determine the sample layers' thicknesses by the cross-section.

SEM works by scanning a focused beam of electrons lighting a sample surface thickness, which then generates secondary and backscattered electrons that are collected by detectors to form an image. The high resolution of SEM images is due to the small wavelength of electrons, allowing for the imaging of sub-micron features. Additionally, SEM can be used to analyze the elemental composition of a sample using energy-dispersive X-ray spectroscopy (EDS), which detects X-rays emitted by the sample when it is bombarded by the electron beam. This allows for the identification and mapping of Mendeleev table elements composition on a surface.

The SEM measurements were performed systematically for all samples by Dr. Corinne Sartel, using the commercial scanning electron microscope JSM 7001F (JEOL).

### **2.2.3 Transmission electron microscopy (TEM):**

Transmission electron microscopy (TEM) measurements were mainly used to characterize the crystal structure of samples and interfaces. In TEM measurement, a high-energy electron beam is transmitted through a thin sample, and the electrons that pass through are collected and focused onto a detector to produce an image. This technique can provide detailed information about the microstructure, crystal structure, and defects in a material. Additionally, selected area electron diffraction (SAED) can be performed using TEM to obtain information about the crystallinity and crystallographic orientations of a material. Thereby, by controlling the size of the electron beam and the position of the sample, the diffraction pattern can be obtained from a specific area of the sample, providing insight into the crystal structure and orientation. SAED can be particularly useful in the

characterization of polycrystalline materials, where the orientation of individual grains can vary.

The TEM measurements were performed by collaborators either in National Yang Ming Chiao Tung University (NYCU) for the  $\text{ZnGa}_2\text{O}_4$  samples elaborated in their lab., or Dr. Amador Pérez-Tomas and coworkers in Catalan Institute of Nanoscience and Nanotechnology (ICN2) for the  $\text{ZnGa}_2\text{O}_4$  samples elaborated in GEMaC. In NYCU, the  $\text{ZnGa}_2\text{O}_4$  films were investigated by high-resolution transmission electron microscopy (HR TEM, JEOL-2100 F CS STEM) equipped a 200-kV field emission electron gun (FEG) and combined with selected area electron diffraction (SAED) (for details see (NYCU Instrumentation Webpage, 2023)). In ICN2, the layers were characterized by a FEI Tecnai G2 F20 with a 200kV field emission gun (FEG) high resolution and analytical TEM.

### **2.2.4 Secondary ion mass spectrometry (SIMS):**

Secondary ion mass spectrometry was used in GEMaC by Dr. Francois Jomard to analyze the chemical composition and elements profile for undoped and doped  $\beta\text{-Ga}_2\text{O}_3$ , using the ions analyzer IMS 7f, CAMECA.

SIMS method involves bombarding a solid sample placed in a vacuum by primary ion beam which has an energy greater than the energy of atoms extraction from the surface of the material. The interaction between the ions beam and the surface of the sample gives rise to different secondary emissions, photons, electrons, or molecules. Secondary ions are the source of the information in this method, they are sorted according to their mass and energy.

### **2.2.5 Raman spectroscopy**

Raman spectroscopy measurements were performed by Dr. Corinne Sartel using Horiba Jobin Yvon Labram HR 8500 in GEMaC. It was used to investigate the vibrational and rotational modes of  $\text{Ga}_2\text{O}_3$  and  $\text{ZnGa}_2\text{O}_4$  layers, thus, identifying the phase of  $\text{Ga}_2\text{O}_3$  and the presence of the cubic spinel  $\text{ZnGa}_2\text{O}_4$ .

Raman spectroscopy provides information about molecular structure, chemical composition, and crystallography. The technique is based on the inelastic scattering of light, known as the Raman effect, which occurs when photons interact with the vibrational modes

of a sample. In a Raman measurement, a laser beam is directed onto the sample, and the scattered light is collected and analyzed. The Raman spectrum is a plot of the intensity of the Raman scattering as a function of the frequency shift from the incident laser beam. The spectrum reveals peaks at specific frequencies, known as Raman bands, which correspond to the vibrational modes of the sample. Each Raman band provides information about the molecular bonds and functional groups present in the sample, allowing for the identification and characterization of the material.

### **2.2.6 X-ray photoelectron spectroscopy (XPS)**

X-ray photoemission spectroscopy (XPS) measurements were used to characterize the local bonding environment as well as the chemical state of the elements, and the chemical compositional analysis. Additionally, the valence band tails can be used to determine the Fermi level positions in the samples (B. J. Carey et al., 2017).

The XPS measurement is based on the study of the kinetic energy distribution of photoelectrons ejected from a sample under the impact of the photon (UV/ X-ray) of known energy  $h\nu$ . The variation of photoelectron binding energy as a function of the chemical environment atoms from which they come is the main interest of this technique (Seah, 1980). The XPS spectrometry provides elemental and chemical information on various types of materials with a lateral resolution ranging from 10 to a few hundred  $\mu\text{m}$ . The depth probed is generally less than 10 nm, depending on the incident photon energy. XPS spectra are obtained by irradiating a material with a beam of X-rays while simultaneously measuring the kinetic energy and number of electrons that escape from the top 0 to 10 nm of the material being analyzed. A typical XPS spectrum is a graph of the number of electrons detected per second (Y-axis, ordinate) versus the binding energy of the electrons detected (X-axis, abscissa). Each element produces a characteristic set of photo-peaks at characteristic binding energy values, then each element that exists in or on the surface of the material can be analyzed. The chemical shift is due to a change in the potential of the electronic level of an atom when it chemically bonds to other atoms.

XPS measurements were performed in Institut Lavoisier Versailles (ILV), UFR des Sciences at Versailles by Dr. Mathieu Frégnaux with the participation of master 2 student Hamid Néggaz, using the Thermofisher Scientific Escalab 250 xi equipped with a mono-

chromated Al- $K_{\alpha}$  anode (1486.6 eV) and a dual flood gun (low energy electron and ion). The photoelectron detection was performed using a constant analyzer energy (CAE) mode (20 eV pass energy). To avoid the surface charge effect, we used carbon tape for drain electrons and Flood Gun (low energy electron beam) for charge compensation and improvement of charge distribution on samples that are not conducting enough. To access the bulk chemical composition, alternate sequences of ion bombardment (Ar) and XPS measurements were used. It allowed us to reconstruct the chemical depth profile of the material. Argon ions were accelerated under 4000 V and projected to the sample surface with an angle of 30°, the XPS measurements were performed subsequently.

## 2.3 Optical characterization

### 2.3.1 Transmittance and reflectance spectroscopy

The optical transmittance and reflectance measurements were used to determine the optical band gaps and check the transparency of thin films in the 200 – 2500 nm wavelength range.

Optical spectrophotometry is a method to measure how much a sample absorbs light by measuring the intensity of light as a beam of light passes through this sample. When light strikes an object, it can be either reflected, transmitted, or absorbed. The measurement setup is fairly straightforward in transmission measurements. To calculate transmittance, a measurement of the source (incident flux,  $\Phi_i$ ) is acquired by placing it in line with the detector without the sample in place, the result of this measurement is the so-called baseline, and allows to subtract the effect of the environment. The sample then is placed between the source and detector, and the transmitted light,  $\Phi_t$  is measured. The ratio of these two measurements is the transmission of the sample (which is calculated automatically):  $T(\lambda) = \frac{\Phi_t(\lambda)}{\Phi_i(\lambda)}$ . The reflectance  $R$  was measured with the same methodology for extracting the “base line” reference.

The band absorption edge can be then determined by Tauc’s relation:

$$(\alpha h\nu)^n \propto (h\nu - E_g) \quad (2 - 2)$$

Where  $\alpha$  is the absorption coefficient,  $h\nu$  is the incident photon energy, and the power factor  $n$  takes 0.5 or 2 for indirect or direct transition, respectively. The  $\alpha$  and  $h\nu$  can be calculated by:

$$\alpha = \ln 10 \times \frac{A}{t} \quad (2 - 3)$$

$$E = h\nu = \frac{hc}{\lambda} \quad (2 - 4)$$

Where  $A$  is the absorbance that can be determined by the transmittance and reflectance,  $c$  is the speed of light,  $\lambda$  is the incident wavelength. Plotting the  $(\alpha h\nu)^2$  versus incident photon energy  $h\nu$ , the band absorption edge can be determined.

GEMaC has a Perkin Elmer LAMBDA 950 2 ways spectrophotometer. So, the baseline is measured at the same time as the one with the sample, by a splitting of source light in two equi-intensity beams. This allows a get rid of the source intensity fluctuations. It is equipped with modules for transmission, reflection, and with an integration sphere for diffusive samples, for the measurements of the transmittance and the reflectance in the 200 – 3300 nm wavelength range and 10 – 770 K temperature interval. I carried out the optical transmittance and reflectance measurements at room temperature in 200 – 2500 nm wavelength range for  $\beta$ -Ga<sub>2</sub>O<sub>3</sub> and ZnGa<sub>2</sub>O<sub>4</sub> thin films.

### 2.3.2 Photoluminescence spectroscopy

Photoluminescence (PL) spectroscopy was used to study the point defects (emission and corresponding defects)

This technique involves the absorption of incident photons by a material and the subsequent emission of photons as the excited electrons return to their ground state. By analyzing the intensity, peak position, and linewidth of the PL spectra, it can provide valuable information about the electronic structure as well as defects and impurities within the material

The PL measurements were carried out by Mr. Guillaume Bouchez in GEMaC, using a home-built photoluminescence spectroscopy set-up, with 266 nm excitation wavelength (YAG laser, FQCW266-10-C, CryLaS), at room temperature. The collected signals were analysed by the spectrometer (IsoPlane 320, Princeton Instrument).

## 2.4 Electrical transport characterization

### 2.4.1 Electrical contact preparation

Samples to be measured in a Van der Pauw configuration were cut by the diamond wire saw (Well 3241, Well Diamond Wire Saws) in a square shape of 10 mm  $\times$  10 mm. Several methods were used to prepare the metals contacts:

(i) Four-point silver paste contacts were made manually at the four corners of the sample (**Figure 2-3**), they are connected by silver wires to the electrodes (Au) in the cell (Linkam, UK) for the electrical measurements. Ag paste contacts were dried and then followed an in-situ annealing during the heating process.

(ii) Radio radio-frequency (RF) sputtering using the shadow mask made for 10 mm  $\times$  10 mm sample (**Figure 2-3 (b)**) in a Van der Pauw configuration (e.g., Ti/Au as shown in **Figure 2-3 (c)**).

(iii) Electrical contact patterns are designed by Klayout and transferred to the sample by photolithography process, then the metal contacts were deposited by RF sputtering. The details of the preparation process will be shown in Chapter 5.

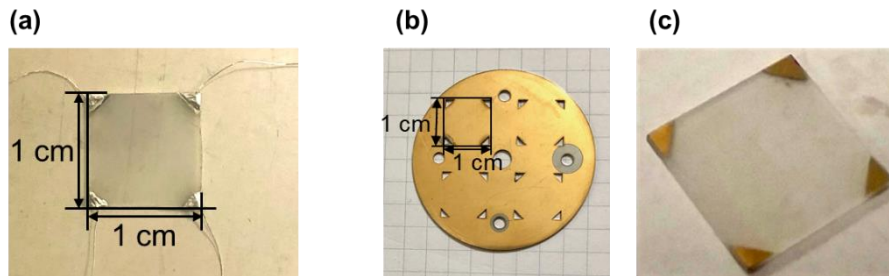


Figure 2-3. (a) Photograph of  $\beta$ -Ga<sub>2</sub>O<sub>3</sub> samples with 4 handmade metallic silver paste contacts, for the resistivity and Hall effect measurements in a Van der Pauw configuration. (b) picture of shadow mask for RF sputtering of metallic contacts. (c) Photograph of  $\beta$ -Ga<sub>2</sub>O<sub>3</sub> samples with sputtered Ti/Au contacts.

### 2.4.2 Current-voltage characteristics and photocurrent test

To characterize the current-voltage ( $I$ - $V$ ) measurements of the electrical contacts (Ohmic or Schottky) two-points  $I$ - $V$  measurements were performed using Keithley 4200 Semiconductor

Characterization System (SCS) (**Figure 2-4 (a)**) by applying direct voltage, tests are configured and executed from the Keithley Interactive Test Environment (KITE). The measurements at high temperatures were with the help of a Linkam temperature control stage.

Besides, to study the photocurrent of  $\text{ZnGa}_2\text{O}_4$  thin films, deuterium tungsten high power (DWHP) was used as the UV source with wavelength of 160 – 400 nm. The assembly is shown in the **Figure 2-4 (b)**. The tests were performed in a dark environment.

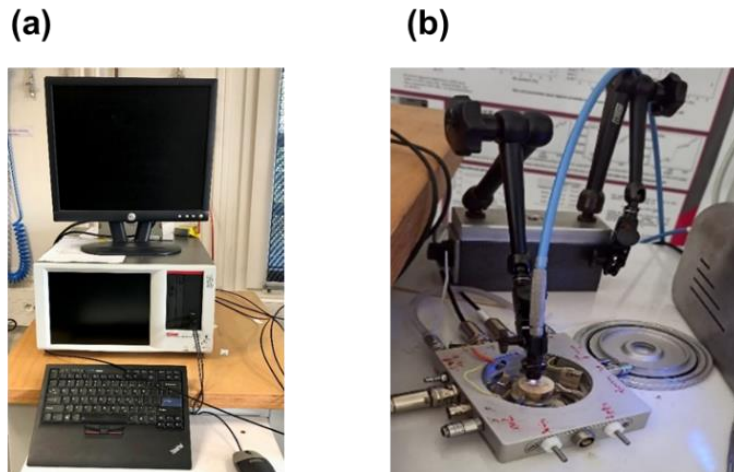


Figure 2-4. (a) Keithley Inc. SCS 4200 Semiconductor Characterization System. (b) Photocurrent test platform with fibered lighting.

### 2.4.3 Hall effect measurements

GEMaC has a home-built “high impedance high temperature” Hall Effect set up in Van Der Pauw configuration, which is specially adapted to measure very resistive ( $R > 10^{10}$  Ohm) materials. It operates in 80 – 850 K temperature interval under various gas atmosphere and [-1.6 T; 1.6 T] magnetic field ranges (**Figure 2-5 (a)**). The sample holder (adapted Linkam cell for triaxial connectors to reduce the noise and leakage currents) is shown in **Figure 2-5 (b)**. The number 1 – 8 indicates, respectively: 1: exits of water-cooling circuit, 2: sample and heating platform, 3: thermometer connections, 4: air pump, 5: nitrogen inlet, 6: measurement points (example  $I$ ) with the cables, 7: water inlet, and 8: measurement points (consequently  $V$ ) with the cables. Triaxial cables and plugs (Keithley) are used to minimize the leakage currents and environment noise.

I have studied the electrical properties of the  $\beta\text{-Ga}_2\text{O}_3$  and  $\text{ZnGa}_2\text{O}_4$  samples using home-built set up in GEMaC.

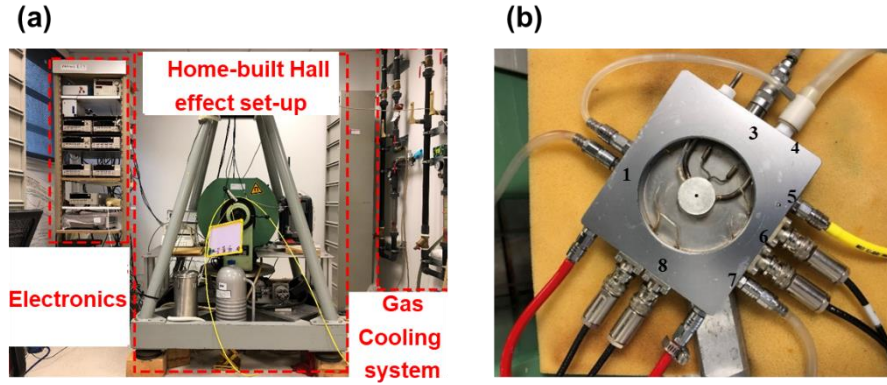


Figure 2-5. (a) Home-built Hall effect set up in Van Der Pauw configuration. (b) Photo of the measurement cell (adapted Linkam Inc. cell).

**Van Der Pauw (VDP) method** is a technique for the evaluation of electrical properties in semiconductor materials, such as resistivity; and carrier density, carrier mobility, via Hall effect. It involves applying a current and measuring voltage using four small contacts on the circumference of a flat, arbitrarily shaped sample of the uniform thin thickness ( $\ll$  sample dimension, inter-contact distances). This method is particularly useful for measuring very small samples because the geometric spacing of the contacts is unimportant. Effects due to a sample's size, which is the approximate probe spacing, can be neglected until contact's size is more than ten times smaller than the sample size (Van Der Pauw, 1958).

Using this method, the resistivity can be derived from a total of eight measurements that are made around the periphery of the sample with the configurations shown in **Figure 2-6 (a)**. Once all the voltage measurements are taken, two values of resistivity,  $\rho_A$  and  $\rho_B$ , are derived as follows:

$$\rho_A = \frac{\pi}{\ln 2} f_A t_s \frac{(V_1 - V_2 + V_3 - V_4)}{4I} \quad (2 - 5)$$

$$\rho_B = \frac{\pi}{\ln 2} f_B t_s \frac{(V_5 - V_6 + V_7 - V_8)}{4I} \quad (2 - 6)$$

Where  $\rho_A$  and  $\rho_B$  are volume resistivities in  $\Omega \cdot \text{cm}$ ;  $t_s$  is the sample thickness in cm;  $\{V_i\}$  represents the DC voltages in volts (V) measured by the voltmeter;  $I$  is the DC current through the sample in amperes (A);  $f_A$  and  $f_B$  are geometrical factors based on sample symmetry, in our case they are equal to 1, because of the square shape of the sample

associated to a small size of metal contacts. Once  $\rho_A$  and  $\rho_B$  are known, the average resistivity ( $\rho_{AVG}$ ) can be determined as follows:

$$\rho_{AVG} = \frac{\rho_A + \rho_B}{2} \quad (2 - 7)$$

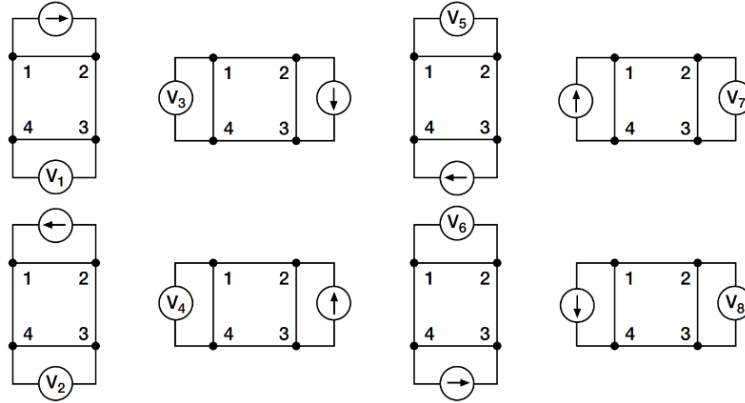


**Figure 2-6.** Van Der Pauw resistivity measurement eight configurations.

### Hall effect, experimental set-up, and measurement details

The Hall Effect is a fundamental measurement to determine carrier type and carrier density; to deduce the free carrier mobility with the known electrical resistivity of a material. It can be observed when a potential difference is observed between the edges of a conducting strip carrying a longitudinal current when placed in a magnetic field perpendicular to the plane of the strip. The basic physical principle underlying the Hall Effect is the Lorentz force, which is a combination of two separate forces: the electric force and the magnetic force. When an electron moves along the electric field direction perpendicular to an applied magnetic field, it experiences a magnetic force  $-q\vartheta \times B$  acting normally to both directions. The resulting Lorentz force  $F$  is therefore equal to  $-q(E + \vartheta \times B)$  where  $q$  is the elementary charge,  $E$  is the electric field,  $\vartheta$  is the particle velocity, and  $B$  is the magnetic field (**Figure 2-7**).

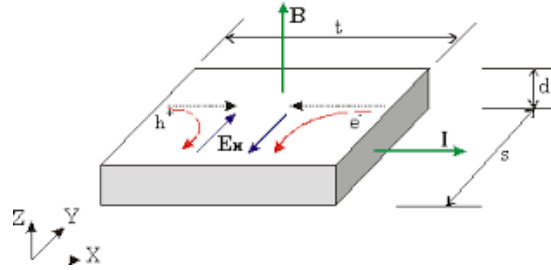


Figure 2-7. The principle of Hall effect for electrons  $e^-$  (right) and for hole  $h$  (left) inducing in stationary state opposite Hall electric field  $E_H$ .

We assume that a constant current  $I$  flows along the x-axis in the presence of a z-directed magnetic field. Electrons subject to the Lorentz force initially drift away from the current direction toward the y-axis, resulting in an excess negative (or positive) surface electrical charge on this side of the sample. This charge results, in a stationary state, in the Hall voltage, a potential drop across the two sides of the sample. This transverse voltage is the Hall voltage  $V_H$  and its magnitude is equal to  $\frac{I \times B}{q \times n \times d}$  where  $I$  is the current,  $B$  is the magnetic field,  $d$  is the sample thickness,  $n$  is the electron concentration (Otherwise,  $p$  if the majority free charge carriers are holes) and  $q$  is the elementary charge. For the majority of free charge carriers, the type (electron  $n$  or hole  $p$ ), the carrier concentration, mobility  $\mu$  can be then determined by following formulas:

$$n = -\frac{1}{e \times R_H}, \text{ or } p = \frac{1}{e \times R_H} \quad (2-8)$$

$$\mu = \frac{|R_H|}{\rho} \quad (2-9)$$

Where the  $R_H$  is the Hall coefficient, it is negative when the majority of the free carriers are electrons, whereas it is positive when the majority of the free carriers are holes.

During the Hall effect measurement, there are several possible errors that can be summarized as follow (Lindberg, 1952):

(i) Voltmeter offset ( $V_{off}$ ): When a voltmeter is not properly zeroed, it introduces an offset voltage ( $V_{off}$ ) to every measurement. This offset remains constant and does not change with the direction of the current or magnetic field.

(ii) Current meter offset ( $I_{off}$ ): Similarly, an improperly zeroed current meter adds an offset current ( $I_{off}$ ) to every measurement. This offset remains consistent and is independent of the current or magnetic field direction.

(iii) Thermoelectric effect (voltage  $V_{Seebeck}$ ): It is also known as the Seebeck effect that will also be presented later in Section 2.4.5. This results in thermoelectric voltages (VTE) due to the Seebeck effect. Thermoelectric voltages can also be generated in the wiring connected to the sample in response to temperature gradients. These thermoelectric voltages are not affected by the current or magnetic field.

(iv) Ettingshausen effect (voltage,  $V_{Ettingshausen}$ ): Even in the absence of an external temperature gradient, the sample itself can create its own temperature gradient. This leads to the Ettingshausen effect, where slow and fast electrons are displaced to different sides of the sample under the influence of the Lorentz force. This internally generated Seebeck effect results in the Ettingshausen effect voltage ( $V_{Ettingshausen}$ ). Unlike other effects,  $V_{Ettingshausen}$  is proportional to both the current and magnetic field, and it cannot be eliminated by reversing the current or magnetic field.

(v) Nernst effect (voltage,  $V_{Nernst}$ ): If there is a longitudinal temperature gradient along the sample, electrons tend to diffuse from the hot end to the cold end, creating a diffusion current affected by a magnetic field. This produces the Nernst effect or Nernst-Ettingshausen effect, which results in the Nernst effect voltage ( $V_{Nernst}$ ).  $V_{Nernst}$  is proportional to the magnetic field but not to the external current.

(vi) Righi-Leduc voltage ( $V_{RL}$ ): Electrons experiencing the Nernst (diffusion) effect also exhibit an Ettingshausen-type effect due to their spread of velocities, creating hot and cold sides. This establishes a transverse Seebeck voltage known as the Righi-Leduc voltage ( $V_{RL}$ ). Similar to the Nernst effect,  $V_{RL}$  is proportional to the magnetic field but not to the external current.

(vii) Misalignment voltage ( $V_M$ ): Geometrical variations and imperfect alignments of contacts lead to a misalignment voltage ( $V_M$ ), which often contributes the most significant spurious component to the measured Hall voltage, as it gives a contribution proportionally to the sample resistivity.

By varying the DC applied current direction, applied magnetic field, and amperemeter and voltmeter configurations (**Figure 2-8**), the majority of errors can be eliminated. We note

that the  $V_1 - V_4$  are measured in a positively applied magnetic field, while  $V_5 - V_8$  are measured in a negatively applied magnetic field. And we note that the current direction  $I_l$  ( $I_3, I_5$ , and  $I_7$ ) is negative. Then, we have:

$$V_1 = -V_H + V_{off} - V_{Ettingshausen} + V_{Nernst} + V_{RL} - V_M + V_{Seebeck} \quad (2 - 10)$$

$$V_2 = +V_H + V_{off} + V_{Ettingshausen} + V_{Nernst} + V_{RL} + V_M + V_{Seebeck} \quad (2 - 11)$$

$$V_5 = +V_H + V_{off} + V_{Ettingshausen} - V_{Nernst} - V_{RL} - V_M + V_{Seebeck} \quad (2 - 12)$$

$$V_6 = -V_H + V_{off} - V_{Ettingshausen} - V_{Nernst} - V_{RL} + V_M + V_{Seebeck} \quad (2 - 13)$$

$$\frac{(V_2 - V_1 + V_5 - V_6)}{4} = V_H + V_{Ettingshausen} \approx V_H \quad (2 - 14)$$

Then the corresponding Hall coefficient  $R_{HC}$  can be calculated by:

$$R_{HC} = \frac{d}{BI} \times \frac{V_2 - V_1 + V_5 - V_6}{4} \quad (2 - 15)$$

Similar measurements are performed using another configuration, and the corresponding Hall coefficient  $R_{HD}$  is:

$$R_{HD} = \frac{(V_4 - V_3 + V_7 - V_8)}{4} \times \frac{d}{BI} \quad (2 - 16)$$

Where  $d$  is the thickness of the thin film. Finally, the Hall coefficient is:

$$R_H = \frac{R_{HC} + R_{HD}}{2} \quad (2 - 17)$$

A verification of Ohmic contact was always carried out before the measurements of resistivity and Hall effect.

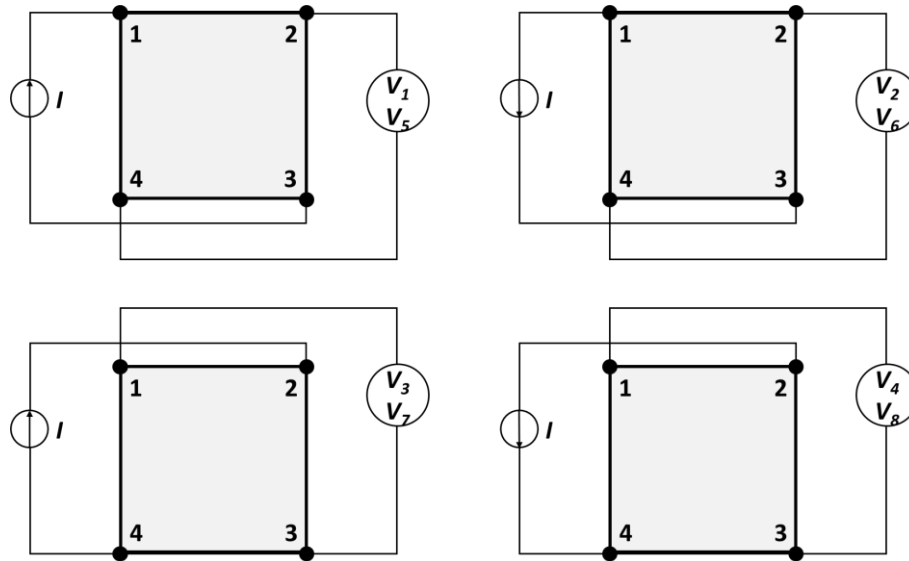


**Figure 2-8.** Van der Pauw Hall effect measurement eight configurations.

### Electrical Hall effect measurements and results validation: a case study

Measuring the electrical transport properties in highly resistive thin films are usually more challenging compared to conducting samples:

(i) Low Hall voltage: High resistivity (due to low carrier concentration) leads to low measurement currents, which results in low Hall voltages. It makes it difficult to distinguish the measured Hall voltages from noise (high Johnson noise, for example), or artefact contributions, such as longitudinal resistivity voltage if misaligned contacts. Indeed, when contacts are misaligned or when the sample is highly resistive, the contact resistance can become a significant portion of the overall resistance, which leads to artefacts and misleading results.

(iii) Conduction mechanism: in hopping conduction, carriers hop between spatially localized states through thermally activated hopping processes, rather than flowing freely delocalized states as in conventional band conduction. Many works reported the anomalies observed in Hall effect measurements when the hopping conduction becomes dominant in the samples (Emin, 1977; Gal'perin and German, n.d.; Holstein, 1973, 1961; Klein, 1985; Movaghar et al., 1981). However, it can be overcome by performing Seebeck effect measurements.

Therefore, in such difficult experimental conditions, after applying the set-up and errors elimination methods presented above, we apply a systematic measurement procedures and

data validation before extracting relevant electrical transport properties behaviours and values. After analyzing and measuring about 30 – 40 resistive *p*-type  $\beta$ -Ga<sub>2</sub>O<sub>3</sub> samples, one illustrative example is given as follow (**Figure 2-9**).

Before performing the electrical measurements, the first step is always to check the Ohmic contact behavior. Ag-paste after drying and then in-situ annealing starts to form Ohmic contact to *p*-type  $\beta$ -Ga<sub>2</sub>O<sub>3</sub> thin films above around 550 K (depending on different samples). **Figure 2-9 (a)** shows a pseudo-linear *I-V* curve at 570 K with nA current values, which becomes perfectly linear in the measurement range at 850 K (**Figure 2-9 (b)**) with  $\mu$ A current values, it ensures that the following Hall effect measurements can be carried out. Then, the characteristics majority charge carriers (via the Hall effect measurements) are validated by:

(i) The Hall voltage ( $V_H$ ) has the same sign as the applied magnetic field, and increases linearly with the increasing magnetic field if the thin film is *p*-type, or opposite sign and decreases linearly if the majority of carriers is electron.

(ii) The Hall voltages measured in complementary configurations ( $V_{HC}$  and  $V_{HD}$ ) have same sign with similar values (difference < 10%).

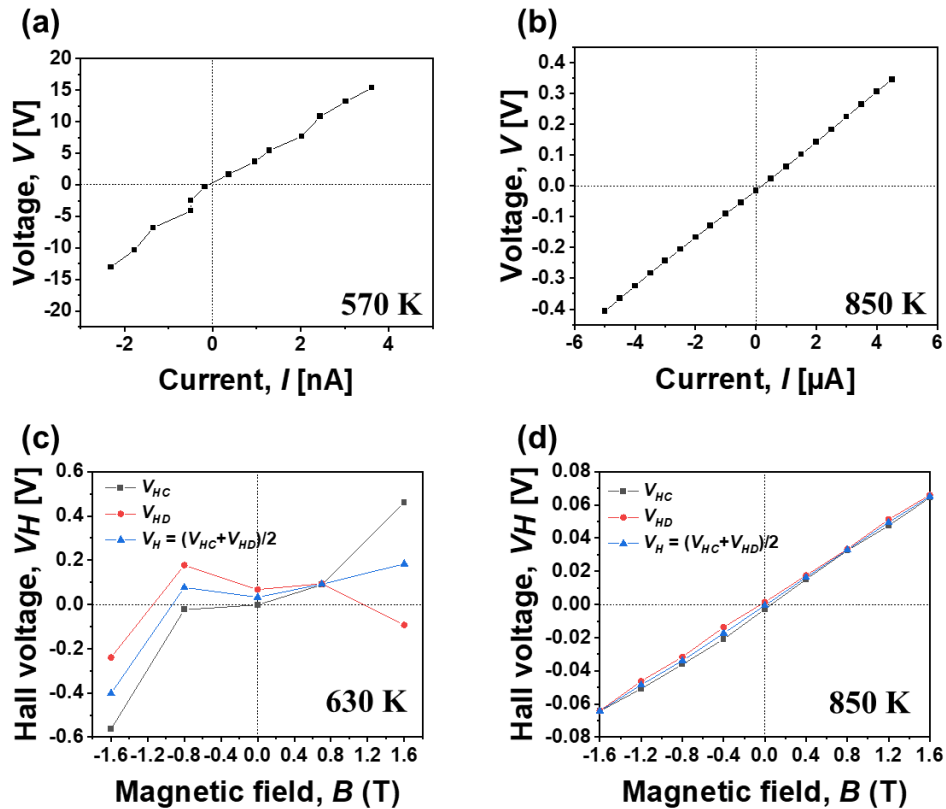


**Figure 2-9.** Results of a representative undoped  $p$ -type  $\beta$ -Ga<sub>2</sub>O<sub>3</sub> thin film: (a) – (b) The current-voltage characteristics at 570 K and 850 K, respectively, and (c) – (d) Hall voltage scanned with the perpendicularly applied magnetic field from -1.6 – +1.6 T at 630 K and 850 K, respectively.

As shown in the **Figure 2-9 (c)**, the Hall effect measurements cannot be validated at 630 K because of too much divergent  $V_{HC}$  and  $V_{HD}$  values, due to the reasons mentioned above. While at 850 K, when there are much more mobile carriers in band-like conduction mechanism, the  $V_{HC}$  and  $V_{HD}$  have comparable values having the same sign as the magnetic field, and the positive slope of Hall voltage ( $V_H = (V_{HC} + V_{HD})/2$ ) vs. magnetic field can be well fitted linearly (**Figure 2-9 (d)**).

#### 2.4.4 Physical property measurement system (PPMS)

The PPMS, Quantum Design Inc. (QD) is an automated low-temperature (2 – 400 K) and high magnet field [-9 T; 9 T] measurement system for electrical transport and magnetic properties of the material (Quantum Design, 2008).

In GEMaC, with PPMS-9T of QD (**Figure 2-10**), I have studied electrical and magneto-transport properties of  $n$ -type ZnGa<sub>2</sub>O<sub>4</sub> samples. in 2 K to 300 K interval, and magnetoresistance 0 – 9 T magnetic fields.

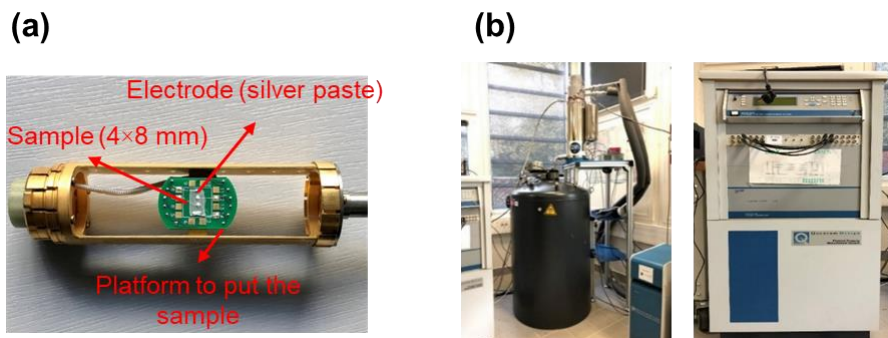


**Figure 2-10.** (a) Photo of a sample holder with mounted sample at rotative platform of PPMS-9T (b) 9T PPMS equipment in GEMaC.

### 2.4.5 Seebeck effect measurements

The Seebeck effect is a phenomenon in which a temperature gradient across a semiconductor generates an electric voltage. When a temperature gradient is applied to a semiconductor, the free charge carriers within the material tend to diffuse from the hotter region to the cooler region. As a result, an imbalance in charge distribution is created, leading to the development of an electric field. This electric field causes the charge carriers to migrate. At equilibrium, a compensating electromotive force caused by the temperature gradient is developed across the semiconductor (Geballe and Hull, 1955). The ratio between the voltage difference induced and the temperature difference is called the Seebeck coefficient, and is defined as:

$$S = \frac{\Delta V}{\Delta T} \left[ \frac{V}{K} \right] \quad (2 - 18)$$

By this convention, the direction of the thermoelectromotive force of the *n*-type semiconductor is from the low-temperature end to the high-temperature end (the Seebeck coefficient is negative), on the contrary, the direction of the thermoelectromotive force of the *p*-type semiconductor is from the high-temperature end to the low-temperature end (the Seebeck coefficient is positive).

GEMaC laboratory has a Home-made set up, consisting of: two Kelvin probes from Cascade (USA) that we can connect to the Keithley SCS4200 equipment by SubMiniature version A (SMA) connectors and two heaters integrated with the stage with temperature controller (20 – 400 °C) (**Figure 2-11**).

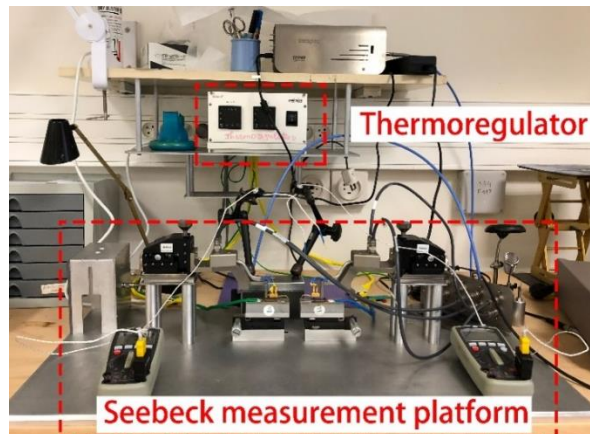


Figure 2-11. Home-built Seebeck Effect in GEMaC.

### 3. $\beta$ -Ga<sub>2</sub>O<sub>3</sub>: Experimental Results and Discussion

In this chapter, I will focus on the characterizations of the undoped and Zn-doped *p*-type  $\beta$ -Ga<sub>2</sub>O<sub>3</sub> thin films grown by the metal organic chemical vapor deposition (MOCVD) technique. The first and essential step before successful acceptor doping is to obtain high-quality undoped layers with a low density of donor defects. The first section (3.1) deals with the structural and electronic properties of undoped  $\beta$ -Ga<sub>2</sub>O<sub>3</sub> thin films grown on *c*-plane sapphire substrate. Owing to the challenges of *p*-type doping in  $\beta$ -Ga<sub>2</sub>O<sub>3</sub>, efforts have been dedicated to finding an effective acceptor dopant at room temperature. Zn is one of the potential candidates among the acceptor dopants. How Zn-doping affects the impurity domination in  $\beta$ -Ga<sub>2</sub>O<sub>3</sub> based on the thermodynamic analysis will be discussed in Section 3.2. Experimental structural, optical, and electrical transport properties of  $\beta$ -Zn:Ga<sub>2</sub>O<sub>3</sub> layers with different doping levels grown on *c*-plane sapphire substrates by MOCVD will be shown in Section 3.3. Since high-power (voltage) electronic applications are important for  $\beta$ -Ga<sub>2</sub>O<sub>3</sub>, the critical electric field  $E_{CR}$  is thus a crucial parameter. The breakdown voltage measurements for the estimation of this critical electric field will be discussed.

#### 3.1 Undoped $\beta$ -Ga<sub>2</sub>O<sub>3</sub> thin films

Prior to studying the acceptor doping effect in  $\beta$ -Ga<sub>2</sub>O<sub>3</sub>, it is necessary to obtain high crystalline quality layers with lower possible donor defects concentration, as they act as “hole-killers”, preventing hole conductivity realization. Most non-intentionally doped wide bandgap oxide semiconductors are predominately *n*-type due to the low formation energy of oxygen vacancies, which are donors compensating the intentional acceptors (e.g., in ZnO). The majority of oxides have such fundamental thermodynamic constraints, making *p*-type doping difficult. However, there is still a small family of oxide compounds which have naturally *p*-type conductivity: Cu<sub>2</sub>O (Napari et al., 2021), CuInO<sub>2</sub> (Yanagi et al., 2001), CuCrO<sub>2</sub> (Banerjee and Chattopadhyay, 2005), SnO (Yang et al., 2015), NiO (Sato et al., 1993), etc.

According to the pioneering work on *p*-type  $\beta$ -Ga<sub>2</sub>O<sub>3</sub> reported by my colleagues (Chikoidze et al., 2017b), based on the thermodynamics analysis,  $\beta$ -Ga<sub>2</sub>O<sub>3</sub> is a favorite case, as it has comparatively high formation energy of native donors – “hole killers”, and

consequently the electrical compensation by intrinsic donors is diminished (Chikoidze et al., 2017b). The native hole conductivity is thus possible, and  $\beta$ -Ga<sub>2</sub>O<sub>3</sub> was also distinguished from other wide band gap oxides (e.g., ZnO, SnO<sub>2</sub>, or In<sub>2</sub>O<sub>3</sub>) that have low donor formation energies. Then, all of the further works were progressed based on these findings.

### 3.1.1 Structural characterizations

The undoped doped  $\beta$ -Ga<sub>2</sub>O<sub>3</sub> samples were grown in a radio-frequency (RF) heated horizontal metal organic chemical vapor deposition (MOCVD) reactor on insulating *c*-plane sapphire Al<sub>2</sub>O<sub>3</sub>(0001) substrates. (details see **Table 3-4**) During the growth, the flow rate of the gallium precursors and oxygen were kept at 6  $\mu$ mol/min and 600 sccm respectively. The growth temperature and pressure were set at  $T = 775$  °C and total pressure in reactor 30 Torr, respectively.

It is well established that  $\beta$ -Ga<sub>2</sub>O<sub>3</sub> can be epitaxially grown on *c*-sapphire with six equivalent orientations following the relationship (Garten et al., 2016; Oshima et al., 2007):  $\beta$ -Ga<sub>2</sub>O<sub>3</sub>(-201)//Al<sub>2</sub>O<sub>3</sub>(0001) and  $\beta$ -Ga<sub>2</sub>O<sub>3</sub> [010]||Al<sub>2</sub>O<sub>3</sub>[-110]. In the X-ray diffraction (XRD) out-of-plane (OP)  $\theta$ - $2\theta$  scan, only  $\beta$ -Ga<sub>2</sub>O<sub>3</sub> (-201) reflection and its harmonics were observed as expected (**Figure 3-1 (a)**). The Bragg angles measured are smaller than those of the bulk, indicating that the lattice is expanded by 0.34% along the normal of the film. The rocking curves of  $\beta$ -Ga<sub>2</sub>O<sub>3</sub> (-201) and its harmonics are of the same shape and angular widths, with a full width at half maximum (FWHM) of  $\sim 3^\circ$  (Inset in **Figure 3-1 (a)**). For in-plane (IP) scan along Al<sub>2</sub>O<sub>3</sub> *b*\*-axis azimuth,  $\beta$ -Ga<sub>2</sub>O<sub>3</sub> (020) and (512) reflections were observed (**Figure 3-1 (b)**). The Bragg angles are larger than those of the bulk, indicating a lattice contraction of about -0.24%. Along Al<sub>2</sub>O<sub>3</sub> *a*-axis azimuth, similar lattice contraction was measured with  $\beta$ -Ga<sub>2</sub>O<sub>3</sub> (-201) reflection. It means that the mean strain is in-plane isotropic. The rocking curve of  $\beta$ -Ga<sub>2</sub>O<sub>3</sub> (020) plane (Inset in **Figure 3-1 (b)**) and that of (201) plane display a FWHM of  $6^\circ$ , *i.e.* the IP misorientation is twice larger than that of OP. The fact that the film lattice expands out-of-plane and contracts in-plane implies an increase in the lattice parameters *a* and *c* by 0.14% and 0.12% respectively with respect to the bulk, as well as an increase in the  $\beta$  angle of 0.31% (**Table 3-1**). In parallel, the parameter *b* is in the contraction of -0.49%.

Table 3-1. Lattice parameters of sample  $\beta$ -Ga<sub>2</sub>O<sub>3</sub>//*c*-sapphire inferred with the OP tensile strain of 0.34% and the IP compressive strain of -0.24% measured.

	<i>a</i> (Å)	<i>b</i> (Å)	<i>c</i> (Å)	$\beta$ (°)
$\beta$ -Ga <sub>2</sub> O <sub>3</sub> this work	12.247	3.025	5.807	104.02
Bulk ref. (Geller, 1960)	12.230	3.040	5.800	103.70
Difference (%)	0.14%	-0.49%	0.12%	0.31%

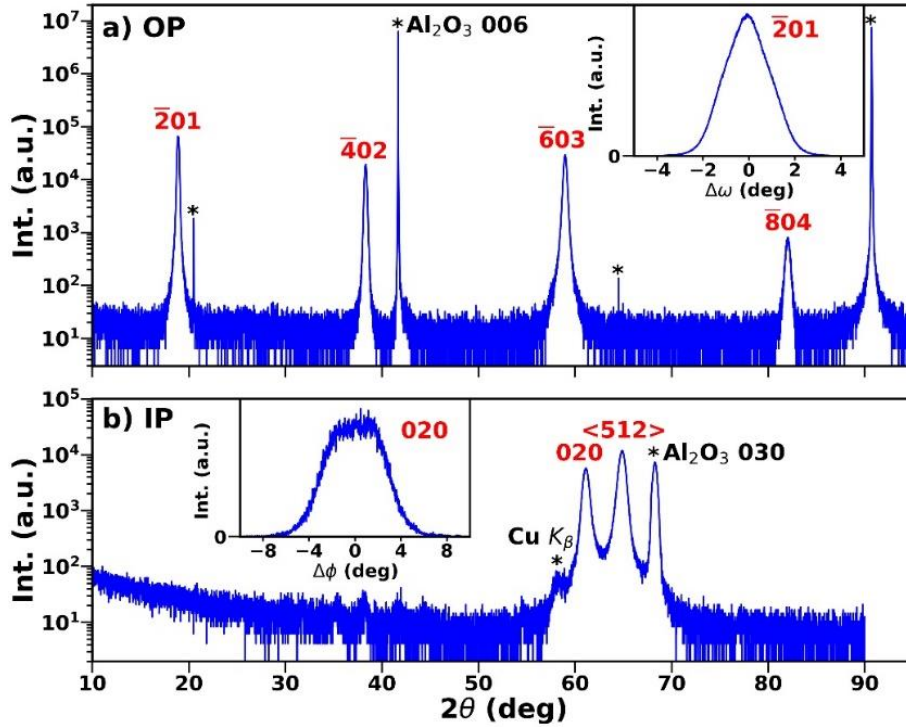


Figure 3-1. XRD and GIXRD scans in sample  $\beta$ -Ga<sub>2</sub>O<sub>3</sub>//*c*-sapphire. (a) Out-of-plane (OP) scan with in the inset the rocking curve of  $\beta$ -Ga<sub>2</sub>O<sub>3</sub> -201 reflection. (b) In-plane (IP) scan along Al<sub>2</sub>O<sub>3</sub> *b*\*-axis azimuth. The rocking curve of  $\beta$ -Ga<sub>2</sub>O<sub>3</sub> 020 reflection is in the inset. Contributions from Cu *K*<sub>β</sub> radiation and substrate are marked by \*.

**Figure 3-2** shows the Raman spectra recorded using 514.5 nm excitation for (-201) textured  $\beta$ -Ga<sub>2</sub>O<sub>3</sub> thin film grown on *c*-plane sapphire substrates, for a bare *c*-plane sapphire (0001) Al<sub>2</sub>O<sub>3</sub>, and for a (100)  $\beta$ -Ga<sub>2</sub>O<sub>3</sub> single crystal. The primitive unit cell of  $\beta$ -Ga<sub>2</sub>O<sub>3</sub> consists of 10 atoms which results in 30 phonon modes; of which 27 are optical modes. At the  $\Gamma$ -point, these belong to the irreducible representation (Dohy et al., 1982).

$$\Gamma_{opt} = 10A_g + 5B_g + 4A_u + 8B_u \quad (3-1)$$

The modes with  $A_g$  and  $B_g$  symmetry are Raman active, while those with odd parity (index  $u$ ) are infrared active. According to the authors, the Raman peaks can be categorized into three groups by specific types of different Ga-O bond vibrations. The Raman spectrum for the (-201) textured  $\beta$ -Ga<sub>2</sub>O<sub>3</sub> thin film grown on  $c$ -sapphire substrates is a combination of  $\beta$ -Ga<sub>2</sub>O<sub>3</sub> and Al<sub>2</sub>O<sub>3</sub> phonon modes (labelled using “\*”). Notably, no Raman phonon modes belonging to other Ga<sub>2</sub>O<sub>3</sub> polymorphs have been detected, demonstrating that we have a single  $\beta$ -Ga<sub>2</sub>O<sub>3</sub> phase. The  $\beta$ -Ga<sub>2</sub>O<sub>3</sub> thin film Raman phonon modes full width at half maximum (FWHM) is close to that of single crystal  $\beta$ -Ga<sub>2</sub>O<sub>3</sub> and this is indicative of good crystallinity.

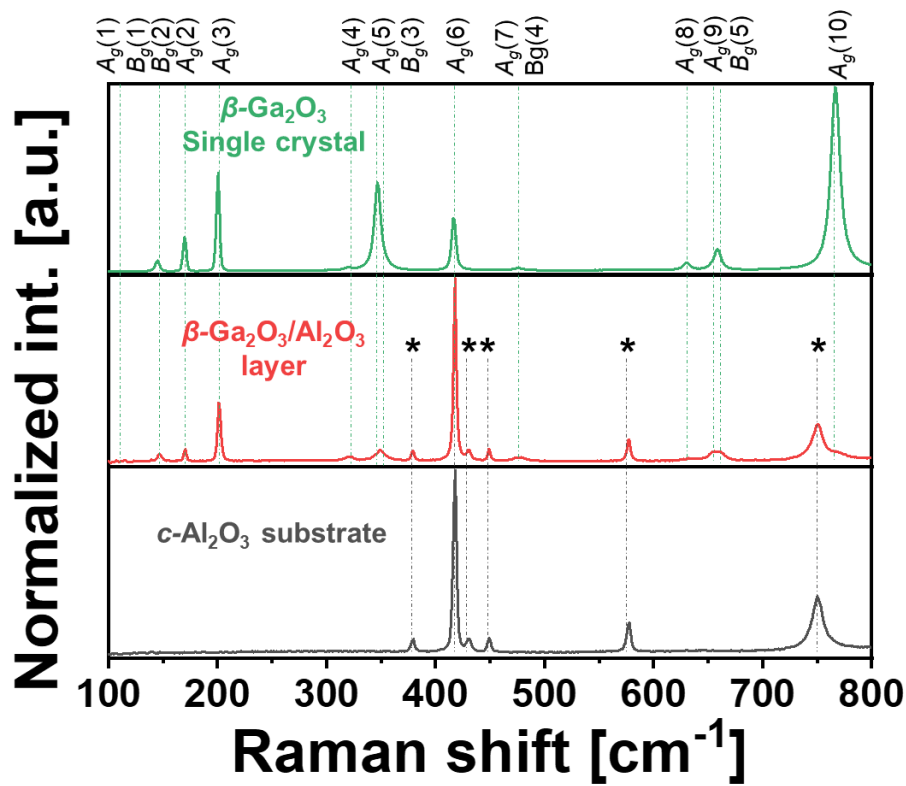


Figure 3-2. Raman spectra recorded using 514.5 nm excitation for: red trace: (-201)  $\beta$ -Ga<sub>2</sub>O<sub>3</sub> thin film grown on  $c$ -sapphire substrates; grey trace: bare  $c$ -sapphire substrate; green trace: (100)  $\beta$ -Ga<sub>2</sub>O<sub>3</sub> single crystal. The phonon modes for  $\beta$ -Ga<sub>2</sub>O<sub>3</sub> are labelled using “#” while the phonon modes for  $a$ -Al<sub>2</sub>O<sub>3</sub> substrate are labelled using “\*”).

### 3.1.2 Electrical transport properties

In this sub-section, a detailed electrical transport properties study for the undoped  $\beta$ -Ga<sub>2</sub>O<sub>3</sub> layers is presented.

To perform the electrical measurements correctly, the first step is to check the Ohmicity of contacts for the undoped  $\beta$ -Ga<sub>2</sub>O<sub>3</sub> sample. The contacts were prepared by painting the silver paste at 4 corners of a square-shaped sample (in a Van der Pauw configuration). Current-voltage (I-V) dependence was measured at 850 K (**Figure 3-3 (a)**), which is the highest measurable temperature for our home-built Hall effect set-up, it assures the linear dependence of voltage to current, thus, the electrical contacts are Ohmic. As shown in **Figure 3-3 (b)**, the sample was measured in the temperature range of 530 – 850 K, at lower temperature measurement was impossible to perform due to very high resistance of the sample. The resistivity  $\rho = 1.2 \times 10^3 \text{ } \Omega \cdot \text{cm}$  at 840 K, it increases with the temperature decreasing, to  $2.6 \times 10^5 \text{ } \Omega \cdot \text{cm}$  at 630 K, showing a typical temperature dependent behavior of a semiconductor. At  $T < 630 \text{ K}$ , the hopping conduction may start to be the dominant conduction mechanism. The activation energy  $E_a = 1.18 \pm 0.02 \text{ eV}$  was then determined using the Arrhenius equation for the electrical conductivity  $\sigma$  versus the temperature  $T$  ( $\ln(\sigma)$  vs.  $1000/T$  plot) (**Figure 3-3 (c)**). **Figure 3-3 (d)** displays the temperature dependent volume resistivities  $\rho_A$  and  $\rho_B$ . As introduced in Chapter 2 (Experimental facilities and methods),  $\rho_A$  and  $\rho_B$  should have similar values (difference  $< 10\%$ ). As shown in **Figure 3-3 (d)**,  $\rho_A$  and  $\rho_B$  have a negligible difference at higher temperatures, indicating that the tested sample as well as the electrical contacts are homogeneous. The difference becomes larger at  $T < 640 \text{ K}$ , which might be attributed to the inhomogeneity of the electrical contacts. Besides, such a high resistance ( $\sim 10 \text{ G}\Omega$ ) to measure nearly attains the limit of our home-built measurement set-up.

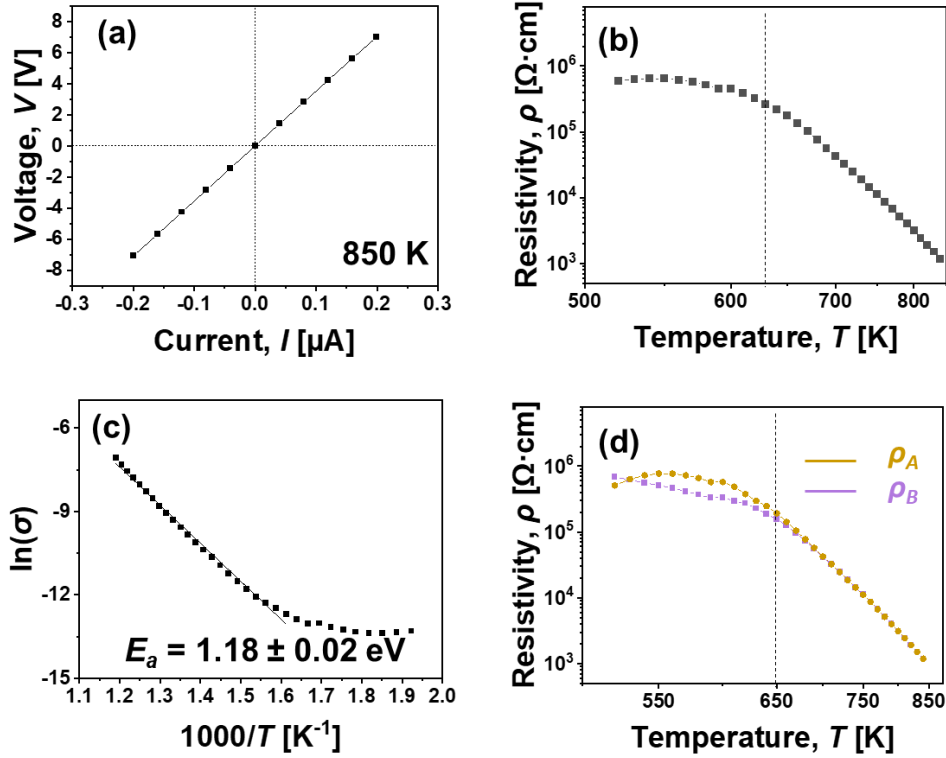


Figure 3-3. (a) Typical  $\beta$ -Ga<sub>2</sub>O<sub>3</sub> Ohmic I–V characteristics at 850 K. (b) Resistivity  $\rho$  versus temperature. (c)  $\ln(\sigma)$  vs.  $1000/T$  plot for the determination of activation energy of conductivity. (d) Temperature dependence of  $\rho_A$  and  $\rho_B$ .

In a non-magnetic material, when the majority of free carriers is  $p$ -type (holes), the Hall voltage ( $V_H$ ) should be positively proportional to the applied magnetic field ( $H$ ), and the values should be positive when the applied magnetic field is positive (vice versa for negative magnetic field). To further validate the sign of majority carriers in the film, the Hall voltage dependence on the applied magnetic field was measured at 850 K with increasing magnetic fields from -1.6 to 1.6 T. As shown in **Figure 3-4 (a)**, the  $V_H$  has the same sign as the applied magnetic field, and increases linearly with a perpendicularly applied increasing magnetic field, indicating that the layer is  $p$ -type. Moreover, the experimental off-set voltage at zero magnetic field is very small. **Figure 3-4 (b)** shows the mobility in the measurement temperature range, the average mobility  $\mu = 8.7 \pm 1.7$  cm<sup>2</sup>/(V·s). Such a sizable hole mobility might be due to good crystallinity. **Figure 3-4 (c)** shows the temperature dependent hole concentration at elevated temperatures. The temperature dependence was then analyzed using the general expression for  $p$ -type semiconductor based on the Boltzmann statistics (as  $E_{VBM} + 3k_B T \ll E_F$  in our case), which is given as follow:

$$\frac{N_A - N_D - p}{p(N_D + p)} = \frac{2}{N_V} e^{\frac{E_A - E_{VBM}}{k_B T}} \quad (3 - 2)$$

Where the  $N_D$ ,  $N_A$ ,  $N_V$ ,  $p$ ,  $E_A$ , and  $k_B$  being the donor density, acceptor density, effective density of states at valence band maximum (VBM), free hole concentration, acceptor level energy, and Boltzmann constant, respectively. In the case of deep acceptor ( $\Delta E_a = E_A - E_{VBM} \gg k_B T$ ,  $N_A > N_D \gg p$ ):

$$\frac{N_A - N_D}{p N_D} = \frac{2}{N_V} e^{\frac{\Delta E_a}{k_B T}} \quad (3 - 3)$$

Thus:

$$p = \frac{N_A - N_D}{N_D} \frac{N_V}{2} e^{-\frac{\Delta E_a}{k_B T}} \quad (3 - 4)$$

With  $N_V \propto T^{3/2}$ .  $\Delta E_a$  in this case equals the ionization energy  $E_i$  of the acceptor level, is obtained from a linear regression on a  $\ln(p \times T^{-3/2})$  vs.  $(1/T)$  plot (**Figure 3-4 (d)**). Following this, the  $E_i$  was determined to be  $1.11 \pm 0.02$  eV, which gives the activation energy in this case. The origin of the conductivity can be attributed to the deep acceptor gallium vacancy ( $V_{Ga}$ ) (Jesenovec et al., 2021b; Lany, 2018; Polyakov et al., 2018).

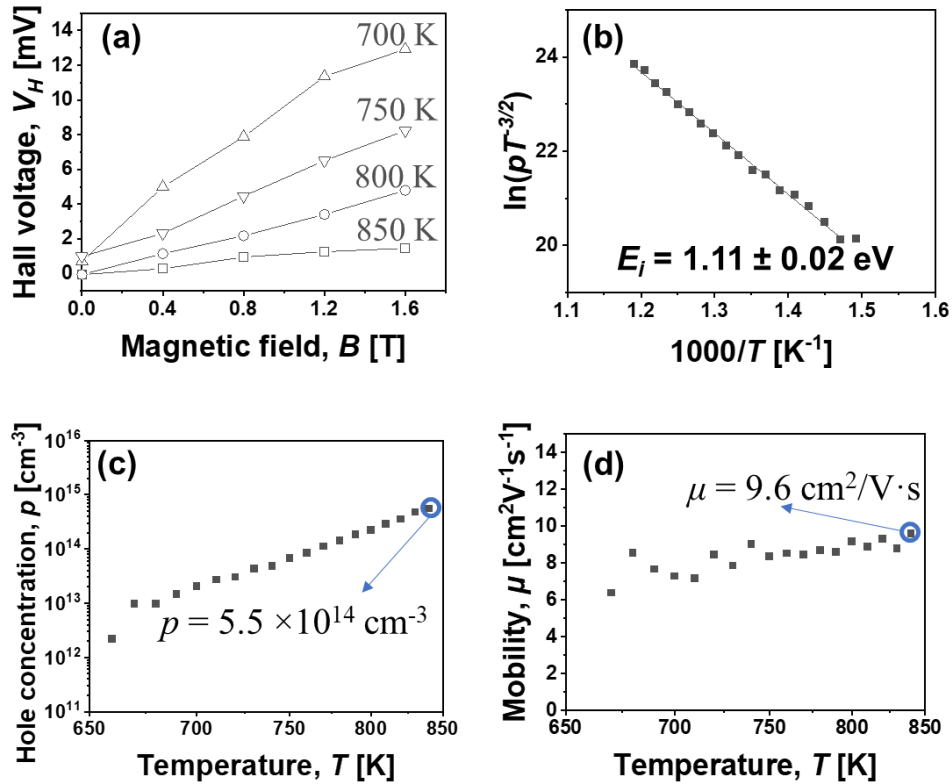


Figure 3-4. (a) Hall voltage ( $V_H$ ) versus magnetic field ( $H$ ) at 800 K and 850 K. (b) Ionization energies of the acceptor center ( $E_i$ ) determination from  $\ln(pT^{-3/2})$  vs.  $(1000/T)$  plot. (c) Temperature dependence of the Hall free hole concentration in log scale. (d) Hall hole mobility as a function of temperature.

### 3.1.3 Optical band gap and photoluminescence

Reflectance and transmittance measurements were conducted on both  $\beta$ -Ga<sub>2</sub>O<sub>3</sub> thin film at room temperature, from 200 to 2000 nm wavelength range. The layer exhibits a high transparency ( $> 80\%$ ) in the vis-NIR range and a sharp cut-off without any other absorption (Figure 3-5). The absorption coefficient ( $\alpha$ ) was then calculated, and the optical band gap ( $E_g$ ) was estimated to be  $4.66 \pm 0.05$  eV using a Tauc plot for direct band gap materials (inset in Figure 3-5).

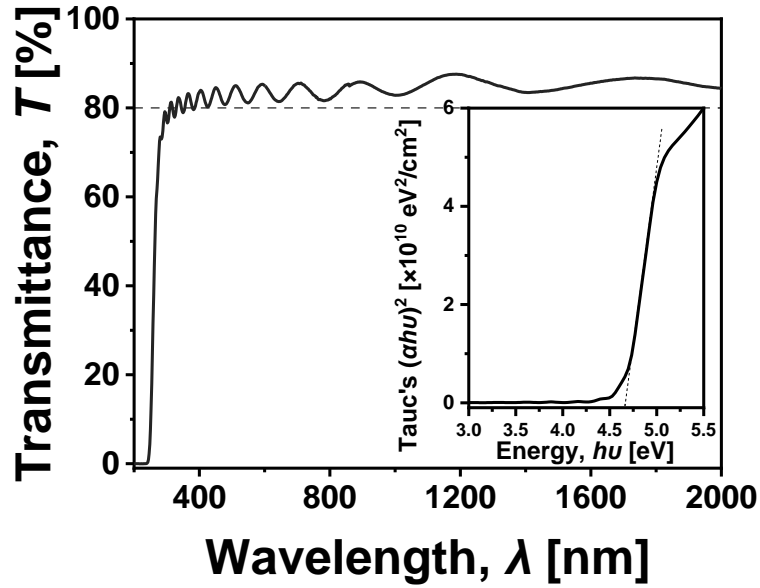


Figure 3-5. Room-temperature optical transmittance for  $\beta$ -Ga<sub>2</sub>O<sub>3</sub> thin film with the estimation of optical band gap by Tauc plot (inset). Oscillations are interferences associated to the film thickness = 450 nm.

The photoluminescence emission spectrum for the undoped  $p$ -type  $\beta$ -Ga<sub>2</sub>O<sub>3</sub> thin layer excited with 266 nm wavelength at 294 K is shown in **Figure 3-6**. A broad and typical emission (with Full Width at Half Maximum (FWHM) around 0.60 eV) centered at  $\sim$ 2.6 eV. Indeed, there are several broad bands typically assigned to intrinsic defects or impurities. For example, peaks at  $\sim$  3.3 – 3.6 eV (UV emission) were correlated with self-trapped holes (STHs) at the intrinsic defects (Ho et al., 2018; Onuma et al., 2013) (e.g. several charged gallium vacancy states  $V_{Ga}^q$ , with  $q = -1, -2, -3$  (Nie et al., 2022)),  $\sim$  2.7 – 3.0 eV (blue emission) were assigned to ( $V_{Ga}$ - $V_O$ ) di-vacancy complex defect (Binet and Gourrier, 1998; Nie et al., 2022),  $\sim$  2.3 – 2.5 eV (green emission) originate from  $O_i$  (Ho et al., 2018), and  $\sim$  1.8 – 2.0 eV (red emission) originate from  $N_O$  (when N doping),  $V_O$  (Onuma et al., 2013; T. Zhang et al., 2013) and  $Cr^{3+}$  impurity (Sun et al., 2020). Very recently, Zhu *et al.* (Zhu et al., 2022) proposed that the  $(V_{Ga} - V_O)^{x-}$  level lies  $\sim$  4.42 – 4.48 eV below the conduction band minimum (CBM) for all their undoped, Si-doped, and Mg-doped  $\beta$ -Ga<sub>2</sub>O<sub>3</sub> single crystals. There is a secondary ultraviolet (UV) emission peak at  $\sim$  3.74 eV, which can be ascribed to the electron transition from the gallium vacancy level, located at about  $\sim$  1 eV from the valence band, as it is quite similar to the ionization energy determined by electrical measurements. Discussion on the luminescence in  $\beta$ -Ga<sub>2</sub>O<sub>3</sub> about the emission origin is still ongoing.

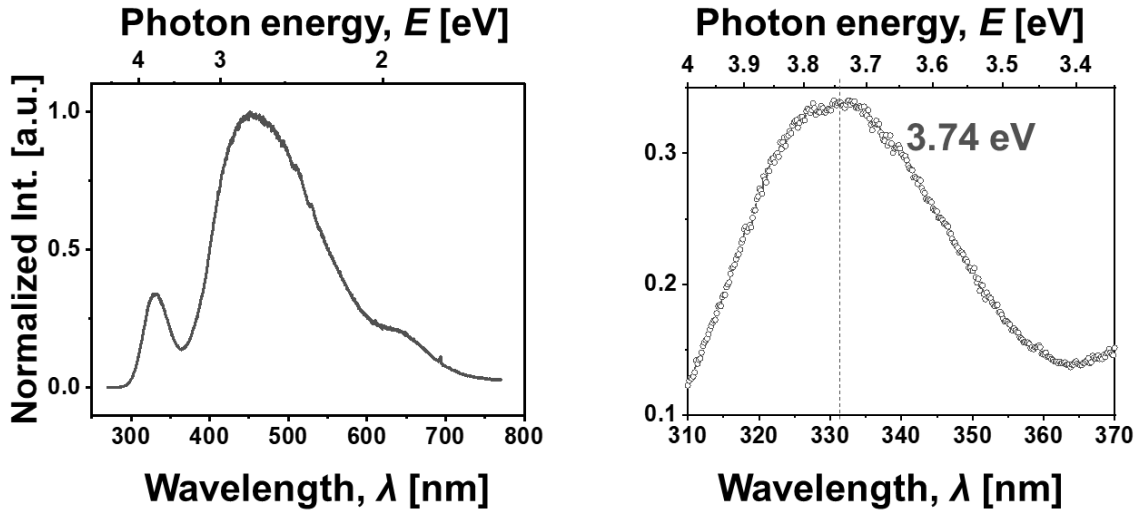


Figure 3-6. Photoluminescence spectrum for undoped  $p$ -type  $\beta$ -Ga<sub>2</sub>O<sub>3</sub> thin layer excited with 266 nm wavelength at 294 K. Right side: enlarged view of the emission located at around 3.7 eV.

### 3.1.4 XPS valence band tail states

X-ray photoelectron spectroscopy (XPS) is a powerful tool for investigating the valence band characteristics of a material, and it can provide evidence of the presence of states within the bandgap as well (B. J. Carey et al., 2017; Wertheim and Hüfner, 1972; Xu et al., 2016). When used in high resolution in the valence band vicinity (i.e., for the lowest binding energies), it is possible to directly detect whether there are states in the lower part of the bandgap (those responsible for  $p$ -type character) (Michling and Schmeißer, 2012). As shown in **Figure 3-7**, there was found to be a clear correlation between the amount of states in the lower half of the bandgap and the  $p$ -type character in the sequence:  $n$ -type (Si-doped) commercial sample as a reference and our  $p$ -type layer. The  $n$ -type control sample is a commercial (Novel Crystal Technology, Inc.) nominally  $n$ -type Si-doped  $\beta$ -Ga<sub>2</sub>O<sub>3</sub> ( $N_D - N_A = 1.3 \times 10^{18} \text{ cm}^{-3}$ ) epitaxy (500 nm) grown on a single crystal  $\beta$ -Ga<sub>2</sub>O<sub>3</sub> (labelled “ $n$ -type (Si-doped)”). For  $\beta$ -Ga<sub>2</sub>O<sub>3</sub> layer, the valence band edge is shifted towards more  $p$ -type using the Ga3d peak as the calibration peak (lower Fermi level implies more  $p$ -type character), see **Figure 3-7 (a)**. A zoom of the smallest binding energies further reveals the presence of states within the band gap (**Figure 3-7 (b)**). The counts per second are normalized to the maximum value in the range of 0–6 eV. The Fermi level is near the conduction band in the case of the commercial Si-doped Ga<sub>2</sub>O<sub>3</sub> reference ( $\sim 4.4$  eV). For the Ga<sub>2</sub>O<sub>3</sub> reference, there is no

indication of further tail states within the band gap. The Fermi level is shifted towards an intrinsic value (i.e., mid-gap) in our  $\beta$ -Ga<sub>2</sub>O<sub>3</sub> layer, which agrees with the semi-insulating behavior found by electrical measurements. Several tail states arise at  $\sim 1.5 - 1.2$  eV from the conduction band.

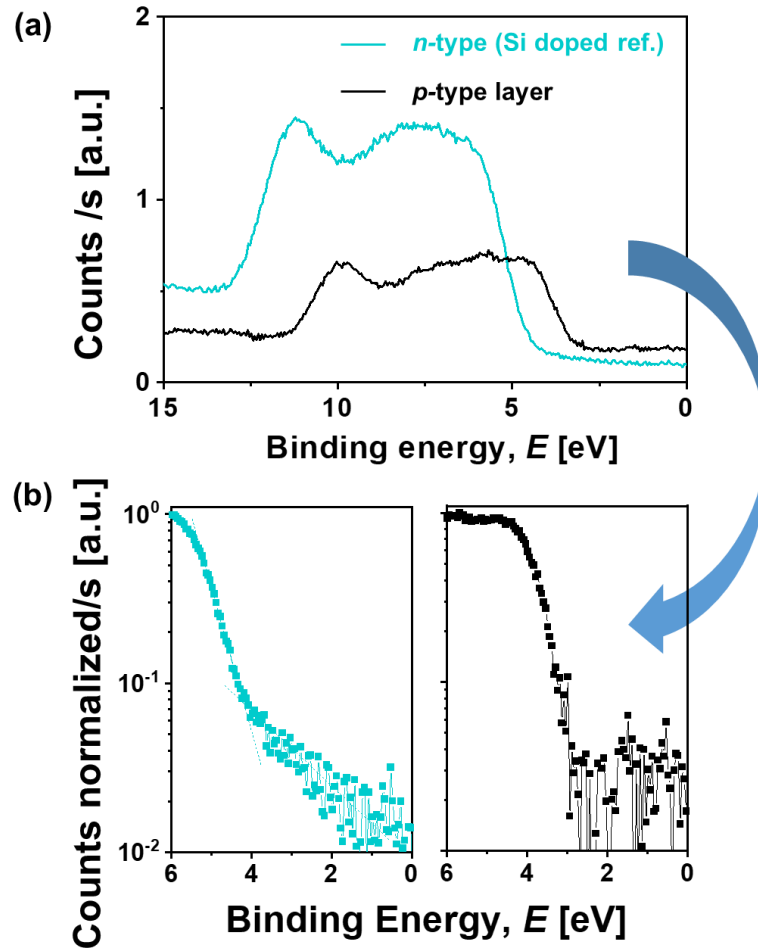


Figure 3-7. (a) XPS valence band of the  $\beta$ -Ga<sub>2</sub>O<sub>3</sub> valence band for a commercial Si-doped (*n*-type) reference and our *p*-type sample. (b) A zoom of the valence band region (VBM) showing the presence of tail states in the lower part of the bandgap for the *p*-type compounds.

### 3.1.5 Influence of the growth temperature on electrical properties

The influence of growth temperature (775 – 825 °C) on electrical properties for undoped  $\beta$ -Ga<sub>2</sub>O<sub>3</sub> has been investigated. The MOCVD growth parameters and the film thicknesses (determined by SEM cross-section) are summarized in **Table 3-2**. Three samples with the only difference being the growth temperature varying from 775 to 825°C, will be

discussed. All the layers have a similar growth rate of around 360 nm/hour independent of the growth temperature.

Table 3-2. Summary of the growth conditions and  $\beta$ -Ga<sub>2</sub>O<sub>3</sub> film thicknesses layers.

N°	substrate	Growth conditions	T [°C]	P <sub>O<sub>2</sub></sub> [Torr]	Time [min]	Thickness [nm]
Ga <sub>2</sub> O <sub>3</sub> -T#1	<i>c</i> -sapphire	Vector gas: Ar	775	12	150	903
Ga <sub>2</sub> O <sub>3</sub> -T#2		TMGa = 12 $\mu$ mol O <sub>2</sub> = 1200 sccm	790			900
Ga <sub>2</sub> O <sub>3</sub> -T#3		<i>P</i> = 38 Torr	825			919

Firstly, electrical contacts were prepared: Ohmic contacts were prepared by silver paste painted at 4 corners of square-shaped samples, in order to carry out Hall Effect measurements in a Van der Pauw configuration. The samples are highly resistive requiring measurements at high temperatures (550 – 850 K). As is shown in **Figure 3-8 (a)**, the higher the deposition temperature, the lower the electrical resistivity (thereby higher the conductivity) of the thin film. For, example, at 850 K,  $\rho_{825\text{ K}} = 3.5 \times 10^2 \Omega \cdot \text{cm}$ ,  $\rho_{790\text{ K}} = 1.3 \times 10^3 \Omega \cdot \text{cm}$ ,  $\rho_{775\text{ K}} = 1.4 \times 10^4 \Omega \cdot \text{cm}$ .

The activation energies of the conductivity were determined to be very similar:  $E_a = 0.90 \pm 0.02$  eV,  $0.89 \pm 0.01$  eV,  $0.84 \pm 0.01$  eV, for 775 °C, 790 °C, and 825 °C grown layer, respectively (**Figure 3-8 (b)**). To determine the sign of majority carriers Hall voltage was scanned versus applied magnetic field from 0 to 1.6 T. **Figure 3-8 (c)** The positive slope and the sign of  $V_H$  confirming that all three samples are of *p*-type. The measured hole concentrations increase with the increasing growth temperature. **Figure 3-8 (d)** shows hole concentrations versus measurement temperatures. It is clear that Hall hole concentrations are significantly different depending on Ga<sub>2</sub>O<sub>3</sub> thin film deposition temperatures. For example, at 850 K,  $p_{825\text{ K}} = 2.1 \times 10^{15} \text{ cm}^{-3}$ ,  $p_{790\text{ K}} = 6.2 \times 10^{14} \text{ cm}^{-3}$ ,  $p_{775\text{ K}} = 2.8 \times 10^{13} \text{ cm}^{-3}$ .

While the activation energies of acceptor obtained by linear fits for  $\ln(pT^{-3/2})$  vs.  $1000/T$  plots are estimated as  $E_a \approx 1.1$  eV for all samples. (**Figure 3-8 (e)**) This activation energy corresponds to native  $V_{\text{Ga}}$  acceptor defect, as was shown in Section 3.1.2, having the same activation energies and different carrier concentrations indicates the different compensation

level in the samples. In other word, with increasing of growth temperature, the compensating native donor defect concentration decreases.

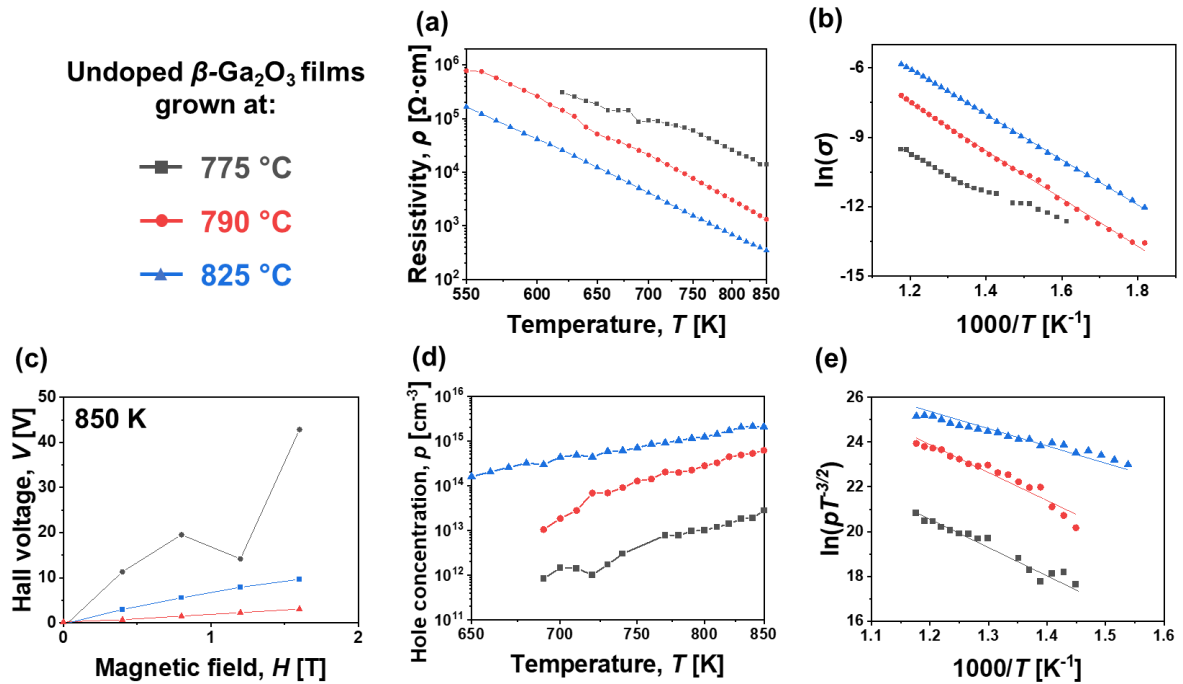


Figure 3-8. (a) Temperature dependence of resistivity. (b)  $\ln(\sigma)$  vs.  $1000/T$  plots and linear fits for the determination of the activation energy of conductivity. (c) Hall voltage ( $V_H$ ) versus applied perpendicular magnetic field ( $H$ ). (d) Hall hole concentrations versus temperatures. (e)  $\ln(pT^{-3/2})$  vs.  $1000/T$  plots and linear fits for the determination of the activation energies of acceptor centers.

Summarizing,  $\beta$ -Ga<sub>2</sub>O<sub>3</sub> thin films deposited on  $c$ -plane sapphire substrate by MOCVD technique were studied by X-ray diffraction and Raman spectroscopy, the results suggest that films are epitaxial and of high crystalline quality without any secondary phase or polymorph of Ga<sub>2</sub>O<sub>3</sub>. Samples exhibit a high transparency ( $> 80\%$ ) in vis-NIR wavelength range with a cut-off at  $\sim 266$  nm associated to the optical gap threshold. The native defect ( $V_{\text{Ga}}$ ) originated  $p$ -type nature of the layer was confirmed by Hall Effect and XPS characterizations. These results pave the way for further acceptor doping in  $\beta$ -Ga<sub>2</sub>O<sub>3</sub>.

## 3.2 Zn doping in $\beta$ -Ga<sub>2</sub>O<sub>3</sub>

Achieving *p*-type conductivity in  $\beta$ -Ga<sub>2</sub>O<sub>3</sub> has been proven to be a great challenge. Researchers have focused on identifying an efficient acceptor dopant, we have selected a II group element, zinc.

### 3.2.1 State of the art for Zn doping in $\beta$ -Ga<sub>2</sub>O<sub>3</sub>

Theoretical works based on first principle calculations suggested that Zn doping (~ 2%) does not change the basic electronic structure of  $\beta$ -Ga<sub>2</sub>O<sub>3</sub>, but only generates an empty energy level above the maximum of the valence band, which is shallow enough to make the Zn-doped  $\beta$ -Ga<sub>2</sub>O<sub>3</sub> a typical *p*-type semiconductor (Li et al., 2012). However, for C. Zhang and co-authors, an atomic Zn concentration of ~ 2.5% has been estimated to introduce shallow levels above the valence band at around 0.33 eV (Zhang et al., 2019). However, several works proposed that Zn introduces a deep acceptor level at > 1.2 eV above the valence band maximum ( $\Delta E_{VBM} + 1.2$  eV) with a low activation rate (Tang et al., 2016), which is difficult to contribute to the *p*-type conductivity (Kyrtos et al., 2018; Lyons, 2018). It is worth noting that the difference may come from the computational methods but also the doping level (i.e., the superlattice size and the number of zinc atoms used). A high *n*-type conductivity was explained by a shallow donor complex Zn<sub>i</sub> - Zn<sub>Ga</sub> for Zn-doped  $\beta$ -Ga<sub>2</sub>O<sub>3</sub> (Hommedal et al., 2023). Co-doping Zn-N has been predicted to offer shallow acceptor levels (0.01 – 0.48 eV) above the VBM (Yan et al., 2021; Zhang et al., 2012b).

There are some experimental works dedicated to high amount (> 1%) Zn incorporation into  $\beta$ -Ga<sub>2</sub>O<sub>3</sub> for different purposes such as improvement of oxygen gas sensing properties (Li et al., 2003), band gap engineering (Guo et al., 2017; Tao et al., 2019), enhancement of the photocatalytic activity (Yamakata et al., 2021).

For electrical properties induced by Zn doping, Feng *et al.* (Feng et al., 2016) demonstrated the *p*-type conductivity using a *p-n* junction. Agnitron Technology Incorporated (USA) reported  $\beta$ -Ga<sub>2</sub>O<sub>3</sub> Zn-doped thin films on *c*-sapphire by MOCVD the incorporation of 10.9 %. Zn XRD patterns yielded a mono-phase polycrystalline structure with an increase of lattice parameters with doping, though room temperature Hall measurements were not successful due to the very high resistivity of the samples (Alema et al., 2017a). Interestingly, Wang *et al.* (X. H. Wang et al., 2014) studied the electrical characterization by Hall effect at room temperature for undoped and Zn doped  $\beta$ -Ga<sub>2</sub>O<sub>3</sub> thin

---

films, showed an electron concentration of  $1.4 \times 10^{14}$  for undoped  $\beta$ -Ga<sub>2</sub>O<sub>3</sub> layer, it was decreased to  $7.2 \times 10^{11}$  cm<sup>-3</sup> after 3 at. % Zn incorporation, and increased to  $6.3 \times 10^{12}$  cm<sup>-3</sup> with further increasing the nominal Zn content at 7 at. %. However, the authors could not validate the carrier type after Zn incorporation, which was attributed to the co-existence of comparable hole and electron concentrations. From cathodoluminescence measurements, the acceptor level of Zn<sub>Ga</sub> is estimated to be 0.26 eV above the valence band maximum. Su *et al.* (Su et al., 2019) deposited Mg-Zn (4.68 at. % (Mg)/ 11.1 at. % (Zn)) co-doped  $\beta$ -Ga<sub>2</sub>O<sub>3</sub> on sapphire (0001), anti-site defect Zn<sub>Ga</sub> was determined as deep acceptors at 0.79 eV by absorption spectra. Zn doping (10 at. %) in  $\beta$ -Ga<sub>2</sub>O<sub>3</sub> has also been observed to stabilize the optical band gap and reduce the dielectric constant for atomic layer deposition (ALD) grown films (Baji et al., 2021).

Experimental works reported about low doping cases (< 1 at. %) are relatively limited. Shrestha *et al.* (Shrestha et al., 2013) studied the properties of 0.59% Zn-doped  $\beta$ -Ga<sub>2</sub>O<sub>3</sub> nano-porous layers for photo-induced hydrogen generation. It has been concluded that the presence of a small amount of zinc doping in  $\beta$ -Ga<sub>2</sub>O<sub>3</sub> can reduce trapping sites at the donor level under the conduction band, and thereby increase the mobility of electrons. On the other hand, zinc doping also creates additional trapping sites as acceptor levels over the valence band, which hampers the activation of holes. An improvement of photocatalytic activity by Zn doping (up to 1 atomic % of zinc) on H<sub>2</sub>O splitting is found and associated with the increase in the mobility and concentration of holes due to the formation of an acceptor level (Sakata et al., 2008). Several recent works showed that Zn acts as an acceptor in  $\beta$ -Ga<sub>2</sub>O<sub>3</sub> for 1.8 wt. % Zn doped thin film grown by Halide Vapor-Phase Epitaxy (HVPE), 0.25 at. % Zn doped bulk crystals by Czochralski (CZ) and vertical gradient freeze (VGF) techniques (Gustafson et al., 2021; Jesenovec et al., 2021a; Pansegrau et al., 2021). The authors (Gustafson et al., 2021; Jesenovec et al., 2021a) proposed that Zn is a deep acceptor with an ionization energy of more than  $\sim 0.7$  eV, and it takes preferentially Ga octahedral site. Such a discrepancy with the theoretical work (Lyons, 2018) that calculated that Ga tetrahedral site is favored for Zn substitution, was explained by the calculations on Ga3d states treatment. Previously reported works on Zn doping in  $\beta$ -Ga<sub>2</sub>O<sub>3</sub> showing acceptor characteristics are summarized in **Table 3-3**.

Table 3-3. Summary of previously reported Zn-doped  $\beta$ -Ga<sub>2</sub>O<sub>3</sub> from the literature, showing Zn related acceptor characteristics. Remarks (a – e) refer to: a) Overall reduction of conductivity/Zn considered as an acceptor; b) determined by photoluminescence; c= determined by cathodoluminescence; d) nanowire; e) determined by Electron paramagnetic resonance (EPR)

Zn [%]	Substrate	Growth	Type	Comments	Ref.
-	Sapphire	Sol-gel	<i>n</i>	Zn related acceptor <sup>a</sup>	(Li et al., 2003)
2.0	Si (111)	RF sputtering	-	Zn related acceptor <sup>b</sup>	(Yue et al., 2012)
0.59	Ga, GaZn alloy	Anodization	-	-	(Shrestha et al., 2013)
3.0 - 7.0	(0001) sapphire	PLD	-	$\Delta E_{VBM} + 0.26$ eV <sup>c</sup>	(X.H. Wang et al., 2014)
1.3 - 3.6	NW <sup>d</sup> / $\beta$ -Ga <sub>2</sub> O <sub>3</sub>	CVD	<i>p</i>	<i>p-n</i> junction	(Feng et al., 2016)
0.69 - 3.03	<i>c</i> -sapphire	RF sputtering	<i>n</i>	Zn related acceptor <sup>a</sup>	(Guo et al., 2017)
11.1	<i>c</i> -sapphire	RF sputtering	<i>p</i>	$\Delta E_{VBM} + 0.79$ eV <sup>b</sup>	(Su et al., 2019)
0.25	Bulk	CZ	<i>p</i>	$\Delta E_{VBM} + 0.65$ eV <sup>e</sup>	(Gustafson et al., 2021; Jesenovec et al., 2021a)
1.8 wt.	<i>c</i> -sapphire	HVPE	<i>p</i>	Zn related acceptor <sup>b</sup>	(Pozina et al., 2021)

To summarize, significant efforts have been dedicated to Zn doping in  $\beta$ -Ga<sub>2</sub>O<sub>3</sub>. However, as expected and experimentally observed, Zn impurities role in  $\beta$ -Ga<sub>2</sub>O<sub>3</sub> depends on various factors for both experimental and theoretical works. While deep levels related to Zn impurity have been identified, there was still a lack of direct evidence of the *p*-type behavior. Zn-induced donor Zn<sub>i</sub> has been proposed theoretically and the increase in electron concentration has been observed experimentally, a comprehensive investigation is still required. The effect of Zn doping strongly depends on growth conditions and doping levels, thus, the aim of my work was to carry out a deep study related to Zn doping effect on electrical and optical properties of  $\beta$ -Ga<sub>2</sub>O<sub>3</sub> thin films.

### 3.2.2 Thermodynamic analysis of point defects for Zn:Ga<sub>2</sub>O<sub>3</sub> system

Zn, as a II group element, is expected to be an acceptor in  $\beta$ -Ga<sub>2</sub>O<sub>3</sub>. However, due to its similar atomic radii to Ga, as well as the similar ionic radii of Zn<sup>2+</sup> and Ga<sup>3+</sup>, it can also occupy an interstitial position acting as a donor. This amphoteric nature of Zn may be responsible for the so-called “impurity auto-compensation” effect. Similar auto-compensation cases have been reported on other II group elements doping in III-IV

semiconductors such as Mg (Miceli and Pasquarello, 2016; Wahl et al., 2021) and Be (Wahl et al., 2022) in GaN and Zn in GaAs (Longini, 1962), I group elements doping in II-VI semiconductor ZnSe (Neumark, 1980). H. Peelaers *et al.* (Peelaers et al., 2019) investigated several II elements (Be, Mg, Ca, Sr, Zn, Cd) doped in  $\beta$ -Ga<sub>2</sub>O<sub>3</sub>, the first-principle calculations based results revealed that all of them can be amphoteric. Later, after our experimental work (Chikoidze et al., 2020b), Zn and Ca doping in  $\beta$ -Ga<sub>2</sub>O<sub>3</sub> have been studied taking both interstitial ( $Zn_i$ ) and substitution ( $Zn_{Ga}$ ) sites into account (Hommedal et al., 2023; Yamakata et al., 2021). A high  $n$ -type conductivity was explained by a shallow donor complex  $Zn_i - Zn_{Ga}$  based on the first-principle calculations (Hommedal et al., 2023).

Therefore, prior to the investigation of Zn doping influence in  $\beta$ -Ga<sub>2</sub>O<sub>3</sub>, it is important to conduct the thermodynamic analysis of point defects for  $\beta$ -Zn:Ga<sub>2</sub>O<sub>3</sub> system, to define the dependences of point defects concentration, charge carriers on growth temperature and oxygen partial pressure in the surrounding atmosphere.

The study of native point defects has been reviewed in Section 1.1.3 (Point defects studies and doping issues). Besides, as stated above, Zn can take both interstitial site ( $Zn_i$ ) and substitute Ga ( $Zn_{Ga}$ ), together with the main acceptor defects in  $\beta$ -Ga<sub>2</sub>O<sub>3</sub>, gallium vacancy ( $V_{Ga}$ ) have been considered here. The analysis was conducted using the Kroger method of quasi-chemical equations. In this approach, the creation of dominant defects and charge carriers are written as chemical reactions. The corresponding mass action laws, together with the electro-neutrality condition and impurity mass balance equation, give a system of equations for the concentrations of the main charged species (acceptor and donor defects, free electrons and holes) existing in the crystal as follow:

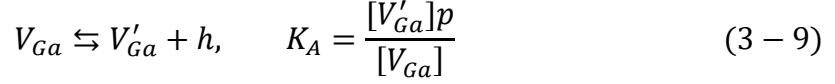
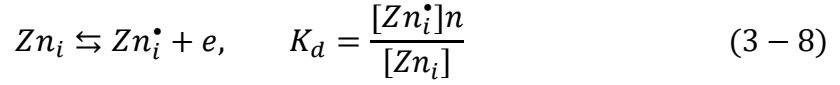
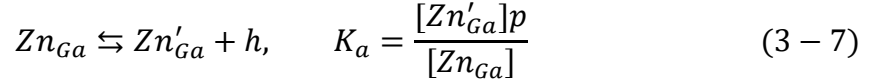
The lattice thermal ionization:

$$\emptyset \rightleftharpoons e + h, \quad K_i = np \quad (3 - 5)$$

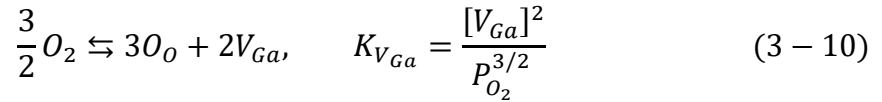
Where  $e$  and  $h$  are electrons and holes, respectively;  $n$  and  $p$  are their concentrations, respectively. Substitutional Zn transfer to interstitial position:

$$Zn_{Ga} \rightleftharpoons Zn_i + V_{Ga}, \quad K_{Zn} = \frac{[Zn_i][V_{Ga}]}{[Zn_{Ga}]} \quad (3 - 6)$$

Where  $Zn_{Ga}$ ,  $Zn_i$ ,  $V_{Ga}$  denote zinc substituting gallium, zinc interstitial, and gallium vacancy, respectively. Ionizations of acceptor and donor impurities, and the native acceptor gallium vacancy:



Where  $Zn'_{Ga}$  and  $V'_{Ga}$  denote positively single-charged zinc substituting gallium and gallium vacancies, respectively;  $[Zn'_{Ga}]$  and  $[V'_{Ga}]$  are their concentrations, respectively.  $Zn^{\bullet}_i$  is the negatively single-charged zinc interstitial with  $[Zn^{\bullet}_i]$  being the concentration. Then, considering the interaction with environment, gas phase:



To find the concentration of defects and free carriers by the system of equations above, the charge-neutrality condition and mass balance equation are then added:

$$n + [V'_{Ga}] + [Zn'_{Ga}] = p + [Zn^{\bullet}_i] \quad (3-11)$$

$$[Zn_i] + [Zn^{\bullet}_i] + [Zn_{Ga}] + [Zn'_{Ga}] = [Zn_{tot}] \quad (3-12)$$

Establish the equilibrium concentrations of electrons and holes, as well as impurities and defects in different charge states. Electro-neutrality and mass balance depend on the total Zn concentration ( $[Zn_{tot}]$ ), temperature ( $T$ ) and pressure ( $P_{O_2}$ ) in surrounding atmosphere.

The equilibrium was calculated using the total pressure of 30 Torr in the MOCVD chamber, which is the parameter we used in the experiments. Three regions depending on the impurity concentration were considered as a function of growth temperature as shown in **Figure 3-9**:

(I) Intrinsic conductivity region: in this region, the concentration of Zn is very low. The dominant species is one-charged intrinsic acceptor  $V'_{Ga}$  and holes. Related equations are considered, and the hole concentration can be determined:

$$p = [V'_{Ga}] = \left( K_A K_{V_{Ga}}^2 P_{O_2}^{\frac{3}{2}} \right)^{1/2} \quad (3-13)$$

(II) Impurity  $p$ -type conductivity region: with the increase of Zn concentration gallium vacancies might be occupied with Zn atoms.  $Zn'_{Ga}$  becomes the dominant species:

$$p = [Zn'_{Ga}] = [Zn_{tot}] \quad (3 - 14)$$

(III) Impurity auto-compensation region: with further increase of Zn concentration, a fraction of Zn atoms occupies interstitial sites.  $Zn'_{Ga}$  and  $Zn_i^\bullet$  are dominant species.

$$p = \left( \frac{K_a K_i K_{V_{Ga}}^{\frac{1}{2}} P_{O_2}^{\frac{3}{4}}}{K_d K_{Zn}} \right)^{\frac{1}{2}} \quad (3 - 15)$$

Such approximations provide a clear picture of doping peculiarities and simplify the calculations. The boundaries between these ranges can be defined by means of discontinuity of concentrations charge carriers or other species.

$$[Zn_{tot}]_{I-II} = \left( K_A K_{V_{Ga}}^{\frac{1}{2}} P_{O_2}^{\frac{3}{4}} \right)^{1/2} \quad (3 - 16)$$

$$[Zn_{tot}]_{II-III} = \left( \frac{K_a K_i K_{V_{Ga}}^{\frac{1}{2}} P_{O_2}^{\frac{3}{4}}}{K_d K_{Zn}} \right)^{1/2} \quad (3 - 17)$$

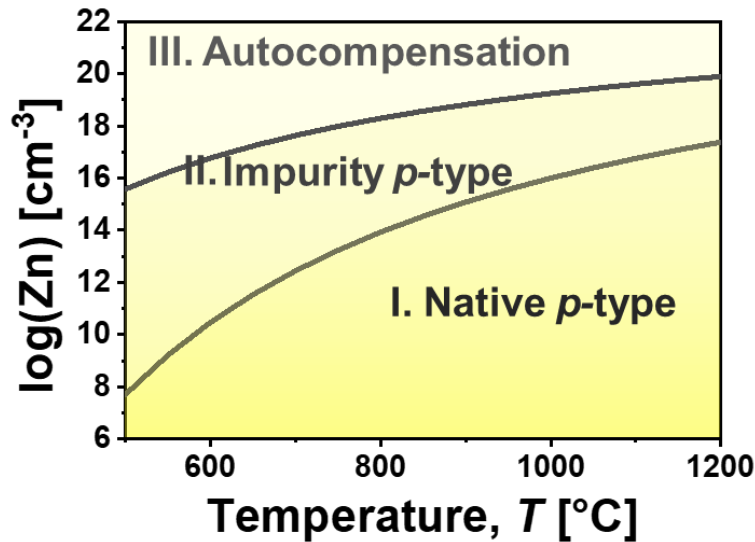


Figure 3-9. Phase diagram of  $\beta$ -Zn:Ga<sub>2</sub>O<sub>3</sub> with three thermodynamical regions: native  $p$ -type, impurity  $p$ -type and impurity auto-compensation, with boundary curves versus temperature.

Based on the thermodynamic analysis, it is possible to achieve  $p$ -type  $\beta$ -Zn:Ga<sub>2</sub>O<sub>3</sub> thin films in all the three regimes by adjusting Zn concentration and growth temperatures. For example, at 800 °C, the acceptor defect  $Zn_{Ga}$  becomes dominant when Zn doping

concentration exceeds  $\sim 10^{14}$  cm<sup>-3</sup>, and the impurity *p*-type conductivity occurs. As the Zn doping concentration further increases to  $\sim 10^{18}$  cm<sup>-3</sup>, Zn starts to occupy interstitial sites. Both donor Zn<sub>i</sub> and acceptor Zn<sub>Ga</sub> defects compensate for each other, leading to the auto-compensation regime.

### 3.3 Zn doped $\beta$ -Ga<sub>2</sub>O<sub>3</sub> thin films: experimental results

The objective was to elaborate Zn-doped  $\beta$ -Ga<sub>2</sub>O<sub>3</sub> thin films, and study experimentally the effect of Zn doping on electronic and optical properties of the samples grown on *c*-plane Al<sub>2</sub>O<sub>3</sub>(0001) and on conducting Si(111) substrates simultaneously in the MOCVD reactor. The conducting Si substrate was used to fabricate vertical parallel plane capacitors, and characterized them vertically in terms of breakdown voltage capability. While the thin films grown on *c*-sapphire substrates were used for the investigation of the electrical transport properties (resistivity, carrier, mobility). Firstly, results for  $\beta$ -Zn:Ga<sub>2</sub>O<sub>3</sub>//*c*-Al<sub>2</sub>O<sub>3</sub> will be discussed. During the growth, the flow rate of the gallium precursor and oxygen were kept at 6  $\mu$ mol/min and 600 sccm respectively. The growth temperature and pressure were set at 775 °C and 30 Torr, respectively. The DEZn flow was varied in the following conditions: 1.6, 2.8, 3.9  $\mu$ mol/min. the growth conditions together with the thicknesses of the layers are summarized in the **Table 3-4**.

Table 3-4. Summary of the growth conditions.

N°	Structure	Growth conditions	DEZn [ $\mu$ mol]	Deposition time [min]	Thickness [nm]
Undoped Ga <sub>2</sub> O <sub>3</sub>	Ga <sub>2</sub> O <sub>3</sub> // <i>c</i> -sapphire Ga <sub>2</sub> O <sub>3</sub> //Si(111)		-	85	450
Zn:Ga <sub>2</sub> O <sub>3</sub> #1		Vector gas: Ar TMGa = 6 $\mu$ mol O <sub>2</sub> = 600 sccm	0.99	60	323
Zn:Ga <sub>2</sub> O <sub>3</sub> #2	Zn:Ga <sub>2</sub> O <sub>3</sub> // <i>c</i> -sapphire Zn:Ga <sub>2</sub> O <sub>3</sub> //Si(111)	<i>P</i> = 30 Torr <i>T</i> = 775 °C	2.3	60	323
Zn:Ga <sub>2</sub> O <sub>3</sub> #3			3.8	90	360

## 3.3.1 Structural and morphological characterizations

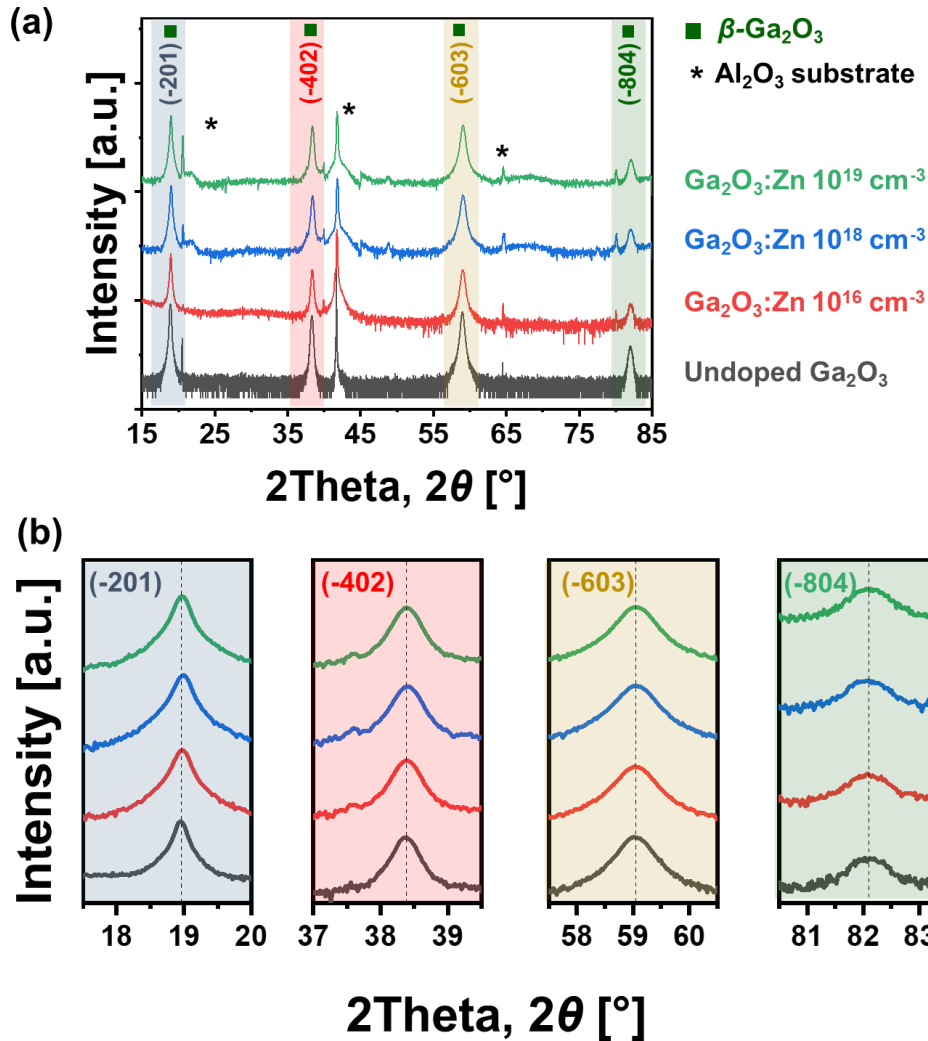


Figure 3-10. (a) XRD patterns for undoped and Zn-doped  $\beta$ -Ga<sub>2</sub>O<sub>3</sub> thin films with different Zn flow (Zn concentration). “\*” refers to XRD peaks of *c*-plane sapphire substrates. (b) Enlarged view of five peaks located at  $2\theta = 18.94^\circ$ ,  $38.38^\circ$ ,  $58.98^\circ$ ,  $82.14^\circ$  to show that, there’s no transition peak.

The phase purity of the films on *c*-plane sapphire substrates was first analyzed by X-ray diffraction (XRD). **Figure 3-10 (a)** displays the results of the XRD  $\theta$ - $2\theta$  scan for the undoped and Zn-doped  $\beta$ -Ga<sub>2</sub>O<sub>3</sub> thin films with different doping levels, in which  $2\theta$  was increased from  $10^\circ$  to  $120^\circ$ . “\*” marked at  $2\theta = 20.62^\circ$ ,  $41.74^\circ$ , and  $64.54^\circ$  refer to the XRD peaks of *c*-plane sapphire substrates. The XRD patterns of these films are very similar. It can be found that all the undoped and Zn-doped  $\beta$ -Ga<sub>2</sub>O<sub>3</sub> layers possess diffraction peaks located near  $2\theta$  positions of  $18.94^\circ$ ,  $38.38^\circ$ ,  $58.98^\circ$ , and  $82.14^\circ$  which correspond to (-201), (-402), (-603), and (-804) preferential planes of  $\{-201\}$  family of monoclinic  $\beta$ -Ga<sub>2</sub>O<sub>3</sub>, respectively,

conforming to JCPDS data of  $\beta$ -Ga<sub>2</sub>O<sub>3</sub> (card no. 00-41-1103). We concluded that the studied thin films are a textured (-201)  $\beta$ -Ga<sub>2</sub>O<sub>3</sub> crystalline phase. No secondary phase other than  $\beta$ -Ga<sub>2</sub>O<sub>3</sub> was found. Moreover, focusing on these peaks (**Figure 3-10 (b)**), all the peaks are at quite similar positions, indicating that the lattice parameters remained comparable although different Zn precursor's flows were used.

**Figure 3-11** shows the secondary-ion mass spectroscopy (SIMS) depth profiles of Zn dopant content for the three samples at different doping levels. The doping concentrations (from low to high) were then determined to be  $1.0 \times 10^{16} \text{ cm}^{-3}$ ,  $1.4 \times 10^{18} \text{ cm}^{-3}$ , and  $2.0 \times 10^{19} \text{ cm}^{-3}$ , respectively. The  $1.0 \times 10^{16} \text{ cm}^{-3}$  is close to the detection limit of SIMS equipment. The Zn distribution in the sample at a doping level of  $2.0 \times 10^{19} \text{ cm}^{-3}$  is homogeneous in depth. For the convenience of writing and reading, these doping concentrations will be referred to  $10^{16} \text{ cm}^{-3}$ ,  $10^{18} \text{ cm}^{-3}$ , and  $10^{19} \text{ cm}^{-3}$ , respectively. To note that the Zn signal intensity corresponding to the doping concentration at  $10^{16} \text{ cm}^{-3}$  is the detection limit.

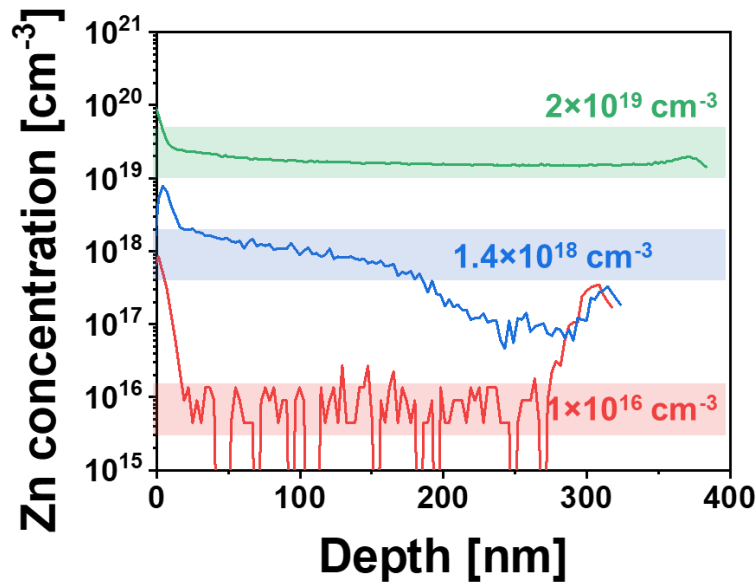


Figure 3-11. SIMS depth profiles for three Zn doped  $\beta$ -Ga<sub>2</sub>O<sub>3</sub> samples grown at Zn flows at 1.6, 2.8, 3.9  $\mu\text{mol}/\text{min}$ , respectively.

**Figure 3-12** displays the scanning electron microscopy (SEM) top-view images of the films deposited on *c*-sapphire substrates. It shows smooth granular surface morphology, while there are irregular agglomerations of particulates resembled at the surface of the undoped film. With the increasing amount of incorporated Zn dopants, the surface becomes smoother and finer, the agglomerations become smaller and then invisible on the film with

$[\text{Zn}] = 10^{19} \text{ cm}^{-3}$ . Such a change of the surface morphology with the increasing Zn doping levels merits a deeper study, on the formation mechanism of 2D and/or 3D defects.

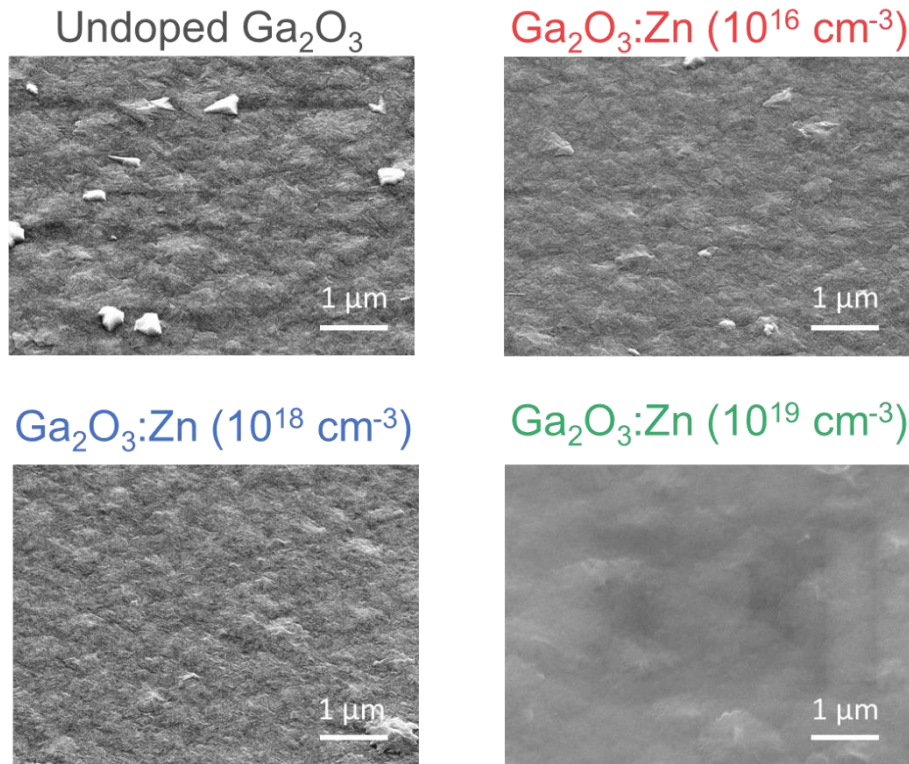


Figure 3-12. Scanning electron microscopy (SEM) top-view images of (a) – (d) undoped,  $[\text{Zn}] = 10^{16} \text{ cm}^{-3}$  doped,  $[\text{Zn}] = 10^{18} \text{ cm}^{-3}$  doped, and  $[\text{Zn}] = 10^{19} \text{ cm}^{-3}$  doped  $\beta$ -Ga<sub>2</sub>O<sub>3</sub> grown on *c*-plane sapphire substrate, respectively.

### 3.3.2 Optical properties

Reflectance and transmittance measurements were conducted on both undoped and Zn-doped  $\beta$ -Ga<sub>2</sub>O<sub>3</sub> thin films at room temperature, covering a broad wavelength range from ultra-violet (UV) to near infra-red (NIR). The transmittance spectra showed that all the thin films exhibit high transparency in the vis-NIR range, with a sharp cut-off in the deep ultra-violet (DUV) region, as depicted in **Figure 3-13 (a)**. The little “cusp” at around 860 nm is artificial for all the spectra, due to the detector change in the spectrophotometer. The average transmittance of the films (with the increasing Zn concentration) in the visible (vis) range (380 – 700 nm) is 83%, 77%, 80%, and 76%, respectively. The absorption coefficient  $\alpha$  of the films was calculated from the transmittance and reflectance measurements, and the optical band gaps  $E_g$  were then estimated using Tauc plot for direct band gap materials, which plots  $(\alpha E)^2$  vs.  $E$  as shown in **Figure 3-13 (b)**. The corresponding “cut-off” wavelengths of

all the films were found to be below 280 nm, falling in the UV-C range. Considering the error bars, the band gaps remained comparable after Zn incorporation.

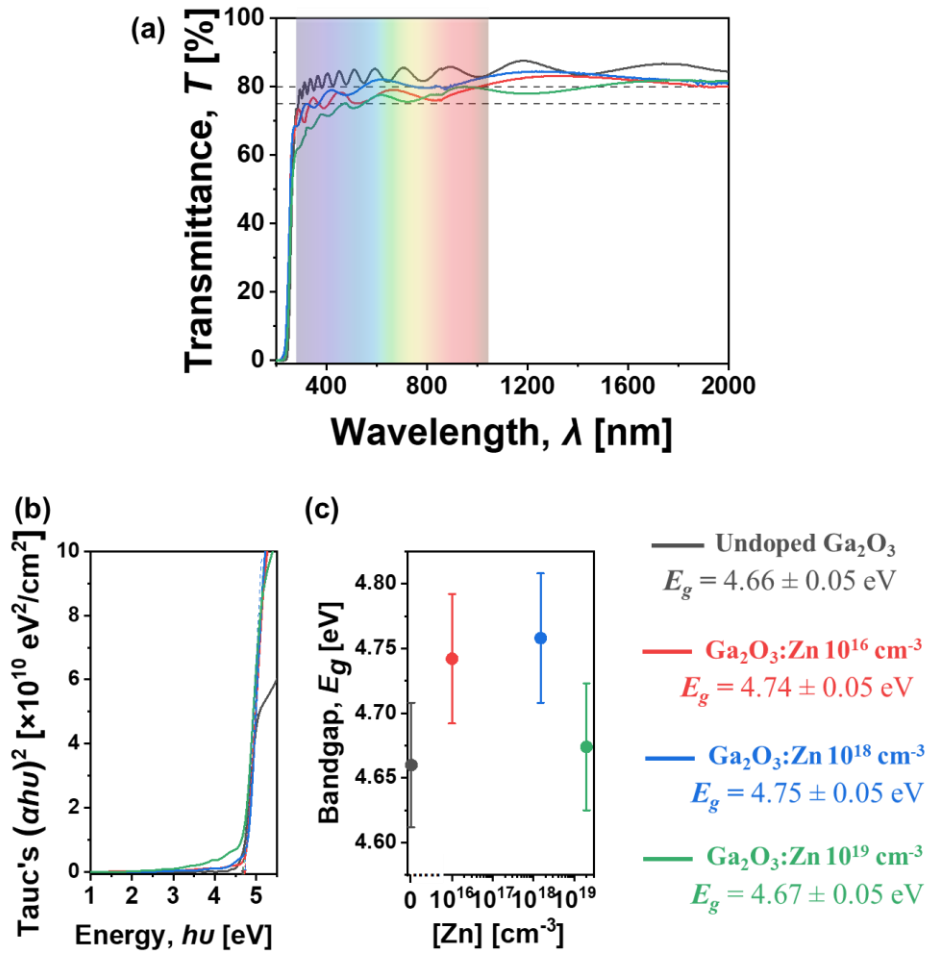


Figure 3-13. (a) Optical transmittance. (b) Tauc plots (for the determination of the optical band gap). (c) Optical band gaps with error bars versus incorporated Zn concentrations. Different oscillations periods are connected to different film thicknesses.

In general, optical properties can be modified in doped materials. After impurities are introduced into the crystal lattice of a semiconductor material, additional energy states can be created within the bandgap. A number of reports have investigated the optical properties of  $\beta$ -Zn:Ga<sub>2</sub>O<sub>3</sub> films and single crystals, the optical band gap can be either slightly increased (Baji et al., 2021), or slightly decreased (Feng et al., 2016; Guo et al., 2017; Yue et al., 2012), or remained comparable of undoped one (Jesenovec et al., 2021a; Pozina et al., 2021; X.H. Wang et al., 2014). When incorporated Zn concentration becomes more significant ( $> 10\%$ ), the influence on the optical band gap will be even more apparent, either increased (Tao et

al., 2019) (due to Burnstein-Moss effect) or decreased (Zhao et al., 2017), while keeping the Ga<sub>2</sub>O<sub>3</sub> structure. To note that the difference between the values of optical  $E_g$  here and that we reported (Chikoidze et al., 2022), comes from two different estimation methods. The optical band gaps were firstly estimated using the Beer-Lambert law (Chen and Jaramillo, 2017), which allows us to calculate the absorption from the transmittance as the films were transparent and only weakly reflected to the eye, at normal incidence. The reflectance of the films was remeasured later with a longer acquisition time, the optical  $E_g$  was then recalculated based on both reflectance and transmittance measurements.

### 3.3.3 Electrical transport properties

The first step as always was to prepare electrical contacts and test their Ohmicity. The contacts were prepared by painting the silver paste at 4 corners of square-shaped samples in a Van der Pauw configuration as described in the methodology chapter, and in the previous section.

The Hall Effect measurements were carried out at the temperature range of 500 – 850 K. As shown in **Figure 3-14**, the positive  $V_H$  increases linearly with a perpendicularly applied increasing magnetic field from 0 to 1.6 T at elevated temperature, indicating that all  $\beta$ -Zn:Ga<sub>2</sub>O<sub>3</sub> samples are  $p$ -type. We can note that this figure shows how a continuous variation of magnetic field up to quite a high value ( $\pm 1.6$  T), gives undisputable evidence of the conductivity type ( $n$  or  $p$ ), independently of zero voltages experimental off-set (changing here from zero, positive to negative values).

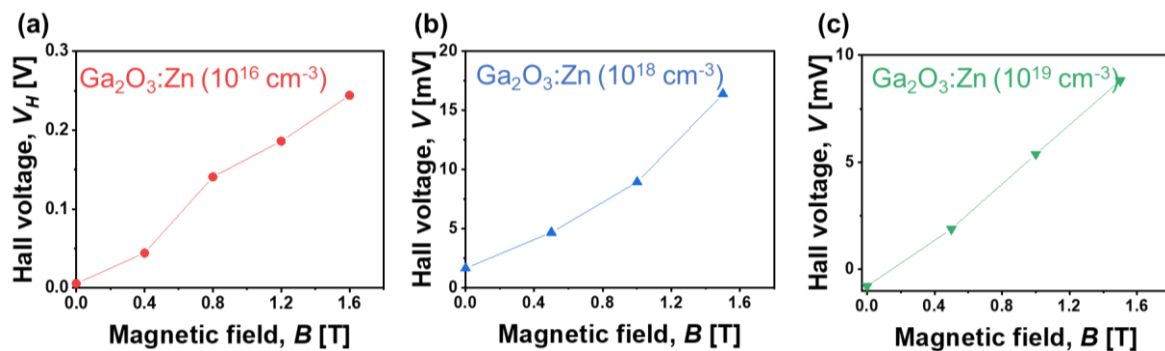


Figure 3-14. Hall voltage ( $V_H$ ) versus magnetic field ( $H$ ) for Zn-doped  $\beta$ -Ga<sub>2</sub>O<sub>3</sub> with increasing doping levels. Each Hall voltage value and corresponding slope are positive, which is an indication of the  $p$ -type conductivity in the samples.

**Figure 3-15 (a)** displays the temperature dependent resistivity of undoped and low ( $[Zn] = 10^{16} \text{ cm}^{-3}$ ) doped  $\beta$ -Ga<sub>2</sub>O<sub>3</sub> thin films in the temperature range of  $T = 500$  to  $850 \text{ K}$ . It is clearly seen that the resistivity was decreased after Zn incorporation comparing to undoped  $\beta$ -Ga<sub>2</sub>O<sub>3</sub> thin film. For example, at  $550 \text{ K}$ , the resistivity is  $\rho = 6.4 \times 10^5 \text{ } \Omega \cdot \text{cm}$  for undoped sample, while  $\rho = 1.1 \times 10^5 \text{ } \Omega \cdot \text{cm}$  for  $10^{16} \text{ cm}^{-3} [Zn]$  doped sample. Two conductivity mechanisms can be distinguished corresponding to band activation at around  $T > 600 \text{ K}$  and hopping conduction regime at lower temperatures. Temperature dependent Hall effect measurements revealed a clear increase in free hole concentration after Zn incorporation compare to undoped films. At  $T = 600 \text{ K}$ , hole concentration  $p = 6.7 \times 10^{12} \text{ cm}^{-3}$  for the undoped sample, while for  $\beta$ -Zn:Ga<sub>2</sub>O<sub>3</sub> it increases up to  $1.7 \times 10^{13} \text{ cm}^{-3}$  **Figure 3-15 (b)**. This result is coherent with **Figure 3-9**, suggesting that for the doping concentration at  $10^{16} \text{ cm}^{-3}$ , the impurity hole conduction might be prevalent. Similar to the previous section, the ionization energy of the acceptor centers can be obtained from a linear regression on a  $\ln(pT^{3/2})$  vs.  $(1/T)$  plot (**Figure 3-15 (c)**). The ionization energy  $E_i = 1.1 \text{ eV}$  for the undoped sample can be related to  $V_{\text{Ga}}$  acceptor level as reported (Chikoidze et al., 2017b; Ekaterine Chikoidze et al., 2019). It was decreased to  $0.77 \text{ eV}$  for  $10^{16} \text{ cm}^{-3} [Zn]$  doped sample. It is believed that Zn substitutes one gallium atom ( $Zn_{\text{Ga}}$ ) thus creating an acceptor level at  $E_i = 0.77 \text{ eV}$  which is completely consistent with the reported thermal activation energy of  $0.65 \text{ eV}$  and  $0.78 \text{ eV}$  determined by electron paramagnetic resonance (EPR) spectroscopy for the two  $Zn_{\text{Ga}}$  sites (Gustafson et al., 2021). Hall hole mobilities are slightly decreased after Zn incorporation (i.e.,  $\mu = 8.7 \pm 1.7 \text{ cm}^2/(\text{V} \cdot \text{s})$  for undoped, and  $\mu = 7.3 \pm 1.1 \text{ cm}^2/(\text{V} \cdot \text{s})$  for  $\beta$ -Zn:Ga<sub>2</sub>O<sub>3</sub> in the measurement temperature range) being in both cases weakly depending on  $T$  (**Figure 3-15 (d)**).

It is interesting to compare our results with a recently published report regarding electrical properties of  $[Zn] = 1.5 \times 10^{18} \text{ cm}^{-3}$  doped Ga<sub>2</sub>O<sub>3</sub> bulk crystals: Jesenovec *et al.* (Jesenovec et al., 2021a) stated that Zn introduced deep acceptor with trapping levels at  $\sim 1.3$  and  $\sim 0.9 \text{ eV}$  above the valence band for one and two holes, respectively, and crystals were insulating. It is supposed that such extremely high resistivity is most probably related to the number of high level unintentional compensating donor impurities presented in the crystal.

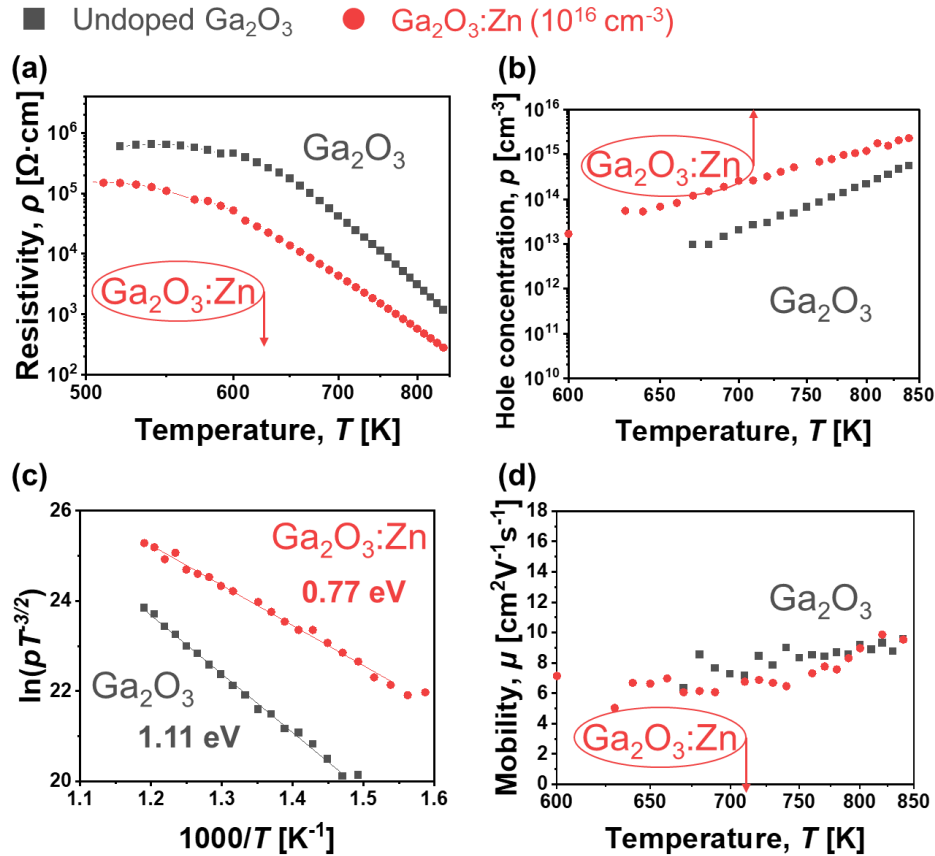


Figure 3-15. (a) Temperature dependence of the resistivity. (b) Hole concentration versus temperature. (c)  $\ln(pT^{-3/2})$  vs.  $1000/T$  plots and linear fits for the determination of the ionization energies. (d) Hall hole mobilities versus temperature. Black squares are for undoped and red disks for Zn-doped Ga<sub>2</sub>O<sub>3</sub> ([Zn] = 10<sup>16</sup> cm<sup>-3</sup>) thin films.

Contrary to low level doped  $\beta$ -Ga<sub>2</sub>O<sub>3</sub> layers, when the incorporated Zn concentration exceeded 10<sup>18</sup> cm<sup>-3</sup>, the resistivity was slightly increased as depicted in **Figure 3-16 (a)**, all films showed normal behavior of semi-insulating material, indicating that Zn is not an effective acceptor dopant at these doping levels. For the [Zn] = 10<sup>18</sup> cm<sup>-3</sup> doped  $\beta$ -Ga<sub>2</sub>O<sub>3</sub> sample, at 800 K, the resistivity and hole concentration was determined to be  $\rho = 9.1 \times 10^3 \Omega\cdot\text{cm}$ ,  $p = 6.7 \times 10^{13} \text{ cm}^{-3}$ , respectively (vs.  $\rho = 4.0 \times 10^3 \Omega\cdot\text{cm}$ ,  $p = 2.2 \times 10^{14} \text{ cm}^{-3}$  for the undoped  $\beta$ -Ga<sub>2</sub>O<sub>3</sub> layer). The activation energy of conductivity was determined to be  $0.99 \pm 0.01 \text{ eV}$ .

Now, I will focus on the sample with [Zn] = 10<sup>19</sup> cm<sup>-3</sup>. At 840 K, Hall effect measurements showed a slight decrease of hole concentrations  $p = 2.1 \times 10^{14} \text{ cm}^{-3}$  compared to  $5.5 \times 10^{14} \text{ cm}^{-3}$  for the undoped sample (**Figure 3-16 (c)**). Indeed, if the auto-compensation

mechanism takes place, Zn dopant cannot increase  $p$ -type conductivity, even more, as we see in the experiment, the “amphoteric” nature of Zn can lead to a decrease in charge carriers. This result corresponds well to the thermodynamic analysis discussed in Section 3.2.2. As shown in **Figure 3-16 (b)**, both undoped and Zn-doped  $\beta$ -Ga<sub>2</sub>O<sub>3</sub> samples exhibit activation energy of conductivity of  $E_a = 1.18 \pm 0.02$  eV. The Hall holes mobility is  $\mu = 2.8 \pm 1.5$  cm<sup>2</sup>/(V·s) in the measurement temperature range (**Figure 3-16 (d)**). Such a decrease in hole mobility can be attributed to the high level of doping, resulting in the increase of scattering on Zn impurities.

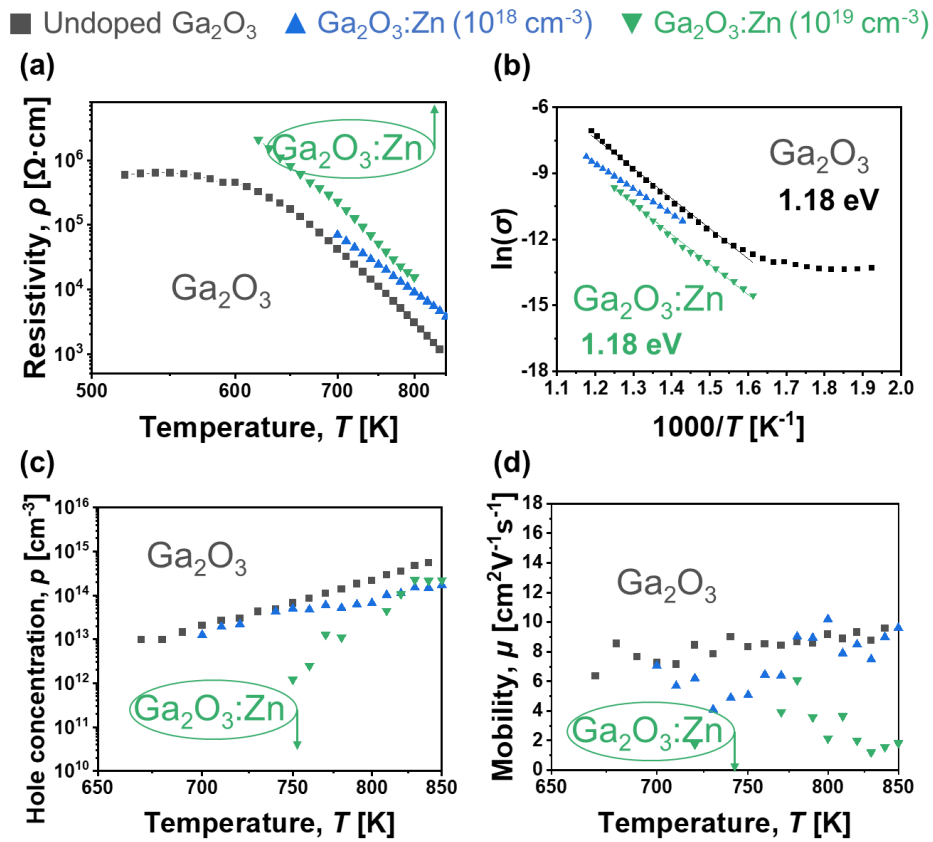


Figure 3-16. (a) Temperature dependence of resistivity. (b)  $\ln(\sigma)$  vs.  $1000/T$  plot for the determination of the activation energies. (c) Hall hole concentrations versus temperature. (d) Hall hole mobilities versus temperature. Samples: undoped (black) and Zn-doped Ga<sub>2</sub>O<sub>3</sub> ([Zn] = 10<sup>18</sup> cm<sup>-3</sup> (blue), 10<sup>19</sup> cm<sup>-3</sup> (green)) thin films.

### 3.3.4 Critical electric field

The critical electric field ( $E_{CR}$ ) is a crucial parameter in the characterization of a material's electrical properties, especially for high voltages operating. It is defined as the

---

maximum electric field that a material can withstand before undergoing an avalanche breakdown. Representative values of the critical electric field for the most common power electronics semiconductors, such as silicon (0.3 MV/cm), 4H-SiC (3.5 MV/cm) (Trew, 1997), GaN (3.9 MV/cm) (Fischer et al., 2016), or AlGaN (5.9 MV/cm (Allerman et al., 2016)) are well known. For other UWBG such as AlN, the  $E_{CR}$  values have also been reported (12 MV/cm (Chu and Kelm, 1975)) while a generally agreed theoretical value for diamond is 10 MV/cm (Wort and Balmer, 2008). For  $\beta$ -Ga<sub>2</sub>O<sub>3</sub>, a common estimation, associated to the band gap value, given in the literature is  $\sim 8$  MV/cm (Higashiwaki et al., 2012). Later, Ghosh and Singisetti (Ghosh and Singisetti, 2018a, 2017, 2014) investigated the impact ionization coefficient for electrons and holes, and in turn, the critical electric field in  $\beta$ -Ga<sub>2</sub>O<sub>3</sub>, several  $E_{CR}$  values of 4.8 – 10.2 MV/cm depending on the crystallographic direction of  $\beta$ -Ga<sub>2</sub>O<sub>3</sub> were estimated. Experimentally, a breakdown field of a  $\beta$ -Ga<sub>2</sub>O<sub>3</sub>//Si simple structure parallel plane MOS capacitor was determined to be 7.27 MV/cm (Li et al., 2019). Zhang *et al.* (Zhang et al., 2022) fabricated and conducted the electric characterizations of two  $p$ -NiO/ $n$ -Ga<sub>2</sub>O<sub>3</sub> diodes with different thicknesses (7.5 and 13  $\mu$ m) of  $\beta$ -Ga<sub>2</sub>O<sub>3</sub> layer. The breakdown voltages were 5.1 and 8.32 kV, respectively, and the corresponding breakdown fields are 6.45 and 6.2 MV/cm, respectively.

#### 3.3.4.1 Impact ionization

This dielectric breakdown capability depends on the free charges (related to native defects or dopants) but also on the semiconductor's fundamental properties (such as bandgap energy  $E_g$ ) and the impact ionization parameters. Impact ionization occurs when an electron or a hole acquires sufficient energy from an external electric field and collides with a semiconductor's crystal lattice, producing an electron-hole pair (i.e., two electrons and a hole in place of the initial electron, or two holes and an electron in place of the initial hole) (as illustrated in **Figure 3-17**). At low electric fields, the electron energy distribution stabilizes as the energy gained from the external electric field is offset by energy loss from collisions (Sun et al., 2012). However, as the electric field strength surpasses a certain threshold (i.e., the critical electric field  $E_{CR}$ ), this process can result in an avalanche effect, where the newly generated carriers gain enough energy to produce further electron-hole pairs, leading to the subsequent multiplication of carriers. In turn, the avalanche breakdown occurs. There are two main types of impact ionization: band-to-band impact ionization and trap-to-band impact ionization. Band-to-band impact ionization (Ghosh and Singisetti, 2018a) occurs

when an electron in the conduction band gains enough energy from the electric field to overcome the band gap and enter the valence band. This process generates an electron-hole pair and releases energy. The newly created electron can then gain energy and produce additional electron-hole pairs, leading to a cascade effect. On the other hand, trap-to-band impact ionization (Yakimov et al., 2020) involves the excitation of an electron from a deep trap level to the conduction band. The domination between these two processes depends on several factors such as the density of trap states, band gap energy, and the external electric field strength. For example, at medium or high field strengths the band-to-band contribution may be expected to dominate. While the trap-to-band can occur at lower electric fields than band-to-band impact ionization and can be important in materials with a high density of states within the gap (Robbins, 1980a, 1980b).

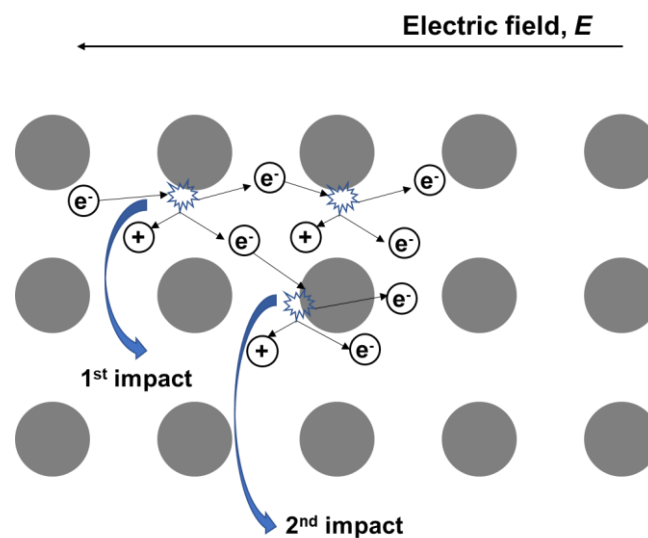


Figure 3-17. Schematic illustration of the impact ionization process (in the case of electron).

In a strong electric field, the probability of impact ionization for electrons is mainly determined by the likelihood that the electron will gain an amount of energy equal to the ionization threshold energy from the field. The electron's energy increase depends on how much it is accelerated by the external field and how much energy is lost through collisions. According to theoreticians (Keldysh, 1960), there are two possibilities for an electron to acquire this energy, either by receiving it from the field without experiencing any collision or gradually through many collisions with less energy lost than gained in each collision. Therefore, the mean free path that determines the average distance that a carrier must travel to obtain sufficient energy for ionization, plays a crucial role (Keldysh, 1960; Wolff, 1954).

This parameter together with the effective mass can be influenced by the energy band structure of the material. Consequently, the impact ionization coefficients of electrons and holes can be different, and depend on the crystallographic directions of a semiconductor (e.g., Si, Ge, GaAs, InP (Anderson and Crowell, 1972; Bude and Hess, 1992)). Monoclinic  $\beta$ -Ga<sub>2</sub>O<sub>3</sub> has a low symmetry, the effective mass of holes can be quite anisotropic as reported (Mock et al., 2017), it also explains the crystallographic direction dependence of the critical electric field (Ghosh and Singiseti, 2018a) as mentioned above. For example, the hole effective mass is fairly anisotropic in  $\vec{a}$ ,  $\vec{b}$ , and  $\vec{c}$  directions in the first and topmost valence band:  $m_{h,a}^* = 1.77m_0$ ,  $m_{h,b}^* > 10m_0$ , and  $m_{h,c}^* = 0.41m_0$  for the first and topmost valence band (Mock et al., 2017).

To summarize, a higher critical electrical field ( $E_{BR}$ ) for a material can be expected with a lower impact ionization coefficient. Additionally, the critical electrical field strength is also dependent on doping density, in an inverse proportion. Therefore, for the same materials, we can expect a higher critical electrical field ( $E_{BR}$ ) at lower density and a shorter mean free path of free carriers.

### 3.3.4.2 Experiment results and discussion

To estimate experimentally the critical electric field, undoped and Zn-doped  $\beta$ -Ga<sub>2</sub>O<sub>3</sub> layers on conductive B-doped Si(111) substrate were simultaneously carried out with the growth on the insulating *c*-plane sapphire substrate. Recall, the objective of the growth on conducting Si substrate ( $\rho < 0.01 \Omega \cdot \text{cm}$ ) is to fabricate a parallel plane capacitor, to carry out the breakdown voltage measurements, and estimate the critical electric field in this simple vertical structure. While the  $\beta$ -Zn:Ga<sub>2</sub>O<sub>3</sub>//*c*-Al<sub>2</sub>O<sub>3</sub> was used for the electrical measurements which were presented in the previous sub-sections.

**Figure 3-18** displays comparable XRD patterns of undoped and Zn-doped (at  $10^{19} \text{ cm}^{-3}$ )  $\beta$ -Ga<sub>2</sub>O<sub>3</sub> thin films on Si (111) substrates. Both layers are polycrystalline with the most intense peaks of  $\{-201\}$  family of  $\beta$ -Ga<sub>2</sub>O<sub>3</sub>, and additional random orientations with tiny XRD peaks. The Zn concentration in  $\beta$ -Zn:Ga<sub>2</sub>O<sub>3</sub> layer estimated by SIMS is  $3.2 \times 10^{19} \text{ cm}^{-3}$ , which is comparable with the simultaneous growth carried out on a sapphire substrate. This value agrees very well with the value extracted from the energy-dispersive X-ray spectroscopy (EDX) profile (0.56%) from high-resolution transmission electron microscopy (TEM) measurements. A thin native SiO<sub>2</sub> layer (2 – 3 nm) at the  $\beta$ -Ga<sub>2</sub>O<sub>3</sub>//Si interface was evidenced as shown in **Figure 3-19 (a)**. The selected area electron diffraction (SAED) image

of the  $\beta$ -Zn:Ga<sub>2</sub>O<sub>3</sub> layer shows multiple irregular satellite spots along the major reflection with a very slight ring diffraction pattern, which is a typical polycrystalline characteristic. Besides, there is an amorphous layer of 15 – 20 nm on the top of SiO<sub>2</sub> layer (**Figure 3-19 (b) – (c)**). Si, being an efficient *n*-type dopant  $\beta$ -Ga<sub>2</sub>O<sub>3</sub>, was not detected in the upper amorphous layer.

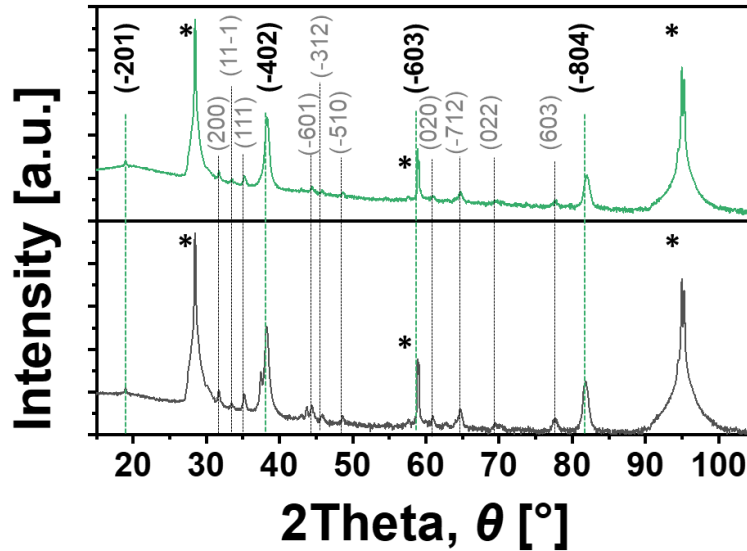


Figure 3-18. XRD patterns of undoped (black) and Zn-doped (green, doping level at  $10^{19}$  cm<sup>-3</sup>)  $\beta$ -Ga<sub>2</sub>O<sub>3</sub> thin films on conducting Si (111) substrates. “\*” refers to the peaks of Si (111) substrates.

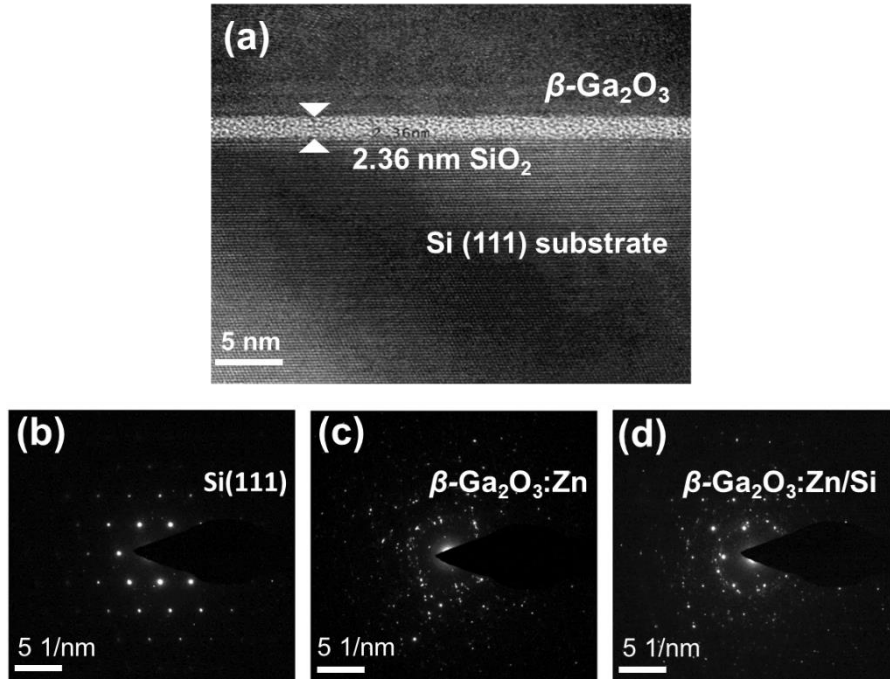


Figure 3-19. (a) High-resolution TEM cross-section image of  $\beta$ -Ga<sub>2</sub>O<sub>3</sub> grown on Si (111) substrate. SAED patterns of (b) the Si(111) substrate, (c)  $\beta$ -Zn:Ga<sub>2</sub>O<sub>3</sub> layer, and (d) interface between  $\beta$ -Zn:Ga<sub>2</sub>O<sub>3</sub> layer and Si substrate, respectively. (Experiment is done in ICN2, Barcelona Spain)

Vertical parallel plane capacitors have been fabricated by depositing Ti (400 nm)/Au (200 nm) contacts onto the undoped and Zn-doped  $p$ -Ga<sub>2</sub>O<sub>3</sub> grown on the conducting Si(111) substrates (**Figure 3-20 (a)**). Negative bias has been applied on an isolated Ohmic contact with the grounded substrate to access the breakdown voltage ( $V_{BR}$ ). The vertical breakdown voltage was determined to be 124 V for the undoped  $\beta$ -Ga<sub>2</sub>O<sub>3</sub>//Si and 540 V for the doped  $\beta$ -Zn:Ga<sub>2</sub>O<sub>3</sub>//Si structures (**Figure 3-20 (b)**). A bare Si substrate with a native SiO<sub>2</sub> (2 – 3 nm thick layer) has been characterized as well. The vertical breakdown voltage (around 10 V) is determined to produce a negligible contribution to the large experimental  $V_{BR}$  of the  $p$ -Ga<sub>2</sub>O<sub>3</sub>//Si structure. Taking into account the experimentally (by SEM) determined thickness of 200 nm ( $\beta$ -Ga<sub>2</sub>O<sub>3</sub>) and 400 nm ( $\beta$ -Zn:Ga<sub>2</sub>O<sub>3</sub>), and extracting bare substrate related  $V_{BR}$  the effective parallel plate critical electric field was determined to be  $E_C = 5.7$  MV/cm for  $\beta$ -Ga<sub>2</sub>O<sub>3</sub> and  $E_C = 13.2$  MV/cm, for  $\beta$ -Zn:Ga<sub>2</sub>O<sub>3</sub> respectively.

To be certain of this critical electric field value for gallium oxide, we need to exclude a possible contribution of the SiO<sub>2</sub> layer breakdown voltage in the measured total voltage. Thus, we estimated an under-value associated to the contribution of a 20 nm thick layer with

a 30 MV/cm critical field. So, the breakdown voltage  $V_{BR} = 480$  V ( $540$  V –  $20$  nm  $\times$   $30$  MV/cm) for the  $\beta$ -Zn:Ga<sub>2</sub>O<sub>3</sub> layer, the corresponding  $E_C = 12.6$  MV/cm. The extraordinary experimental critical electrical field value of  $13.2$  MV is believed to be due to the Zn-doped  $p$ -type nature of the  $\beta$ -Ga<sub>2</sub>O<sub>3</sub>, the origins of the delayed impact ionization rate are the very deep native acceptor centers (most likely, gallium vacancies  $V_{Ga}$ ) and smaller mean free path.

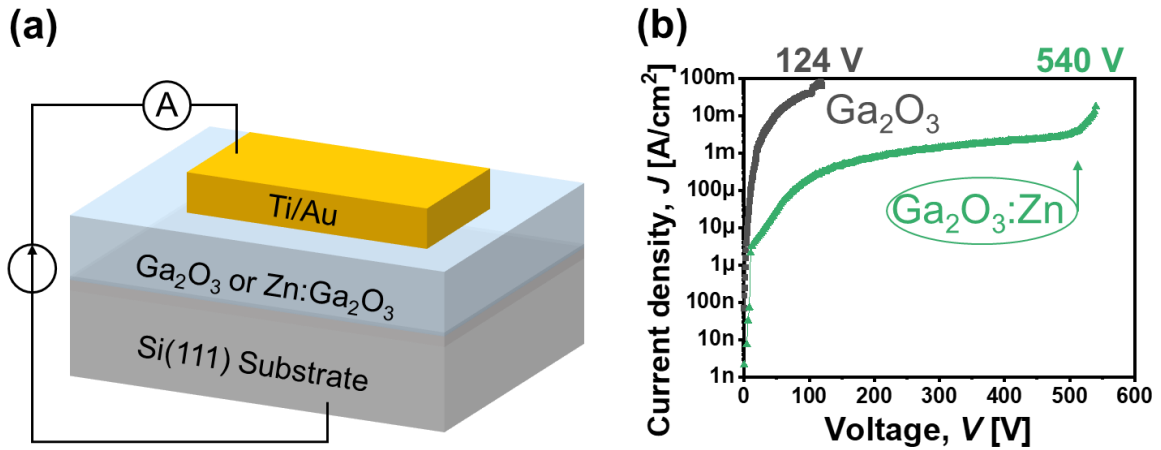


Figure 3-20. (a) Sketch of the vertical heterojunction structures ( $\beta$ -Ga<sub>2</sub>O<sub>3</sub>/Si and  $\beta$ -Zn:Ga<sub>2</sub>O<sub>3</sub>//Si) with Ti/Au metal contacts on the top of the Ga<sub>2</sub>O<sub>3</sub> layers. (b) Experimental I–V curves of vertical breakdown voltage measurements through the  $\beta$ -Ga<sub>2</sub>O<sub>3</sub>//Si and  $\beta$ -Zn:Ga<sub>2</sub>O<sub>3</sub>:Zn//Si structures, indicating a hard breakdown voltage up to 124 V and 540 V at room temperature, respectively.

### 3.3.5 Summary

The results in Section 3.3 can be summarized as follow:

Zn can be successfully incorporated in  $\beta$ -Ga<sub>2</sub>O<sub>3</sub> thin films with the doping levels of  $10^{16}$  –  $10^{19}$  cm<sup>-3</sup> without the appearance of transition peaks or secondary phase by MOCVD, while maintaining a high transparency ( $\sim 80\%$ ) in vis-NIR wavelength range and an ultra-wide band gap (with a cut-off wavelength of 260 – 266 nm). When  $[Zn] > 10^{21}$  cm<sup>-3</sup>, the  $\beta$ -Zn:Ga<sub>2</sub>O<sub>3</sub> thin film was amorphous. **Figure 3-21** summarizes the results related to electrical transport results, as follow:

(i) When  $Zn = 10^{16}$  cm<sup>-3</sup>, the  $p$ -type conductivity can be enhanced in  $\beta$ -Ga<sub>2</sub>O<sub>3</sub>. The origin is attributed to the substitution defect  $Zn_{Ga}$  with an ionization energy of  $E_i = 0.77$  eV. It is direct evidence that the Zn is an acceptor dopant in  $\beta$ -Ga<sub>2</sub>O<sub>3</sub>.

(ii) With the increasing doping level when  $[Zn] > 10^{18} \text{ cm}^{-3}$ , Zn is not an effective acceptor dopant, the “auto compensation” effect takes place, resulting in a decrease in hole concentration.

(iii) On the base of impact ionization theory, we hypothesized that the critical electric field can be increased by reducing the impact ionization probability (shortening the mean free path of free carriers, decreasing the carrier concentration). Taking advantage of the “auto compensation” effect of Zn doping, breakdown voltage measurements were carried out for parallel capacitors based on  $\beta$ -Ga<sub>2</sub>O<sub>3</sub>//Si and  $\beta$ -Ga<sub>2</sub>O<sub>3</sub>:Zn//Si structures. The corresponding critical electric fields were deduced to be  $E_{CR} = 5.7$  and 13.2 MV/cm, respectively.

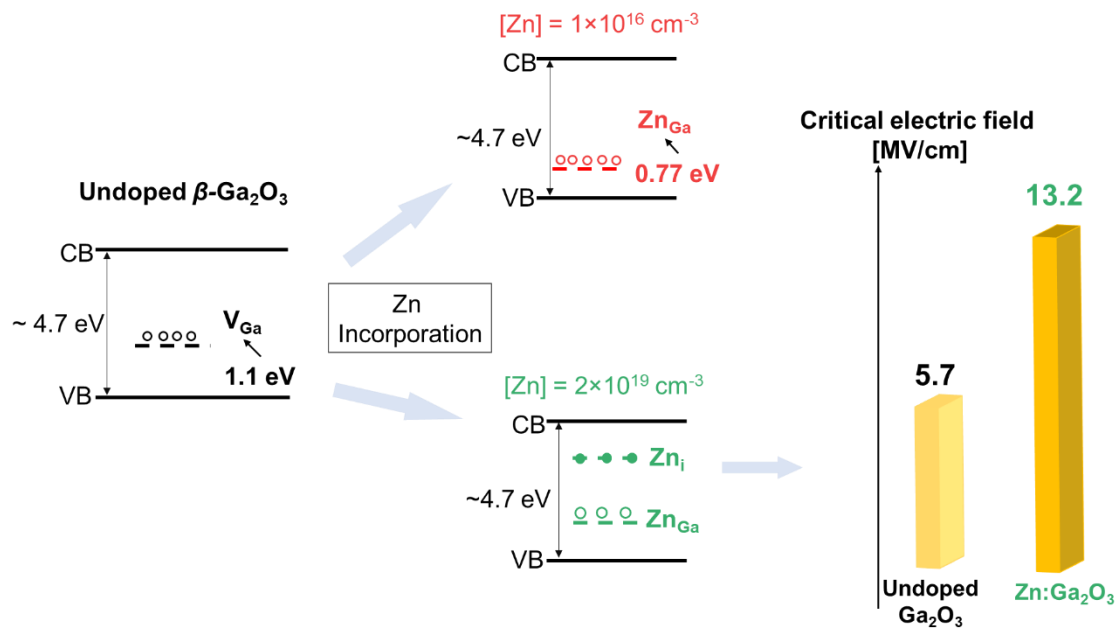


Figure 3-21. Schematic illustration of Zn doping effect.

---

---

## 4. ZnGa<sub>2</sub>O<sub>4</sub>: Experimental Results and Discussion

In this chapter, I will focus on the characterizations of the spinel zinc gallate (ZnGa<sub>2</sub>O<sub>4</sub>) thin films grown by metal-organic chemical vapor deposition (MOCVD) on *c*-plane sapphire substrates. With the increasing Zn incorporation in  $\beta$ -Ga<sub>2</sub>O<sub>3</sub> (Zn at. % > 6.85%), the spinel ZnGa<sub>2</sub>O<sub>4</sub> starts to form. In the first section (Section 4.1), I will discuss the transformation of pure  $\beta$ -Ga<sub>2</sub>O<sub>3</sub> to a mixed phase of  $\beta$ -Ga<sub>2</sub>O<sub>3</sub> and ZnGa<sub>2</sub>O<sub>4</sub>, later to pure ZnGa<sub>2</sub>O<sub>4</sub> spinel. The bipolar dopability (*n*-type and *p*-type) was theoretically predicted for ZnGa<sub>2</sub>O<sub>4</sub> (Paudel et al., 2011b; Shi et al., 2014). Experimentally, the first *p*-type (at high temperature) ZnGa<sub>2</sub>O<sub>4</sub> thin films have been reported by colleagues in GEMaC (Chikoidze et al., 2020a). The conductivity was attributed to Zn<sub>Ga</sub> anti-site defect with an ionization energy of carriers  $E_i = 0.93$  eV. Besides, native *n*-type conductivity ( $n = 10^{20}$  cm<sup>-3</sup>) in ZnGa<sub>2</sub>O<sub>4</sub> thin films has been shown (Look et al., 2020), but the origin of conductivity and the conduction mechanism are still open questions. In Section 4.2, I show a comparative analysis of structural, optical, chemical, and electrical measurements for native semi-insulating *p*-type and highly conducting *n*-type ZnGa<sub>2</sub>O<sub>4</sub> thin films grown by the MOCVD technique. In Section 4.3, the influence of oxygen content during the growth on the electrical properties of ZnGa<sub>2</sub>O<sub>4</sub> thin films will be discussed. In the last section of this chapter (Section 4.4), the breakdown voltage measurements for the assessment of the critical electric field will be shown.

### 4.1 From $\beta$ -Ga<sub>2</sub>O<sub>3</sub> to ZnGa<sub>2</sub>O<sub>4</sub>: structural characterizations

The objective was to study the structural transformation of  $\beta$ -Ga<sub>2</sub>O<sub>3</sub> thin films from monoclinic structure to cubic spinel ZnGa<sub>2</sub>O<sub>4</sub>, with increasing Zn incorporation. A series of samples with different Zn precursor flows were grown on both *c*-sapphire and conducting Si(111) substrates using the MOCVD technique. Same as in Chapter 3, the electrical transport measurements were carried out on the films grown on insulating sapphire substrates, while Ga<sub>2</sub>O<sub>3</sub>:Zn//Si was elaborated to fabricate parallel plane capacitors, to conduct the breakdown voltage measurements.

During the film deposition, the O<sub>2</sub> flow was set at 1200 sccm, the oxygen partial pressure was estimated to be 12 Torr. The Zn precursor flow was ranging (3.88 – 8.9

μmol/min). The growth parameters, Zn content in the films determined by EDX, and the thicknesses are summarized in **Table 4-1**.

Table 4-1. Growth conditions of pure and Zn incorporated β-Ga<sub>2</sub>O<sub>3</sub>.

N°	Structure	Growth conditions	DEZn [μmol/min]	[Zn] (%)	Thickness [nm]
Undoped	Ga <sub>2</sub> O <sub>3</sub> //c-sapphire	Vector gas: Ar	0	-	953
ZnGaO-#1	Zn:Ga <sub>2</sub> O <sub>3</sub> //c-sapphire Zn:Ga <sub>2</sub> O <sub>3</sub> //Si	TMGa = 11 μmol/min	3.9	6.85	1000
ZnGaO-#2		O <sub>2</sub> = 1200 sccm	7.0	14.04	1238
ZnGaO-#3		T = 775 °C, P = 38 Torr	8.9	15.83	1154
		Time = 150 min			

**Figure 4-1 (a)** displays the XRD patterns for undoped and Zn-doped thin films. The diffraction peaks corresponding to the *c*-sapphire substrate are labelled “\*”. For the undoped sample, the five peaks with the increasing  $2\theta$  position correspond to the crystalline plans (-201), (-402), (-603), (-804) and (-1005) of the monoclinic β-Ga<sub>2</sub>O<sub>3</sub>, respectively. Focusing on Zn incorporated samples, they possess five diffraction peaks located near  $2\theta$  positions of 18.5 – 19.0°, 37.5 – 38.5°, 57.0 – 59.0°, 79.5 – 82.5°, and 106.0 – 110.5°. There are new peaks shifted to lower  $2\theta$  values appear and become more intense with the increasing Zn content, while simultaneously the reflections corresponding to β-Ga<sub>2</sub>O<sub>3</sub> start to be less intense and diminish at the end. As shown in **Figure 4-1 (b)**, the enlarged views for these  $2\theta$  positions show the same situation for all the peaks. The double peaks presented in the sample with 6.85%[Zn] indicate the coexistence of two crystalline phases. When Zn content increased up to 14.04%, the peaks corresponding to β-Ga<sub>2</sub>O<sub>3</sub> do not exist anymore. These new peaks appear at  $2\theta$  values of 18.47, 37.40, 57.50, 79.70, and 106.42° are attributed to the cubic spinel ZnGa<sub>2</sub>O<sub>4</sub>, and correspond to (111), (222), (333), (444), and (555) plans, respectively. The shift in  $2\theta$  peak position of ZnGa<sub>2</sub>O<sub>4</sub> can be ascribed to the inclusion of Zn<sup>2+</sup> in the β-Ga<sub>2</sub>O<sub>3</sub> structure, and the increasing *d*-spacing (interplanar distance). Similar results are also reported by other groups with high Zn incorporation concentrations in β-Ga<sub>2</sub>O<sub>3</sub> (Alema et al., 2017a; Horng et al., 2017).

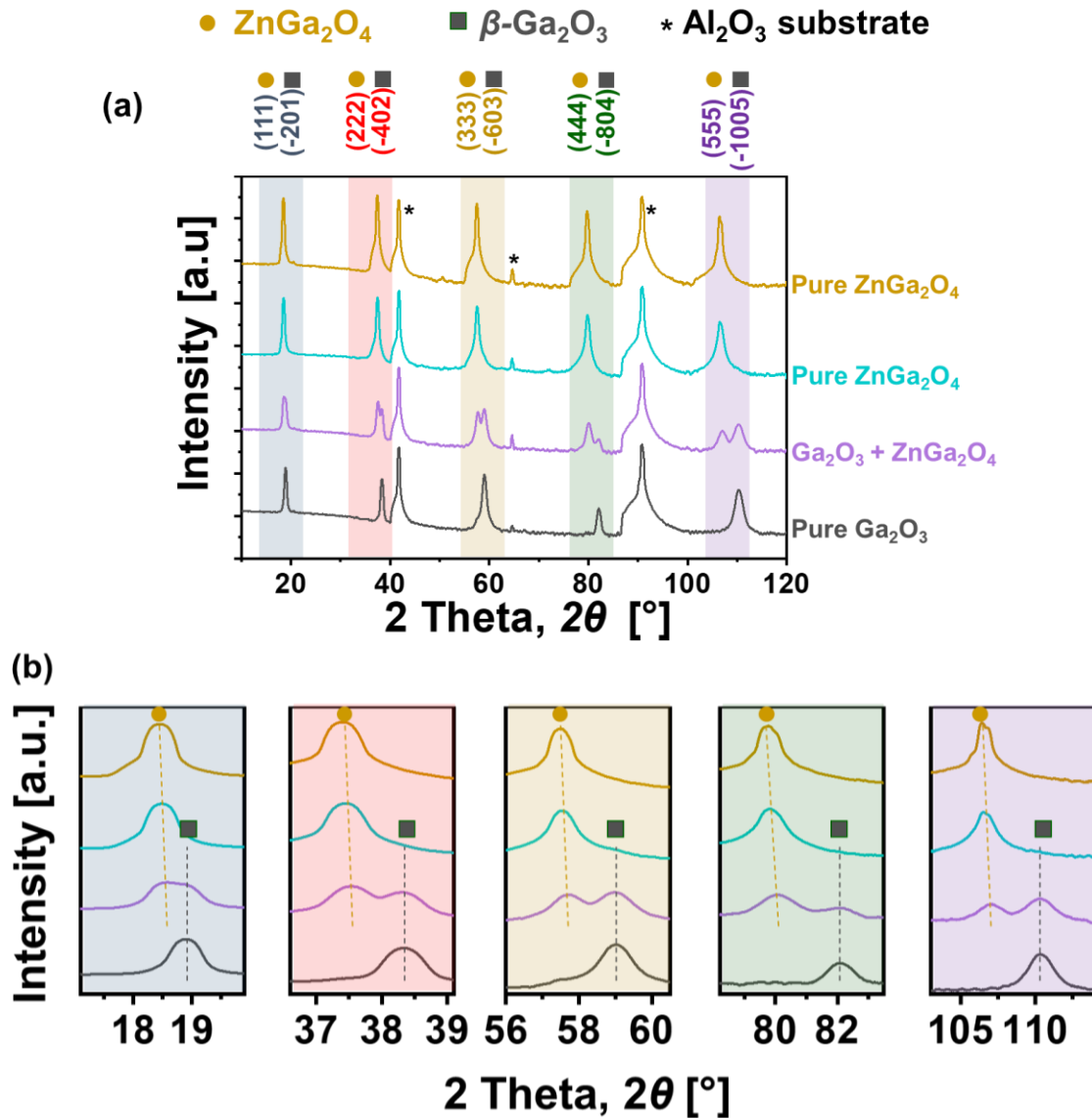


Figure 4-1. (a) XRD patterns for undoped and Zn incorporated  $\beta$ -Ga<sub>2</sub>O<sub>3</sub> thin films with different Zn flow (Zn concentration). “\*” refers to the peaks of *c*-plane sapphire substrates. (b) Enlarged views for  $2\theta = 17.1 - 19.9^\circ$ ,  $36.6 - 39.1^\circ$ ,  $56.0 - 60.5^\circ$ ,  $78.2 - 83.5^\circ$ , and  $103.0 - 114.0^\circ$  to show the double-peak features and the transition of peaks.

Although the observed XRD families of the Bragg reflections of monoclinic and spinel cubic are compatible, their distinct lattice symmetries result in different vibrational modes of Raman scattering. ZnGa<sub>2</sub>O<sub>4</sub> exhibits mainly A<sub>1g</sub> (709.7 cm<sup>-1</sup>) and T<sub>2g</sub> (603.1 cm<sup>-1</sup>) vibration modes (Figure 4-2), in good agreement with previously reported work (López-Moreno et al., 2011; Relvas et al., 2019). Besides, it is interesting to note that the vibration

mode  $E_g$  at 397.2 cm<sup>-1</sup> for cubic spinel ZnGa<sub>2</sub>O<sub>4</sub> observed in the mixed phase disappeared in the pure spinel, it needs further investigation.

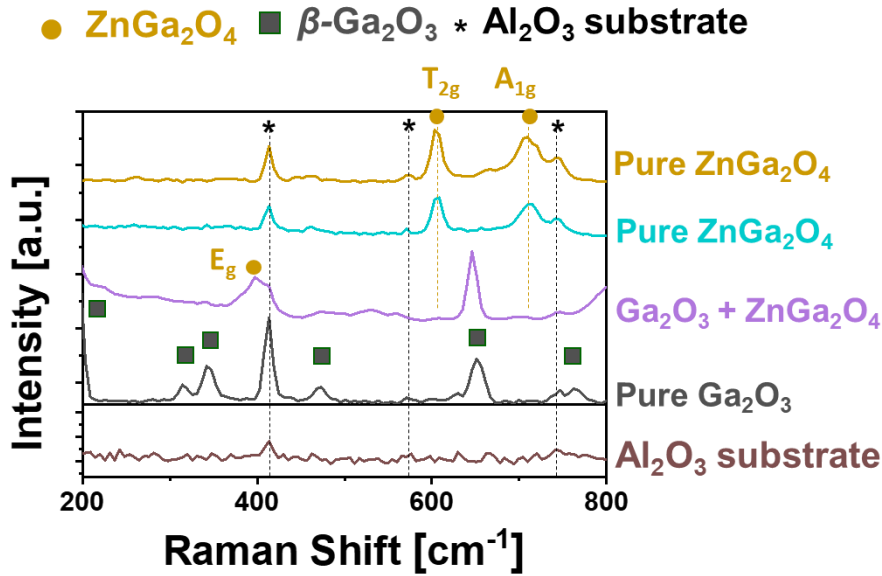


Figure 4-2. Raman scattering spectra for pure  $\beta$ -Ga<sub>2</sub>O<sub>3</sub>, mixed GaO/ZnGaO, and pure ZnGa<sub>2</sub>O<sub>4</sub>.

In this section, the transition from pure  $\beta$ -Ga<sub>2</sub>O<sub>3</sub> to pure ZnGa<sub>2</sub>O<sub>4</sub> with increasing Zn incorporation is demonstrated by the structural characterizations. It is shown that when [Zn] > 14.04%, monoclinic  $\beta$ -Ga<sub>2</sub>O<sub>3</sub> transforms completely to cubic spinel ZnGa<sub>2</sub>O<sub>4</sub>. The physical properties of ZnGa<sub>2</sub>O<sub>4</sub> thin films will be discussed in the following sections.

## 4.2 Bipolar self-doping in ultra-wide band gap spinel ZnGa<sub>2</sub>O<sub>4</sub>

As mentioned in Section 1.2 (state of the art for ZnGa<sub>2</sub>O<sub>4</sub>), the doping centers in spinel oxide are specific because of crystalline symmetry (interstitials and anti-sites). According to theoretical calculation, both *n*-type and *p*-type can be achieved for spinel ZnGa<sub>2</sub>O<sub>4</sub> (Paudel et al., 2011b; Shi et al., 2014) by the intrinsic antisite defects (Ga<sub>Zn</sub> or Zn<sub>Ga</sub>, respectively) through the cations inversion, while tuning the cations quantity. Such disordered distribution of cations belongs to the so-called “self-doping” effects (Shi et al., 2014; Zhang and Wei, 2002).

As natural for an ultra-wide bandgap oxide Fermi level lying near the mid-gap, poor conductivity (if any) has been found for undoped as-grown ZnGa<sub>2</sub>O<sub>4</sub> thin films (Horng et al.,

2017; Krishna et al., 2005; Yan et al., 2005). However, high electron conductivity was already reported in the past for hydrogen annealed ZnGa<sub>2</sub>O<sub>4</sub> thin films (Krishna et al., 2005; Omata et al., 1994). Besides, intrinsic donor electron conductivity has also been reported for some bulk blue colored crystals (Galazka et al., 2019) thin films grown by pulsed laser deposition (PLD) (Look et al., 2020), and metal-organic chemical vapor deposition (MOCVD) (L. C. Cheng et al., 2018). In these conducting ultra-wide transparent conducting oxides (TCOs), different electron concentrations ranging from  $5.9 \times 10^{16} \text{ cm}^{-3}$  (Horng et al., 2017; Shen et al., 2017; W.-K. Wang et al., 2019a) to  $6.16 \times 10^{19} \text{ cm}^{-3}$  (Look et al., 2020) have been reported. The *n*-type conductivity was usually explained by the presence of oxygen vacancies (Kim et al., 2004; Krishna et al., 2005; Omata et al., 1994; Yan et al., 2005), but they are well-known to arguably be deep centers in ZnGa<sub>2</sub>O<sub>4</sub> (Pandey et al., 1999; Paudel et al., 2011b; Shi et al., 2014). Although these observations and that a bunch of theoretical works deals with the issue (De Vos et al., 2016; Stoica and S Lo, 2014; Xia et al., 2018), the actual phenomenological origin and mechanisms of the ZnGa<sub>2</sub>O<sub>4</sub> spinel self-doping remain elusive.

It should be underlined that experimentally, study related to *p*-type ZnGa<sub>2</sub>O<sub>4</sub> is very limited so far. It has been demonstrated the first time by GEMaC colleagues, a native high-temperature *p*-type conductivity for ZnGa<sub>2</sub>O<sub>4</sub> thin films elaborated by MOCVD (Chikoidze et al., 2020a). The conductivity was attributed to antisite defects Zn<sub>Ga</sub> with an ionization energy of carriers around  $E_i = 0.93 \text{ eV}$  (Chikoidze et al., 2020a).

The objective of my study in the framework of collaborative (several labs) work was to determine the origin of the *n*-type conductivity in ZnGa<sub>2</sub>O<sub>4</sub> layer mechanism of conduction and later to make a comparative analysis of native *p*-type and *n*-type ZnGa<sub>2</sub>O<sub>4</sub> thin films by a range of spectroscopic and transport measurement techniques.

All ZnGa<sub>2</sub>O<sub>4</sub>//*c*-sapphire thin films were grown by MOCVD in GEMaC and in National Chiao Tung University. The growth condition as well as the thicknesses of the layers are summarized in **Table 4-2**.

Table 4-2. Growth conditions of two ZnGa<sub>2</sub>O<sub>4</sub> thin films.

P (total) [Torr]	O <sub>2</sub>	Time [min]	Temperature [°C]	Ga precursor [μmol/min]	DEZn [μmol/min]	Thickness [nm]	Type
35	1200 sccm	150	775	11 (TMGa)	8.9	1154	<i>p</i>
25	0.022 mol/min	30	850	27 (TEGa)	49	190	<i>n</i>

#### 4.2.1 Structural studies of *n*-type and *p*-type ZnGa<sub>2</sub>O<sub>4</sub> thin films

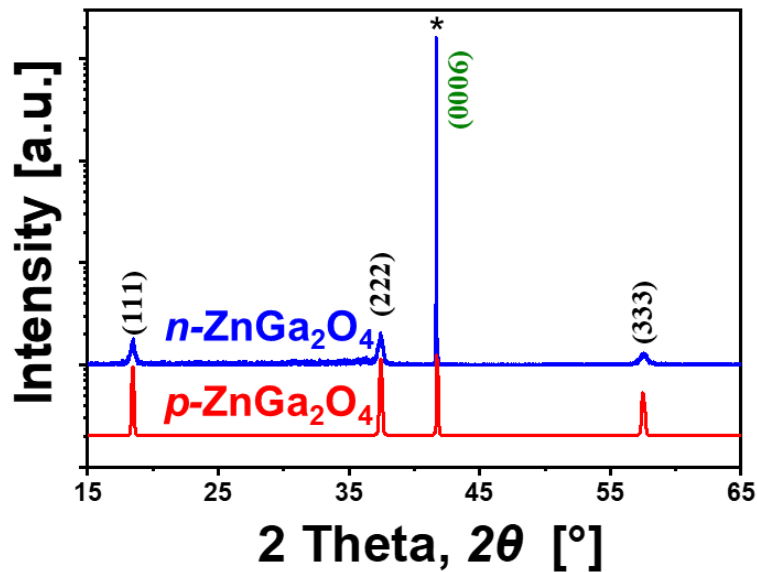


Figure 4-3. (a) X-ray diffractograms of as-grown *n*-type and *p*-type ZnGa<sub>2</sub>O<sub>4</sub> thin films grown *c*-sapphire, the peak labelled by “\*” indicates the XRD reflection corresponding to the sapphire substrate.

The XRD spectra between 15° and 65° (**Figure 4-3**) show that both ZnGa<sub>2</sub>O<sub>4</sub> thin films are very similar. The three XRD peaks of the as-grown *n*-type layer are at  $2\theta$  values of 18.47°, 37.40°, and 57.50°, while those of *p*-type film are at  $2\theta$  values of 18.45°, 37.42°, and 57.56°, respectively. These 3 peaks correspond to the {111} plane family, their indexes in *Fd-3m* space group are (111), (222), and (333), respectively. Additionally, the corresponding lattice parameter of *n*-ZnGa<sub>2</sub>O<sub>4</sub> films is estimated to be 8.32 Å while it is 8.33 Å for *p*-ZnGa<sub>2</sub>O<sub>4</sub> films.

The High-Resolution Transmission Electron Microscopy (HRTEM) analysis for *n*-type and *p*-type ZnGa<sub>2</sub>O<sub>4</sub> thin films are shown in **Figure 4-4 (a)-(b)**. **Figure 4-4 (c)** displays the

selected area electron diffraction (SAED) pattern of the *n*-ZnGa<sub>2</sub>O<sub>4</sub> film. Moreover, a super-period of 3-unit cell period along the [110] direction is evidenced in the SAED image (Figure 4-4 (c)), and qualitatively seen in the direct space image (Figure 4-4 (a)), while its origin needs more investigation. Figure 4-4 (d) shows the fast Fourier transform of the TEM image. Both images indicate that the ZnGa<sub>2</sub>O<sub>4</sub> films have a “single-crystalline” structure.

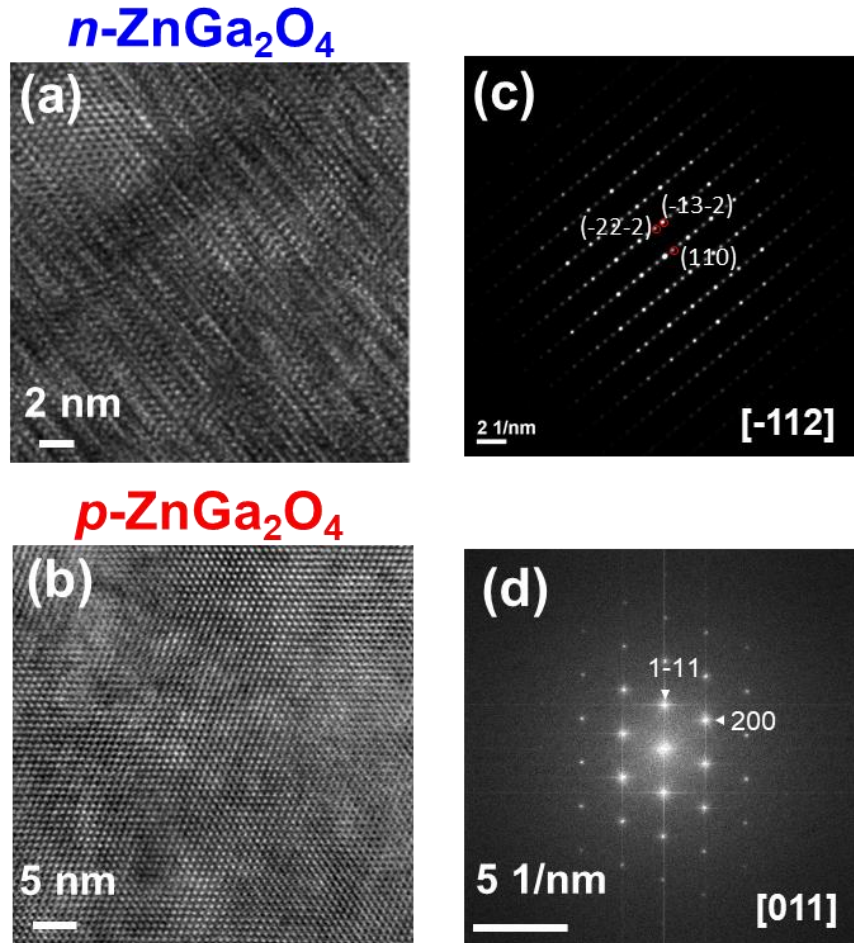


Figure 4-4. High-resolution transmission electron microscope (HRTEM) images for (a) *n*-type ZnGa<sub>2</sub>O<sub>4</sub> thin film and (b) *p*-type ZnGa<sub>2</sub>O<sub>4</sub> thin film. (c) SAED images of *n*-ZnGa<sub>2</sub>O<sub>4</sub> and (d) The fast Fourier transform of the image *p*-ZnGa<sub>2</sub>O<sub>4</sub>. The experiments were carried out in National Chiao Tung University.

#### 4.2.2 Electronic properties of *n*-type and *p*-type ZnGa<sub>2</sub>O<sub>4</sub> thin films

X-ray photoelectron spectroscopy (XPS) measurements were carried out by Dr. Mathieu Frégnaux at Institute Lavoisier de Versailles (ILV), UFR des Sciences at Versailles. It was used firstly to identify the potential impurities contamination. Figure 4-5 shows the room-temperature XPS spectra of *n*-ZnGa<sub>2</sub>O<sub>4</sub> sample, the 3 curves correspond to 3 different

places of probing on the sample surface. Ga, Na, Zn, O, and C have been detected. Films grown by MOCVD always contain a certain amount of carbon contamination from organometallic precursors used during the growth (Y. Chen et al., 2015; Kim and Kim, 2004; Takiguchi and Miyajima, 2017), it can be largely reduced by post-annealing treatment. Besides, Na measured is merely trace elements in the sample. The conclusion is that there are no external impurities with important quantities except carbon on the surface.

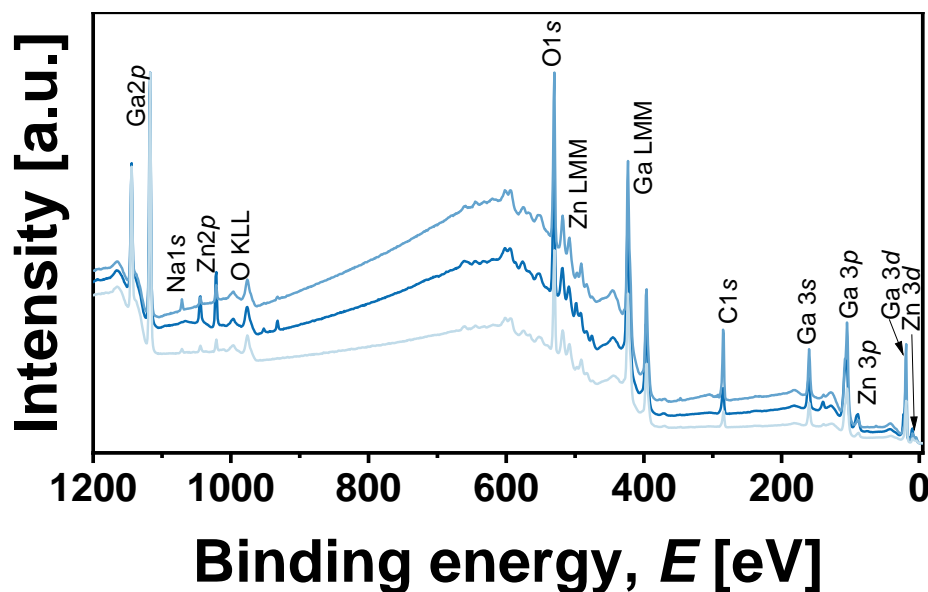
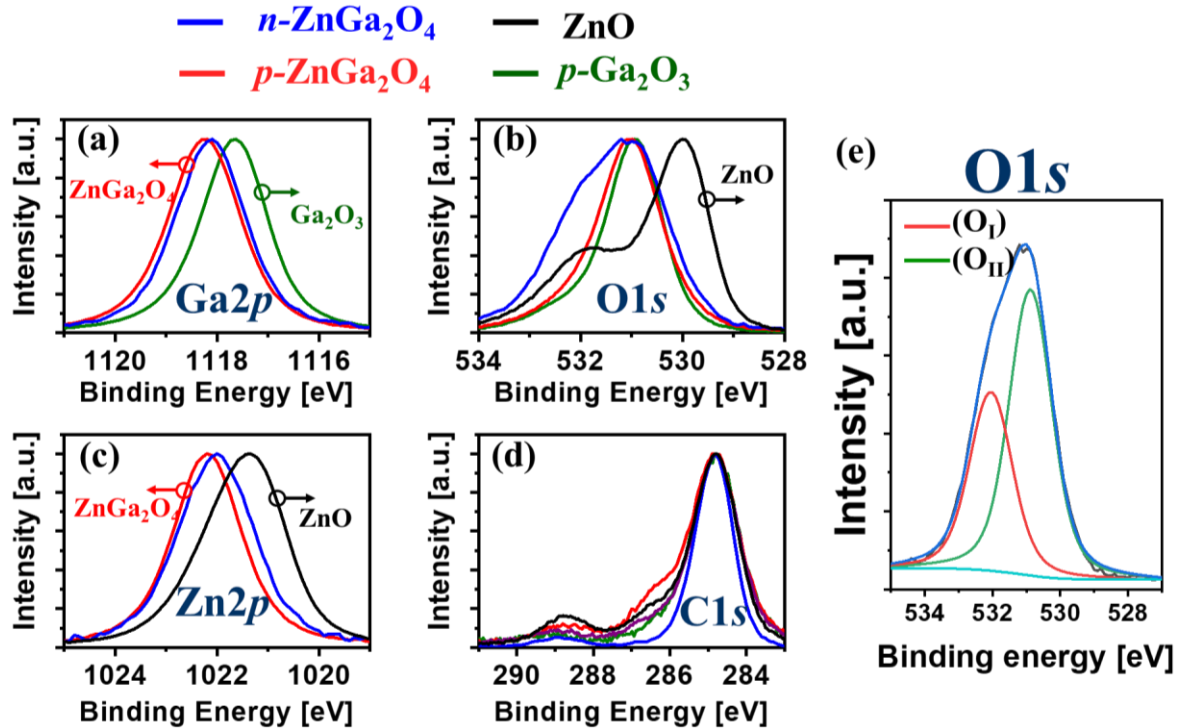


Figure 4-5. XPS spectra of 3 probed places on the surface of *n*-ZnGa<sub>2</sub>O<sub>4</sub> sample.

In addition to surface elemental investigation, XPS also provides information of Ga, Zn and O local bonding environment as well as the chemical state for the different *n*- and *p*-ZnGa<sub>2</sub>O<sub>4</sub> surfaces. The shift of local atomic binding energies is attributable to the cation formal oxidation state, the identity of its nearest-neighbor (Ga or Zn) and its bonding hybridization. As recently reminded by De Souza *et al.* (De Souza and Mueller, 2021) and Walsh *et al.* (Walsh et al., 2018), the XPS element binding energy in a solid are governed not only by the parent atom but also by the atomic arrangement in the compound. The O1s, Zn2p<sub>3/2</sub>, Ga2p<sub>3/2</sub>, and C1s core levels have been analyzed. Adventitious carbon contamination C1s at 284.8 eV (**Figure 4-6 (d)**) was used as calibration for all the spectra in the absence of a better procedure (Greczynski and Hultman, 2020). One first observation is that, regardless of whether is *n*- or *p*-ZnGa<sub>2</sub>O<sub>4</sub>, the Ga and Zn core level binding energies (BEs) are larger for spinel ZnGa<sub>2</sub>O<sub>4</sub> (the complex oxide from binary Ga<sub>2</sub>O<sub>3</sub>:ZnO) than for either, reference monoclinic β-Ga<sub>2</sub>O<sub>3</sub> (*p*-type) and wurtzite ZnO (*n*-type), which is a result

consistent with previous literature. It is customary to attribute the cation's shift towards higher binding energies to larger oxidation states although, in theory, the Zn<sup>2+</sup> and Ga<sup>3+</sup> are in the same oxidation state in ZnGa<sub>2</sub>O<sub>4</sub>, Ga<sub>2</sub>O<sub>3</sub>, and ZnO. For example, the Ga2 $p_{3/2}$  peak in reference monoclinic Ga<sub>2</sub>O<sub>3</sub> appears at a smaller binding energy of 1117.6 eV which perhaps may be understood because of the reduced coordination of half of the metal ions. There are two kinds of coordination for Ga<sup>3+</sup> ions in  $\beta$ -Ga<sub>2</sub>O<sub>3</sub> structure, namely tetrahedral T<sub>d</sub> and octahedral O<sub>h</sub> whose average inter-ionic distances are the following (Geller, 1960): (i) Ga (T<sub>d</sub>): Ga–O = 1.83 Å and O–O = 3.02 Å. (ii) Ga (O<sub>h</sub>): Ga–O = 2.00 Å and O–O = 2.84 Å. The inter-ionic distances for ZnGa<sub>2</sub>O<sub>4</sub> are: Zn(T<sub>d</sub>)-O = 1.95 Å and Ga(O<sub>h</sub>)-O = 2.00 Å, respectively (Errandonea et al., 2009). All the Zn–O bonds are tetrahedral for both, normal ZnGa<sub>2</sub>O<sub>4</sub> and reference wurtzite ZnO where Zn–O bond lengths are usually reported to be T<sub>d</sub> Zn–O ~2.0 Å (Zn–Zn/O–O ~3.2 Å).

Focusing on the ZnGa<sub>2</sub>O<sub>4</sub> samples, the Ga2 $p_{3/2}$  (**Figure 4-6 (a)**) and Zn2 $p_{3/2}$  (**Figure 4-6 (c)**) peaks appear at 1118.2 eV and 1022.2 eV for *p*-ZnGa<sub>2</sub>O<sub>4</sub> and at 1118.1 eV and 1022.0 eV for *n*-ZnGa<sub>2</sub>O<sub>4</sub>, respectively. Therefore, it can be concluded that the effect of self-doping in the ZnGa<sub>2</sub>O<sub>4</sub> cation's shift on Zn2 $p$  ( $\Delta$ BE ~0.2 eV) and Ga2 $p$  ( $\Delta$ BE ~0.1 eV) is rather small (when compared with the ZnGa<sub>2</sub>O<sub>4</sub> vs Ga<sub>2</sub>O<sub>3</sub> or ZnO energy shifts  $\Delta$ BE ~0.7 eV). In contrast to simple binary oxides, where dominant defects are vacancies and interstitials, dominant defects in spinels are suggested to be antisites (Perkins et al., 2011; Zakutayev et al., 2012). These antisites are donor (Ga<sub>Zn</sub>) [donor-like Ga<sup>3+</sup>(O<sub>h</sub>)-on-T<sub>d</sub> antisite defects] and acceptor (Zn<sub>Ga</sub>) [acceptor-like Zn<sup>2+</sup>(T<sub>d</sub>)-on-O<sub>h</sub> antisite defects]. The degree of inversion in zinc gallate has been estimated by the deconvolution of the Ga2 $p$  and Zn2 $p$  XPS peaks in two components at different binding energies (BEs) (Li, 2010). For *p*-ZnGa<sub>2</sub>O<sub>4</sub>, Ga2 $p_{3/2}$  peak appears at 1118.2 eV. By deconvolution, a normal Ga<sup>3+</sup> (O<sub>h</sub>) and an inversion Ga<sup>3+</sup> (T<sub>d</sub>) appear at 1118.3 eV and 1116.8 eV, respectively. Whereas a Zn2 $p_{3/2}$  normal Zn<sup>2+</sup>(T<sub>d</sub>) and an inversion Zn<sup>2+</sup>(O<sub>h</sub>) are at ~1022 eV and ~1023 eV, respectively. The inversion sites Zn<sub>Ga</sub> and Ga<sub>Zn</sub> could be estimated to ~5.3% and ~2.8% of the total area of Zn2 $p_{3/2}$  and Ga2 $p_{3/2}$ , respectively (Chikoidze et al., 2020a). Nevertheless, the binding energy curve of Zn2 $p$  and Ga2 $p$  of *n*-ZnGa<sub>2</sub>O<sub>4</sub> is well symmetric, indicating a unique chemical contribution on each atomic binding energy implying that the antisite defects are either, too few to be detected or inexistent. This already suggests a different origin for the self-doping in the case of donors and acceptors.



**Figure 4-6.** Zoom (intensity normalized) of the main XPS peaks for (a) gallium (Ga<sub>2p</sub> - Ga<sub>2p<sub>3/2</sub></sub>), (b) oxygen (O<sub>1s</sub>), (c) zinc (Zn<sub>2p</sub> - Zn<sub>2p<sub>3/2</sub></sub>), (d) adventitious carbon contamination (C<sub>1s</sub>, calibration for C-C bonds at 284.8 eV) of *n*-type ZnGa<sub>2</sub>O<sub>4</sub>, pure  $\beta$ -Ga<sub>2</sub>O<sub>3</sub>, pure wurtzite ZnO and *p*-type ZnGa<sub>2</sub>O<sub>4</sub> for comparison. (e) Deconvolution of the main contributions of the O<sub>1s</sub> oxygen peak for spinel ZnGa<sub>2</sub>O<sub>4</sub>.

Regarding the anion (oxygen O<sub>1s</sub>) as shown in **Figure 4-6 (b)**, the metal oxide oxygen peak binding energy in ZnO (~ 530 eV) (e.g. (Al-Gaashani et al., 2013)) and that in spinel ZnGa<sub>2</sub>O<sub>4</sub> (~ 531 eV) have a notable difference. In contrast, the metal oxide peak in ZnGa<sub>2</sub>O<sub>4</sub> and Ga<sub>2</sub>O<sub>3</sub> appears at the same energy (~531 eV). There is also a clear difference in the O<sub>1s</sub> shoulder features between *n*-ZnGa<sub>2</sub>O<sub>4</sub> and *p*-ZnGa<sub>2</sub>O<sub>4</sub> which is clearly visible for *n*-ZnGa<sub>2</sub>O<sub>4</sub> (as for *n*-ZnO) and much smaller for *p*-ZnGa<sub>2</sub>O<sub>4</sub> (as for *p*-Ga<sub>2</sub>O<sub>3</sub>). Interestingly, the most notable difference between *n*-type and *p*-type ZnGa<sub>2</sub>O<sub>4</sub> precisely is found in the shape of the O<sub>1s</sub>. A double feature at higher binding energy can be seen clearly in the *n*-ZnGa<sub>2</sub>O<sub>4</sub> peak. In zinc oxide thin films (but also in many other metal-oxide semiconductors), this oxygen shoulder (O<sub>II</sub>) has been related to hydroxide (Marrani et al., 2014), hydrate (Majumder et al., 2003) or oxygen deficiency (Kumar et al., 2013). The absence of shoulder features in *p*-ZnGa<sub>2</sub>O<sub>4</sub> and *p*-Ga<sub>2</sub>O<sub>3</sub> O<sub>1s</sub> may be correlated with a lower donor compensation (e.g. very low concentration of oxygen vacancies). In *n*-type ZnGa<sub>2</sub>O<sub>4</sub>, the O<sub>1s</sub> lattice peak appears at

530.9 eV, and the shoulder maxima was found at 532.1 eV (**Figure 4-6 (e)**). Again, according to the interpretation proposed by Dupin *et al.* (Dupin *et al.*, 2000; Wu *et al.*, 2015), the lower BE peak is assigned to O<sup>2-</sup> ions, the middle BE peak to O<sup>1-</sup> ions, and the higher BE peak to O<sub>Chem</sub>, chemically adsorbed oxygen on the surface. In any case, based on the observables, the degenerated *n*-type ZnGa<sub>2</sub>O<sub>4</sub> doping has a minimum impact on core Ga2*p*, a moderate impact on core Zn2*p*, and, a clear impact on the core O1s shoulder features. A simple coherent explanation of these facts implies Ga vacancies and modified Zn-O hybridization. XPS atomic quantification suggests an oxygen-deficient scenario with oxygen/metal ratio of ~1, and, perhaps more trustable, Ga/Zn was determined to be ~1.9, revealing the Zinc-rich condition of *n*-ZnGa<sub>2</sub>O<sub>4</sub>. However, recall again that no signature of ZnO has been found structurally either by XRD or by TEM analysis and that *n*-ZnGa<sub>2</sub>O<sub>4</sub> is considered a pure spinel in nature.

### 4.2.3 Valence Band and Optical Band gap of *n*- and *p*-ZnGa<sub>2</sub>O<sub>4</sub> layers

I would like to focus on the experimental valence band features extracted from the XPS analysis, as shown in Figure 4-7. All the valence band edge has been shifted using the adventitious C-C 284.8 eV following the same procedure as with the core levels (**Figure 4-6 (c)**). The experimental valence band width of the ZnGa<sub>2</sub>O<sub>4</sub> thin films is around ~8 eV, having to main contributions; the top of the valence (lower binding energies) is ascribed to O2*p* states while there is an important contribution at larger binding energies due to Zn3*d* states peaking at 10.8 eV (*n*-ZnGa<sub>2</sub>O<sub>4</sub>) and 8.2 eV (*p*-ZnGa<sub>2</sub>O<sub>4</sub>). So, the binding energy shifts ( $\Delta$ BE ~2.6 eV) of the valence band Zn3*d* peaks (when comparing *n*-type and *p*-type ZnGa<sub>2</sub>O<sub>4</sub>) is much more pronounced than the one from the core levels. Again, there is a strong reminiscence of the *n*-ZnO valence band shape and *n*-ZnGa<sub>2</sub>O<sub>4</sub> in terms of intensity and energy, except for a valley located at 8,6 eV for ZnO (as if the Zn3*d* and O2*p* states were more separated for ZnO). Analogously, Ga3*d* features present in ZnGa<sub>2</sub>O<sub>3</sub> and Ga<sub>2</sub>O<sub>3</sub> in the second valence band peaks at 20.3 eV for *n*-ZnGa<sub>2</sub>O<sub>4</sub> and Ga<sub>2</sub>O<sub>3</sub> (either *n* or *p*) while peaks at 17.7 eV for *p*-ZnGa<sub>2</sub>O<sub>4</sub> ( $\Delta$ BE ~2.6 eV). Therefore, in practice, the Fermi level (as determined from the top band slope) is shifted ~2.8 eV from *p*-ZnGa<sub>2</sub>O<sub>4</sub> ( $E_F$  ~ 0.5 eV), up to  $E_F$  ~3.3 eV for *n*-ZnGa<sub>2</sub>O<sub>4</sub>. This result agrees well with the fact that the Fermi energy is in the upper part of the bandgap for *n*-ZnGa<sub>2</sub>O<sub>4</sub> and in the lower half of the bandgap for *p*-ZnGa<sub>2</sub>O<sub>4</sub>. However, considering an electronic bandgap of ~5 eV for *n*-ZnGa<sub>2</sub>O<sub>4</sub>, the Fermi

level is still around  $\sim 1.9$  eV from the conduction band edge ( $E_c$ ). Thus, this would not explain the high concentration of free carriers at room temperature for  $n$ -ZnGa<sub>2</sub>O<sub>4</sub>. A plausible explanation for the room temperature conductivity of  $n$ -ZnGa<sub>2</sub>O<sub>4</sub> is the formation of an impurity conductive band (Kabilova et al., 2019) as revealed by optical spectroscopy.

Optical transmittance and optical bandgap determination by Tauc's plot for  $n$ -ZnGa<sub>2</sub>O<sub>4</sub> and  $p$ -ZnGa<sub>2</sub>O<sub>4</sub> samples are shown in Figure 4-8. The  $p$ -type thin layer exhibits high transparency  $> 80\%$ , and the  $n$ -type has even higher transparency  $\sim 95\%$  in 360 to 1000 nm wavelength range. The values of optical bandgaps determined from absorption edges in UV region are 4.9 eV and 4.8 eV, respectively (**Figure 4-8 (b)**). Contrary to the sharp edge of  $p$ -ZnGa<sub>2</sub>O<sub>4</sub>, for the  $n$ -ZnGa<sub>2</sub>O<sub>4</sub> sample, there is another absorption band at around 360 nm (Figure 4-8 **(a)**). Such an absorption band has been already reported in conducting thin films (Look et al., 2020) without clear identification of the origin. Interestingly, other groups have observed PL emissions peaking at 340 nm in zinc gallate and this emission has been associated with Ga<sup>3+</sup> ions substitution into the Zn<sup>2+</sup> ions site (W.-K. Wang et al., 2019b, 2019a). Our results suggest however that, rather than Ga<sub>Zn</sub> antisites, this absorption at 360 nm ( $\sim 3.4$  eV) might be associated with Zn atoms having strong bond with oxygen, leading to Zn-O hybridization. The position of this band agrees with the findings from XPS analysis (location of Fermi level). At high doping levels, the neighboring impurities have overlapping wave functions causing the single donor level to split and turn into a band, known as an impurity band. The states in the impurity band are localized, resulting in electron transport that is dominated by tunneling and hopping (Kabilova et al., 2019) as we will demonstrate in the following section.

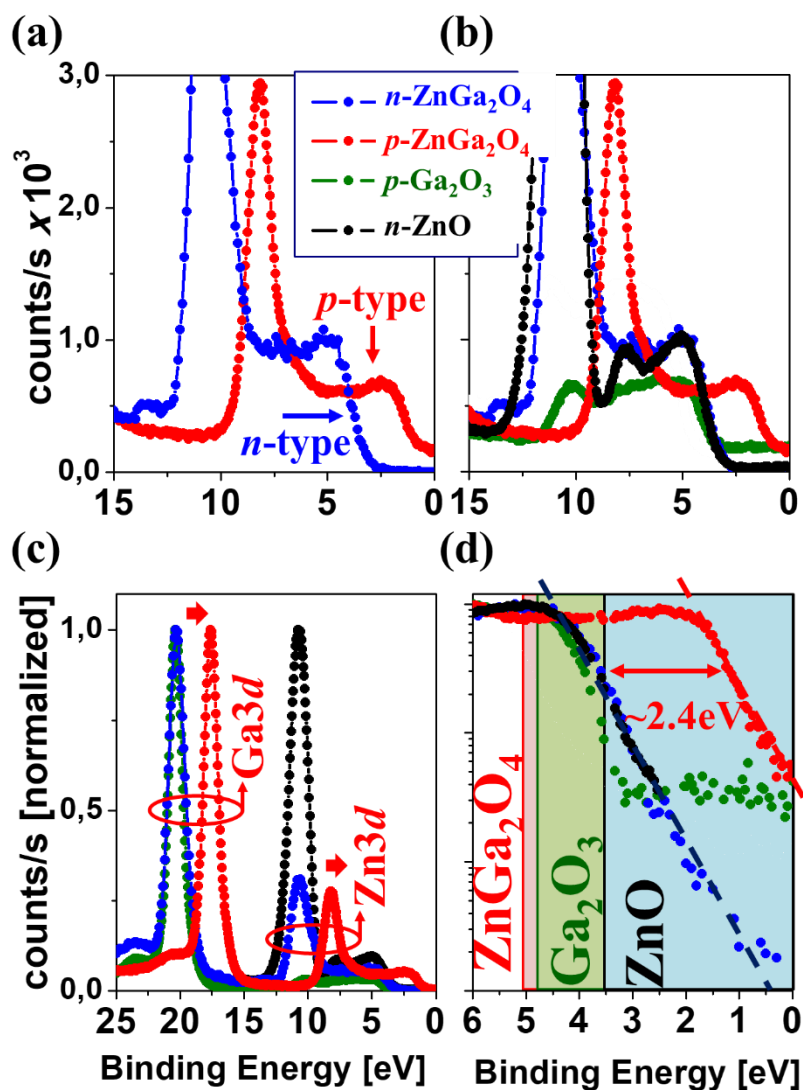


Figure 4-7. (a) Experimental XPS high-resolution valence band for the *n*-type ZnGa<sub>2</sub>O<sub>4</sub> and *p*-type ZnGa<sub>2</sub>O<sub>4</sub> as a reference. (b) Experimental XPS high-resolution of the first valence band group for *n*-type ZnGa<sub>2</sub>O<sub>4</sub>, *p*-type ZnGa<sub>2</sub>O<sub>4</sub>, pure ZnO and pure *p*-type β-Ga<sub>2</sub>O<sub>3</sub> for comparison. (c) Idem, for the first and the second group of valence bands. (d) A zoom of the valence band region (VBM) showing the presence of tail states in the lower part of the bandgap for the *p*-type compounds (the value of the bandgap is depicted for ZnO, β-Ga<sub>2</sub>O<sub>3</sub> and ZnGa<sub>2</sub>O<sub>4</sub>).

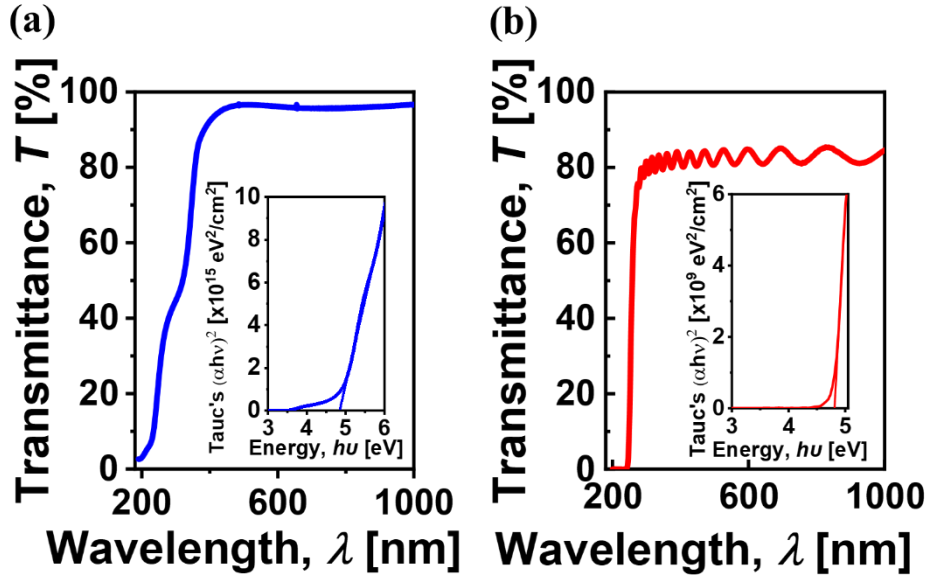


Figure 4-8. Room temperature optical transmittance spectra and in inset direct bandgap determination by Tauc's plot for both *n*-type (a) and *p*-type ZnGa<sub>2</sub>O<sub>4</sub> (b) thin films.

#### 4.2.4 Electrical Transport properties of *n*- and *p*-ZnGa<sub>2</sub>O<sub>4</sub> layers

Electrical transport measurement of undoped *p*-type ZnGa<sub>2</sub>O<sub>4</sub> thin film was carried out in a Van der Pauw configuration, **Figure 4-9 (c), (d)**. As the layer's resistance below 500 K exceeded the measurement limit of our set-up ( $\sim 5 \times 10^{10} \Omega$ ), the measurement was performed only at high temperatures (500 – 850 K). The pure *p*-ZnGa<sub>2</sub>O<sub>4</sub> thin film is highly resistive:  $\rho = 1.3 \times 10^3 \Omega \cdot \text{cm}$  with a hole concentration of  $p = 1.6 \times 10^{15} \text{ cm}^{-3}$  at 850K. This *p*-type conductivity was explained by the fact of self dopability, ie. presence of acceptor antisite (Zn<sub>Ga</sub>) defects (Chikoidze et al., 2020a). Though, conductivity is quite low, indicating that those samples are of low inversion degree of cations, still not very far from stoichiometric composition. The measured mobilities were between 7 - 10  $\text{cm}^2/(\text{V} \cdot \text{s})$ , high values for this temperature range. Further work is required to find growth condition with enhancing possibility of acceptor Zn<sub>Ga</sub> defects formation, leading to higher hole conductivity.

Very differently, for *n*-type ZnGa<sub>2</sub>O<sub>4</sub> 190 nm film at room temperature, Van Der Pauw configuration resistivity was found to be exceptionally low:  $\rho = 3.2 \times 10^{-2} \Omega \cdot \text{cm}$ . Hall effect measurement at 300 K with magnetic field of 1.6 T reveals an electron concentration of  $n = 3.7 \times 10^{19} \text{ cm}^{-3}$ , and a mobility of  $\mu = 5.3 \text{ cm}^2 \text{ V}^{-1} \text{ s}^{-1}$ . Additionally, the Seebeck Effect has confirmed *n*-type conductivity of the thin layer, with a Seebeck coefficient of  $S_{300\text{K}} = -30.2$

$\mu\text{V/K}$ . Oxygen vacancies are traditionally considered the source of electrons in semiconductor oxides and for ZnGa<sub>2</sub>O<sub>4</sub> spinel the same origin has already been proposed in several works (Kim et al., 2004; Krishna et al., 2005; Omata et al., 1994; Yan et al., 2005). However, oxygen vacancy as a native Frenkel type defect is supposed to be a deep level defects in ultra-wide bandgap ZnGa<sub>2</sub>O<sub>4</sub> (Pandey et al., 1999; Paudel et al., 2011b; Shi et al., 2014), thus it cannot be the origin of high electron concentrations at room temperature.

To elucidate the mechanism of conductivity, the temperature dependence electrical transport measurements of the *n*-type ZnGa<sub>2</sub>O<sub>4</sub> has been carried out in four-point aligned configuration by physical property measurement system (PPMS-9T), **Figure 4-9 (a)**. The resistivity values are  $2.7 - 6.9 \times 10^{-2} \Omega \cdot \text{cm}$  for 2 – 300 K. The resistivity is almost invariant in the 100 - 300 K temperature range, while exhibiting a tendency to increase when  $T < 100$  K. To the best of our knowledge, such highly conducting thin films have only been reported by D. Look *et al.* (Look et al., 2020),  $\rho = 4.2 \times 10^{-2} \Omega \cdot \text{cm}$  for a PLD deposited sample, and  $\rho = 5.6 \times 10^{-3} \Omega \cdot \text{cm}$  for a MOCVD grown sample (L. C. Cheng et al., 2018; Shen et al., 2017).

Observing such a high electrical conductivity in ultra-wide bandgap material, one can think about surface conduction caused by the charge accumulation (Vasheghani Farahani et al., 2014; K. H. L. Zhang et al., 2013). Though we are discarding this hypothesis since it is not observed any signature of surface 2D conductivity (decrease resistivity with temperature and hockey-stick shape of  $\rho(T)$ ) (E. Chikoidze et al., 2019; Gu et al., 2014; Halim et al., 2014; Nistor et al., 2009; Noun et al., 2007). Thus, the only probable explanation for such high electrical conduction can be the so-called self-doping effect.

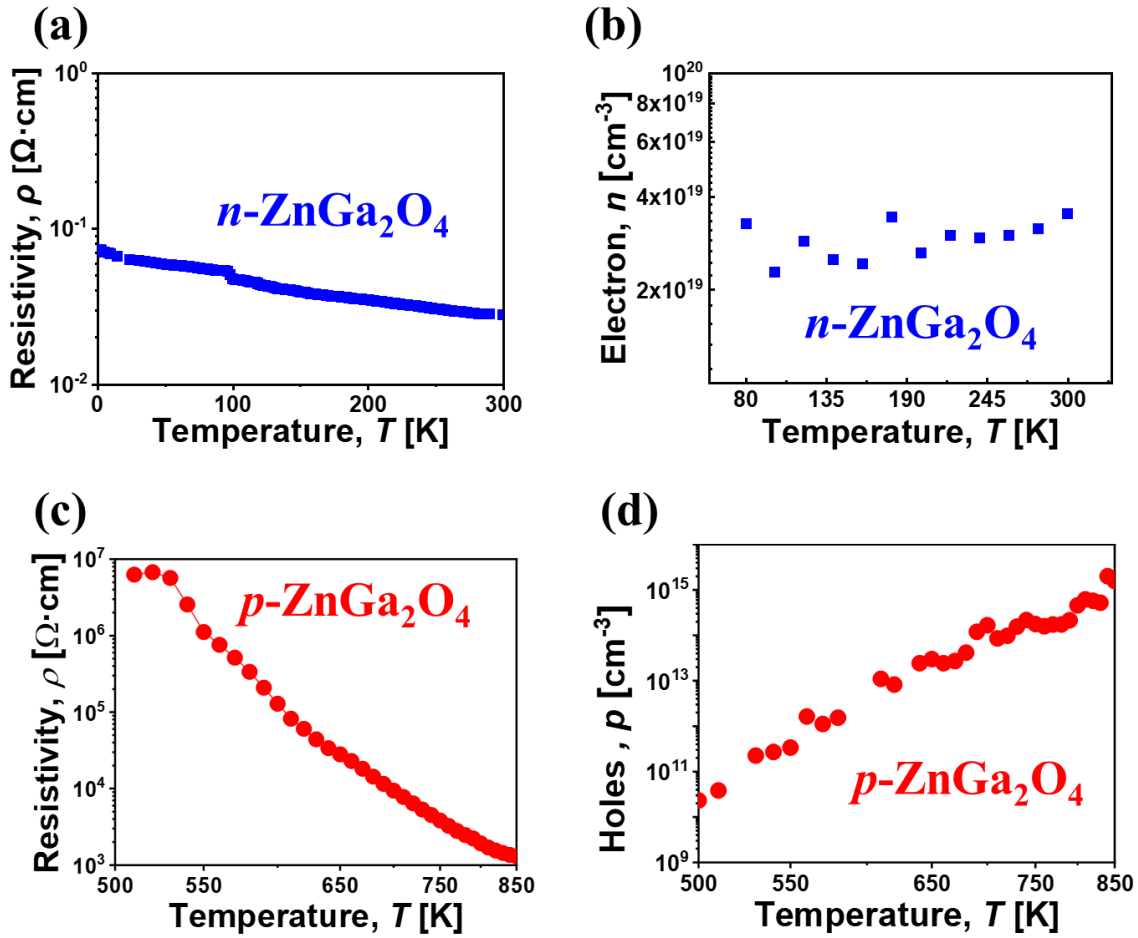


Figure 4-9. *n*-ZnGa<sub>2</sub>O<sub>4</sub> thin film (a) electrical resistivity versus temperature dependence from aligned four-probe measurements; (b) electron concentration from Hall effect measurements in Van der Pauw configuration. Pure *p*-type ZnGa<sub>2</sub>O<sub>4</sub> layer (c) electrical resistivity and (d) hole concentration versus temperature determined from Hall effect measurement.

Comparing XRD spectra (Figure 4-3), TEM images (Figure 4-4), electrical transport properties (Figure 4-9), XPS for local bonding environment of Zn, Ga, O (Figure 4-5), and optical transmittance (Figure 4-8), for *n*-type ZnGa<sub>2</sub>O<sub>4</sub> and *p*-type ZnGa<sub>2</sub>O<sub>4</sub> thin films, the most remarkable differences come from the binding energy of O1s and valence band tails.

The last features have a great similarity with ZnO, while the material is structurally ZnGa<sub>2</sub>O<sub>4</sub>. Indeed, the defect-defect interaction has already been considered of natively *n*-type conductivity ZnO. This interaction is driven by the quantum mechanical hybridization between two donor-like defects, the deep donor oxygen vacancy  $V_O$  and the shallow donor zinc interstitial  $Zn_i$  (Asghar et al., 2013; Kim and Park, 2009). This interaction happens in

our Zn-rich and O-deficient zinc gallate, and significantly reduces the total energy of the system, leading to a high electron concentration of Zn<sub>i</sub> (Kim and Park, 2009). Even Zn<sub>i</sub> though they are not as energetically favorable as antisite defects Zn<sub>Ga</sub> and Ga<sub>Zn</sub> in stoichiometric ZnGa<sub>2</sub>O<sub>4</sub> (Paudel et al., 2011b; Zhang and Zunger, 2010). An energy level is introduced by these defects within the gap, mainly 3.4 eV from the valence band (determined from XPS valence band tails and optical spectrum). Evidently, this donor level is relatively deep (bandgap  $E_g = 4.9$  eV) and cannot be activated at room temperature, thus being the source of free carriers. Consequently, we suppose that observed room temperature electrical conductivity might be rather due to localized carriers within the defect band, as it happens for impurity conduction for highly doped semiconductors.

We have analyzed the electrical transport properties considering this hypothesis. Localization of free carriers leads to different hopping mechanism depending on temperature regions. Indeed, two slopes could be distinguished by  $\log(\sigma)$  versus  $1/T$  plot ( $\sigma = 1/\rho$ ). As shown by **Figure 4-10 (a)**, the first “high temperature” interval corresponds to nearest-neighbor hopping (NNH) conduction. The conductivity in the nearest-neighbor hopping regime can be simply described by the expression  $\sigma(T) = \sigma_0 T^{-1} \exp(-\varepsilon/K_B T)$  (Shklovskii and Efros, 1984), where  $\sigma_0$  being a function of the impurity concentration is independent of the temperature  $T$ ,  $k_B$  is the Boltzmann constant,  $\varepsilon$  is an activation energy for hops from one site to the nearest one in the impurity band, it is temperature independent and was estimated as  $E_a = 20.9$  meV (**Figure 4-10 (a)**). With lower temperatures ( $< 100$  K), electrons do not have enough energy to hop at the nearest-neighbor sites. Thus, the variable range hopping (VRH) takes place and as it is shown in **Figure 4-10 (b)**, the conductivity in this temperature interval can be well fitted with  $T^{-1/4}$  dependence, corresponding to Mott’s VRH mechanism.

As has been demonstrated, in undoped non-stoichiometric *n*-type ZnGa<sub>2</sub>O<sub>4</sub> the self-doping effect is due to hybridization between zinc and oxygen orbitals. Such a rich number of point defects usually lead a system disorder where the periodic potential in the crystal structure is destroyed. Other hand, such a disorder could lead to carrier localization which is the so-called Anderson’s localization, and the high level of the disorder can induce a metal to insulator transition (MIT) (Anderson, 1958; Siegrist et al., 2011; Ying et al., 2016). However, for our *n*-type zinc gallate sample, there is no important change of resistivity, which could indicate the metal-insulator transition (MIT) (**Figure 4-10 (a)**). It emerges that

the disorder due to the self-doping effect is not strong enough, indicating the relatively low deviation from stoichiometry.

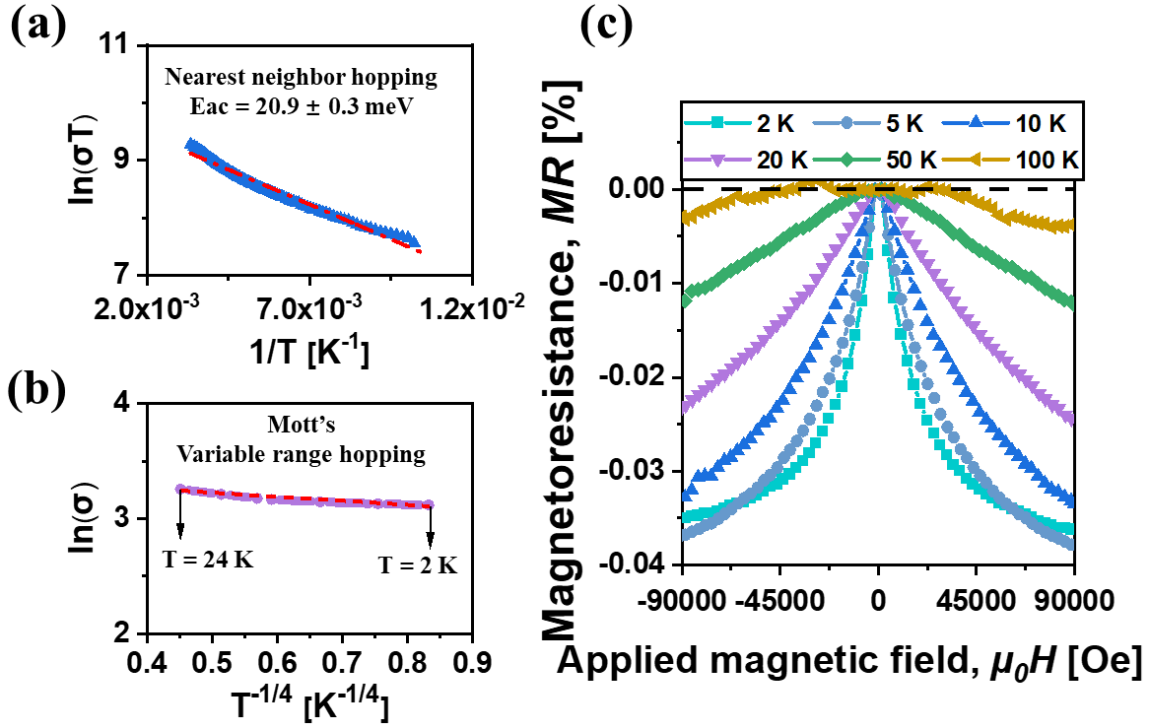


Figure 4-10. *n*-type ZnGa<sub>2</sub>O<sub>4</sub> (a)  $\log(\sigma T)$  versus  $1/T$  in the nearest-neighbor hopping regime; (b)  $\ln(\sigma)$  versus  $T^{-1/4}$  showing the variable range hopping regime (VRH); (c) Resistance versus magnetic field at different temperatures (2 – 100 K) in perpendicular to current magnetic field orientation. Measurements were done in four-probe aligned configuration.

To further understand the conduction mechanism, the magnetoresistance (MR, in %) was measured with a magnetic field applied perpendicular to the film plane (i.e. the current). The resistances as a function of the magnetic field for *n*-type ZnGa<sub>2</sub>O<sub>4</sub> thin film at different temperature are shown by Figure 4-10 (c). The MR decreases with the increasing field (absolute value), and is negative from 2 K up to 100 K, then vanishes at  $T > 100$  K. Such negative magnetoresistance is usually observed for nonmagnetic semiconductors when heavily doped (Chikoidze et al., 2016; Sasaki and de Bruyn Ouboter, 1961; Toyozawa, 1962). In the present case, in the undoped *n*-ZnGa<sub>2</sub>O<sub>4</sub> high concentration of carriers is related to native defects. We could think that there is a conducting channel similar to the “impurity band” in external impurity doped semiconductors. Such a “self-impurity” band we attribute to the Zn related donor defect.

### 4.2.5 Summary

High quality *p*-type and *n*-type ZnGa<sub>2</sub>O<sub>4</sub> epilayers can be grown by tuning, oxygen flow and cation ratio during metal-organic chemical vapor (MOCVD) deposition. State-of-the-art analytical techniques provide no evidence of contamination or secondary phases. The intrinsic conductivity can be tuned up to 10 orders of magnitude as summarized in **Figure 4-11**. These experimental facts raise-up the immediate question: what is the origin of the high *n*-type conductivity in ultra-wide band gap ZnGa<sub>2</sub>O<sub>4</sub>. Here, based on complementary structural, chemical, optical and electrical transport measurements, we conclude that the origin of high room temperature *n*-type conductivity ( $\sim 3.2 \times 10^{-2} \Omega \text{ cm}$  at room temperature) is related to the “self-impurity” band located at  $E_v + \sim 3.4 \text{ eV}$  from the valence band edge. This band is a consequence of Zn-O orbital’s hybridization in Zn-rich and O-deficient ZnGa<sub>2</sub>O<sub>4</sub> material. While other hand, hole conductivity ZnGa<sub>2</sub>O<sub>4</sub> occurred thanks to Zn<sub>Ga</sub> antisite defects.

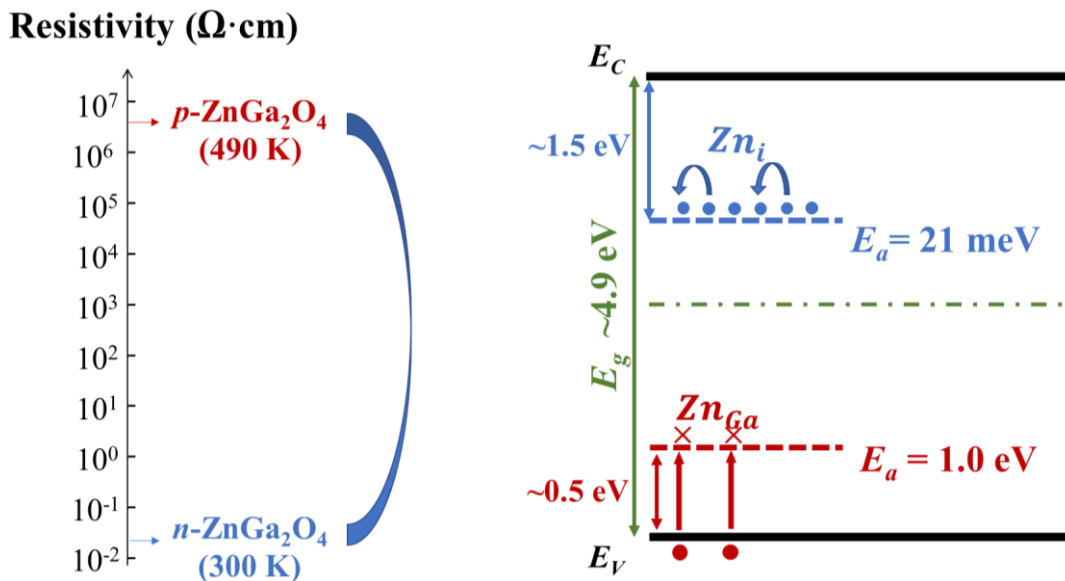


Figure 4-11. Schematic summary showing the intrinsic conductivity difference between conducting *n*-type and semi-insulating *p*-type ZnGa<sub>2</sub>O<sub>4</sub> thin films, with the corresponding conduction mechanism and origin of the conductivity.

### 4.3 Influence of the oxygen content on the electrical properties

In this section, I will present an ongoing work that has the objective to study the influence of oxygen content on the electrical transport properties of ZnGa<sub>2</sub>O<sub>4</sub> thin films. Samples were deposited on *c*-sapphire substrates by metal organic vapor deposition (MOCVD) in National Chiao Tung University. Diethylzinc (DEZn), triethylgallium (TEGa), and oxygen were used as the precursors, the growth time was 30 minutes. After the growth, one sample was cooled with an O<sub>2</sub> flow of 1000 sccm, while the precursors were all cut for the other one. The growth parameters and the thickness of two samples are summarized in the **Table 4-3**.

Table 4-3. Growth parameters and the thickness of samples.

N <sup>o</sup>	Growth conditions	O <sub>2</sub> flow [sccm]	Time [min]	O <sub>2</sub> during cooling [sccm]	Thickness [nm]
ZnGa <sub>2</sub> O <sub>4</sub> -#1	DEZn = 100 sccm TEGa = 100 sccm	500	30	-	105
ZnGa <sub>2</sub> O <sub>4</sub> -#2	T = 720 °C	700		1000	120

#### 4.3.1 Structural characterization

**Figure 4-12** shows the X-ray diffraction (XRD) patterns of  $\theta$ - $2\theta$  scan for both as-grown ZnGa<sub>2</sub>O<sub>4</sub> film and that cooled in O<sub>2</sub>, in which  $2\theta$  was increased from 15° to 65°. Both thin films possess three XRD peaks located at  $2\theta$  positions of 18.50°, 37.46°, and 57.56°, corresponding to (111), (222), and (333) ZnGa<sub>2</sub>O<sub>4</sub> planes, respectively. Compared to our previously reported work (Chi et al., 2021), the slight shift of the  $2\theta$  positions can result from different Zn content, as demonstrated by Horng *et al.* (Horng et al., 2017). Low values of full width at half maximum (FWHM) of 0.172° for the ZnGa<sub>2</sub>O<sub>4</sub>-#1 sample indicates the high crystalline quality of the layer. The crystallinity was slightly improved to 0.171° for ZnGa<sub>2</sub>O<sub>4</sub>-#2 that was cooled in O<sub>2</sub>.

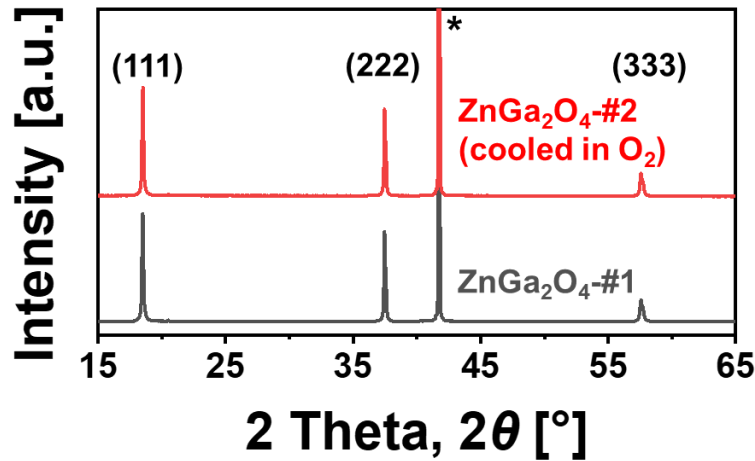


Figure 4-12. Cu-K $\alpha$  XRD  $\theta$ - $2\theta$  patterns of both ZnGa<sub>2</sub>O<sub>4</sub> thin films, the *c*-plane sapphire substrate is labelled as “\*”.

The structural characteristics of the ZnGa<sub>2</sub>O<sub>4</sub>-#1 layer were further investigated by transmission electron microscopy (TEM). As shown in **Figure 4-13 (a)**, the cross-sectional image reveals a dense structure. The thickness was then determined to be 105 nm. The selected area electron diffraction (SAED) pattern (**Figure 4-13 (c)**) from **Figure 4-13 (b)**, indicates that the ZnGa<sub>2</sub>O<sub>4</sub> film has a single-crystalline structure, and the ZnGa<sub>2</sub>O<sub>4</sub> phase of the film was formed along the [111] direction with a  $[\bar{2}, 1, 1]$  zone axis.

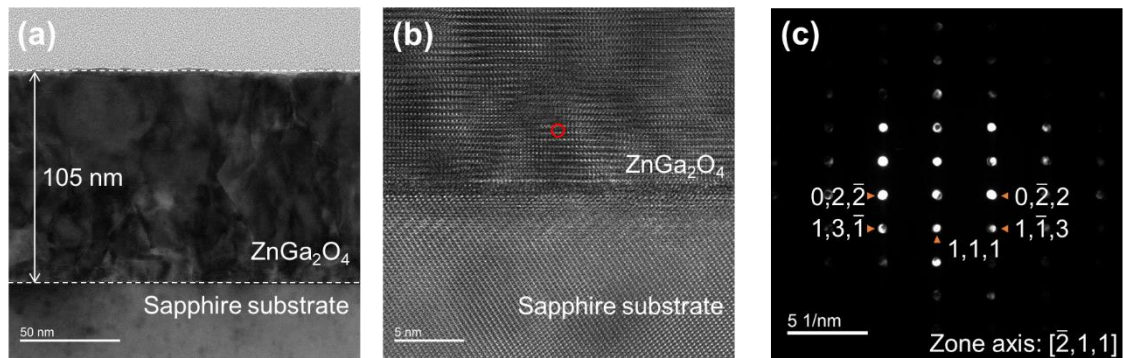


Figure 4-13. (a) TEM cross-section image of ZnGa<sub>2</sub>O<sub>4</sub>-#1 thin film. (b) High resolution TEM image. (c) SAED pattern of the ZnGa<sub>2</sub>O<sub>4</sub>-#1 film, selected part is shown in the red circle in figure (b). The results were provided by collaborators from National Chiao Tung University.

### 4.3.2 Electrical transport properties

To study the actual influence of the O<sub>2</sub> content on the electrical properties of the spinel ZnGa<sub>2</sub>O<sub>4</sub> layers, we conducted the electrical resistivity and Hall effect measurements at various temperatures in a Van der Pauw configuration for both thin films. Four electrical contacts by silver paste were painted on the corners of both square-shaped (1 × 1 cm<sup>2</sup>) samples.

**Figure 4-14 (a)** shows a quasi-Ohmic current–voltage ( $I$ – $V$ ) characteristics of the ZnGa<sub>2</sub>O<sub>4</sub>-#1 thin film. The temperature-dependent resistivity ( $\rho$ ) in the range of 80 – 500 K is shown in **Figure 4-14 (b)**, the resistivity decreased very slightly from  $4.9 \times 10^{-1} \Omega \cdot \text{cm}$  at 80 K to  $1.6 \times 10^{-1} \Omega \cdot \text{cm}$  at 500 K. From the temperature dependence of the conductivity  $\sigma$ , in  $\ln(\sigma)$  versus  $1000/T$  plot (**Figure 4-14 (c)**), a single law can be fitted to the entire curve in the measurement temperature range, and a tiny activation of conductivity as  $E_a = 10 \pm 0.4$  meV was determined using the Arrhenius equation. Despite multiple attempts over the entire temperature range, the Hall effect measurements could not be validated due to the anomalous sign of the Hall coefficient. Generally, this observation might be due to the hopping conduction (too low mobility) or elevated charged carriers (too low Hall voltage). The  $n$ -type nature was later confirmed by the Seebeck effect. Compared to the  $n$ -type sample discussed in Section 5.2, the conductivity of this sample is one order of magnitude less, which can be explained by different growth parameters.

Interestingly, contrary to ZnGa<sub>2</sub>O<sub>4</sub>-#1, the ZnGa<sub>2</sub>O<sub>4</sub>-#2 layer (that was cooled in O<sub>2</sub>) exhibits a semi-insulating nature. As shown in **Figure 4-14 (d)**, the  $I$ – $V$  characteristic has been tested at 750 K firstly, indicating the Ohmic characteristics of the Ag paste to  $p$ -type ZnGa<sub>2</sub>O<sub>4</sub> layer. The temperature dependent resistivity is shown in **Figure 4-14 (e)**, where the resistivity increased from  $1.9 \times 10^2 \Omega \cdot \text{cm}$  at 750 K to  $6.1 \times 10^4 \Omega \cdot \text{cm}$  at 550 K. Compared to ZnGa<sub>2</sub>O<sub>4</sub>-#1, a rise of at least 7 orders of magnitude (estimated at room temperature) in ZnGa<sub>2</sub>O<sub>4</sub>-#2 layer with a higher O<sub>2</sub> content. To determine the type of the majority carriers, the Hall voltage ( $V_H$ ) dependence on the applied magnetic field was measured at 750 K. As shown in **Figure 4-14 (g)**, the positive  $V_H$  increases with a perpendicularly applied magnetic field, evidencing that the layer cooled in O<sub>2</sub> is  $p$ -type. The activation energy of conductivity was also increased to  $E_a = 1.01 \pm 0.04$  eV (**Figure 4-14 (f)**), by 100 times more than that of the  $n$ -type ZnGa<sub>2</sub>O<sub>4</sub>-#1 sample. The hole concentration as a function of temperature is

presented in **Figure 4-14 (h)**. We deduce the mobility  $\mu = 2.3 - 8.5 \text{ cm}^2/(\text{V}\cdot\text{s})$  within the measurement temperature range.

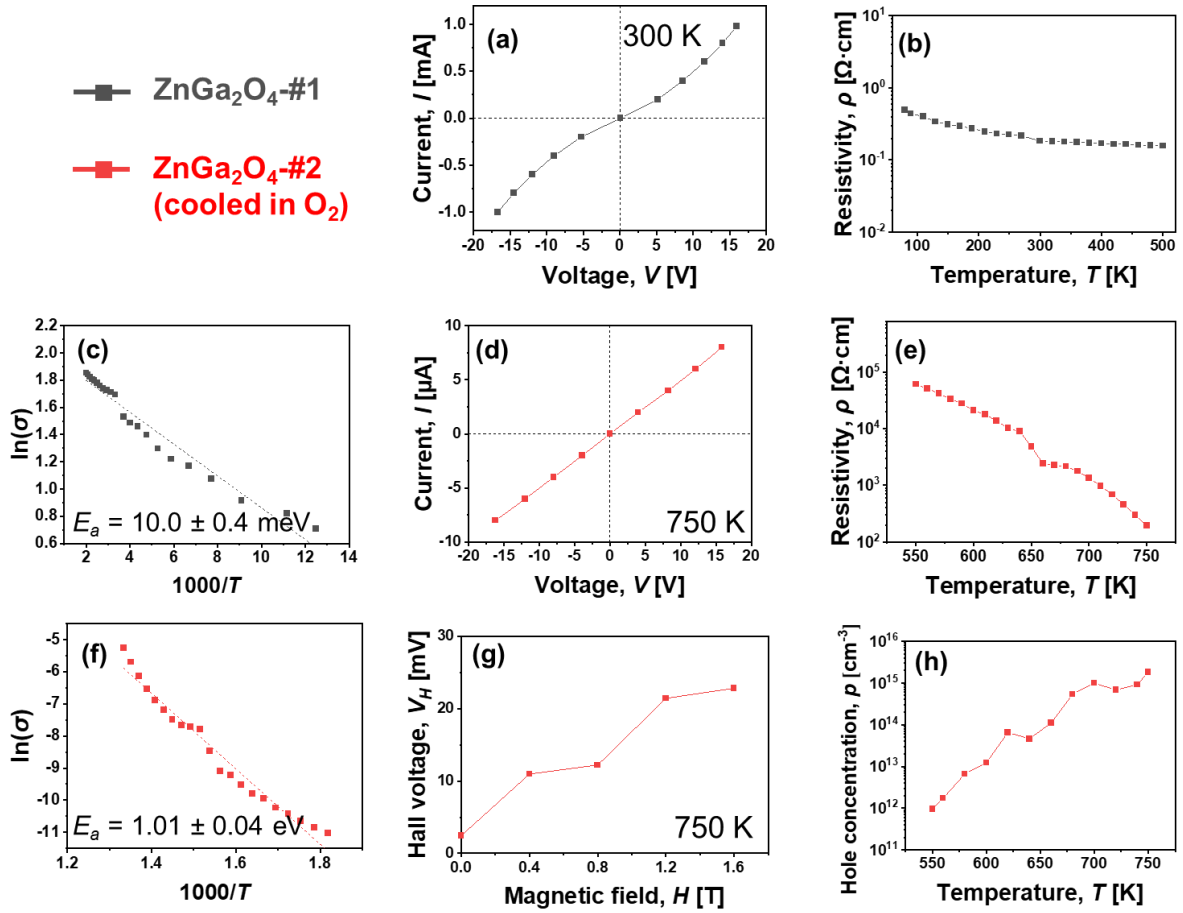


Figure 4-14. For ZnGa<sub>2</sub>O<sub>4</sub>-#1 thin film: (a) Current-voltage (*I-V*) characteristics at 300 K; (b) Temperature-dependent resistivity ( $\rho$ ) in the range of 80 – 500 K; (c)  $\ln(\sigma)$  versus  $1000/T$  for the determination of the activation energy of the conductivity. For the ZnGa<sub>2</sub>O<sub>4</sub>-#2 which was cooled in O<sub>2</sub>: (d) *I-V* curve at 750 K; (e) Temperature-dependent resistivity in the range of 550 – 750 K; (f)  $\ln(\sigma)$  versus  $1000/T$ ; (g) Hall voltage ( $V_H$ ) versus magnetic field at 750 K, both the values of the Hall voltage and the slope are positive, indicating the *p*-type conductivity of the ZnGa<sub>2</sub>O<sub>4</sub> sample; (h) Temperature-dependent hole concentration ( $p$ ) in 550 – 750 K.

### 4.3.3 Optical transmittance

**Figure 4-15** displays the room-temperature transmittance spectra for (i) ZnGa<sub>2</sub>O<sub>4</sub>-#1, (ii) O<sub>2</sub> cooled ZnGa<sub>2</sub>O<sub>4</sub>-#2 layers, and (iii) the *n*-type ZnGa<sub>2</sub>O<sub>4</sub> thin film discussed in Section 4.2 that has an obvious double absorption in optical spectrum (**Figure 4-8 (a)**), and an one

face polished bare sapphire substrate as reference. For clearness: the backside of the sapphire substrates was not polished for all these three samples, leading to an underestimation of the transmittance for all three samples. Different from the *n*-type ZnGa<sub>2</sub>O<sub>4</sub> thin film discussed in Section 4.2, there is only one absorption at the band edge ( $\sim 4.8$  eV) for other two ZnGa<sub>2</sub>O<sub>4</sub> thin films. The sapphire substrate reference shows that the non-polished backside scattering has no influence on the mid-gap absorption.

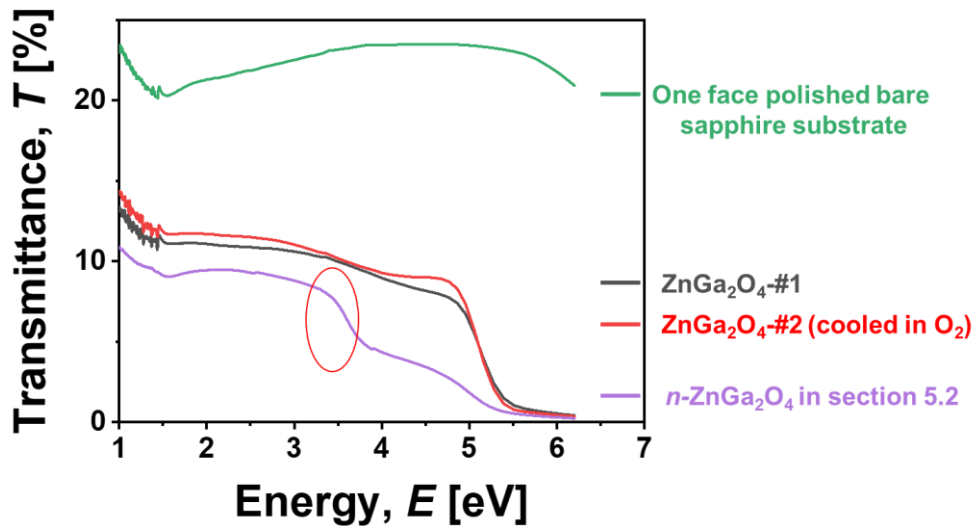


Figure 4-15. Optical transmittance for as grown, O<sub>2</sub> cooled ZnGa<sub>2</sub>O<sub>4</sub> samples, *n*-type ZnGa<sub>2</sub>O<sub>4</sub> thin film discussed in Section 4.2, and only one face polished bare sapphire substrate as reference.

#### 4.3.4 Electronic properties

To study the chemical environment of elements, XPS measurements of both samples were carried out by Dr. Mathieu Frégnaux at Institute Lavoisier de Versailles (ILV), UFR des Sciences at Versailles. The O1s, Zn2p<sub>3/2</sub>, Ga2p<sub>3/2</sub>, and C1s core levels have been analyzed. The adventitious carbon contamination related peak C1s was calibrated at 284.8 eV for both spectra (**Figure 4-16 (d)**). Ga2p<sub>3/2</sub> binding energy peaks appear at 1117.4 and 1117.8 eV for ZnGa<sub>2</sub>O<sub>4</sub>-#1 and ZnGa<sub>2</sub>O<sub>4</sub>-#2 samples, respectively (**Figure 4-16 (a)**). For Zn2p<sub>3/2</sub> peaks, sample ZnGa<sub>2</sub>O<sub>4</sub>-#1 has a much lower intensity than sample ZnGa<sub>2</sub>O<sub>4</sub>-#2 cooled in O<sub>2</sub> (**Figure 4-16 (b)**), indicating an important Zn deficient nature in ZnGa<sub>2</sub>O<sub>4</sub>-#1. Regarding O1s peaks, the shoulder feature for the *n*-type ZnGa<sub>2</sub>O<sub>4</sub> thin film discussed in Section 4.2 (**Figure 4-6 (b)**) was not observed here (**Figure 4-16 (b)**).

Therefore, considering the inexistence of double absorption in optical transmittance, the conducting ZnGa<sub>2</sub>O<sub>4</sub>-#1 sample may have a different origin of conductivity from the *n*-type ZnGa<sub>2</sub>O<sub>4</sub> thin film discussed in Section 4.2.

Besides, Zn2*p*<sub>3/2</sub> and O1*s* peaks for both samples have non-symmetrical shapes, suggesting different contributions to atomic binding energies. For Zn2*p*<sub>3/2</sub> peak in sample ZnGa<sub>2</sub>O<sub>4</sub>-#2 that was cooled in O<sub>2</sub>, it evidences the existence of both tetrahedral and octahedral (Zn<sub>Ga</sub>) sites (Chikoidze et al., 2020a; Li et al., 2017), the inversion degree can be determined by deconvoluting the peaks which is under progress.

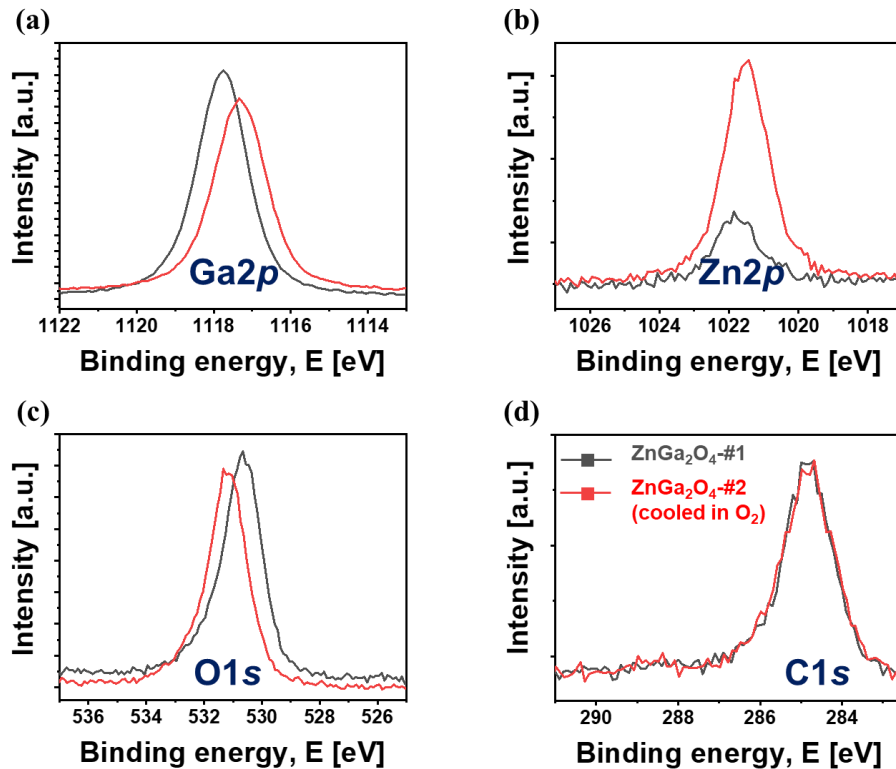


Figure 4-16. XPS peaks for (a) gallium (Ga2*p* - Ga2*p*<sub>3/2</sub>), (b) zinc (Zn2*p* - Zn2*p*<sub>3/2</sub>), (c) oxygen (O1*s*), (d) adventitious carbon contamination (C1*s*, calibration for C-C bonds at 284.8 eV) of both ZnGa<sub>2</sub>O<sub>4</sub>-#1 and ZnGa<sub>2</sub>O<sub>4</sub>-#2 samples.

Considering the experimental facts, we hypothesized that the electron conductivity may originate from the surface conduction. Surface conduction can be induced by several factors such as the surface-state (Zhang and Yates, 2012), and adsorption of metal adatoms (Wang et al., 2021), hydrogen (Kim et al., 2019), etc. The hydrogen (or hydroxyl -OH group) related surface conduction can be modified by the presence of oxygen (Qin et al., 2019). To confirm the hypothesis, XPS core levels of O1*s* and valence band tails should be properly treated.

For example, the contribution of surface adsorption can be analyzed by the deconvolution of O1s peaks (Horng et al., 2021). The surface electron accumulation induced band bending can be determined based on the valence band tails (Navarro-Quezada et al., 2015a; Swallow et al., 2019), the analysis on these samples is ongoing.

### 4.3.5 Photo-sensibility test

As presented in the state of the art, ZnGa<sub>2</sub>O<sub>4</sub> shows great potentiality in the applications of deep ultraviolet (DUV) photodetectors. Here, my objective was to demonstrate the photo-sensibility of our ZnGa<sub>2</sub>O<sub>4</sub>-#2 thin film that was cooled in O<sub>2</sub> and has a *p*-type semi-insulating nature. It is a preliminary investigation of the photo-sensibility of the ZnGa<sub>2</sub>O<sub>4</sub> layer without any specific metallization. The test probes are tungsten covered by silver paste. The test was carried out at room temperature, and an UV lamp of 190 – 400 nm was used for the illumination.

At room temperature, the ZnGa<sub>2</sub>O<sub>4</sub>-#2 thin film exhibits a tiny dark current. For example, at 10 V, the current under darkness was  $I_{\text{dark}} = 12.6$  pA, while it was increased to 2.7 nA under UV illumination (**Figure 4-17 (a)**). The ratio between photo-current ( $I_{\text{photo}}$ ) and dark current ( $I_{\text{dark}}$ ) is  $\sim 10^3$ , showing a great photo-sensibility. **Figure 4-17 (b)** shows the time-dependence of the photo-response measured under periodically on/off switched UV illumination with a bias of 5 V. Though the photo-sensibility is quite satisfactory for the thin film without any metallization, the response time was not quick enough. For example, the rise time ( $\tau_{\text{on}}$ ) was determined to be  $\sim 10$  s. However, a faster response speed can be expected after depositing metal contacts (e.g., Ti/Pt/Au) to fabricate a metal-semiconductor-metal (MSM) photodetector, and following an annealing process (Horng et al., 2021; Sood et al., 2021; Tsai et al., 2019).

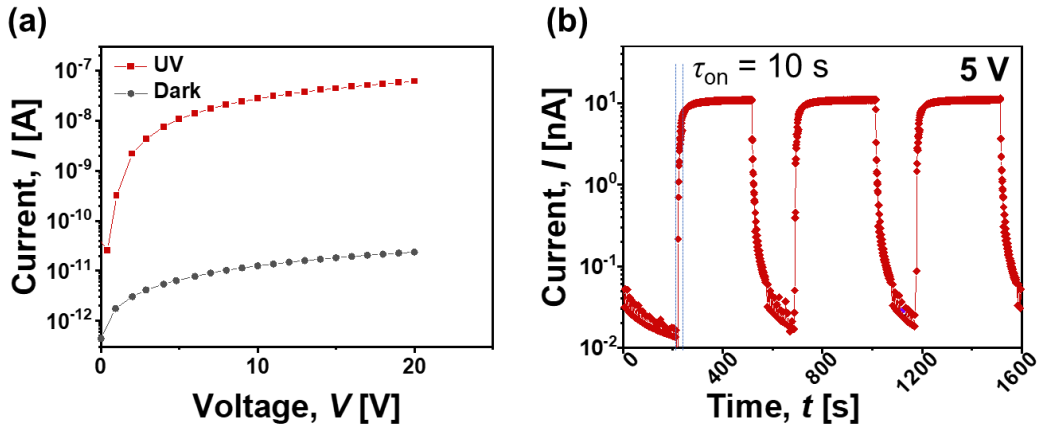


Figure 4-17. (a) room-temperature  $I$ - $V$  curves under dark and illumination. (b) Dynamic photo-response under UV lamp illumination at a 5 V bias of the ZnGa<sub>2</sub>O<sub>4</sub>-#2 thin film.

## 4.4 Estimation of the critical electric field for ZnGa<sub>2</sub>O<sub>4</sub>

The objective of this section is to estimate experimentally the critical electric field for the  $p$ -type ZnGa<sub>2</sub>O<sub>4</sub>. To the best of our knowledge, the critical electric field ( $E_{CR}$ ) of the ultra-wide band gap semiconductor ZnGa<sub>2</sub>O<sub>4</sub> has yet been reported. While it is a crucial parameter for one semiconductor material to evaluate its breakdown capability. Thus, analogously to  $p$ -type  $\beta$ -Ga<sub>2</sub>O<sub>3</sub> in the previous chapter, the breakdown voltage measurements were carried out, for the estimation of the critical electric field for the  $p$ -type ZnGa<sub>2</sub>O<sub>4</sub>. Recall again, the ZnGa<sub>2</sub>O<sub>4</sub> layers were simultaneously grown on insulating sapphire and conducting Si substrates. Electrical transport properties were studied for ZnGa<sub>2</sub>O<sub>4</sub> grown on insulating sapphire substrate, as the sapphire substrate is insulating up to high temperatures thus preventing parasitic leakage through the substrate. While a parallel capacitor was fabricated based on ZnGa<sub>2</sub>O<sub>4</sub>/Si, for the vertical breakdown voltage characterization.

### 4.4.1 Structural characterization for ZnGa<sub>2</sub>O<sub>4</sub>/Si

**Figure 4-18** shows the Cu-K $\alpha$  X-ray diffraction (XRD) spectra of ZnGa<sub>2</sub>O<sub>4</sub> thin films grown on Si(111) and Al<sub>2</sub>O<sub>3</sub>(0001). According to the PDF 28-1240 file, it is pure ZnGa<sub>2</sub>O<sub>4</sub> spinel without a secondary phase. Film on Si(111) is polycrystalline without any preferential texturation, similar to XRD pattern reported by Galazka *et al.* (Galazka *et al.*, 2019) for their melt-grown bulk ZnGa<sub>2</sub>O<sub>4</sub> spinel, milled in a randomly oriented powder. For films on Al<sub>2</sub>O<sub>3</sub>(0001) substrates, XRD peaks appearing at 18.6°, 37.6°, 57.6°, 79.7°, and 106.6°

correspond to the (111), (222), (333), (444), and (555) planes of the cubic spinel ZnGa<sub>2</sub>O<sub>4</sub>, respectively, as reported by previous literature ( Chikoidze et al., 2020; Yu et al., 2021).

ZnGa<sub>2</sub>O<sub>4</sub> thin films can be grown on sapphire substrates by MOCVD, PLD as mentioned above, with a preferential orientation along [111] of cubic spinel and equivalent direction for Al<sub>2</sub>O<sub>3</sub>(0001). Analogously, ZnGa<sub>2</sub>O<sub>4</sub> thin films have also been grown on Si substrates by atomic layer deposition (ALD) (Yu et al., 2021), PLD (Yi et al., 2003), and RF magnetron sputtering (W.-K. Wang et al., 2019b). A larger lattice mismatch between ZnGa<sub>2</sub>O<sub>4</sub> and Si(100) (which may also contain a native ultra-thin SiO<sub>2</sub> interlayer) results in a relatively weaker orientation of crystallite in the ZnGa<sub>2</sub>O<sub>4</sub> grown on Si substrate than that on sapphire (0001) (W.-K. Wang et al., 2019b). The full width at half maximum (FWHM) values were measured as 0.29° and 0.49° for ZnGa<sub>2</sub>O<sub>4</sub> (111) on sapphire and Si(100) substrates, respectively, indicating also a smaller size of crystallites in the case of Si(111) substrates with respect to Al<sub>2</sub>O<sub>3</sub>(0001) ones.

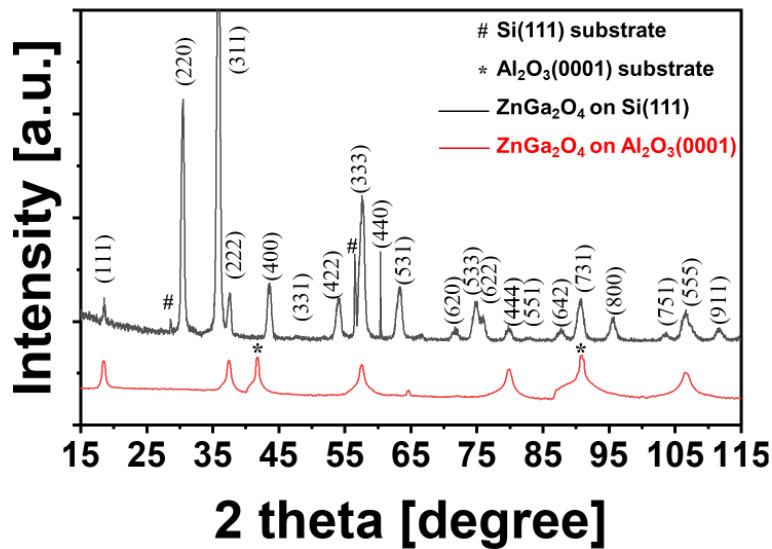


**Figure 4-18.** Cu- $K\alpha$  XRD spectra of ZnGa<sub>2</sub>O<sub>4</sub> thin film grown on Si(111) (black), and Al<sub>2</sub>O<sub>3</sub>(0001) (red). \* and # correspond respectively to Al<sub>2</sub>O<sub>3</sub>(0001) and Si(111) Bragg reflections.

#### 4.4.2 Electrical transport properties of ZnGa<sub>2</sub>O<sub>4</sub>//c-Al<sub>2</sub>O<sub>3</sub>

According to the kinetic ionization impact theory as discussed previously, to achieve large critical electric fields, it is mandatory to obtain a sample with low remote carrier concentration to reduce the onset of the impact ionization process. Here, we conducted the

electrical transport measurements to show the semi-insulating nature of the later. The Ohmic contacts were prepared with silver paint at the four corners of the sample. The resistivity and Hall effect measurements were performed, in a Van der Pauw configuration with perpendicularly to current applied magnetic fields varying from 0 to 1.6 T, in 550 to 850 K temperature range.

**Figure 4-19 (a)** shows a typical Ohmic current–voltage ( $I$ – $V$ ) behavior at different temperatures. The ohmic contact was made with silver paste painted at four corners of the sample in a square shape. The resistivity versus temperature for the spinel ZnGa<sub>2</sub>O<sub>4</sub> sample is shown in **Figure 4-19 (b)**. At 850 K, the resistivity was measured as  $1.9 \times 10^2 \Omega \cdot \text{cm}$ , and increased to  $5.3 \times 10^4 \Omega \cdot \text{cm}$  at 550 K. Hall voltage ( $V_H$ ) versus magnetic field (0 – 1.6 T) at 700 – 850 K for a ZnGa<sub>2</sub>O<sub>4</sub> sample is shown in **Figure 4-19 (c)**, the positive  $V_H$  increases with a perpendicularly applied magnetic field in a Van der Pauw configuration, which evidenced that our spinel ZnGa<sub>2</sub>O<sub>4</sub> thin film has  $p$ -type conductivity at elevated temperature. The temperature dependence for Hall hole concentration is shown in **Figure 4-19 (d)** for  $p$ -type ZnGa<sub>2</sub>O<sub>4</sub> film, the hole concentration was measured between  $8.8 \times 10^{11}$  and  $3.7 \times 10^{15} \text{ cm}^{-3}$  at 550 – 850 K. Although the hopping behavior starts to pronounce below 600 K, extrapolating the band-activated regime of the hole concentration versus temperature at the higher temperatures, the hole density is below  $10^{11} \text{ cm}^{-3}$  at 300 K, confirming the low level of  $p$ -type doping with the applied growth conditions. The mobility of the  $p$ -type ZnGa<sub>2</sub>O<sub>4</sub> thin film varies between 9 and  $15 \text{ cm}^2/(\text{V} \cdot \text{s})$ .

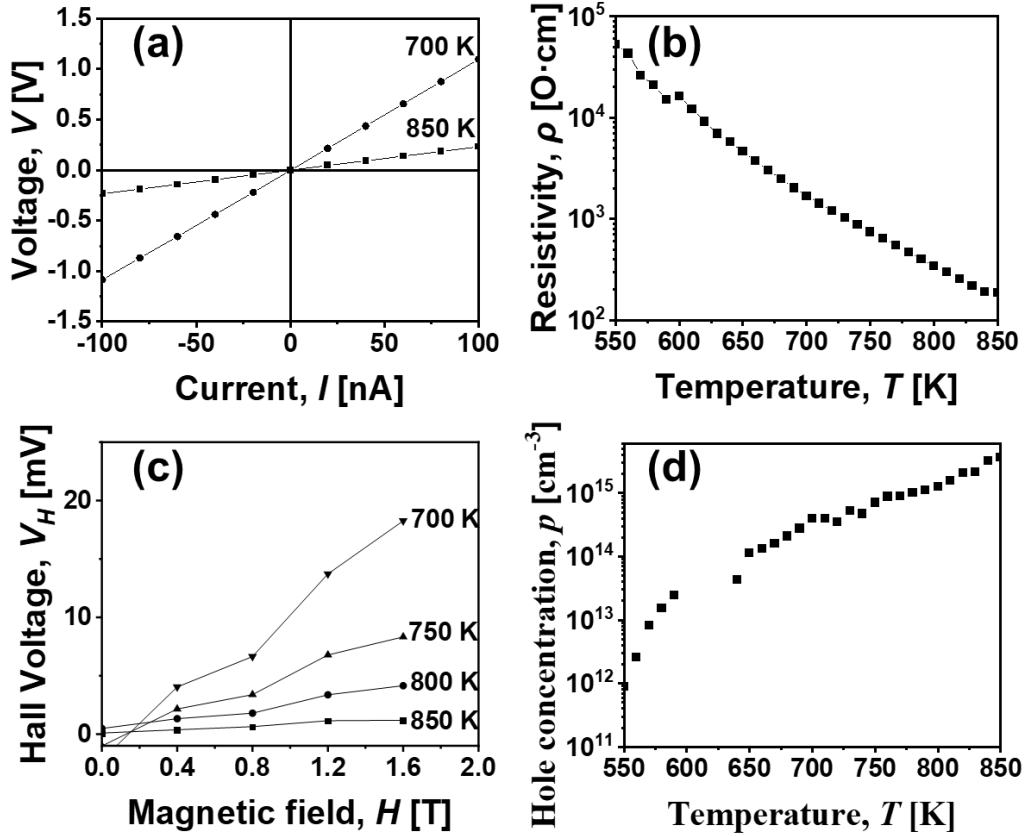


**Figure 4-19.** (a) Ohmic  $I$ - $V$  characteristics at 700K and 850 K (b) Resistivity versus temperature. (c) Hall voltage ( $V_H$ ) versus magnetic field at different temperatures (700 – 850 K). The Hall voltage is positive and increase with the increasing applied magnetic field, indicating the  $p$ -type conductivity in ZnGa<sub>2</sub>O<sub>4</sub> layer. (d) Temperature dependence for Hall free hole concentration for ZnGa<sub>2</sub>O<sub>4</sub> thin film.

#### 4.4.3 Critical electric field of ZnGa<sub>2</sub>O<sub>4</sub>

To determine the vertical critical electric field experimentally, vertical parallel plane capacitors has been fabricated by depositing Ti/Au contacts (with a size of  $170 \mu\text{m} \times 300 \mu\text{m}$ ) onto  $p$ -type ZnGa<sub>2</sub>O<sub>4</sub> grown onto the conducting Si thin films (**Figure 4-20 (a)**). **Figure 4-20 (b)** shows the scanning electron microscopy (SEM) cross-section image revealing that the thickness of the ZnGa<sub>2</sub>O<sub>4</sub>//Si is 600 nm. Negative bias has been applied on an isolated Ohmic contact with the grounded substrate to access the breakdown voltage. The vertical breakdown voltage  $V_{BR}$  was in the range of 270 to 350 V (**Figure 4-20 (c)**). It can be pointed out that a low leakage current below  $1 \text{ mA/mm}^2$  is observed all the way to the breakdown voltage. A thin SiO<sub>2</sub> layer (2 nm) at the interface ZnGa<sub>2</sub>O<sub>4</sub>//Si can often be seen (W.-K. Wang et al., 2019b) after the growth. To exclude the influence of the SiO<sub>2</sub> layer, a bare Si substrate

with a native SiO<sub>2</sub> (2 – 3 nm thick layer) has been characterized as well. The vertical breakdown voltage of around 10 V (Chikoidze et al., 2020c) is considered to produce a negligible contribution to the experimentally measured  $V_{BR}$  of  $p$ -type ZnGa<sub>2</sub>O<sub>4</sub>//Si structure. Taking the experimentally determined 600 nm thickness for the ZnGa<sub>2</sub>O<sub>4</sub> layer and extracting bare Si substrate related  $V_{BR}$  into account, the average vertical critical electric field across the film can be as high as  $E_{CR} = 5.3$  MV/cm, which is already significantly larger than the one from SiC and (single crystal) GaN.

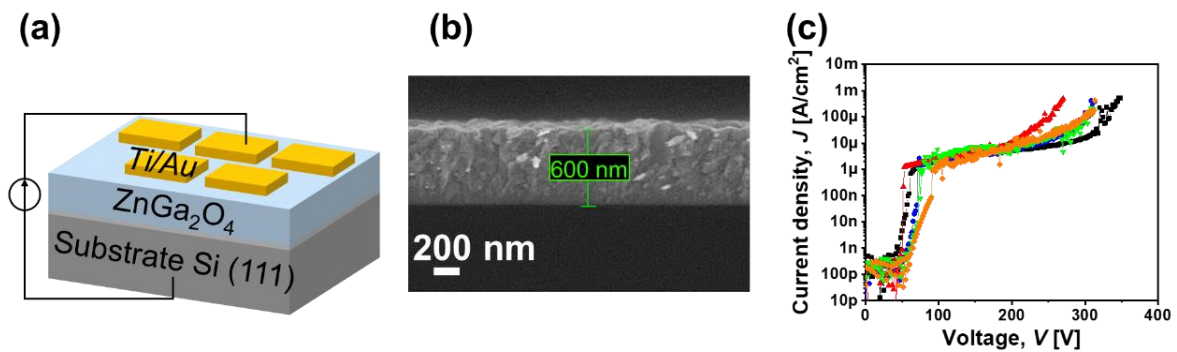


**Figure 4-20.** (a) Sketch of the vertical heterojunction structure with Ti/Au metal contacts. (b) SEM cross-section image of ZnGa<sub>2</sub>O<sub>4</sub> polycrystalline film deposited on Si(111). The estimated thickness of the film is 600 nm. (c) Experimental  $I$ - $V$  curves of vertical breakdown voltage measurements through the ZnGa<sub>2</sub>O<sub>4</sub>//Si structure, indicating a breakdown voltage up to 350 V at room temperature.

## 4.5 Summary

Spinel ZnGa<sub>2</sub>O<sub>4</sub> has emerged recently, the study on the electrical properties and conduction mechanism of this ultra-wide band gap semiconductor is still very limited. However, a few general rules for getting  $n$ -type or  $p$ -type can still be summarized. Based on the first principles calculations, Sabino *et al.* (Sabino et al., 2022) suggested that the  $n$ -type conductivity is very difficult to be achieved under oxygen-rich condition, which agrees well with our findings in Section 4.3. While a semi-insulating  $p$ -type nature can be expected with a near stoichiometric growth (Chikoidze et al., 2020a). Theoretically, to get  $p$ -type conductivity, a Zn-rich condition should be attained (Paudel et al., 2011b; Sabino et al., 2022; Shi et al., 2014). Besides, the important influence of oxygen has been proposed (Horng et al., 2017; Lee et al., 2001; Omata et al., 1994; Yan et al., 2005), while a detailed investigation of the mechanism is still required. The results in this chapter can be summarized as follow:

(i) A higher O<sub>2</sub> flow (tuning from 600 to 1200 sccm) can enhance the Zn incorporation in  $\beta$ -Ga<sub>2</sub>O<sub>3</sub> during MOCVD growth. With the [Zn] > 6.85 at. %, the spinel ZnGa<sub>2</sub>O<sub>4</sub> can form on *c*-sapphire substrates. When [Zn] reaches 14 at. %, monoclinic  $\beta$ -Ga<sub>2</sub>O<sub>3</sub> transform to cubic spinel ZnGa<sub>2</sub>O<sub>4</sub> completely.

(ii) The native bipolar conductivity of spinel ZnGa<sub>2</sub>O<sub>4</sub> has been shown. The high electron conductivity was attributed to the hopping conduction mechanism of Zn<sub>i</sub> in a “self-impurity” band created by Zn<sub>i</sub>-V<sub>O</sub> located at the mid-gap.

(iii) The influence of O<sub>2</sub> content on electrical properties was demonstrated, the ZnGa<sub>2</sub>O<sub>4</sub> thin film can be transformed from conducting *n*-type to semi-insulating *p*-type (at least on the surface) with a higher O<sub>2</sub> flow during the growth and cooled in O<sub>2</sub>. While the conduction mechanism and the origin of the conductivity are still under discovery.

(iv) The breakdown voltage measurements were carried out for parallel plane capacitors based on the *p*-ZnGa<sub>2</sub>O<sub>4</sub>//Si structure. The critical electric field was estimated at 5.3 MV/cm.

## 5. Electrical Contacts to $p$ -type $\beta$ -Ga<sub>2</sub>O<sub>3</sub>

This chapter is dedicated to the preliminary results of the metal electrical contact study for  $p$ -type  $\beta$ -Ga<sub>2</sub>O<sub>3</sub>. My objective was to establish a protocol for electrical contact preparation by photolithography, followed by  $I$ - $V$  characterization tests. As metals for investigation, Ti/Pt/Au, Pt, and Ag were selected. I will present the state of the art related to Ohmic contacts mainly for  $n$ -type  $\beta$ -Ga<sub>2</sub>O<sub>3</sub> in Section 5.1. Section 5.2 focuses on the experimental methods I have used and the experimental results/discussion are presented in Section 5.3.

### 5.1 State of the art

Many promising  $\beta$ -Ga<sub>2</sub>O<sub>3</sub> based electronic and opto-electronic devices have been reported last several years, including Schottky barrier diode (SBD) (Hu et al., 2022; Li et al., 2021), field effect transistors (FET) (Higashiwaki et al., 2012; Lv et al., 2020; Zheng et al., 2022), photodetectors (Oshima et al., 2007; Wu et al., 2022). The performance of SBD is characterized by breakdown voltage ( $V_{BR}$ ) and on-resistance ( $R_{on}$ ) that are dependent on the Schottky contacts, while a good Ohmic contact is necessary requirement for metal oxide semiconductor field effect transistor (MOSFET). An Ohmic contact to  $n$ -type semiconductors can be achieved when the Schottky barrier height ( $\Phi_B$ ) is negative,  $\Phi_B$  can be described by the Schottky–Mott rule (Mott, 1938):

$$\Phi_B = \Phi_M - \chi_S$$

Where  $\Phi_M$  and  $\chi_S$  being metal work function and semiconductor electron affinity, respectively. The electron affinity of bulk Ga<sub>2</sub>O<sub>3</sub> single crystal with electron concentration of  $2 - 6 \times 10^{17} \text{ cm}^{-3}$  grown by Czochralski method (Galazka et al., 2010) was estimated as  $4.00 \pm 0.05 \text{ eV}$  (Mohamed et al., 2012). Therefore, in the ideal case, an Ohmic contact to  $\beta$ -Ga<sub>2</sub>O<sub>3</sub> can be formed by choosing the metals with work function of lower than  $\sim 4 \text{ eV}$ . However,  $\Phi_B$  established at the metal-Ga<sub>2</sub>O<sub>3</sub> interface can be influenced by the Fermi level pinning originating from (i) metal-induced gap states (MIGS) (Bhattacharyya et al., 2020; Monch, 1990), (ii) the presence of surface states (Lingaparthi et al., 2020), (iii) adsorbates during the preparation process, or other factors. For example, Lovejoy *et al.* (Lovejoy et al., 2012) demonstrated the negatively charged surface defects of as-grown  $n$ -type Ga<sub>2</sub>O<sub>3</sub> make

the band bend upwards by X-ray photoemission spectroscopy (XPS), which complicates the formation of Ohmic contact (Müller et al., 2015; Pearton et al., 2018). However, as Swallow *et al.* (Swallow et al., 2019) reported, suggested by XPS measurements, the hydrogen terminated surface of bulk (-201)  $\beta$ -Ga<sub>2</sub>O<sub>3</sub> leads to electron accumulation and downward band bending. According to the authors, this difference is attributed either to the use of the wrong bandgap energy and/or to the underestimation of the surface valence band maximum (VBM) with respect to the Fermi level. A post-annealing up to 800 °C can remove the hydrogen from the surface, resulting in surface electron depletion and upward band bending (Navarro-Quezada et al., 2015b; Swallow et al., 2019).

As a result, it is often found that  $\Phi_B$  is either independent or weakly dependent on  $\Phi_M$  (Huan et al., 2018; Xue et al., 2018). Indeed, Yao *et al.* (Yao et al., 2017) investigated nine contact metals with low-to-moderate work function (Ti, In, Ag, Sn, W, Mo, Sc, Zn, and Zr) to Sn doped  $\beta$ -Ga<sub>2</sub>O<sub>3</sub> (dopant level at  $5 \times 10^{18} \text{ cm}^{-3}$ ), only Ti contact with Au capping layer and In contact after annealing at 600 °C are Ohmic, though the latter one has poor morphology. The current-voltage characterization of all other metal contacts to  $\beta$ -Ga<sub>2</sub>O<sub>3</sub> did not display good linearity even after annealing at temperatures up to 600 – 800 °C.

Though the difficulties mentioned above, there are several approaches to achieving the Ohmic contact to  $\beta$ -Ga<sub>2</sub>O<sub>3</sub>. (i) the Schottky–Mott relation can be used as a guide for preliminary selection of metals with sufficiently low work functions. (ii) Heavily doping can facilitate the tunneling effect to reduce contact resistance, the commonly used approach is Si-implantation (Higashiwaki et al., 2013; Sasaki et al., 2013; Wong et al., 2016). (iii) surface treatment such as reactive-ion-etching (RIE) (Higashiwaki et al., 2012), Ar plasma bombardment (H. Zhou et al., 2017) have been performed to reduce the contact resistance, and the introduction of surface defects such as oxygen vacancies has been considered as the mechanism. (iv) post-metallization annealing has been demonstrated to improve the Ohmic contact effectively.

For *n*-type  $\beta$ -Ga<sub>2</sub>O<sub>3</sub>, Ti/Au is a good candidate of Ohmic contact, which has also been widely used for the time being (Higashiwaki et al., 2013; Lee and Peterson, 2019a; Liu et al., 2019; Lyle et al., 2021; Sasaki et al., 2013; Wong et al., 2016). The choice of Ti is based on its low work functions, while Au is a capping layer to protect Ti from oxidation. For Si-implanted  $\beta$ -Ga<sub>2</sub>O<sub>3</sub> with a dopant concentration of  $\sim 5 \times 10^{19} \text{ cm}^{-3}$ , the specific contact resistance ( $\rho_c$ ) of the Ohmic contact formed by Ti/Au can be as low as  $\sim 10^{-6} \Omega \cdot \text{cm}^2$  after a

rapid-thermal-annealing at 450 °C or 470 °C under N<sub>2</sub> (Higashiwaki et al., 2013; Sasaki et al., 2013). Recently, Lee *et al.* (Lee et al., 2022b, 2022a; Lee and Peterson, 2020, 2019a, 2019b) investigated intensively Ti/Au contact to  $\beta$ -Ga<sub>2</sub>O<sub>3</sub>. It was shown that Ti can attract oxygen from  $\beta$ -Ga<sub>2</sub>O<sub>3</sub> forming a  $n$ -type Ti-TiO<sub>x</sub> layer to reduce the barrier height during a rapid thermal annealing (RTA) process (1 min at 470 °C) (Lee and Peterson, 2019a), while the contact can be degraded following a higher annealing temperature (e.g., 520 °C (Lee et al., 2022b)) or a longer annealing period (e.g., 10 or 15 mins (Lee and Peterson, 2019b)), due to the in-diffusion of Au into the Ti-TiO<sub>x</sub> layer and out-diffusion of Ga from  $\beta$ -Ga<sub>2</sub>O<sub>3</sub>. Additionally, the effect of anisotropy on Ti/Au contact was demonstrated (Lee et al., 2022a), Ti/Au metallization on (100) and (010) oriented  $\beta$ -Ga<sub>2</sub>O<sub>3</sub> followed a RTA at 470 °C for 1 min showed specific contact resistivity of  $5.1 \times 10^{-5} \Omega \cdot \text{cm}^2$  and  $3.3 \times 10^{-3} \Omega \cdot \text{cm}^2$ , respectively. Besides, a few groups has demonstrated  $\beta$ -Ga<sub>2</sub>O<sub>3</sub> based photodetector (Feng et al., 2014) and field effect transistor (FET) (Ma and Yoo, 2019) by using Cr/Au to form Ohmic contact. Mg/Au metal contact has also been demonstrated to form Ohmic contact to slightly Sn doped  $\beta$ -Ga<sub>2</sub>O<sub>3</sub> ( $n = 4 \times 10^{17} \text{ cm}^{-3}$ ), after a post-annealing at 500 °C for 2 minutes under Ar gas, the  $\rho_c$  was estimated as  $2.1 \times 10^{-5} \Omega \cdot \text{cm}^2$  (J. Shi et al., 2019). Intermediate semiconductor layers such as Al-doped ZnO (AZO) (P. H. Carey et al., 2017a), Indium Tin Oxide (ITO) (P. H. Carey et al., 2017b; Oshima et al., 2016) have been inserted between Ga<sub>2</sub>O<sub>3</sub> and metal. As shown in **Figure 5-1**, the purpose is to facilitate electron transport by reducing the barrier height, the conduction band offsets between AZO, ITO and Ga<sub>2</sub>O<sub>3</sub> are 0.79 eV, and 0.32 eV, respectively. The  $\rho_c$  were determined as  $2.82 \times 10^{-5}$ , and  $6.3 \times 10^{-5} \Omega \cdot \text{cm}^2$  for AZO/Ti/Au and ITO/Ti/Au stacks to  $\beta$ -Ga<sub>2</sub>O<sub>3</sub>, respectively.

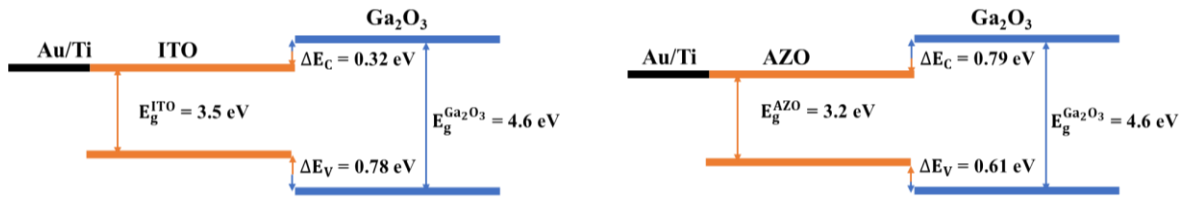


Figure 5-1. Schematic of band diagram for (a) Au/Ti/ITO and (b) Au/Ti/AZO on GaO.

However, the study on  $p$ -type  $\beta$ -Ga<sub>2</sub>O<sub>3</sub> is quite challenging. Indeed, for  $p$ -type, going back to Schottky-Mott rule, the expression of Schottky barrier becomes  $\Phi_B = \chi_S + E_g - \Phi_M$ , with  $E_g$  the energy band gap. So metal candidates might need to have  $\Phi_M > \chi_S + E_g$ . Published studies for  $p$ -type  $\beta$ -Ga<sub>2</sub>O<sub>3</sub> are limited. Au (Bai et al., 2022) and In (Liu et al.,

2022) were used to form Ohmic contact to *p*-type  $\beta$ -Ga<sub>2</sub>O<sub>3</sub>. It is clear that further investigation is required.

## 5.2 Experimental methods

### 5.2.1 Circular transmission line model (CTLM) method

High-quality Ohmic contacts between metal and semiconductors with a low contact resistance ( $R_C$ ) play a crucial role in reducing the operating voltage of high-power semiconductor devices. For usual thin film resistance measurement, the total resistance measured is composed of the electrical contact resistance ( $R_{C1}$ ,  $R_{C2}$ ), metal resistance ( $R_{M1}$ ,  $R_{M2}$ ) and the sheet resistance ( $R_S$ ):  $R_{tot} = R_{M1} + R_{C1} + R_S + R_{C2} + R_{M2}$  (**Figure 5-2**), where the metal resistances  $R_{M1}$  and  $R_{M2}$  can be neglected with respect to other terms for semiconductors.

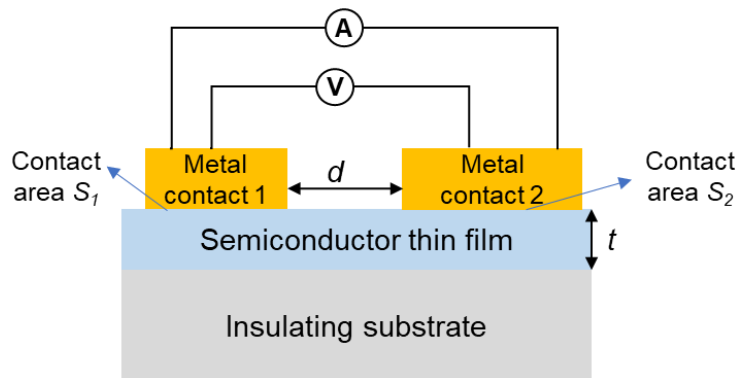


Figure 5-2. Schematic cross-sectional illustration of equivalent circuit during the current-voltage characterization.

For a given interface between two materials, the intrinsic quantity is the specific contact resistance  $\rho_C$ , defined as  $\rho_C = R_C \times S$ , where  $S$  is the contact area. In the case of equal dimensions between metal contact patterns,  $R_{tot} = 2R_C + R_S$ . When  $S_1 \gg S_2$ , for a same  $\rho_C$  of the metal-semiconductor contact, the contribution of  $R_{C1}$  can be neglected compared to  $R_{C2}$ . Consequently, a way to reduce practically the contact resistance in technological device, is to increase the contact area. Therefore, it is important to determine a proper method to examine the electrical contact resistance, which allows to further improve the electrical contact performance. The contact resistance  $R_C$  is usually evaluated by  $\rho_C/S$  (Chang et al.,

1971), where  $S$  is the contact area, and  $\rho_C$  being the specific contact resistance cannot be measured directly and must be inferred from a measurement on the same Ohmic contact structure as the device, but with a specially prepared test pattern. For testing the  $I$ - $V$  characteristic of the metal-semiconductor Ohmic contact, several transmission line measurement (TLM) models have been developed. The original rectangular TLM layout first proposed by Shockley in 1964 (Shockley et al., 1964) provided a possibility to determine the  $\rho_C$  for ohmic contacts. This method defines an array of rectangle patterns of metal contacts with the same dimension ( $Z \times w$ ) but different inter-distance ( $d_i$ ) (**Figure 5-3 (a)**). The total resistance can then be expressed as:

$$R_{tot} = \frac{R_S}{Z} d_i + 2R_C \quad (5 - 1)$$

Therefore, the sheet resistance of the sample is deduced from the slope  $\frac{R_S}{Z}$  of the  $R_{tot}$  vs. gap spacing  $d_i$  plot (**Figure 5-3 (c)**). It was demonstrated that the majority of the voltage drop underneath the metal contact takes place within the length of  $\sqrt{\frac{\rho_C}{R_S}}$ , which is defined as the transfer length  $L_T$  (**Figure 5-3 (b)**). The specific contact resistance can be then determined:

$$\rho_C = L_T^2 \cdot R_S = \frac{(Z \cdot \text{intercept}(y))^2}{4 \cdot \text{slope}} \quad (5 - 2)$$

However, this TLM method requires a mesa etch step, which is not only technically difficult but also affects measurement precision (Parsons et al., 1994; Reeves and Harrison, 1982). A concentric TLM model proposed by Reeves (Reeves, 1980) could efficiently avoid the requirement of mesa etching and improves precision. However, the complex calculation procedure and imprecise measurement of contact end resistance will result in a large inaccuracy in the extraction of the specific contact resistance (Xu et al., 2006). At the time being, the circular transmission line measurement (CTLTM) model is commonly used, it consists of an inner metal contact and an outer metal contact that are separated by a metal-free ring (Goyal et al., 2016; Lee et al., 2022b; Marlow and Das, 1982; Sheoran et al., 2022) (**Figure 5-4**). Employing this sophisticated model, the value of  $\rho_C$  by deriving the sheet resistivity ( $R_S$ ) and transfer length ( $L_T$ ) can be computed from the correlation between the total resistance and the pattern size.

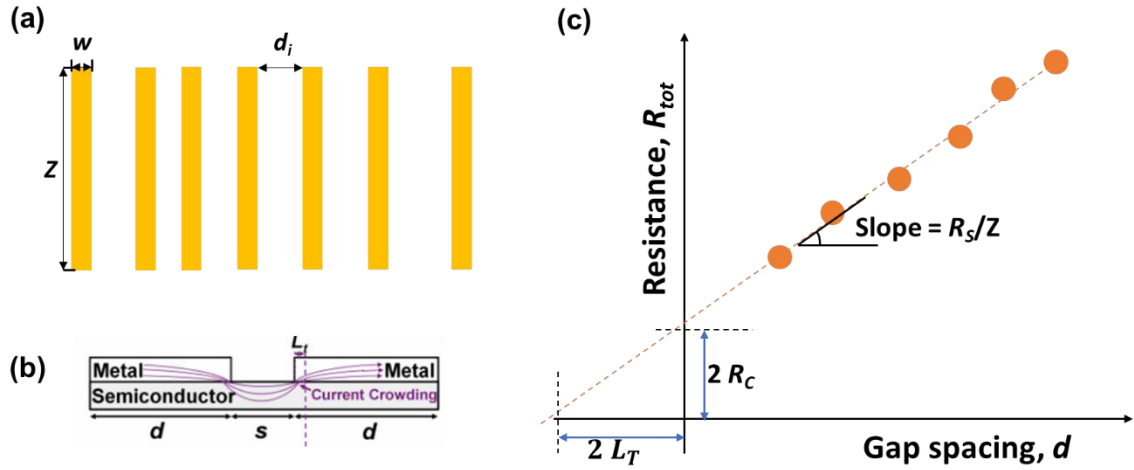


Figure 5-3. Schematic illustration of the transfer length method (a) patterns, (b) schema to show the transfer length (Hao Yu et al., 2014), (c) contact resistance and sheet resistance determination by  $R_{tot}$  vs.  $d_i$  plot.

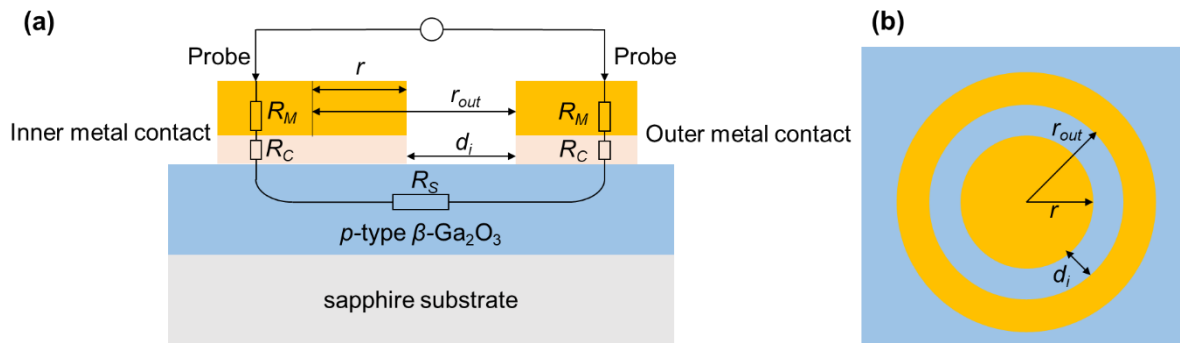


Figure 5-4. (a) Schematic cross-sectional diagram of equivalent circuit in the CTLM measurement technique. The metallization is formed on the inner pad and the areas outside the rings. Where  $r$  is the radius of the inner circle (inner metal pad),  $r_{out}$  is the outer circle radii,  $d_i$  is the gap spacing between inner and the outer circles. Each group of CTLM pattern includes 6 rings with constant inner circle radius ( $r$ ) but different outer circle radii ( $r_{out}$ ). (b) Corresponding schematic top-view of electrodes in a single CTLM pattern.

## 5.2.2 Photolithography and metal deposition process

Photolithography is a process used to transfer desired patterns onto the sample using UV light. Different photoresists and different materials have different properties that can affect the effectiveness of the photolithography process. Therefore, the spin-coating and photolithography parameters, such as maximum spin coating speed and time, exposure time,

and developing time need to be optimized to ensure the desired pattern is accurately transferred onto the material surface. For example, a thicker photoresist layer can be expected with a higher maximum spin coating speed, then, the exposure and development time should be increased to efficiently remove the exposed photoresist.

Since it is the first time to deposit metal contacts on  $\beta$ -Ga<sub>2</sub>O<sub>3</sub> through the photolithography process in GEMaC, I started with the adjustment of lithography parameters. The patterns were designed in the software Klayout. The photolithography process steps are as follow:

(i) Cleaning: The substrate surface is cleaned to remove any contaminants or particles that could interfere with the subsequent steps. The samples were cleaned by sonication in acetone and then 2-propanol for 10 min each, followed by 1 min rinsing in deionized (DI) water and blowing dry with ultra-high purity N<sub>2</sub> gas.

(ii) Spin coating: A thin layer of photoresist is applied to the substrate by spinning it at a high speed. AZ1512HS and AR-P 5350 were used as photoresists deposited by the spin coater POLOS SPIN150i (**Figure 5-5 (a)**).

(iii) Soft baking: Bakery at 100 °C for 1 min for sample deposited photoresist AZ1512HS, and 2 mins for sample deposited photoresist AR-P 5350, to remove the moisture and harden the photoresist.

(iv) Alignment: The substrate is aligned with a mask containing the desired pattern, which is positioned between the substrate and a light source using Smart Print (**Figure 5-5 (b)**). This equipment is compatible with the g-line (light sensitivity at ~ 435 nm) photoresists.

(v) UV exposure: The substrate is exposed to UV light with the objective of  $\times 1$ , through the mask designed (e.g., **Figure 5-5 (c)**). The light power density using this objective is fixed at 10.2 mW/cm<sup>2</sup>.

(vi) Development: The substrate is immersed in a developer solution that removes the soluble regions of the photoresist, leaving behind the desired pattern. The corresponding developer for AZ1512HS is the AZ developer solution, for AR-P 5350 is a mixed AR 300-35 solution and DI water (1:2). After the development, the samples were immersed in DI water to stop the reactions.

(vii) Post-baking: The remaining photoresist can be hardened by post-baking at a high temperature, making it resistant to subsequent etching or deposition processes. However, this step is not required for the used photoresists.

(vii) Metal deposition: The patterned substrate is deposited onto the patterned regions by RF-sputtering machine Leybold Z400, carried out by Dr. Bruno Bérini. Three kinds of metal contacts were selected:

(vii-1) Ag (200 nm). It was selected systematically given that the Ag paste was used to make Ohmic contact to *p*-type  $\beta$ -Ga<sub>2</sub>O<sub>3</sub> thin films for electrical measurements, for the determination of the specific contact resistance.

(vii-2) Multilayer of Ti (50 nm)/Pt (50 nm)/Au (200 nm), it was selected systematically since it forms Ohmic contact to *n*-type  $\beta$ -Ga<sub>2</sub>O<sub>3</sub>, *p*-type GaN (Zhou et al., 2000), and boron-doped *p*-type diamond (Chen et al., 2004; Hoff et al., 1996). The additional layer of Pt was used to prevent the interdiffusion of Ti and Au, and finally of Au in Ga<sub>2</sub>O<sub>3</sub> film, at elevated temperatures (up to 500 °C), (Hoff et al., 1996) which are usually our resistance measurement conditions.

(vii-3) Pt (200 nm). Based on Schottky–Mott relation, it is easier to form Ohmic contact to *p*-type semiconductor using a metal with higher work function. According to the CRC Handbook of Chemistry and Physics (Haynes, 2014), Pt has the highest work function ( $\Phi_M = 5.6 - 6$  eV) among the metals.

(viii) Lift-off: lift-off process was carried out by immersing the metal coated sample into acetone solution.

(ix) Post-annealing: The metal contacts were then annealed in nitrogen for 30 min at 500 °C as suggested (Chen et al., 2004; Hoff et al., 1996).

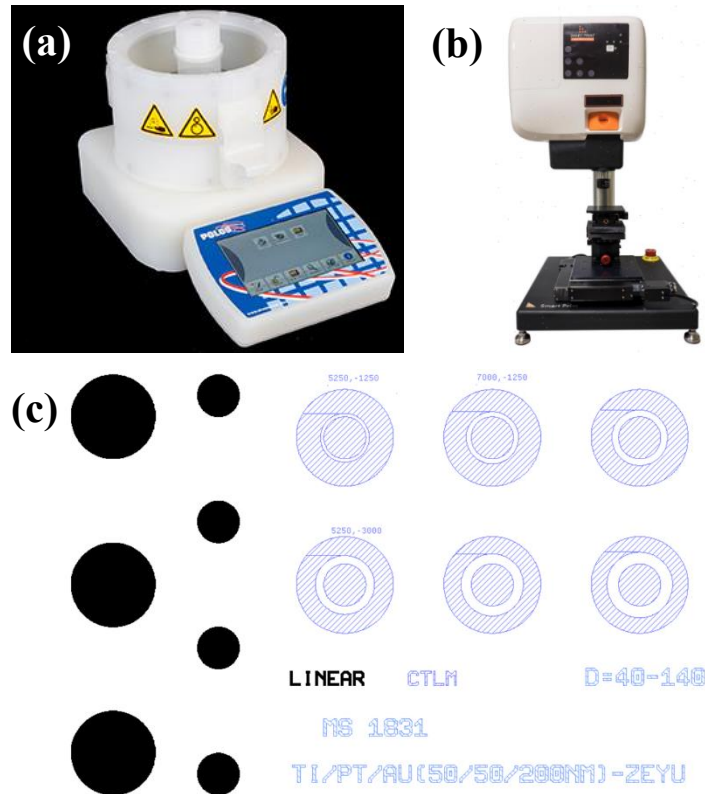


Figure 5-5. (a) spin coater “POLOS SPIN150i” in GEMaC. (b) UV-exposure equipment “Smart Print” in GEMaC. (c) An example of designed pattern for lithography process. Right part is circular transmission line model (CTLM) patterns for the contact resistance study, the diameter of inner circular is 0.25 mm, the ring between two circulars are 40, 60, 80, 100, 120, 140  $\mu\text{m}$ , respectively.

The maximum spin coating speed, exposure time, and development time parameters were adjusted in several trails (numbered from 1 to 10) to get the optimal pattern dimension, which are summarized in **Table 5-1**. Chronologically, the g-line sensitive photoresist AZ 1512 HS that was recognized for a high resist contrast (high development rate and minimized dark erosion), was first used. The parameters first used was the trial n<sup>o</sup>1. After the metal deposition and lift-off process, the microscopy image (**Figure 5-6 (a)**) shows that the metal could not be efficiently removed after the lift-off, suggesting that either the photoresist layer was too thick, or the exposure/development time was insufficient. The resist film thickness with the maximum spin coating speed of 4000 tr/min was approximately 1.2  $\mu\text{m}$ , and can be decreased to 1.0  $\mu\text{m}$  at 6000 tr/min. The exposure and development times were also gradually extended. However, the desired pattern was not obtained though the parameters were doubled (**Figure 5-6 (b)**). Except for the uncleared part in the gap, the edge of the outer ring is over-cleaned. The photoresist AR-P 5350 that has a high resolution (0.5  $\mu\text{m}$ ) and good

adhesion properties was then used. Several microscopy images are shown in **Figure 5-6 (c) – (f)** as examples, with the corresponding designed gap spacings. Trails n° 5-7 with the maximum spin coating speed at 4000 tr/min are shown in **Figure 5-6 (c) – (e)**, respectively, the photoresist was not removed as designed, which was attributed to the thick resist later (~1  $\mu$ m). A zoom view of the edges of the gap ring is shown in **Figure 5-6 (e)**, where the left resist is visible. The spin coating speed was further increased to 4500 tr/min, and the trail n°9 was selected as the optimal parameters' combination and shown in **Figure 5-6 (f)**.

Table 5-1. Adjustment of parameters for lithography process.

Photoresist	Trial n°	Max. spin coating speed [tr/min]	Exposure time [s]	Development time [s]
AZ 1512 HS	1	4000	20	10
	2	6000	20	10
	3	6000	40	10
	4	6000	40	30
AR-P 5350	5	4000	20	10
	6	4000	20	8
	7	4000	30	10
	8	4500	30	10
	9	4500	30	8
	10	4500	20	8

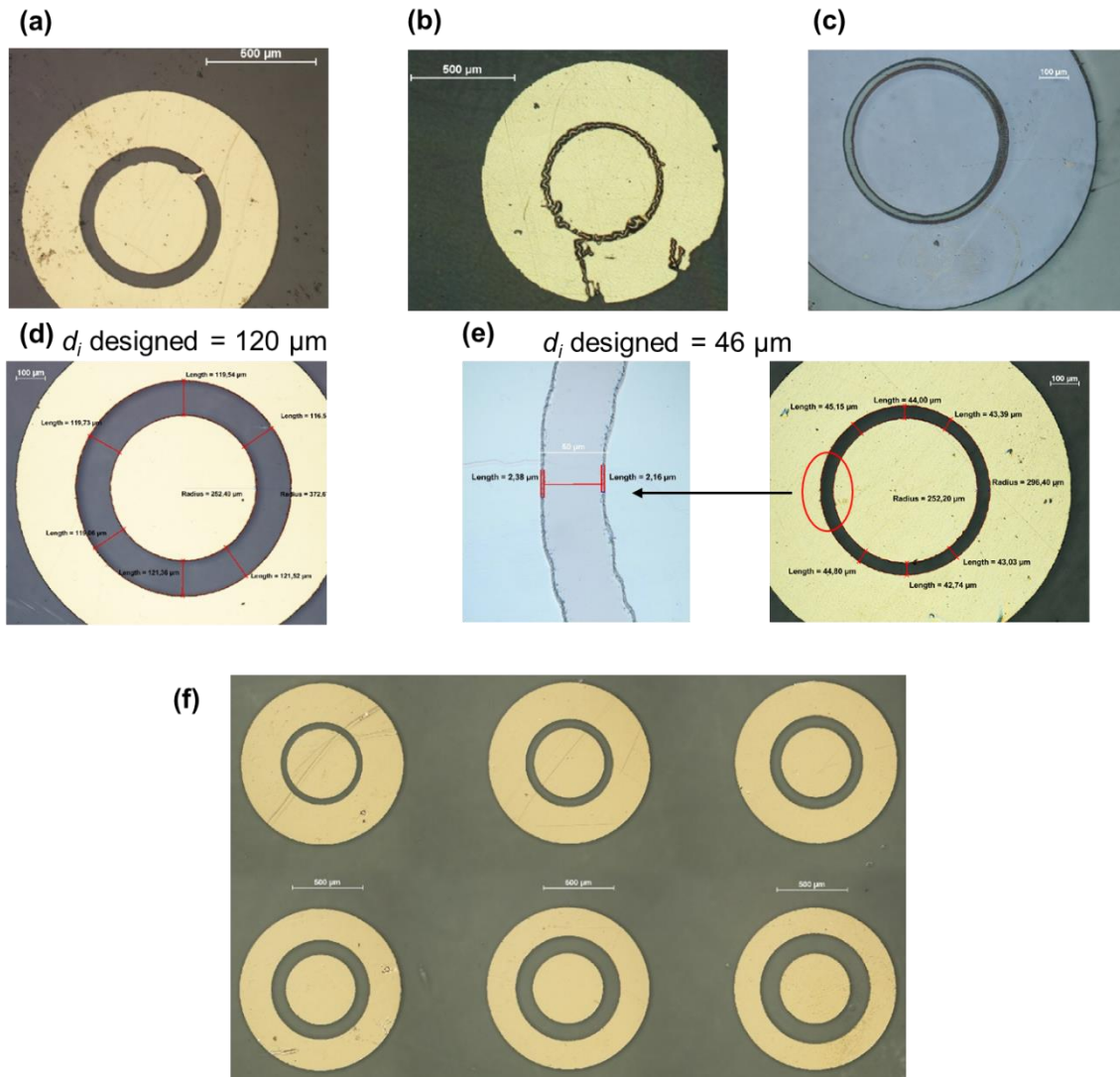


Figure 5-6. Microscope image of the CTLM patterns for trail (a) n°1, (b) n°4, (c) n°5 (after development, before metal deposition), (d) n°6 (designed gap  $d_i = 120 \mu\text{m}$ ), (e) n°7 (designed gap  $d_i = 46 \mu\text{m}$ ) with the enlarged view of the gap, (f) n°9. The lithography parameters for each trail are summarized in the **Table 5-2**. For figure (g), due to the limit of magnification, the whole group of patterns could not be captured together, each concentric circle was captured separately with the same magnification and then merged.

### 5.2.3 Calculation and measurement methods

The measurement accuracy of the specific contact resistance  $R_C$  is generally susceptible to three factors:

(i) Electrical measurement technique. More specifically, the four-probe technique can effectively reduce the series resistance resulting from the probes, the contact between the

probes and the metal pad in the two-probe measurement. I used the two-probe measurement for the manipulation convenience (tiny patterns without micro-probe station equipment), and the series resistance resulting from the probes is considered negligible for the highly resistive *p*-type  $\beta$ -Ga<sub>2</sub>O<sub>3</sub>. The resistance of an Ohmic contact is typically determined by the  $I$ - $V$  measurement. If an  $I$ - $V$  characteristic demonstrates a unique linear relationship, then the total resistance can be calculated using the slope of the straight line. In this work, the voltage was swept through  $n$  steps, the real voltage  $U_k$  applied and the corresponding current  $I_k$  were then measured. The statistical total resistance  $R_{tot}$  and its uncertainty can be expressed as:

$$R_{tot} = R_0 + \Delta R = \frac{\sum_k^n \frac{U_k}{I_k}}{n} + \sqrt{\frac{\sum_k^n \left(\frac{U_k}{I_k}\right)^2}{n}} \quad (5 - 3)$$

Here, the contact resistances were measured at different temperatures using a KEITHLEY 4200-SCS (Semiconductor Characterization System) with a measurement cell (Linkam, UK) with tungsten contact probes.

(ii) Contact area correction. The contact areas are typically expected to be equivalent to the size of the pattern designed by the photolithography mask. In this work, one group of designed CTLM pattern consists of 6 rings with a constant inner circle radius ( $r$ ) of 250  $\mu\text{m}$  and varying outer circle radii ( $r_{out}$ ) ranging from 40  $\mu\text{m}$  to 140  $\mu\text{m}$ . In reality, the contact areas are impacted by the diffraction of ultraviolet light during the exposure, the actual radius will thus be influenced during the lift-off or metal deposition process. Thus, the contact areas should be calculated by measuring their actual radii. the inner circle radius ( $r$ ), outer circle radii ( $r_{out}$ ), and their uncertainties were determined by microscope (Nikon L-UEPI) equipped with a measurement system "NIS Elements". The average of the six values obtained by six measurements with  $\sim 60^\circ$  between each measurement was calculated to estimate the  $d_i$  of the contact patterns:

$$d_i = \frac{1}{6} \sum_k^6 d_k = \sum_k^6 (r_{out_k} - r_k) \quad (5 - 4)$$

Therefore, the specific contact resistance  $\rho_C$  and the sheet resistance  $R_C$  can be estimated by plotting the total resistance  $R_{tot}$  versus gap spacing  $d$ .

The designed and measured dimensions of the CTLM patterns for Ti/Pt/Au and Pt contacts are summarized in **Table 5-2**. The designed patterns were successfully transferred

to  $\beta$ -Ga<sub>2</sub>O<sub>3</sub> thin film using the adjusted photolithography parameters, for Ti/Pt/Au pad in particular. The relative error ( $\frac{|d_{i,measured} - d_{i,designed}|}{d_{i,designed}}$ ) is generally less than 3%. The error [%] becomes smaller with the increasing ring size, which may be due to the precision limit of the lithography equipment (the pixel size for  $\times 1$  objective is 7.12  $\mu\text{m}$ , and the smallest achievable structure is  $< 23 \mu\text{m}$ ). A similar trend can be found in Pt contact as well, though it has a larger error than for Ti/Pt/Au contact.

Table 5-2. Designed and measured  $r$  and  $d_i$  with uncertainties for Ti/Pt/Au and Pt contact.

Metal contact	$r$ ( $\mu\text{m}$ )	$d_i$ ( $\mu\text{m}$ ), for six rings					
		Ring 1	Ring 2	Ring 3	Ring 4	Ring 5	Ring 6
Designed	250	40	60	80	100	120	140
Ti/Pt/Au	251.2 $\pm$ 0.5	41.2 $\pm$ 0.4	60.7 $\pm$ 0.5	81.7 $\pm$ 1.0	101.7 $\pm$ 0.8	121.8 $\pm$ 0.5	141.6 $\pm$ 0.7
Pt	252.3 $\pm$ 0.9	47.7 $\pm$ 1.0	65.8 $\pm$ 1.5	84.7 $\pm$ 0.7	104.9 $\pm$ 1.1	124.8 $\pm$ 0.7	142.5 $\pm$ 0.9

(iii) Simplification or approximation of the CTLM function. Modified Bessel function that can describe the current distribution on a circular contact surface, was used to improve the accuracy of the extraction of the specific contact resistance as suggested by several works (Banerjee et al., 2020; Liu et al., 2018; Pan et al., 2013).

$$R_{tot} = \frac{R_S}{2\pi} \left[ \ln\left(\frac{r_{out}}{r}\right) + \frac{L_T}{r} \cdot \frac{I_0(r/L_T)}{I_1(r/L_T)} + \frac{L_T}{r_{out}} \cdot \frac{K_0(r_{out}/L_T)}{K_1(r_{out}/L_T)} \right] \quad (5 - 5)$$

where  $I_0$  ( $I_1$ ) and  $K_0$  ( $K_1$ ) are the zero-order (first-order) modified Bessel functions, of first and second kind, respectively. The equation is generally expressed as:

$$R_{tot} = \frac{R_S}{2\pi} \left[ \ln\left(\frac{r_{out}}{r}\right) + L_T \left( \frac{1}{r_{out}} + \frac{1}{r} \right) \right] \quad (5 - 6)$$

The simplification for  $I_0/I_1 = 1$  and  $K_0/K_1 = 1$  relies on the assumption that the  $r_{out}$  and  $r$  are at least four times greater than  $L_T$  (Liu et al., 2018). However, this condition was not satisfied in our case after plotting  $R_{tot}$  vs.  $\ln\left(\frac{r_{out}}{r}\right)$ . For example, **Figure 5-7** shows the  $R_{tot}$  plotted versus  $\ln(r_{out}/r)$  at 700 K, the extracted transfer length  $L_T$  is even comparable with the inner radius  $r$ . One explanation is that the plot is, in fact, not linear, the slope might be underestimated, thus leading to an underestimation of sheet resistance and a large intercept at y axis. As a result, the transfer length is overestimated. To make a correct fitting, it is necessary to make a Taylor expansion of the Bessel functions (6 – 5), and calculate the  $L_T$  with corresponding  $r_{out}/r$ . However, these obtained results may be influenced by other factors

that will be discussed below, the method might not be applicable here. The sheet resistance ( $R_S$ ), specific contact resistance ( $\rho_C$ ) were determined by the  $R_{tot}$  vs.  $d_i$  plot:  $R_S = 2\pi r_{out} \times slope$ ,  $\rho_C = (L_T)^2 \times R_S$  (Jacobs et al., 2002; Klootwijk and Timmering, 2004).

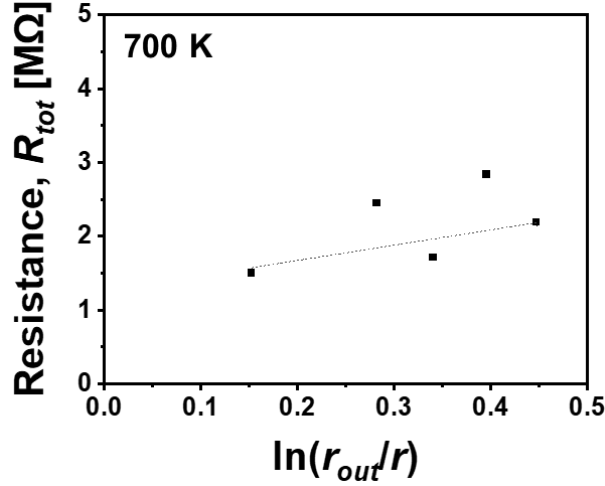


Figure 5-7.  $R_{tot}$  plotted versus  $\ln(r_{out}/r)$  at 700 K.

### 5.3 Experimental results and discussion

The Zn-doped  $\beta$ -Ga<sub>2</sub>O<sub>3</sub> samples were grown in a by metal organic chemical vapor deposition (MOCVD) reactor on insulating *r*-plane sapphire substrates at 775 °C. The doping concentration is  $[Zn] = 2 \times 10^{19} \text{ cm}^{-3}$  determined by SIMS.

Please note that the study on sputtered Ag contact resistance is still in process. Here, **Figure 5-8** shows the linear  $I$ - $V$  curves of sputtered Ag contact in a Van der Pauw configuration on *p*-type  $\beta$ -Ga<sub>2</sub>O<sub>3</sub>, at temperatures  $T$  decreasing between 700 K and 500 K (in this temporal order), indicating the Ohmic behavior at the tested temperature range.

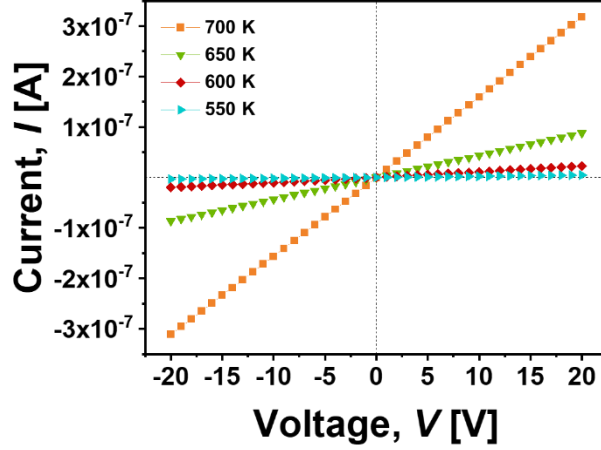


Figure 5-8.  $I$ - $V$  curves for sputtered Ag contact at temperatures ranging between 700 – 550 K.

**Figure 5-9 (a)-(d)** show the  $I$ - $V$  characteristics of Ti/Pt/Au contact at temperatures between 700 K and 550 K, all the curves are linear in the measurement temperature range. A tiny change in the slope can be found at  $T = 550$  K, and at  $T < 500$  K, it started to rectify. The total resistance  $R_{tot}$  as a function of measured gap spacing  $d_i$  (**Table 5-2**) at different temperatures is shown in **Figure 5-10**. Not as expected, the plots are not linear. To know qualitatively the nature of Ti/Pt/Au contact, the results at 700 K, 650 K, and 450 K were nevertheless fitted (**Figure 5-10 (a), (b), and (f)**, respectively). The calculated sheet resistance ( $R_S$ ) of  $\beta$ -Ga<sub>2</sub>O<sub>3</sub> film and the specific contact resistance ( $\rho_C$ ) are labelled in the **figure 8**. At 700 K, the sheet resistance  $R_S = 3.8 \pm 2.9 \times 10^6 \Omega/\text{sq}$ , the specific contact resistance  $\rho_C = 4.9 \pm 1.2 \times 10^2 \Omega \cdot \text{cm}^2$ . While they were increased to  $R_S = 7.6 \pm 4.6 \times 10^9 \Omega/\text{sq}$ ,  $\rho_C = 3.8 \pm 1.1 \times 10^5 \Omega \cdot \text{cm}^2$  at 450 K. It is clear that the contact resistance increased significantly with the decreasing temperature, with an “exponential-like” dependence (**Figure 5-11 (a)**) in the semi-log plotting for both quantities versus T).

The usually dominant transport mechanisms of Schottky type M-S contact, including thermionic emission and thermionic field emission, are strongly influenced by the temperature (Fontserè et al., 2011). The corresponding total current density equation can be given by (Rideout, 1975; Rideout and Crowell, 1970):

$$J_{total} = J_r \left[ \exp\left(\frac{qV}{nk_B T}\right) - \exp\left(\left(\frac{1}{n} - 1\right)\frac{qV}{k_B T}\right) \right] \quad (5 - 7)$$

Where  $J_r = A^*T^2 \exp\left(-\frac{q\Phi_b}{k_B T}\right)$ ,  $A^*$  is the Richardson constant for the semiconductor,  $k_B$  is the Boltzmann's constant,  $\Phi_b$  is the barrier height,  $T$  is the temperature,  $V$  is the applied forward bias,  $n$  is the diode ideality factor.

When the impurity concentration is further increased, the barrier thickness becomes thin enough for a significant number of carriers to tunnel through. This mechanism of current transport is known as field emission tunneling, which is not dependent on temperature, and is the dominant mode of current transport in metal-semiconductor Ohmic contacts. The specific contact resistance follows the relation in the case of  $n$ -type doping, with the donor concentration  $N_D$  (Greco et al., 2016):

$$\rho_C \propto \exp\left(\frac{\Phi_b}{\sqrt{N_D}}\right) \quad (5 - 8)$$

Therefore, observing the temperature dependent specific contact resistance, it is suggested that a barrier exists between the Ti/Pt/Au contact and  $p$ -type  $\beta$ -Ga<sub>2</sub>O<sub>3</sub>, which was reduced during measurements with increasing temperatures. Therefore, the linear behavior of  $I$ - $V$  curves, the Ti/Pt/Au contact forms “quasi-Ohmic” contact to  $p$ -type  $\beta$ -Ga<sub>2</sub>O<sub>3</sub> around zero for current density in the measurement temperature range.

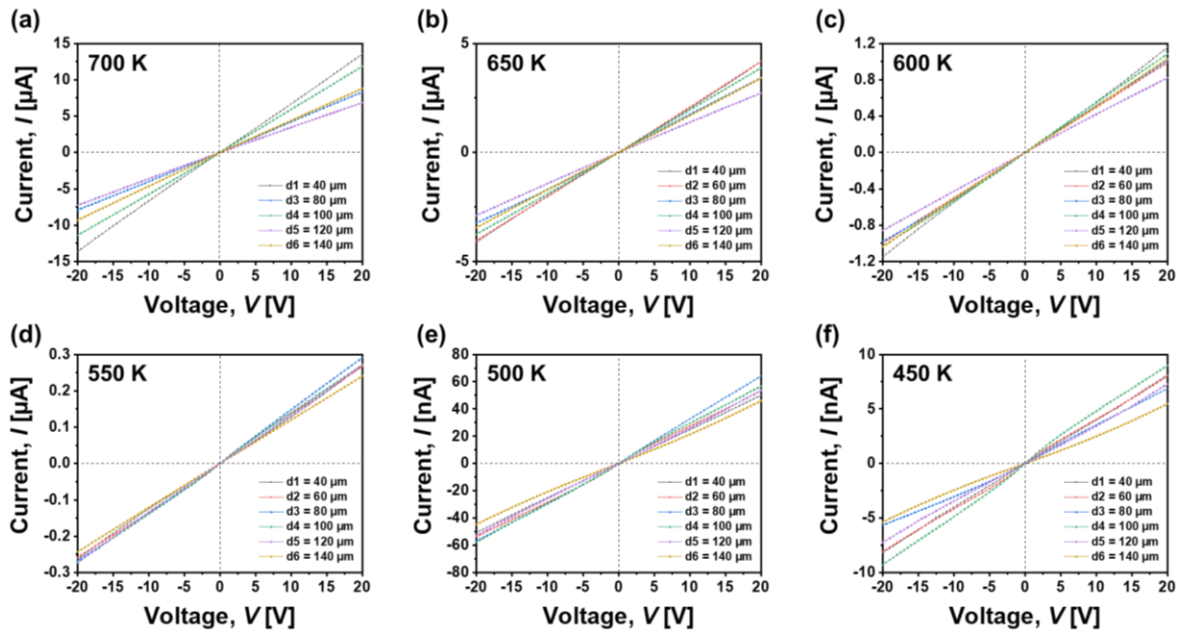


Figure 5-9.  $I$ - $V$  curves of Ti/Pt/Au contact at different temperatures (700 – 450 K), and different spacing  $d_i$ .

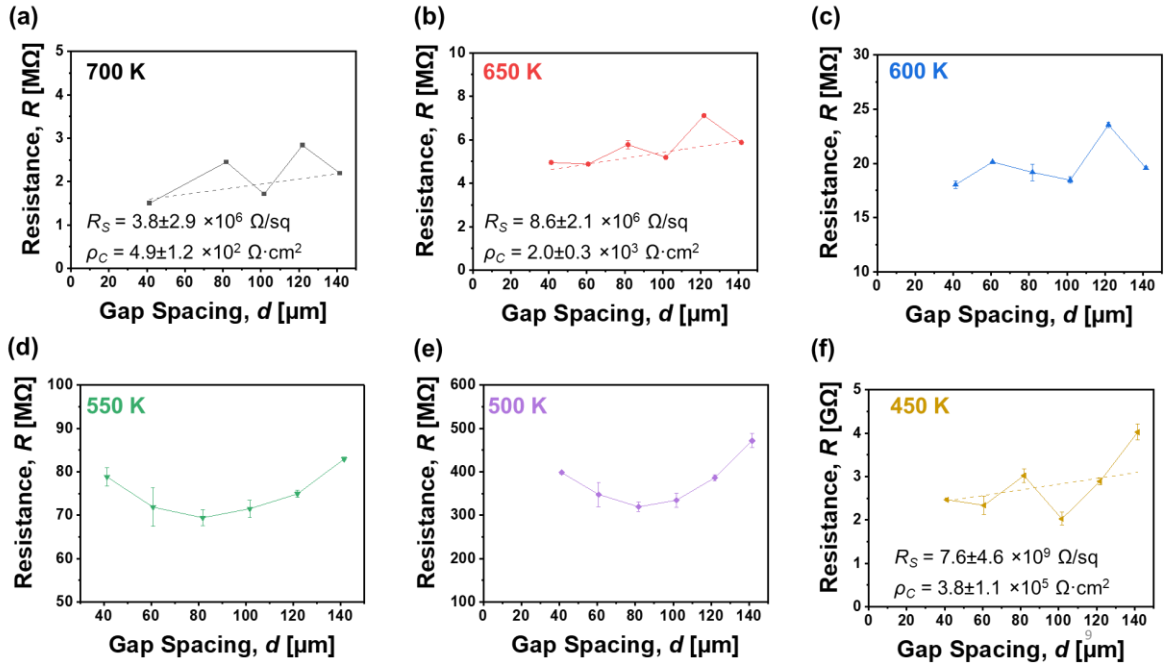


Figure 5-10. Total resistance  $R_{tot}$  plotted versus gap spacing  $d_i$  for Ti/Pt/Au contact between  $T = 700$  K and 450 K.

One possible explanation for the results seen in the total resistance plotted versus gap spacing could be attributed to interdiffusion of metals and gallium, although a layer of Pt was deposited between Ti and Au to prevent the interdiffusion, an annealing for the contact was made at 500 °C for 30 min, and the measurement temperatures were no more than 423 °C. Indeed, for example, the pattern with gap spacing  $d_6 = 140 \mu\text{m}$  was remeasured at 600 K (327 °C) after all the  $I$ - $V$  tests and shown in **Figure 5-11 (b)**, the first measurement (from **Figure 5-9 (c)**, the  $I$ - $V$  curve in yellow) was put for comparison. The total resistance increased  $\sim 10$  times after several measurements at elevated temperatures, which might be due to the degradation of the contact. Such contact deterioration that might be induced by the interdiffusion of metals/cation can be further confirmed by energy-dispersive X-ray spectroscopy (EDX) carried out for the sample cross-section, which is programmed to be done, as it is important to know the high temperature stability of the electrical contact. Besides, the areas of the outer metal contacts are different for each concentric cycle group, leading to the varying ratio  $S_{outer}/S_{inner} \sim 1.5 - 4$  depending on the gap spacing. Subsequently, it is also a factor that influences the analysis of measured resistance.

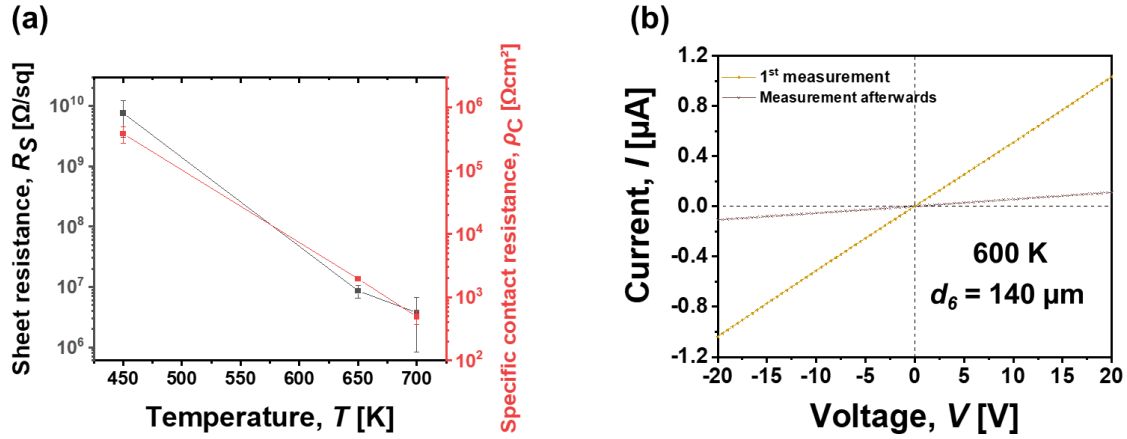


Figure 5-11. (a) The calculated sheet resistance ( $R_S$ ) (black) of  $\beta$ -Ga<sub>2</sub>O<sub>3</sub> film and the specific contact resistance ( $\rho_C$ ) (red) plotted versus temperature in semi-log shifted scales. (b) The first measurement (black) and the final measurement (dark yellow) after conducting all the  $I$ - $V$  tests for the pattern with gap spacing  $d_i = 140 \mu\text{m}$  at 600 K.

The measurement temperatures were then reduced to  $T_{max} = 600 \text{ K}$ . **Figure 5-12** shows the  $I$ - $V$  characteristics of Pt contact at  $T = 500 - 600 \text{ K}$ . The current measured at 600 K was of several nA depending on the gap spacings, while it was  $\sim \mu\text{A}$  for Ti/Pt/Au contact. Besides, it starts to rectify at  $T = 500 \text{ K}$  with  $I < 0.1 \text{ nA}$ , indicating the Schottky contact behavior.

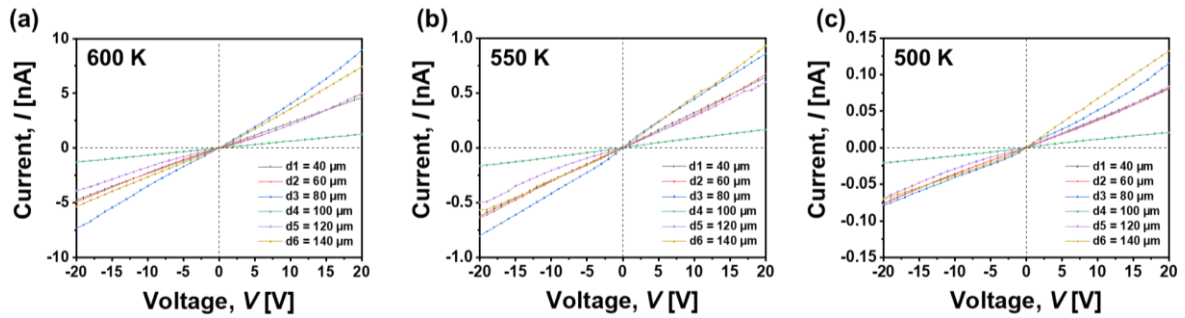


Figure 5-12.  $I$ - $V$  curves of Pt contact at different temperatures (600 – 500 K).

## 5.4 Summary and next steps

Photolithography parameters has been first adjusted to get the desired dimensions of patterns, Ag, Ti/Pt/Au and Pt contacts were deposited on *p*-type  $\beta$ -Ga<sub>2</sub>O<sub>3</sub> thin films.  $I$ - $V$  curves of Ag/ $\beta$ -Ga<sub>2</sub>O<sub>3</sub> are linear at 550 – 700 K temperature range, indicating an Ohmic behavior. Pt/ $\beta$ -Ga<sub>2</sub>O<sub>3</sub> contact starts to rectify at  $T < 500 \text{ K}$ . Ti/Pt/Au forms a quasi-Ohmic contact to *p*-type  $\beta$ -Ga<sub>2</sub>O<sub>3</sub> in the measurement temperature range.

The CTLM method for the determination of specific contact resistance was applied for Ti/Pt/Au contact, while the results are difficult to analyze. To go further in this metallic contact study, I propose the following next steps:

(i) High measurement temperatures are susceptible to degrading the contacts (by interdiffusion). Therefore, lower measurement temperatures ( $T < 300$  °C) should be used.

(ii) The non-linear plots of total resistance  $R_{tot}$  versus gap spacing  $d_i$  may also be attributed to the inhomogeneity of the sample surfaces and different outer areas. Thus, an entire outer metal pattern (**Figure 5-13**) of an area much larger than the inner metal contact should be used during the lithography process, with the same inter area. Thus, we can neglect the outer contact contribution to R total with respect to the inner contact contribution.

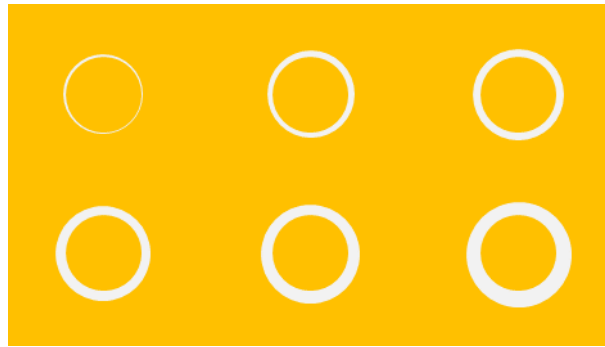


Figure 5-13. Schematic illustration for a new version of CTLM patterns, with large outer metallic electrode.

(iii) Considering the interlayers (AZO, ITO, or Ti-TiO<sub>x</sub>) used to reduce the barrier height, natural *p*-type semiconductors NiO or Cu<sub>2</sub>O can be used as the first layer of the metal contact pad, e.g., NiO/Ni/Pt/Au or Cu<sub>2</sub>O/Pt/Au. NiO (NiO<sub>x</sub>) layer can be deposited by either directly sputtering from a NiO target (Freitas et al., 2018; Zhang et al., 2022) or oxidation from a seed layer of metal Ni (Qiao et al., 2000). Cu<sub>2</sub>O can also be directly deposited on *n*-Ga<sub>2</sub>O<sub>3</sub> to make *p-n* junction diode (Watahiki et al., 2017).

All developments are long, but are important for the integration of *p*-type Ga<sub>2</sub>O<sub>3</sub> materials on real devices.

---

---

## 6. Conclusion and Perspectives

### Conclusion

In this PhD thesis work, the electronic properties of two ultra-wide band gap semiconductors,  $\beta$ -Ga<sub>2</sub>O<sub>3</sub> and ZnGa<sub>2</sub>O<sub>4</sub>, having potentiality for high power electronic devices and UV photodetectors, were studied. The results in this manuscript can be summarized in three main parts as below:

(i) Hole conductivity realization: *p*-type doping in ultra-wide band gap is well-known to be challenging, the prerequisite for further *p*-type doping is to get a highly compensated semi-insulating  $\beta$ -Ga<sub>2</sub>O<sub>3</sub> thin film. Therefore, firstly, high crystalline quality undoped  $\beta$ -Ga<sub>2</sub>O<sub>3</sub> layers were epitaxially grown on *c*-plane sapphire substrates using the MOCVD technique. For the film grown at  $T = 775$  °C,  $P = 30$  Torr, with the gallium precursor flow fixed at 6  $\mu$ mol/min, and O<sub>2</sub> flow at 600 sccm, it exhibited high transparency (> 80%) in the visible to near-infrared wavelength range with an optical band gap of  $E_g = 4.66 \pm 0.05$  eV. The *p*-type conductivity at high temperatures ( $T = 550 - 850$  K) was shown by Hall effect measurements. The native *p*-type conductivity is attributed to the native gallium vacancy ( $V_{Ga}$ ) acceptor defect with an ionization energy of  $E_i \sim 1.2$  eV. This achievement encouraged us to study acceptor doping in  $\beta$ -Ga<sub>2</sub>O<sub>3</sub>.

Zn, as a II group element, was selected as an acceptor dopant. Thermodynamic analysis suggested that Zn can take interstitial site or substitute Ga, forming Zn<sub>i</sub> donor defect or Zn<sub>Ga</sub> acceptor defect depending on the growth conditions (pressure, temperature) and the doping level. For example, at the total pressure  $P = 30$  Torr in the growth chamber, if growth temperature  $T = 800$  °C, the impurity *p*-type conductivity can take place when Zn concentration  $> 10^{14}$  cm<sup>-3</sup>. while when  $[Zn] \sim 10^{18}$  cm<sup>-3</sup>, Zn atoms start to occupy interstitial sites and consequently, Zn<sub>i</sub> donor and Zn<sub>Ga</sub> acceptor defects compensate each other, resulting in the so-called impurity “auto-compensation” effect. Following the conclusions from the thermodynamic analysis, the experimental study has been carried out. Undoped and Zn doped  $\beta$ -Ga<sub>2</sub>O<sub>3</sub> thin films were grown by MOCVD technique, structural and compositional analysis showed the successful incorporation of Zn thin films in  $10^{16} - 10^{19}$  cm<sup>-3</sup> range, while keeping the monoclinic  $\beta$ -Ga<sub>2</sub>O<sub>3</sub> structure. The films are of high transparency (~80%) in the visible to near-infrared range and possess an ultra-wide band gap with a cut-off wavelength

---

of 260 – 266 nm. When  $[Zn] = 10^{16} \text{ cm}^{-3}$ ,  $p$ -type conductivity in  $\beta\text{-Ga}_2\text{O}_3$  is enhanced (e.g., at 800 K,  $\rho = 5.8 \times 10^2 \text{ } \Omega \cdot \text{cm}$  and  $p = 1.2 \times 10^{15} \text{ cm}^{-3}$ , vs.  $\rho = 3.1 \times 10^3 \text{ } \Omega \cdot \text{cm}$  and  $2.2 \times 10^{14} \text{ cm}^{-3}$  for undoped thin film). This fact proves that Zn is an active acceptor dopant in  $\beta\text{-Ga}_2\text{O}_3$ . The ionization energy was determined to be  $E_i = 0.77 \text{ eV}$ , which corresponds to the  $Zn_{Ga}$  (octahedral site) defect according to the EPR study in the literature. As the doping level increases  $[Zn] > 10^{18} \text{ cm}^{-3}$ , the “auto-compensation” effect occurs, thus hole concentrations are reduced. However, the first “negative” result could be used in a “positive” way. Based on the kinetic impact ionization theory, it is suggested that the critical electric field  $E_{CR}$  can be increased by decreasing the impact ionization probability (by shortening the mean free path of free carriers and reducing carrier concentration). Therefore, by leveraging the “auto-compensation” effect of Zn doping, we proposed that the critical electric field ( $E_{CR}$ ) of  $\beta\text{-Ga}_2\text{O}_3$  can be further increased. To prove this concept experimentally, parallel capacitors based on  $\beta\text{-Ga}_2\text{O}_3//\text{Si}$  and  $\beta\text{-Ga}_2\text{O}_3:\text{Zn}//\text{Si}$  ( $[Zn] = 10^{19} \text{ cm}^{-3}$ ) structures were fabricated to estimate experimentally the  $E_{CR}$  values of undoped and Zn doped  $\beta\text{-Ga}_2\text{O}_3$ .  $E_{CR} = 5.7 \text{ MV/cm}$  was determined for  $\beta\text{-Ga}_2\text{O}_3//\text{Si}$  structure, while it was significantly increased up to  $E_{CR} = 13.2 \text{ MV/cm}$  for  $\beta\text{-Ga}_2\text{O}_3:\text{Zn}//\text{Si}$ .

(ii) Spinel  $ZnGa_2O_4$ : The incorporation of Zn in  $\beta\text{-Ga}_2\text{O}_3$  was enhanced increasing the  $O_2$  flow rate during MOCVD growth (ranging from 600 to 1200 sccm). Under the same growth conditions (temperature, gallium and zinc precursors’ flows, etc) except for a higher  $O_2$  flow fixed at 1200 sccm, cubic spinel  $ZnGa_2O_4$  is formed. The mixed structure (at Zn concentration between 6.85 at. % and 14 at. %) of  $\beta\text{-Ga}_2\text{O}_3$  and  $ZnGa_2O_4$  was evidenced by both XRD patterns and Raman spectra. At a Zn concentration of 14.04 at. %, the monoclinic  $\beta\text{-Ga}_2\text{O}_3$  completely transforms into cubic spinel  $ZnGa_2O_4$ .

As a ternary semiconductor, spinel oxide is known to have a higher flexibility of doping than binary compounds, due to the three ions with different valences at different sites. Here, intrinsic room-temperature conducting ( $\rho = 2.7 \times 10^{-2} \text{ } \Omega \cdot \text{cm}$ )  $n$ -type ( $n = 10^{19} \text{ cm}^{-3}$ ) and semi-insulating  $p$ -type ( $\rho = 10^6 \text{ } \Omega \cdot \text{cm}$ ,  $p = 10^{11} \text{ cm}^{-3}$  at 550 K)  $ZnGa_2O_4$  thin films were studied. All thin films MOCVD technique are of high crystalline quality with band gaps  $E_g > 4.8 \text{ eV}$ . An absorption peak at about 3.3 eV was evidenced for the  $n$ -type  $ZnGa_2O_4$  layer, without the identification of any additional phases. According to the investigation of electronic properties, it is suggested that the high electron conductivity ( $\sigma = 3.7 \times 10^1 \text{ S/cm}$ ) in Zn-rich and O-deficient  $ZnGa_2O_4$  thin films can be attributed to  $Zn_i\text{-}V_O$  defect related “self-impurity”

---

band located at the mid-gap. While the hole conductivity in near-stoichiometric condition originates from deep acceptor  $Zn_{Ga}$  defect. Interestingly, experimental results show that the  $ZnGa_2O_4$  native conductivity can be controlled within 10 orders of magnitude range. I also aimed to further understand the impact of oxygen content on the electronic properties in the  $ZnGa_2O_4$  layers, which is an ongoing work. By The first observations, the room temperature resistivity increases from  $\rho = 1.8 \times 10^{-1} \Omega \cdot \text{cm}$  to  $\rho \gg 10^5 \Omega \cdot \text{cm}$ . A preliminary test of the photocurrent for the  $p$ -type  $ZnGa_2O_4$  layer showed an important UV sensibility ( $I_{UV}/I_{dark} \sim 10^3$  without metallization). The vertical geometry breakdown voltage measurements of the  $p$ - $ZnGa_2O_4$ //Si structure delivered breakdown voltage up to 350 V, resulting in  $E_{CR} > 5.3$  MV/cm. It is also the first experimental determination of the critical electric field for  $ZnGa_2O_4$ .

(iii) Electrical contacts: I have carried out a preliminary study to elaborate on the electrical metal contacts for  $p$ -type  $\beta$ - $Ga_2O_3$ . My first task was to adjust photolithography parameters, in order to get the desired dimensions of patterns, followed by the sputtering of Ag, Pt, and Ti/Pt/Au contacts on  $p$ -type  $\beta$ - $Ga_2O_3$ //sapphire samples, post-annealing at 500 °C under  $N_2$ , and the  $I$ - $V$  characterizations. Ag forms Ohmic contact in the 550 – 700 K measurement temperature range, the estimation of the contact resistance is ongoing work. Pt/ $\beta$ - $Ga_2O_3$  contact showed quasi-linear behavior at  $T = 600$  and 550 K, while started to rectify clearly at  $T \leq 500$  K.  $I$ - $V$  curves of Ti/Pt/Au contact to  $p$ -type  $\beta$ - $Ga_2O_3$  suggested that the contact is Ohmic at  $T > 550$  K. However, the specific contact resistance extracted using the circular transmission line model (CTLM) approach is temperature dependent (at  $T = 450$  – 700 K), suggesting that this metal contact pad may form quasi-Ohmic contact in the measurement temperature range. Additionally, the measured resistance of Ti/Pt/Au/ $\beta$ - $Ga_2O_3$  did not increase linearly with the increasing gap spacing between the inner and outer metal contacts, which made the analysis and the extraction of parameters of the CTLM based measurements not accurate.

However, the existing difficulties I met have been analyzed, the degradation of metal contacts might be due to the interdiffusion of metal/cation (Au, Ga) after measurements at high temperatures (up to 700 K); another factor that could influence the extraction of sheet resistance and the specific contact resistance, is the varying outer metal contact area. In light of these issues, the next steps can be proposed to improve the  $I$ - $V$  characterizations, as presented bellow as a perspective.

---

## Perspectives

Both  $\beta$ -Ga<sub>2</sub>O<sub>3</sub> and ZnGa<sub>2</sub>O<sub>4</sub> exhibit tremendous potential for next-generation power electronic applications, while  $\beta$ -Ga<sub>2</sub>O<sub>3</sub> has witnessed more significant advancements in this area compared to ZnGa<sub>2</sub>O<sub>4</sub>. To unlock the full potential of these materials, the deeper study of point defects, and in turn, the control of electrical conductivity is very important. Therefore, several future works can be envisaged:

(i) The exploration of defects complexes, such as V<sub>Ga</sub>-V<sub>O</sub> and V<sub>Ga</sub>-Ga<sub>i</sub>-V<sub>Ga</sub>, in  $\beta$ -Ga<sub>2</sub>O<sub>3</sub>, is still in its early stages. These defects may exhibit diverse charge states, leading to distinct and significant effects on the properties and behavior of  $\beta$ -Ga<sub>2</sub>O<sub>3</sub> (Frodason et al., 2021; Ingebrigtsen et al., 2019b; Johnson et al., 2019; McGlone et al., 2019; Usseinov et al., 2022). Further research in this area is crucial to unraveling the roles of these complex defects. Positron annihilation (Karjalainen et al., 2021; Korhonen et al., 2015; Tuomisto et al., 2019) and scanning transmission electron microscopy measurements are powerful tools to study such defects, combining with GEMaC's home-built Hall effect measurement set up, the roles of complex defects may be expected to put in evidence. The experimental characterizations of these defects by electronic transport studies as well as DLTS spectroscopy, etc., will make it possible to stimulate the *ab-initio* calculations by experimental parameters.

(ii) The study on the electrical properties as well as the point defects of ZnGa<sub>2</sub>O<sub>4</sub> is only starting, there is much to explore and understand the roles of point defects in both *n*-type and *p*-type electrical conductivity. Here, the next step is to continue the work to fully understand the conduction mechanism and its origin (bulk, surface). Surface conduction due to charge accumulation can be studied by XPS analysis on the valence band tails and by electrochemical.

(iii) Regarding the investigation related to electric metal contact to *p*-type  $\beta$ -Ga<sub>2</sub>O<sub>3</sub>, the degradation of (Ti/Pt/Au) contacts at high measurement temperatures up to  $T = 700$  K can be studied by the energy-dispersive X-ray spectroscopy. Otherwise, it was decided to work at lower measurement temperatures ( $T < 300$  °C) that are sufficient for future power device operations. Besides, there should be an entire outer metal pattern, which has a uniform and neglected contact resistance for all the  $I$ - $V$  measurements. Additionally, depositing a natural *p*-type NiO interlayer ( $\sim 10 - 20$  nm) between the *p*-type  $\beta$ -Ga<sub>2</sub>O<sub>3</sub> and the metal (e.g., Pt/Au) contacts. Besides the Ohmic contact, a Schottky contact is also necessary for the DLTS spectroscopy.

---

## References

- Akiyama, T., Kawamura, T., Ito, T., 2023. Role of charged oxygen vacancies and substrate lattice constraint on structural stability of Ga<sub>2</sub>O<sub>3</sub> polymorphs. *Appl. Phys. Express* 16, 015508. <https://doi.org/10.35848/1882-0786/acb12e>
- Alema, F., Hertog, B., Ledyaeov, O., Volovik, D., Thoma, G., Miller, R., Osinsky, A., Mukhopadhyay, P., Bakhshi, S., Ali, H., Schoenfeld, W.V., 2017a. Solar blind photodetector based on epitaxial zinc doped Ga<sub>2</sub>O<sub>3</sub> thin film: Solar blind photodetector based on ZnGaO thin film. *Phys. Status Solidi A* 214, 1600688. <https://doi.org/10.1002/pssa.201600688>
- Alema, F., Hertog, B., Osinsky, A., Mukhopadhyay, P., Toporkov, M., Schoenfeld, W.V., 2017b. Fast growth rate of epitaxial  $\beta$ -Ga<sub>2</sub>O<sub>3</sub> by close coupled showerhead MOCVD. *J. Cryst. Growth* 475, 77–82. <https://doi.org/10.1016/j.jcrysgro.2017.06.001>
- Alema, F., Zhang, Y., Osinsky, A., Valente, N., Mauze, A., Itoh, T., Speck, J.S., 2019. Low temperature electron mobility exceeding 104 cm<sup>2</sup>/V s in MOCVD grown  $\beta$ -Ga<sub>2</sub>O<sub>3</sub>. *APL Mater.* 7, 121110. <https://doi.org/10.1063/1.5132954>
- Al-Gaashani, R., Radiman, S., Daud, A.R., Tabet, N., Al-Douri, Y., 2013. XPS and optical studies of different morphologies of ZnO nanostructures prepared by microwave methods. *Ceram. Int.* 39, 2283–2292. <https://doi.org/10.1016/j.ceramint.2012.08.075>
- Allerman, A. a., Armstrong, A. m., Fischer, A. j., Dickerson, J. r., Crawford, M. h., King, M. p., Moseley, M. w., Wierer, J. j., Kaplar, R. j., 2016. Al<sub>0.3</sub>Ga<sub>0.7</sub>N PN diode with breakdown voltage >1600 V. *Electron. Lett.* 52, 1319–1321. <https://doi.org/10.1049/el.2016.1280>
- Anderson, C.L., Crowell, C.R., 1972. Threshold Energies for Electron-Hole Pair Production by Impact Ionization in Semiconductors. *Phys. Rev. B* 5, 2267–2272. <https://doi.org/10.1103/PhysRevB.5.2267>
- Anderson, P.W., 1958. Absence of Diffusion in Certain Random Lattices. *Phys. Rev.* 109, 1492–1505. <https://doi.org/10.1103/PhysRev.109.1492>
- Asghar, M., Mahmood, K., Ferguson, I.T., Raja, M.Y.A., Xie, Y.H., Tsu, R., Hasan, M.-A., 2013. Investigation of VO–Zni native donor complex in MBE grown bulk ZnO. *Semicond. Sci. Technol.* 28, 105019. <https://doi.org/10.1088/0268-1242/28/10/105019>
- Aubay, E., Gourier, D., 1993. Magnetic bistability and Overhauser shift of conduction electrons in gallium oxide. *Phys. Rev. B* 47, 15023–15036. <https://doi.org/10.1103/PhysRevB.47.15023>
- Bai, R., Zhao, B., Ling, K., Li, K., Liu, X., 2022. Dilute-selenium alloying: A possible perspective for achieving p-type conductivity of  $\beta$ -gallium oxide. *J. Alloys Compd.* 891, 161969. <https://doi.org/10.1016/j.jallcom.2021.161969>
- Bairagi, S., Hsiao, C.-L., Magnusson, R., Birch, J., Chu, J.P., Tarntair, F.-G., Horng, R.-H., Järendahl, K., 2022. Zinc gallate (ZnGa<sub>2</sub>O<sub>4</sub>) epitaxial thin films: determination of optical properties and bandgap estimation using spectroscopic ellipsometry. *Opt. Mater. Express* 12, 3284–3295. <https://doi.org/10.1364/OME.462668>

- 
- Baji, Z., Cora, I., Horváth, Z.E., Agócs, E., Szabó, Z., 2021. Atomic layer deposition and characterization of Zn-doped Ga<sub>2</sub>O<sub>3</sub> films. *J. Vac. Sci. Technol. A* 39, 032411. <https://doi.org/10.1116/6.0000838>
- Baldini, M., Albrecht, M., Fiedler, A., Irmscher, K., Klimm, D., Schewski, R., Wagner, G., 2016. Semiconducting Sn-doped  $\beta$ -Ga<sub>2</sub>O<sub>3</sub> homoepitaxial layers grown by metal organic vapour-phase epitaxy. *J. Mater. Sci.* 51, 3650–3656. <https://doi.org/10.1007/s10853-015-9693-6>
- Banerjee, A.N., Chattopadhyay, K.K., 2005. Recent developments in the emerging field of crystalline p-type transparent conducting oxide thin films. *Prog. Cryst. Growth Charact. Mater.* 50, 52–105. <https://doi.org/10.1016/j.pcrysgrow.2005.10.001>
- Banerjee, S., Wong, P.Y., Zhang, P., 2020. Contact resistance and current crowding in tunneling type circular nano-contacts. *J. Phys. Appl. Phys.* 53, 355301. <https://doi.org/10.1088/1361-6463/ab8fe0>
- Bhandari, S., Zvanut, M.E., 2021. Charge trapping at Fe due to midgap levels in Ga<sub>2</sub>O<sub>3</sub>. *J. Appl. Phys.* 129, 085703. <https://doi.org/10.1063/5.0042622>
- Bhattacharyya, A., Ranga, P., Saleh, M., Roy, S., Scarpulla, M.A., Lynn, K.G., Krishnamoorthy, S., 2020. Schottky Barrier Height Engineering in  $\beta$ -Ga<sub>2</sub>O<sub>3</sub> Using SiO<sub>2</sub> Interlayer Dielectric. *IEEE J. Electron Devices Soc.* 8, 286–294. <https://doi.org/10.1109/JEDS.2020.2974260>
- Binet, L., Gourier, D., 1998. ORIGIN OF THE BLUE LUMINESCENCE OF  $\beta$ -Ga<sub>2</sub>O<sub>3</sub>. *J. Phys. Chem. Solids* 59, 1241–1249. [https://doi.org/10.1016/S0022-3697\(98\)00047-X](https://doi.org/10.1016/S0022-3697(98)00047-X)
- Binet, L., Gourier, D., Minot, C., 1994. Relation between Electron Band Structure and Magnetic Bistability of Conduction Electrons in  $\beta$ -Ga<sub>2</sub>O<sub>3</sub>. *J. Solid State Chem.* 113, 420–433. <https://doi.org/10.1006/jssc.1994.1390>
- Blasse, G., Bril, A., 1970. Some observations on the luminescence of  $\beta$ -Ga<sub>2</sub>O<sub>3</sub>. *J. Phys. Chem. Solids* 31, 707–711. [https://doi.org/10.1016/0022-3697\(70\)90204-0](https://doi.org/10.1016/0022-3697(70)90204-0)
- Bose, 2017. Power Electronics in Smart Grid and Renewable Energy Systems [Scanning the Issue]. *Proc. IEEE* 105, 2007–2010. <https://doi.org/10.1109/JPROC.2017.2752538>
- Boy, J., Handweg, M., Mitdank, R., Galazka, Z., Fischer, S.F., 2020. Charge carrier density, mobility, and Seebeck coefficient of melt-grown bulk ZnGa<sub>2</sub>O<sub>4</sub> single crystals. *AIP Adv.* 10, 055005. <https://doi.org/10.1063/5.0002847>
- Bragg, W.H., 1915. XXX. The structure of the spinel group of crystals. *Lond. Edinb. Dublin Philos. Mag. J. Sci.* 30, 305–315. <https://doi.org/10.1080/14786440808635400>
- Brik, M.G., 2010. First-principles calculations of electronic, optical and elastic properties of ZnAl<sub>2</sub>S<sub>4</sub> and ZnGa<sub>2</sub>O<sub>4</sub>. *J. Phys. Chem. Solids* 71, 1435–1442. <https://doi.org/10.1016/j.jpcs.2010.07.007>
- Bude, J., Hess, K., 1992. Thresholds of impact ionization in semiconductors. *J. Appl. Phys.* 72, 3554–3561. <https://doi.org/10.1063/1.351434>
- Cai, X., Sabino, F.P., Janotti, A., Wei, S.-H., 2021. Approach to achieving a  $p$ -type transparent conducting oxide: Doping of bismuth-alloyed  $\beta$ -Ga<sub>2</sub>O<sub>3</sub> with a strongly correlated band edge state. *Phys. Rev. B* 103, 115205. <https://doi.org/10.1103/PhysRevB.103.115205>
-

- 
- Can, M.M., Hassnain Jaffari, G., Aksoy, S., Shah, S.I., Firat, T., 2013. Synthesis and characterization of ZnGa<sub>2</sub>O<sub>4</sub> particles prepared by solid state reaction. *J. Alloys Compd.* 549, 303–307. <https://doi.org/10.1016/j.jallcom.2012.08.137>
- Cao, Q., He, L., Xiao, H., Feng, X., Lv, Y., Ma, J., 2018.  $\beta$ -Ga<sub>2</sub>O<sub>3</sub> epitaxial films deposited on epi-GaN/sapphire (0001) substrates by MOCVD. *Mater. Sci. Semicond. Process.* 77, 58–63. <https://doi.org/10.1016/j.mssp.2018.01.010>
- Carey, B.J., Ou, J.Z., Clark, R.M., Berean, K.J., Zavabeti, A., Chesman, A.S.R., Russo, S.P., Lau, D.W.M., Xu, Z.-Q., Bao, Q., Kavehei, O., Gibson, B.C., Dickey, M.D., Kaner, R.B., Daeneke, T., Kalantar-Zadeh, K., 2017. Wafer-scale two-dimensional semiconductors from printed oxide skin of liquid metals. *Nat. Commun.* 8, 14482. <https://doi.org/10.1038/ncomms14482>
- Carey, P.H., Yang, J., Ren, F., Hays, D.C., Pearton, S.J., Jang, S., Kuramata, A., Kravchenko, I.I., 2017a. Ohmic contacts on n-type  $\beta$ -Ga<sub>2</sub>O<sub>3</sub> using AZO/Ti/Au. *AIP Adv.* 7, 095313. <https://doi.org/10.1063/1.4996172>
- Carey, P.H., Yang, J., Ren, F., Hays, D.C., Pearton, S.J., Kuramata, A., Kravchenko, I.I., 2017b. Improvement of Ohmic contacts on Ga<sub>2</sub>O<sub>3</sub> through use of ITO-interlayers. *J. Vac. Sci. Technol. B* 35, 061201. <https://doi.org/10.1116/1.4995816>
- Chang, C.Y., Fang, Y.K., Sze, S.M., 1971. Specific contact resistance of metal-semiconductor barriers. *Solid-State Electron.* 14, 541–550. [https://doi.org/10.1016/0038-1101\(71\)90129-8](https://doi.org/10.1016/0038-1101(71)90129-8)
- Chase, A.O., 1964. Growth of  $\beta$ -Ga<sub>2</sub>O<sub>3</sub> by the Verneuil Technique. *J. Am. Ceram. Soc.* 47, 470–470. <https://doi.org/10.1111/j.1151-2916.1964.tb14442.x>
- Chatterjee, B., Zeng, K., Nordquist, C.D., Singiseti, U., Choi, S., 2019. Device-Level Thermal Management of Gallium Oxide Field-Effect Transistors. *IEEE Trans. Compon. Packag. Manuf. Technol.* 9, 2352–2365. <https://doi.org/10.1109/TCPMT.2019.2923356>
- Chen, C., Li, G., Liu, Y., 2015. Synthesis of ZnGa<sub>2</sub>O<sub>4</sub> assisted by high-energy ball milling and its gas-sensing characteristics. *Powder Technol.* 281, 7–11. <https://doi.org/10.1016/j.powtec.2015.04.041>
- Chen, Y., Liang, H., Xia, X., Shen, R., Liu, Y., Luo, Y., Du, G., 2015. Effect of growth pressure on the characteristics of  $\beta$ -Ga<sub>2</sub>O<sub>3</sub> films grown on GaAs (100) substrates by MOCVD method. *Appl. Surf. Sci.* 325, 258–261. <https://doi.org/10.1016/j.apsusc.2014.11.074>
- Chen, Y.G., Ogura, M., Yamasaki, S., Okushi, H., 2004. Investigation of specific contact resistance of ohmic contacts to B-doped homoepitaxial diamond using transmission line model. *Diam. Relat. Mater.* 13, 2121–2124. <https://doi.org/10.1016/j.diamond.2004.07.001>
- Chen, Z., Jaramillo, T.F., 2017. The Use of UV-visible Spectroscopy to Measure the Band Gap of a Semiconductor.
- Cheng, L.-C., Huang, C.-Y., Horng, R.-H., 2018. Thickness Effect on Operational Modes of ZnGa<sub>2</sub>O<sub>4</sub> MOSFETs. *IEEE J. Electron Devices Soc.* 6, 432–437. <https://doi.org/10.1109/JEDS.2018.2803078>
- Cheng, L.C., Huang, C.Y., Horng, R.H., 2018. Thickness effect on operational modes of ZnGa<sub>2</sub>O<sub>4</sub> MOSFETs. *IEEE J Electron Devices Soc* 6, 432.
-

- 
- Cheng, L.-C., Wu, M.-R., Huang, C.-Y., Juang, T.-K., Liu, P.-L., Horng, R.-H., 2019. Effect of Defects on the Properties of ZnGa<sub>2</sub>O<sub>4</sub> Thin-Film Transistors. *ACS Appl. Electron. Mater.* 1, 253–259. <https://doi.org/10.1021/acsaelm.8b00093>
- Chi, Z., Asher, J.J., Jennings, M.R., Chikoidze, E., Pérez-Tomás, A., 2022. Ga<sub>2</sub>O<sub>3</sub> and Related Ultra-Wide Bandgap Power Semiconductor Oxides: New Energy Electronics Solutions for CO<sub>2</sub> Emission Mitigation. *Materials* 15, 1164. <https://doi.org/10.3390/ma15031164>
- Chi, Z., Tarntair, F.-G., Frégnaux, M., Wu, W.-Y., Sartel, C., Madaci, I., Chapon, P., Sallet, V., Dumont, Y., Pérez-Tomás, A., Horng, R.H., Chikoidze, E., 2021. Bipolar self-doping in ultra-wide bandgap spinel ZnGa<sub>2</sub>O<sub>4</sub>. *Mater. Today Phys.* 20, 100466. <https://doi.org/10.1016/j.mtphys.2021.100466>
- Chikoidze, E., Fellous, A., Perez-Tomas, A., Sauthier, G., Tchelidze, T., Ton-That, C., Huynh, T.T., Phillips, M., Russell, S., Jennings, M., Berini, B., Jomard, F., Dumont, Y., 2017a. P-type β-gallium oxide: A new perspective for power and optoelectronic devices. *Mater. Today Phys.* 3, 118–126. <https://doi.org/10.1016/j.mtphys.2017.10.002>
- Chikoidze, E., Fellous, A., Perez-Tomas, A., Sauthier, G., Tchelidze, T., Ton-That, C., Huynh, T.T., Phillips, M., Russell, S., Jennings, M., Berini, B., Jomard, F., Dumont, Y., 2017b. P-type β-gallium oxide: A new perspective for power and optoelectronic devices. *Mater. Today Phys.* 3, 118–126. <https://doi.org/10.1016/j.mtphys.2017.10.002>
- Chikoidze, E., Rogers, D.J., Teherani, F.H., Rubio, C., Sauthier, G., Bardeleben, H.J.V., Tchelidze, T., Ton-That, C., Fellous, A., Bove, P., Sandana, E.V., Dumont, Y., Perez-Tomas, A., 2019. Puzzling robust 2D metallic conductivity in undoped β-Ga<sub>2</sub>O<sub>3</sub> thin films. *Mater. Today Phys.* 8, 10–17. <https://doi.org/10.1016/j.mtphys.2018.11.006>
- Chikoidze, E., Sartel, C., Madaci, I., Mohamed, H., Vilar, C., Ballesteros, B., Belarre, F., del Corro, E., Vales-Castro, P., Sauthier, G., Li, L., Jennings, M., Sallet, V., Dumont, Y., Pérez-Tomás, A., 2020a. p-Type Ultrawide-Band-Gap Spinel ZnGa<sub>2</sub>O<sub>4</sub>: New Perspectives for Energy Electronics. *Cryst. Growth Des.* 20, 2535–2546. <https://doi.org/10.1021/acs.cgd.9b01669>
- Chikoidze, Ekaterine, Sartel, C., Mohamed, H., Madaci, I., Tchelidze, T., Modreanu, M., Vales-Castro, P., Rubio, C., Arnold, C., Sallet, V., Dumont, Y., Perez-Tomas, A., 2019. Enhancing the intrinsic p-type conductivity of the ultra-wide bandgap Ga<sub>2</sub>O<sub>3</sub> semiconductor. *J. Mater. Chem. C* 7, 10231–10239. <https://doi.org/10.1039/c9tc02910a>
- Chikoidze, E., Sartel, C., Yamano, H., Chi, Z., Bouchez, G., Jomard, F., Sallet, V., Guillot, G., Boukheddaden, K., Pérez-Tomás, A., Tchelidze, T., Dumont, Y., 2022. Electrical properties of p-type Zn:Ga<sub>2</sub>O<sub>3</sub> thin films. *J. Vac. Sci. Technol. A* 40, 043401. <https://doi.org/10.1116/6.0001766>
- Chikoidze, E., Tchelidze, T., Sartel, C., Chi, Z., Kabouche, R., Madaci, I., Rubio, C., Mohamed, H., Sallet, V., Medjdoub, F., Perez-Tomas, A., Dumont, Y., 2020b. Ultra-high critical electric field of 13.2 MV/cm for Zn-doped p-type β-Ga<sub>2</sub>O<sub>3</sub>. *Mater. Today Phys.* 15, 100263. <https://doi.org/10.1016/j.mtphys.2020.100263>

- 
- Chikoidze, E., Tchelidze, T., Sartel, C., Chi, Z., Kabouche, R., Madaci, I., Rubio, C., Mohamed, H., Sallet, V., Medjdoub, F., Perez-Tomas, A., Dumont, Y., 2020c. Ultra-high critical electric field of 13.2 MV/cm for Zn-doped *p*-type  $\beta$ -Ga<sub>2</sub>O<sub>3</sub> 15.
- Chikoidze, E., von Bardeleben, H.J., Akaiwa, K., Shigematsu, E., Kaneko, K., Fujita, S., Dumont, Y., 2016. Electrical, optical, and magnetic properties of Sn doped  $\alpha$ -Ga<sub>2</sub>O<sub>3</sub> thin films. *J. Appl. Phys.* 120, 025109. <https://doi.org/10.1063/1.4958860>
- Chu, T.L., Kelm, R.W., 1975. The Preparation and Properties of Aluminum Nitride Films. *J. Electrochem. Soc.* 122, 995. <https://doi.org/10.1149/1.2134385>
- COP21 Webpage, 2015. La conférence de Paris ou COP21 [WWW Document]. Fr. Dipl. - Ministère Eur. Aff. Étrangères. URL <https://www.diplomatie.gouv.fr/fr/politique-etrangere-de-la-france/climat-et-environnement/la-lutte-contre-les-changements-climatiques/la-conference-de-paris-ou-cop21/> (accessed 4.4.22).
- COP26 Webpage, 2021. UN Climate Change Conference (COP26) at the SEC – Glasgow 2021 [WWW Document]. UN Clim. Change Conf. COP26 SEC – Glasg. 2021. URL <https://ukcop26.org/> (accessed 4.4.22).
- Cui, H., Mohamed, H.F., Xia, C., Sai, Q., Zhou, W., Qi, H., Zhao, J., Si, J., Ji, X., 2019. Tuning electrical conductivity of  $\beta$ -Ga<sub>2</sub>O<sub>3</sub> single crystals by Ta doping. *J. Alloys Compd.* 788, 925–928. <https://doi.org/10.1016/j.jallcom.2019.02.076>
- Cullity, B.D., 1956. Elements of X-ray Diffraction.
- Dazai, T., Yasui, S., Taniyama, T., Itoh, M., 2020. Cation-Deficiency-Induced Crystal-Site Engineering for ZnGa<sub>2</sub>O<sub>4</sub>:Mn<sup>2+</sup> Thin Film. *Inorg. Chem.* 59, 8744–8748. <https://doi.org/10.1021/acs.inorgchem.0c00359>
- De Souza, R.A., Mueller, D.N., 2021. Electrochemical methods for determining ionic charge in solids. *Nat. Mater.* 20, 443–446. <https://doi.org/10.1038/s41563-020-0790-9>
- De Vos, A., Lejaeghere, K., Vanpoucke, D.E.P., Joos, J.J., Smet, P.F., Hemelsoet, K., 2016. First-Principles Study of Antisite Defect Configurations in ZnGa<sub>2</sub>O<sub>4</sub>:Cr Persistent Phosphors. *Inorg. Chem.* 55, 2402–2412. <https://doi.org/10.1021/acs.inorgchem.5b02805>
- Deák, P., Duy Ho, Q., Seemann, F., Aradi, B., Lorke, M., Frauenheim, T., 2017. Choosing the correct hybrid for defect calculations: A case study on intrinsic carrier trapping in  $\beta$ -Ga<sub>2</sub>O<sub>3</sub>. *Phys. Rev. B* 95, 075208. <https://doi.org/10.1103/PhysRevB.95.075208>
- Dixit, H., Tandon, N., Cottenier, S., Saniz, R., Lamoen, D., Partoens, B., Van Speybroeck, V., Waroquier, M., 2011. Electronic structure and band gap of zinc spinel oxides beyond LDA: ZnAl<sub>2</sub>O<sub>4</sub>, ZnGa<sub>2</sub>O<sub>4</sub> and ZnIn<sub>2</sub>O<sub>4</sub>. *New J. Phys.* 13, 063002. <https://doi.org/10.1088/1367-2630/13/6/063002>
- Dohy, D., Lucazeau, G., Revcolevschi, A., 1982. Raman spectra and valence force field of single-crystalline  $\beta$ -Ga<sub>2</sub>O<sub>3</sub>. *J. Solid State Chem.* 45, 180–192. [https://doi.org/10.1016/0022-4596\(82\)90274-2](https://doi.org/10.1016/0022-4596(82)90274-2)
- Dong, L., Jia, R., Xin, B., Peng, B., Zhang, Y., 2017. Effects of oxygen vacancies on the structural and optical properties of  $\beta$ -Ga<sub>2</sub>O<sub>3</sub>. *Sci. Rep.* 7, 40160. <https://doi.org/10.1038/srep40160>

- 
- Dupin, J.-C., Gonbeau, D., Vinatier, P., Levasseur, A., 2000. Systematic XPS studies of metal oxides, hydroxides and peroxides. *Phys. Chem. Chem. Phys.* 2, 1319–1324. <https://doi.org/10.1039/A908800H>
- Emin, D., 1977. The sign of the Hall effect in hopping conduction. *Philos. Mag. J. Theor. Exp. Appl. Phys.* 35, 1189–1198. <https://doi.org/10.1080/14786437708232944>
- Errandonea, D., Kumar, R.S., Manjón, F.J., Ursaki, V.V., Rusu, E.V., 2009. Post-spinel transformations and equation of state in  $\text{ZnGa}_2\text{O}_4$ : Determination at high pressure by in situ x-ray diffraction. *Phys. Rev. B* 79, 024103. <https://doi.org/10.1103/PhysRevB.79.024103>
- Ezeh, C.V., Egbo, K.O., Musah, J.-D., Yu, K.M., 2023. Wide gap p-type NiO-Ga<sub>2</sub>O<sub>3</sub> alloy via electronic band engineering. *J. Alloys Compd.* 932, 167275. <https://doi.org/10.1016/j.jallcom.2022.167275>
- Feng, Q., Liu, J., Yang, Y., Pan, D., Xing, Y., Shi, X., Xia, X., Liang, H., 2016. Catalytic growth and characterization of single crystalline Zn doped p-type  $\beta$ -Ga<sub>2</sub>O<sub>3</sub> nanowires. *J. Alloys Compd.* 687, 964–968. <https://doi.org/10.1016/j.jallcom.2016.06.274>
- Feng, W., Wang, X., Zhang, J., Wang, L., Zheng, W., Hu, P., Cao, W., Yang, B., 2014. Synthesis of two-dimensional  $\beta$ -Ga<sub>2</sub>O<sub>3</sub> nanosheets for high-performance solar blind photodetectors. *J. Mater. Chem. C* 2, 3254–3259. <https://doi.org/10.1039/C3TC31899K>
- Feng, Z., Anhar Uddin Bhuiyan, A.F.M., Karim, M.R., Zhao, H., 2019. MOCVD homoepitaxy of Si-doped (010)  $\beta$ -Ga<sub>2</sub>O<sub>3</sub> thin films with superior transport properties. *Appl. Phys. Lett.* 114, 250601. <https://doi.org/10.1063/1.5109678>
- Feng, Z., Bhuiyan, A.F.M.A.U., Xia, Z., Moore, W., Chen, Z., McGlone, J.F., Daughton, D.R., Arehart, A.R., Ringel, S.A., Rajan, S., Zhao, H., 2020. Probing Charge Transport and Background Doping in Metal-Organic Chemical Vapor Deposition-Grown (010)  $\beta$ -Ga<sub>2</sub>O<sub>3</sub>. *Phys. Status Solidi RRL – Rapid Res. Lett.* 14, 2000145. <https://doi.org/10.1002/pssr.202000145>
- Fischer, A.J., Dickerson, J.R., Armstrong, A.M., Moseley, M.W., Crawford, M.H., King, M.P., Allerman, A.A., Kaplar, R.J., van Heukelom, M.S., Wierer, J.J., 2016. High voltage and high current density vertical GaN power diodes. *Electron. Lett.* 52. <https://doi.org/10.1049/el.2016.1156>
- Fontserè, A., Pérez-Tomás, A., Placidi, M., Fernández-Martínez, P., Baron, N., Chenot, S., Cordier, Y., Moreno, J.C., Gammon, P.M., Jennings, M.R., 2011. Temperature dependence of Al/Ti-based Ohmic contact to GaN devices: HEMT and MOSFET. *Microelectron. Eng.* 88, 3140–3144. <https://doi.org/10.1016/j.mee.2011.06.015>
- Freitas, J., Kuramata, A., Glaser, E., Koehler, A., Tadjer, M., Luna, L., Feigelson, B., Mahadik, N., Hobart, K., Kub, F., 2018. Ga<sub>2</sub>O<sub>3</sub> Schottky barrier and heterojunction diodes for power electronics applications, in: Chyi, J.-I., Morkoç, H., Fujioka, H. (Eds.), Gallium Nitride Materials and Devices XIII. Presented at the Gallium Nitride Materials and Devices XIII, SPIE, San Francisco, United States, p. 37. <https://doi.org/10.1117/12.2292211>
- Frodason, Y.K., Zimmermann, C., Verhoeven, E.F., Weiser, P.M., Vines, L., Varley, J.B., 2021. Multistability of isolated and hydrogenated Ga–O divacancies in  $\beta$ -Ga<sub>2</sub>O<sub>3</sub>. *Phys. Rev. Mater.* 5, 025402. <https://doi.org/10.1103/PhysRevMaterials.5.025402>
-

- 
- Galazka, Z., 2018.  $\beta$ -Ga<sub>2</sub>O<sub>3</sub> for wide-bandgap electronics and optoelectronics. *Semicond. Sci. Technol.* 33, 113001. <https://doi.org/10.1088/1361-6641/aadf78>
- Galazka, Z., Ganschow, S., Irmischer, K., Klimm, D., Albrecht, M., Schewski, R., Pietsch, M., Schulz, T., Dittmar, A., Kwasniewski, A., Grueneberg, R., Anooz, S.B., Popp, A., Juda, U., Hanke, I.M., Schroeder, T., Bickermann, M., 2021. Bulk single crystals of  $\beta$ -Ga<sub>2</sub>O<sub>3</sub> and Ga-based spinels as ultra-wide bandgap transparent semiconducting oxides. *Prog. Cryst. Growth Charact. Mater.* 67, 100511. <https://doi.org/10.1016/j.pcrysgrow.2020.100511>
- Galazka, Z., Ganschow, S., Schewski, R., Irmischer, K., Klimm, D., Kwasniewski, A., Pietsch, M., Fiedler, A., Schulze-Jonack, I., Albrecht, M., Schröder, T., Bickermann, M., 2019. Ultra-wide bandgap, conductive, high mobility, and high quality melt-grown bulk ZnGa<sub>2</sub>O<sub>4</sub> single crystals. *APL Mater.* 7, 022512. <https://doi.org/10.1063/1.5053867>
- Galazka, Z., Irmischer, K., Schewski, R., Hanke, I.M., Pietsch, M., Ganschow, S., Klimm, D., Dittmar, A., Fiedler, A., Schroeder, T., Bickermann, M., 2020a. Czochralski-grown bulk  $\beta$ -Ga<sub>2</sub>O<sub>3</sub> single crystals doped with mono-, di-, tri-, and tetravalent ions. *J. Cryst. Growth* 529, 125297. <https://doi.org/10.1016/j.jcrysgro.2019.125297>
- Galazka, Z., Irmischer, K., Uecker, R., Bertram, R., Pietsch, M., Kwasniewski, A., Naumann, M., Schulz, T., Schewski, R., Klimm, D., Bickermann, M., 2014. On the bulk  $\beta$ -Ga<sub>2</sub>O<sub>3</sub> single crystals grown by the Czochralski method. *J. Cryst. Growth* 404, 184–191. <https://doi.org/10.1016/j.jcrysgro.2014.07.021>
- Galazka, Z., Schewski, R., Irmischer, K., Drozdowski, W., Witkowski, M.E., Makowski, M., Wojtowicz, A.J., Hanke, I.M., Pietsch, M., Schulz, T., Klimm, D., Ganschow, S., Dittmar, A., Fiedler, A., Schroeder, T., Bickermann, M., 2020b. Bulk  $\beta$ -Ga<sub>2</sub>O<sub>3</sub> single crystals doped with Ce, Ce+Si, Ce+Al, and Ce+Al+Si for detection of nuclear radiation. *J. Alloys Compd.* 818, 152842. <https://doi.org/10.1016/j.jallcom.2019.152842>
- Galazka, Z., Uecker, R., Irmischer, K., Albrecht, M., Klimm, D., Pietsch, M., Brützam, M., Bertram, R., Ganschow, S., Fornari, R., 2010. Czochralski growth and characterization of  $\beta$ -Ga<sub>2</sub>O<sub>3</sub> single crystals. *Cryst. Res. Technol.* 45, 1229–1236. <https://doi.org/10.1002/crat.201000341>
- Galazka, Z., Uecker, R., Klimm, D., Irmischer, K., Naumann, M., Pietsch, M., Kwasniewski, A., Bertram, R., Ganschow, S., Bickermann, M., 2016. Scaling-Up of Bulk  $\beta$ -Ga<sub>2</sub>O<sub>3</sub> Single Crystals by the Czochralski Method. *ECS J. Solid State Sci. Technol.* 6, Q3007. <https://doi.org/10.1149/2.0021702jss>
- Gal'perin, M., German, P., n.d. Halleffect under hoppingconductionconditions.
- Garten, L.M., Zakutayev, A., Perkins, J.D., Gorman, B.P., Ndione, P.F., Ginley, D.S., 2016. Structure property relationships in gallium oxide thin films grown by pulsed laser deposition. *MRS Commun.* 6, 348–353. <https://doi.org/10.1557/mrc.2016.50>
- Gazit, D., Feigelson, R.S., 1988. Laser-heated pedestal growth of high Tc Bi-Sr-Ca-Cu-O superconducting fibers. *J. Cryst. Growth* 91, 318–330. [https://doi.org/10.1016/0022-0248\(88\)90245-X](https://doi.org/10.1016/0022-0248(88)90245-X)
- Geballe, T.H., Hull, G.W., 1955. Seebeck Effect in Silicon. *Phys. Rev.* 98, 940–947. <https://doi.org/10.1103/PhysRev.98.940>
-

- 
- Geller, S., 1960. Crystal Structure of  $\beta$ -Ga<sub>2</sub>O<sub>3</sub>. *J. Chem. Phys.* 33, 676–684. <https://doi.org/10.1063/1.1731237>
- Ghosh, K., Singiseti, U., 2018a. Impact ionization in  $\beta$ -Ga<sub>2</sub>O<sub>3</sub>. *J. Appl. Phys.* 124. <https://doi.org/10.1063/1.5034120>
- Ghosh, K., Singiseti, U., 2018b. Impact Ionization in  $\beta$ -Ga<sub>2</sub>O<sub>3</sub>. *ArXiv170509203 Cond-Mat*.
- Ghosh, K., Singiseti, U., 2017. Ab initio velocity-field curves in monoclinic  $\beta$ -Ga<sub>2</sub>O<sub>3</sub>. *J. Appl. Phys.* 122, 035702. <https://doi.org/10.1063/1.4986174>
- Ghosh, K., Singiseti, U., 2014. Calculation of electron impact ionization co-efficient in  $\beta$ -Ga<sub>2</sub>O<sub>3</sub>, in: 72nd Device Research Conference. Presented at the 2014 72nd Annual Device Research Conference (DRC), IEEE, Santa Barbara, CA, USA, pp. 71–72. <https://doi.org/10.1109/DRC.2014.6872302>
- Gong, H., Wang, Z., Yu, X., Ren, F., Yang, Y., Lv, Y., Feng, Z., Gu, S., Zhang, R., Zheng, Y., Ye, J., 2021. Field-Plated NiO/Ga<sub>2</sub>O<sub>3</sub> p-n Heterojunction Power Diodes With High-Temperature Thermal Stability and Near Unity Ideality Factors. *IEEE J. Electron Devices Soc.* 9, 1166–1171. <https://doi.org/10.1109/JEDS.2021.3130305>
- Goto, K., Konishi, K., Murakami, H., Kumagai, Y., Monemar, B., Higashiwaki, M., Kuramata, A., Yamakoshi, S., 2018. Halide vapor phase epitaxy of Si doped  $\beta$ -Ga<sub>2</sub>O<sub>3</sub> and its electrical properties. *Thin Solid Films* 666, 182–184. <https://doi.org/10.1016/j.tsf.2018.09.006>
- Goyal, A., Zakutayev, A., Stevanović, V., Lany, S., 2021. Computational Fermi level engineering and doping-type conversion of Ga<sub>2</sub>O<sub>3</sub> via three-step synthesis process. *ArXiv210316639 Cond-Mat*.
- Goyal, N., Dusari, S., Bardong, J., Medjdoub, F., Kenda, A., Binder, A., 2016. Multilayer Pt/Al based ohmic contacts for AlGa<sub>N</sub>/Ga<sub>N</sub> heterostructures stable up to 600 °C ambient air. *Solid-State Electron.* 116, 107–110. <https://doi.org/10.1016/j.sse.2015.12.002>
- Greco, G., Iucolano, F., Roccaforte, F., 2016. Ohmic contacts to Gallium Nitride materials. *Appl. Surf. Sci.* 383, 324–345. <https://doi.org/10.1016/j.apsusc.2016.04.016>
- Greczynski, G., Hultman, L., 2020. X-ray photoelectron spectroscopy: Towards reliable binding energy referencing. *Prog. Mater. Sci.* 107, 100591. <https://doi.org/10.1016/j.pmatsci.2019.100591>
- Gu, M., Wolf, S.A., Lu, J., 2014. Two-Dimensional Mott Insulators in SrVO<sub>3</sub> Ultrathin Films. *Adv. Mater. Interfaces* 1, 1300126. <https://doi.org/10.1002/admi.201300126>
- Guo, D., Guo, Q., Chen, Z., Wu, Z., Li, P., Tang, W., 2019. Review of Ga<sub>2</sub>O<sub>3</sub>-based optoelectronic devices. *Mater. Today Phys.* 11, 100157. <https://doi.org/10.1016/j.mtphys.2019.100157>
- Guo, D., Qin, X., Lv, M., Shi, H., Su, Y., Yao, G., Wang, S., Li, C., Li, P., Tang, W., 2017. Decrease of oxygen vacancy by Zn-doped for improving solar-blind photoelectric performance in  $\beta$ -Ga<sub>2</sub>O<sub>3</sub> thin films. *Electron. Mater. Lett.* 13, 483–488. <https://doi.org/10.1007/s13391-017-7072-y>

- 
- Guo, Z., Verma, A., Wu, X., Sun, F., Hickman, A., Masui, T., Kuramata, A., Higashiwaki, M., Jena, D., Luo, T., 2015. Anisotropic thermal conductivity in single crystal  $\beta$ -gallium oxide. *Appl. Phys. Lett.* 106, 111909. <https://doi.org/10.1063/1.4916078>
- Gustafson, T.D., Jesenovec, J., Lenyk, C.A., Giles, N.C., McCloy, J.S., McCluskey, M.D., Halliburton, L.E., 2021. Zn acceptors in  $\beta$ -Ga<sub>2</sub>O<sub>3</sub> crystals. *J. Appl. Phys.* 129, 155701. <https://doi.org/10.1063/5.0047947>
- Hajnal, Z., Mir  J., Kiss, G., R i, F., De k, P., Herndon, R.C., Kuperberg, J.M., 1999. Role of oxygen vacancy defect states in the n-type conduction of  $\beta$ -Ga<sub>2</sub>O<sub>3</sub>. *J. Appl. Phys.* 86, 3792–3796. <https://doi.org/10.1063/1.371289>
- Halim, J., Lukatskaya, M.R., Cook, K.M., Lu, J., Smith, C.R., N slund, L.-., May, S.J., Hultman, L., Gogotsi, Y., Eklund, P., Barsoum, M.W., 2014. Transparent Conductive Two-Dimensional Titanium Carbide Epitaxial Thin Films. *Chem. Mater.* 26, 2374–2381. <https://doi.org/10.1021/cm500641a>
- Hao Yu, Schaeckers, M., Schram, T., Collaert, N., De Meyer, K., Horiguchi, N., Thean, A., Barla, K., 2014. A Simplified Method for (Circular) Transmission Line Model Simulation and Ultralow Contact Resistivity Extraction. *IEEE Electron Device Lett.* 35, 957–959. <https://doi.org/10.1109/LED.2014.2340821>
- Harwig, T., Schoonman, J., 1978. Electrical properties of  $\beta$ -Ga<sub>2</sub>O<sub>3</sub> single crystals. II. *J. Solid State Chem.* 23, 205–211. [https://doi.org/10.1016/0022-4596\(78\)90066-X](https://doi.org/10.1016/0022-4596(78)90066-X)
- Haynes, W.M., 2014. *CRC Handbook of Chemistry and Physics*. CRC Press.
- He, H., Orlando, R., Blanco, M.A., Pandey, R., Amzallag, E., Baraille, I., R at, M., 2006. First-principles study of the structural, electronic, and optical properties of  $\{\mathrm{Ga}\}_2\{\mathrm{O}\}_3$  in its monoclinic and hexagonal phases. *Phys. Rev. B* 74, 195123. <https://doi.org/10.1103/PhysRevB.74.195123>
- He, X., Wang, M., Meng, J., Hu, J., Jiang, Y., 2022. The effect of vacancy defects on the electronic properties of  $\beta$ -Ga<sub>2</sub>O<sub>3</sub>. *Comput. Mater. Sci.* 215, 111777. <https://doi.org/10.1016/j.commatsci.2022.111777>
- Higashiwaki, M., Konishi, K., Sasaki, K., Goto, K., Nomura, K., Thieu, Q.T., Togashi, R., Murakami, H., Kumagai, Y., Monemar, B., Koukitu, A., Kuramata, A., Yamakoshi, S., 2016a. Temperature-dependent capacitance–voltage and current–voltage characteristics of Pt/Ga<sub>2</sub>O<sub>3</sub> (001) Schottky barrier diodes fabricated on n–Ga<sub>2</sub>O<sub>3</sub> drift layers grown by halide vapor phase epitaxy. *Appl. Phys. Lett.* 108, 133503. <https://doi.org/10.1063/1.4945267>
- Higashiwaki, M., Sasaki, K., Kamimura, T., Hoi Wong, M., Krishnamurthy, D., Kuramata, A., Masui, T., Yamakoshi, S., 2013. Depletion-mode Ga<sub>2</sub>O<sub>3</sub> metal-oxide-semiconductor field-effect transistors on  $\beta$ -Ga<sub>2</sub>O<sub>3</sub> (010) substrates and temperature dependence of their device characteristics. *Appl. Phys. Lett.* 103, 123511. <https://doi.org/10.1063/1.4821858>
- Higashiwaki, M., Sasaki, K., Kuramata, A., Masui, T., Yamakoshi, S., 2012. Gallium oxide (Ga<sub>2</sub>O<sub>3</sub>) metal-semiconductor field-effect transistors on single-crystal  $\beta$ -Ga<sub>2</sub>O<sub>3</sub> (010) substrates. *Appl. Phys. Lett.* 100, 013504. <https://doi.org/10.1063/1.3674287>
- Higashiwaki, M., Sasaki, K., Murakami, H., Kumagai, Y., Koukitu, A., Kuramata, A., Masui, T., Yamakoshi, S., 2016b. Recent progress in Ga<sub>2</sub>O<sub>3</sub> power devices. *Semicond. Sci. Technol.* 31, 034001. <https://doi.org/10.1088/0268-1242/31/3/034001>
-

- 
- Hill, R.J., Craig, J.R., Gibbs, G.V., 1979. Systematics of the spinel structure type. *Phys. Chem. Miner.* 4, 317–339. <https://doi.org/10.1007/BF00307535>
- Ho, Q.D., Frauenheim, T., Deák, P., 2018. Origin of photoluminescence in  $\beta\text{-Ga}_2\text{O}_3$ . *Phys. Rev. B* 97, 115163. <https://doi.org/10.1103/PhysRevB.97.115163>
- Hoff, H.A., Waytena, G.L., Vold, C.L., Suehle, J.S., Isaacson, I.P., Rebbert, M.L., Ma, D.I., Harris, K., 1996. Ohmic contacts to semiconducting diamond using a Ti/Pt/Au trilayer metallization scheme. *Diam. Relat. Mater.* 5, 1450–1456. [https://doi.org/10.1016/S0925-9635\(96\)00566-3](https://doi.org/10.1016/S0925-9635(96)00566-3)
- Holstein, T., 1973. Sign of the hall coefficient in hopping-type charge-transport. *Philos. Mag.* 27, 225–233. <https://doi.org/10.1080/14786437308228926>
- Holstein, T., 1961. Hall Effect in Impurity Conduction. *Phys. Rev.* 124, 1329–1347. <https://doi.org/10.1103/PhysRev.124.1329>
- Hommedal, Y.K., Frodason, Y.K., Vines, L., Johansen, K.M.H., 2023. Trap-limited diffusion of Zn in  $\beta\text{-Ga}_2\text{O}_3$ . *Phys. Rev. Mater.* 7, 035401. <https://doi.org/10.1103/PhysRevMaterials.7.035401>
- Horng, R.-H., Huang, C.-Y., Ou, S.-L., Juang, T.-K., Liu, P.-L., 2017. Epitaxial Growth of  $\text{ZnGa}_2\text{O}_4$ : A New, Deep Ultraviolet Semiconductor Candidate. *Cryst. Growth Des.* 17, 6071–6078. <https://doi.org/10.1021/acs.cgd.7b01159>
- Horng, R.-H., Huang, P.-H., Li, Y.-S., Tarntair, F.-G., Tan, C.S., 2021. Reliability study on deep-ultraviolet photodetectors based on  $\text{ZnGa}_2\text{O}_4$  epilayers grown by MOCVD. *Appl. Surf. Sci.* 555, 149657. <https://doi.org/10.1016/j.apsusc.2021.149657>
- Hoshikawa, K., Kobayashi, T., Matsuki, Y., Ohba, E., Kobayashi, T., 2020a. 2-inch diameter (1 0 0)  $\beta\text{-Ga}_2\text{O}_3$  crystal growth by the vertical Bridgman technique in a resistance heating furnace in ambient air. *J. Cryst. Growth* 545, 125724. <https://doi.org/10.1016/j.jcrysgro.2020.125724>
- Hoshikawa, K., Kobayashi, T., Ohba, E., Kobayashi, T., 2020b. 50 mm diameter Sn-doped (001)  $\beta\text{-Ga}_2\text{O}_3$  crystal growth using the vertical Bridgeman technique in ambient air. *J. Cryst. Growth* 546, 125778. <https://doi.org/10.1016/j.jcrysgro.2020.125778>
- Hoshikawa, K., Ohba, E., Kobayashi, T., Yanagisawa, J., Miyagawa, C., Nakamura, Y., 2016. Growth of  $\beta\text{-Ga}_2\text{O}_3$  single crystals using vertical Bridgman method in ambient air. *J. Cryst. Growth* 447, 36–41. <https://doi.org/10.1016/j.jcrysgro.2016.04.022>
- Hossain, E., Kulkarni, R., Mondal, R., Guddolian, S., Rahman, A.A., Thamizhavel, A., Bhattacharya, A., 2019. Optimization of Gas Ambient for High Quality  $\beta\text{-Ga}_2\text{O}_3$  Single Crystals Grown by the Optical Floating Zone Technique. *ECS J. Solid State Sci. Technol.* 8, Q3144. <https://doi.org/10.1149/2.0261907jss>
- Hu, H., Feng, Z., Wang, Y., Liu, Y., Dong, H., Liu, Y.-Y., Hao, Y., Han, G., 2022. The role of surface pretreatment by low temperature  $\text{O}_2$  gas annealing for  $\beta\text{-Ga}_2\text{O}_3$  Schottky barrier diodes. *Appl. Phys. Lett.* 120, 073501. <https://doi.org/10.1063/5.0080343>
- Hu, Z., Lv, Y., Zhao, C., Feng, Q., Feng, Z., Dang, K., Tian, X., Zhang, Y., Ning, J., Zhou, H., Kang, X., Zhang, J., Hao, Y., 2020. Beveled Fluoride Plasma Treatment for Vertical  $\beta\text{-Ga}_2\text{O}_3$  Schottky Barrier Diode With High Reverse Blocking Voltage and Low Turn-On Voltage. *IEEE Electron Device Lett.* 41, 441–444. <https://doi.org/10.1109/LED.2020.2968587>
-

- 
- Huan, Y.-W., Sun, S.-M., Gu, C.-J., Liu, W.-J., Ding, S.-J., Yu, H.-Y., Xia, C.-T., Zhang, D.W., 2018. Recent Advances in  $\beta$ -Ga<sub>2</sub>O<sub>3</sub>–Metal Contacts. *Nanoscale Res. Lett.* 13, 246. <https://doi.org/10.1186/s11671-018-2667-2>
- Huang, P.-H., Shen, Y.-C., Tung, C.-Y., Huang, C.-Y., Tan, C.S., Horng, R.-H., 2020. Energy-Saving ZnGa<sub>2</sub>O<sub>4</sub> Phototransistor Improved by Thermal Annealing. *ACS Appl. Electron. Mater.* 2, 3515–3521. <https://doi.org/10.1021/acsaelm.0c00394>
- Ingebrigtsen, M.E., Kuznetsov, A.Yu., Svensson, B.G., Alfieri, G., Mihaila, A., Badstübner, U., Perron, A., Vines, L., Varley, J.B., 2019a. Impact of proton irradiation on conductivity and deep level defects in  $\beta$ -Ga<sub>2</sub>O<sub>3</sub>. *APL Mater.* 7, 022510. <https://doi.org/10.1063/1.5054826>
- Ingebrigtsen, M.E., Kuznetsov, A.Yu., Svensson, B.G., Alfieri, G., Mihaila, A., Vines, L., 2019b. Generation and metastability of deep level states in  $\beta$ -Ga<sub>2</sub>O<sub>3</sub> exposed to reverse bias at elevated temperatures. *J. Appl. Phys.* 125, 185706. <https://doi.org/10.1063/1.5088655>
- Irmscher, K., Galazka, Z., Pietsch, M., Uecker, R., Fornari, R., 2011. Electrical properties of  $\beta$ -Ga<sub>2</sub>O<sub>3</sub> single crystals grown by the Czochralski method. *J. Appl. Phys.* 110, 063720. <https://doi.org/10.1063/1.3642962>
- Islam, M.M., Liedke, M.O., Winarski, D., Butterling, M., Wagner, A., Hosemann, P., Wang, Y., Uberuaga, B., Selim, F.A., 2020. Chemical manipulation of hydrogen induced high p-type and n-type conductivity in Ga<sub>2</sub>O<sub>3</sub>. *Sci. Rep.* 10, 6134. <https://doi.org/10.1038/s41598-020-62948-2>
- Jacobs, B., Kramer, M.C.J.C.M., Geluk, E.J., Karouta, F., 2002. Optimisation of the Ti/Al/Ni/Au ohmic contact on AlGa<sub>N</sub>/Ga<sub>N</sub> FET structures. *J. Cryst. Growth* 241, 15–18. [https://doi.org/10.1016/S0022-0248\(02\)00920-X](https://doi.org/10.1016/S0022-0248(02)00920-X)
- Jang, Y., Hong, S., Seo, J., Cho, H., Char, K., Galazka, Z., 2020. Thin film transistors based on ultra-wide bandgap spinel ZnGa<sub>2</sub>O<sub>4</sub>. *Appl. Phys. Lett.* 116, 202104. <https://doi.org/10.1063/5.0007716>
- Janowitz, C., Scherer, V., Mohamed, M., Krapf, A., Dwelk, H., Manzke, R., Galazka, Z., Uecker, R., Irmscher, K., Fornari, R., Michling, M., Schmeißer, D., Weber, J.R., Varley, J.B., Walle, C.G.V. de, 2011. Experimental electronic structure of In<sub>2</sub>O<sub>3</sub> and Ga<sub>2</sub>O<sub>3</sub>. *New J. Phys.* 13, 085014. <https://doi.org/10.1088/1367-2630/13/8/085014>
- Jeong, I.-K., Park, H.L., Mho, S., 1998. Two self-activated optical centers of blue emission in zinc gallate. *Solid State Commun.* 105, 179–183. [https://doi.org/10.1016/S0038-1098\(97\)10101-6](https://doi.org/10.1016/S0038-1098(97)10101-6)
- Jesenovec, J., Varley, J., Karcher, S.E., McCloy, J.S., 2021a. Electronic and optical properties of Zn-doped  $\beta$ -Ga<sub>2</sub>O<sub>3</sub> Czochralski single crystals. *J. Appl. Phys.* 129, 225702. <https://doi.org/10.1063/5.0050468>
- Jesenovec, J., Weber, M.H., Pansegrau, C., McCluskey, M.D., Lynn, K.G., McCloy, J.S., 2021b. Gallium vacancy formation in oxygen annealed  $\beta$ -Ga<sub>2</sub>O<sub>3</sub>. *J. Appl. Phys.* 129, 245701. <https://doi.org/10.1063/5.0053325>
- Jiang, P., Qian, X., Li, X., Yang, R., 2018. Three-dimensional anisotropic thermal conductivity tensor of single crystalline  $\beta$ -Ga<sub>2</sub>O<sub>3</sub>. *Appl. Phys. Lett.* 113, 232105. <https://doi.org/10.1063/1.5054573>
-

- 
- Jiang, Z.X., Wu, Z.Y., Ma, C.C., Deng, J.N., Zhang, H., Xu, Y., Ye, J.D., Fang, Z.L., Zhang, G.Q., Kang, J.Y., Zhang, T.-Y., 2020. P-type  $\beta$ -Ga<sub>2</sub>O<sub>3</sub> metal-semiconductor-metal solar-blind photodetectors with extremely high responsivity and gain-bandwidth product. *Mater. Today Phys.* 14, 100226. <https://doi.org/10.1016/j.mtphys.2020.100226>
- Johnson, J.M., Chen, Z., Varley, J.B., Jackson, C.M., Farzana, E., Zhang, Z., Arehart, A.R., Huang, H.-L., Genc, A., Ringel, S.A., Van de Walle, C.G., Muller, D.A., Hwang, J., 2019. Unusual Formation of Point-Defect Complexes in the Ultrawide-Band-Gap Semiconductor  $\beta$ -Ga<sub>2</sub>O<sub>3</sub>. *Phys. Rev. X* 9, 041027. <https://doi.org/10.1103/PhysRevX.9.041027>
- Kabilova, Z., Kurdak, C., Peterson, R.L., 2019. Observation of impurity band conduction and variable range hopping in heavily doped (010)  $\beta$ -Ga<sub>2</sub>O<sub>3</sub>. *Semicond. Sci. Technol.* 34, 03LT02. <https://doi.org/10.1088/1361-6641/ab0150>
- Kahan, H.M., Macfarlane, R.M., 2003. Optical and Microwave Spectra of Cr<sup>3+</sup> in the Spinel ZnGa<sub>2</sub>O<sub>4</sub>. *J. Chem. Phys.* 54, 5197–5205. <https://doi.org/10.1063/1.1674815>
- Kananen, B.E., Halliburton, L.E., Stevens, K.T., Foundos, G.K., Giles, N.C., 2017. Gallium vacancies in  $\beta$ -Ga<sub>2</sub>O<sub>3</sub> crystals. *Appl. Phys. Lett.* 110, 202104. <https://doi.org/10.1063/1.4983814>
- Kaneko, K., Masuda, Y., Kan, S., Takahashi, I., Kato, Y., Shinohe, T., Fujita, S., 2021. Ultra-wide bandgap corundum-structured p-type  $\alpha$ -(Ir,Ga)<sub>2</sub>O<sub>3</sub> alloys for  $\alpha$ -Ga<sub>2</sub>O<sub>3</sub> electronics. *Appl. Phys. Lett.* 118, 102104. <https://doi.org/10.1063/5.0027297>
- Karazhanov, S.Zh., Ravindran, P., 2010. Ab Initio Study Of Double Oxides ZnX<sub>2</sub>O<sub>4</sub> (X=Al, Ga, In) Having Spinel Structure: ZnX<sub>2</sub>O<sub>4</sub> (X=Al, Ga, In) Spinals. *J. Am. Ceram. Soc.* 93, 3335–3341. <https://doi.org/10.1111/j.1551-2916.2010.03864.x>
- Karjalainen, A., Makkonen, I., Etula, J., Goto, K., Murakami, H., Kumagai, Y., Tuomisto, F., 2021. Split Ga vacancies in n-type and semi-insulating  $\beta$ -Ga<sub>2</sub>O<sub>3</sub> single crystals. *Appl. Phys. Lett.* 118, 072104. <https://doi.org/10.1063/5.0033930>
- Keldysh, L. V., 1960. Kinetic Theory of Impact Ionization in Semiconductors. *J Exptl Theor. Phys USSR* 37, 713–727.
- Kim, H.J., Song, I.C., Sim, J.H., Kim, H., Kim, D., Ihm, Y.E., Choo, W.K., 2004. Electrical and magnetic properties of spinel-type magnetic semiconductor ZnCo<sub>2</sub>O<sub>4</sub> grown by reactive magnetron sputtering. *J. Appl. Phys.* 95, 7387–7389. <https://doi.org/10.1063/1.1688571>
- Kim, H.W., Kim, N.H., 2004. Formation of amorphous and crystalline gallium oxide nanowires by metalorganic chemical vapor deposition. *Appl. Surf. Sci.* 233, 294–298. <https://doi.org/10.1016/j.apsusc.2004.03.262>
- Kim, J., Ren, F., J. Pearton, S., 2019. Will surface effects dominate in quasi-two-dimensional gallium oxide for electronic and photonic devices? *Nanoscale Horiz.* 4, 1251–1255. <https://doi.org/10.1039/C9NH00273A>
- Kim, Y.-S., Park, C.H., 2009. Rich Variety of Defects in ZnO via an Attractive Interaction between O Vacancies and Zn Interstitials: Origin of n-Type Doping. *Phys. Rev. Lett.* 102, 086403. <https://doi.org/10.1103/PhysRevLett.102.086403>

- 
- Klein, R.S., 1985. Investigation of the Hall effect in impurity-hopping conduction. *Phys. Rev. B* 31, 2014–2021. <https://doi.org/10.1103/PhysRevB.31.2014>
- Klootwijk, J.H., Timmering, C.E., 2004. Merits and limitations of circular TLM structures for contact resistance determination for novel III-V HBTs. *Proc. 2004 Int. Conf. Microelectron. Test Struct. IEEE Cat No04CH37516* 247–252.
- Korhonen, E., Tuomisto, F., Gogova, D., Wagner, G., Baldini, M., Galazka, Z., Schewski, R., Albrecht, M., 2015. Electrical compensation by Ga vacancies in Ga<sub>2</sub>O<sub>3</sub> thin films. *Appl. Phys. Lett.* 106, 242103. <https://doi.org/10.1063/1.4922814>
- Krishna, K.M., Nisha, M., Reshmi, R., Manoj, R., Asha, A.S., Jayaraj, M.K., 2005. ELECTRICAL AND OPTICAL PROPERTIES OF ZnGa<sub>2</sub>O<sub>4</sub> THIN FILMS DEPOSITED BY PULSED LASER DEPOSITION. *Mater. FORUM* 29, 243–247.
- Kumar, V., Swart, H.C., Ntwaaborwa, O.M., Kroon, R.E., Terblans, J.J., Shaat, S.K.K., Yousif, A., Duvenhage, M.M., 2013. Origin of the red emission in zinc oxide nanophosphors. *Mater. Lett.* 101, 57–60. <https://doi.org/10.1016/j.matlet.2013.03.073>
- Kuramata, A., Koshi, K., Watanabe, S., Yamaoka, Y., Masui, T., Yamakoshi, S., 2016. High-quality β-Ga<sub>2</sub>O<sub>3</sub> single crystals grown by edge-defined film-fed growth. *Jpn. J. Appl. Phys.* 55, 1202A2. <https://doi.org/10.7567/JJAP.55.1202A2>
- Kuramata, A., Koshi, K., Watanabe, S., Yamaoka, Y., Masui, T., Yamakoshi, S., Corporation, T., 2018. Bulk Crystal Growth of Ga<sub>2</sub>O<sub>3</sub>. *Oxide-Based Mater. Devices IX* 10533. <https://doi.org/10.1117/12.2301405>
- Kyrtsos, A., Matsubara, M., Bellotti, E., 2018. On the feasibility of p-type Ga<sub>2</sub>O<sub>3</sub>. *Appl. Phys. Lett.* 112, 032108. <https://doi.org/10.1063/1.5009423>
- Lany, S., 2018. Defect phase diagram for doping of Ga<sub>2</sub>O<sub>3</sub>. *APL Mater.* 6, 046103. <https://doi.org/10.1063/1.5019938>
- Lee, M.-H., Chou, T.-S., Bin Anooz, S., Galazka, Z., Popp, A., Peterson, R.L., 2022a. Exploiting the Nanostructural Anisotropy of β-Ga<sub>2</sub>O<sub>3</sub> to Demonstrate Giant Improvement in Titanium/Gold Ohmic Contacts. *ACS Nano* 16, 11988–11997. <https://doi.org/10.1021/acsnano.2c01957>
- Lee, M.-H., Chou, T.-S., Bin Anooz, S., Galazka, Z., Popp, A., Peterson, R.L., 2022b. Effect of post-metallization anneal on (100) Ga<sub>2</sub>O<sub>3</sub>/Ti–Au ohmic contact performance and interfacial degradation. *APL Mater.* 10, 091105. <https://doi.org/10.1063/5.0096245>
- Lee, M.-H., Peterson, R.L., 2020. Accelerated Aging Stability of β-Ga<sub>2</sub>O<sub>3</sub>–Titanium/Gold Ohmic Interfaces. *ACS Appl. Mater. Interfaces* 12, 46277–46287. <https://doi.org/10.1021/acsmi.0c10598>
- Lee, M.-H., Peterson, R.L., 2019a. Interfacial reactions of titanium/gold ohmic contacts with Sn-doped β-Ga<sub>2</sub>O<sub>3</sub>. *APL Mater.* 7, 022524. <https://doi.org/10.1063/1.5054624>
- Lee, M.-H., Peterson, R.L., 2019b. Annealing Induced Interfacial Evolution of Titanium/Gold Metallization on Unintentionally Doped β-Ga<sub>2</sub>O<sub>3</sub>. *ECS J. Solid State Sci. Technol.* 8, Q3176. <https://doi.org/10.1149/2.0321907jss>
- Lee, Y.E., Norton, D.P., Budai, J.D., Wei, Y., 2001. Enhanced ultraviolet photoconductivity in semiconducting ZnGa<sub>2</sub>O<sub>4</sub> thin films. *J. Appl. Phys.* 90, 3863–3866. <https://doi.org/10.1063/1.1396829>
-

- 
- Leedy, K.D., Chabak, K.D., Vasilyev, V., Look, D.C., Boeckl, J.J., Brown, J.L., Tetlak, S.E., Green, A.J., Moser, N.A., Crespo, A., Thomson, D.B., Fitch, R.C., McCandless, J.P., Jessen, G.H., 2017. Highly conductive homoepitaxial Si-doped Ga<sub>2</sub>O<sub>3</sub> films on (010) β-Ga<sub>2</sub>O<sub>3</sub> by pulsed laser deposition. *Appl. Phys. Lett.* 111, 012103. <https://doi.org/10.1063/1.4991363>
- Li, C., Yan, J.L., Zhang, L.Y., Zhao, G., 2012. Electronic structures and optical properties of Zn-doped β-Ga<sub>2</sub>O<sub>3</sub> with different doping sites. *Chin. Phys. B* 21, 1–6. <https://doi.org/10.1088/1674-1056/21/12/127104>
- Li, J., 2010. Cation distribution dependence of magnetic properties of sol–gel prepared MnFe<sub>2</sub>O<sub>4</sub> spinel ferrite nanoparticles. *J. Magn. Magn. Mater.* 5.
- Li, L., Liao, F., Hu, X., 2020. The possibility of N–P codoping to realize P type β-Ga<sub>2</sub>O<sub>3</sub>. *Superlattices Microstruct.* 141, 106502. <https://doi.org/10.1016/j.spmi.2020.106502>
- Li, N., Duan, X., Yu, F., Jiang, H., 2017. Effects of preparation method and temperature on the cation distribution of ZnGa<sub>2</sub>O<sub>4</sub> spinel studied by X-ray photoelectron spectroscopy. *Vacuum* 142, 1–4. <https://doi.org/10.1016/j.vacuum.2017.04.035>
- Li, W., Nomoto, K., Hu, Z., Jena, D., Xing, H.G., 2021. ON-Resistance of Ga<sub>2</sub>O<sub>3</sub> Trench-MOS Schottky Barrier Diodes: Role of Sidewall Interface Trapping. *IEEE Trans. Electron Devices* 68, 2420–2426. <https://doi.org/10.1109/TED.2021.3067856>
- Li, X., Lu, H.L., Ma, H.P., Yang, J.G., Chen, J.X., Huang, W., Guo, Q., Feng, J.J., Zhang, D.W., 2019. Chemical, optical, and electrical characterization of Ga<sub>2</sub>O<sub>3</sub> thin films grown by plasma-enhanced atomic layer deposition. *Curr. Appl. Phys.* 19, 72–81. <https://doi.org/10.1016/j.cap.2018.11.013>
- Li, Y., Trinchi, A., Wlodarski, W., Galatsis, K., Kalantar-zadeh, K., 2003. Investigation of the oxygen gas sensing performance of Ga<sub>2</sub>O<sub>3</sub> thin films with different dopants. *Sens. Actuators B Chem.* 93, 431–434. [https://doi.org/10.1016/S0925-4005\(03\)00171-0](https://doi.org/10.1016/S0925-4005(03)00171-0)
- Li, Z., Jiao, T., Yu, J., Hu, D., Lv, Y., Li, W., Dong, X., Zhang, B., Zhang, Y., Feng, Z., Li, G., Du, G., 2020. Single crystalline β-Ga<sub>2</sub>O<sub>3</sub> homoepitaxial films grown by MOCVD. *Vacuum* 178, 109440. <https://doi.org/10.1016/j.vacuum.2020.109440>
- Lindberg, O., 1952. Hall Effect. *Proc. IRE* 40, 1414–1419. <https://doi.org/10.1109/JRPROC.1952.273972>
- Lingaparathi, R., Thieu, Q.T., Koshi, K., Wakimoto, D., Sasaki, K., Kuramata, A., 2020. Surface states on (001) oriented β-Ga<sub>2</sub>O<sub>3</sub> epilayers, their origin, and their effect on the electrical properties of Schottky barrier diodes. *Appl. Phys. Lett.* 116, 092101. <https://doi.org/10.1063/1.5142246>
- Liu, T., Huang, R., Li, F., Huang, Z., Zhang, J., Liu, J., Zhang, L., Zhang, S., Dingsun, A., Yang, H., 2018. Study on the measurement accuracy of circular transmission line model for low-resistance Ohmic contacts on III-V wide band-gap semiconductors. *Curr. Appl. Phys.* 18, 853–858. <https://doi.org/10.1016/j.cap.2018.03.012>
- Liu, Y., Wei, S., Shan, C., Zhao, M., Lien, S.-Y., Lee, M., 2022. Compositions and properties of high-conductivity nitrogen-doped p-type β-Ga<sub>2</sub>O<sub>3</sub> films prepared by the thermal oxidation of GaN in N<sub>2</sub>O ambient. *J. Mater. Res. Technol.* 21, 3113–3128. <https://doi.org/10.1016/j.jmrt.2022.10.110>
- Liu, Z., Zhi, Y., Li, S., Liu, Y., Tang, X., Yan, Z., Li, P., Li, X., Guo, D., Wu, Z., Tang, W., 2019. Comparison of optoelectrical characteristics between Schottky and Ohmic
-

- 
- contacts to  $\beta$ -Ga<sub>2</sub>O<sub>3</sub> thin film. *J. Phys. Appl. Phys.* 53, 085105. <https://doi.org/10.1088/1361-6463/ab596f>
- Longini, R.L., 1962. Rapid zinc diffusion in gallium arsenide. *Solid State Electron.* 5, 127–130. [https://doi.org/10.1016/0038-1101\(62\)90002-3](https://doi.org/10.1016/0038-1101(62)90002-3)
- Look, D.C., Leedy, K.D., Horng, R.-H., Santia, M.D., Badescu, S.C., 2020. Electrical and optical properties of degenerate and semi-insulating ZnGa<sub>2</sub>O<sub>4</sub>: Electron/phonon scattering elucidated by quantum magnetoconductivity. *Appl. Phys. Lett.* 116, 252104. <https://doi.org/10.1063/5.0014827>
- López-Moreno, S., Rodríguez-Hernández, P., Muñoz, A., Romero, A. h., Manjón, F. j., Errandonea, D., Rusu, E., Ursaki, V. v., 2011. Lattice dynamics of ZnAl<sub>2</sub>O<sub>4</sub> and ZnGa<sub>2</sub>O<sub>4</sub> under high pressure. *Ann. Phys.* 523, 157–167. <https://doi.org/10.1002/andp.201000096>
- Lorenz, M.R., Woods, J.F., Gambino, R.J., 1967. Some electrical properties of the semiconductor  $\beta$  Ga<sub>2</sub>O<sub>3</sub>. *J. Phys. Chem. Solids* 28, 403–404. [https://doi.org/10.1016/0022-3697\(67\)90305-8](https://doi.org/10.1016/0022-3697(67)90305-8)
- Lovejoy, T.C., Chen, R., Zheng, X., Villora, E.G., Shimamura, K., Yoshikawa, H., Yamashita, Y., Ueda, S., Kobayashi, K., Dunham, S.T., Ohuchi, F.S., Olmstead, M.A., 2012. Band bending and surface defects in  $\beta$ -Ga<sub>2</sub>O<sub>3</sub>. *Appl. Phys. Lett.* 100, 181602. <https://doi.org/10.1063/1.4711014>
- Lu, X., Bian, W., Li, Y., Zhu, H., Fu, Z., Zhang, Q., 2017. Cation distributions and microwave dielectric properties of Cu-substituted ZnGa<sub>2</sub>O<sub>4</sub> spinel ceramics. *Ceram. Int.* 43, 13839–13844. <https://doi.org/10.1016/j.ceramint.2017.07.104>
- Luan, S., Dong, L., Ma, X., Jia, R., 2020. The further investigation of N-doped  $\beta$ -Ga<sub>2</sub>O<sub>3</sub> thin films with native defects for Schottky-barrier diode. *J. Alloys Compd.* 812, 152026. <https://doi.org/10.1016/j.jallcom.2019.152026>
- Luchecko, A., Zhydachevskyy, Y., Ubizskii, S., Kravets, O., Popov, A.I., Rogulis, U., Elsts, E., Bulur, E., Suchocki, A., 2019. Afterglow, TL and OSL properties of Mn<sup>2+</sup>-doped ZnGa<sub>2</sub>O<sub>4</sub> phosphor. *Sci. Rep.* 9, 9544. <https://doi.org/10.1038/s41598-019-45869-7>
- Lv, Y., Liu, H., Zhou, X., Wang, Y., Song, X., Cai, Y., Yan, Q., Wang, C., Liang, S., Zhang, J., Feng, Z., Zhou, H., Cai, S., Hao, Y., 2020. Lateral  $\beta$ -Ga<sub>2</sub>O<sub>3</sub> MOSFETs With High Power Figure of Merit of 277 MW/cm<sup>2</sup>. *IEEE Electron Device Lett.* 41, 537–540. <https://doi.org/10.1109/LED.2020.2974515>
- Lyle, L.A.M., Back, T.C., Bowers, C.T., Green, A.J., Chabak, K.D., Dorsey, D.L., Heller, E.R., Porter, L.M., 2021. Electrical and chemical analysis of Ti/Au contacts to  $\beta$ -Ga<sub>2</sub>O<sub>3</sub>. *APL Mater.* 9, 061104. <https://doi.org/10.1063/5.0051340>
- Lyons, J.L., 2018. A survey of acceptor dopants for  $\beta$ -Ga<sub>2</sub>O<sub>3</sub>. *Semicond. Sci. Technol.* 33, 05LT02. <https://doi.org/10.1088/1361-6641/aaba98>
- Lyu, S., Pasquarello, A., 2020. Band alignment at  $\beta$ -Ga<sub>2</sub>O<sub>3</sub>/III-N (III = Al, Ga) interfaces through hybrid functional calculations. *Appl. Phys. Lett.* 117, 102103. <https://doi.org/10.1063/5.0020442>
- Ma, C., Wu, Z., Jiang, Z., Chen, Y., Ruan, W., Zhang, H., Zhu, H., Zhang, G., Kang, J., Zhang, T.-Y., Chu, J., Fang, Z., 2022. Exploring the feasibility and conduction

- 
- mechanisms of P-type nitrogen-doped  $\beta$ -Ga<sub>2</sub>O<sub>3</sub> with high hole mobility. *J. Mater. Chem. C* 10, 6673–6681. <https://doi.org/10.1039/D1TC05324H>
- Ma, J., Lin, J., Liu, J., Li, F., Liu, Y., Yang, G., 2020. Achieving high conductivity p-type Ga<sub>2</sub>O<sub>3</sub> through Al-N and In-N co-doping. *Chem. Phys. Lett.* 746, 137308. <https://doi.org/10.1016/j.cplett.2020.137308>
- Ma, J., Yoo, G., 2019. Low Subthreshold Swing Double-Gate  $\beta$ -Ga<sub>2</sub>O<sub>3</sub> Field-Effect Transistors With Polycrystalline Hafnium Oxide Dielectrics. *IEEE Electron Device Lett.* 40, 1317–1320. <https://doi.org/10.1109/LED.2019.2924680>
- Ma, X., Zhang, Y., Dong, L., Jia, R., 2017. First-principles calculations of electronic and optical properties of aluminum-doped  $\beta$ -Ga<sub>2</sub>O<sub>3</sub> with intrinsic defects. *Results Phys.* 7, 1582–1589. <https://doi.org/10.1016/j.rinp.2017.04.023>
- Majumder, S.B., Jain, M., Dobal, P.S., Katiyar, R.S., 2003. Investigations on solution derived aluminium doped zinc oxide thin films. *Mater. Sci. Eng. B* 103, 16–25. [https://doi.org/10.1016/S0921-5107\(03\)00128-4](https://doi.org/10.1016/S0921-5107(03)00128-4)
- Maldiney, T., Bessière, A., Seguin, J., Teston, E., Sharma, S.K., Viana, B., Bos, A.J.J., Dorenbos, P., Bessodes, M., Gourier, D., Scherman, D., Richard, C., 2014. The in vivo activation of persistent nanophosphors for optical imaging of vascularization, tumours and grafted cells. *Nat. Mater.* 13, 418–426. <https://doi.org/10.1038/nmat3908>
- Marlow, G.S., Das, M.B., 1982. The effects of contact size and non-zero metal resistance on the determination of specific contact resistance. *Solid-State Electron.* 25, 91–94. [https://doi.org/10.1016/0038-1101\(82\)90036-3](https://doi.org/10.1016/0038-1101(82)90036-3)
- Marrani, A.G., Caprioli, F., Boccia, A., Zanoni, R., Decker, F., 2014. Electrochemically deposited ZnO films: an XPS study on the evolution of their surface hydroxide and defect composition upon thermal annealing. *J. Solid State Electrochem.* 18, 505–513. <https://doi.org/10.1007/s10008-013-2281-2>
- Mastro, M.A., Eddy, C.R., Jr., Tadjer, M.J., Hite, J.K., Kim, J., Pearton, S.J., 2020. Assessment of the (010)  $\beta$ -Ga<sub>2</sub>O<sub>3</sub> surface and substrate specification. *J. Vac. Sci. Technol. A* 39, 013408. <https://doi.org/10.1116/6.0000725>
- Matsubara, M., Bellotti, E., Kyrtos, A., 2017. Migration mechanisms and diffusion barriers of vacancies in  $\{\mathrm{Ga}\}_2\{\mathrm{O}\}_3$ . *Phys. Rev. B* 95, 245202. <https://doi.org/10.1103/PhysRevB.95.245202>
- McCluskey, M.D., 2020. Point defects in Ga<sub>2</sub>O<sub>3</sub>. *J. Appl. Phys.* 127, 101101. <https://doi.org/10.1063/1.5142195>
- McGlone, J.F., Xia, Z., Joishi, C., Lodha, S., Rajan, S., Ringel, S., Arehart, A.R., 2019. Identification of critical buffer traps in Si  $\delta$ -doped  $\beta$ -Ga<sub>2</sub>O<sub>3</sub> MESFETs. *Appl. Phys. Lett.* 115, 153501. <https://doi.org/10.1063/1.5118250>
- Miceli, G., Pasquarello, A., 2016. Self-compensation due to point defects in Mg-doped GaN. *Phys. Rev. B* 93, 165207. <https://doi.org/10.1103/PhysRevB.93.165207>
- Michling, M., Schmeißer, D., 2012. Resonant Photoemission at the O1s threshold to characterize  $\beta$ -Ga<sub>2</sub>O<sub>3</sub> single crystals. *IOP Conf. Ser. Mater. Sci. Eng.* 34, 012002. <https://doi.org/10.1088/1757-899X/34/1/012002>
- Mock, A., Korlacki, R., Briley, C., Darakchieva, V., Monemar, B., Kumagai, Y., Goto, K., Higashiwaki, M., Schubert, M., 2017. Band-to-band transitions, selection rules,
-

- 
- effective mass and exciton binding energy parameters in monoclinic  $\beta$ -Ga<sub>2</sub>O<sub>3</sub>. Phys. Rev. B 96, 245205. <https://doi.org/10.1103/PhysRevB.96.245205>
- Mohamed, M., Irmischer, K., Janowitz, C., Galazka, Z., Manzke, R., Fornari, R., 2012. Schottky barrier height of Au on the transparent semiconducting oxide  $\beta$ -Ga<sub>2</sub>O<sub>3</sub>. Appl. Phys. Lett. 101, 132106. <https://doi.org/10.1063/1.4755770>
- Monch, W., 1990. On the physics of metal-semiconductor interfaces. Rep. Prog. Phys. 53, 221–278. <https://doi.org/10.1088/0034-4885/53/3/001>
- Mott, N.F., 1938. Note on the contact between a metal and an insulator or semi-conductor. Math. Proc. Camb. Philos. Soc. 34, 568–572. <https://doi.org/10.1017/S0305004100020570>
- Movaghar, B., Pohlmann, B., Wurtz, D., 1981. The Hall mobility in hopping conduction. J. Phys. C Solid State Phys. 14, 5127–5137. <https://doi.org/10.1088/0022-3719/14/33/020>
- Muhammed, M.M., Peres, M., Yamashita, Y., Morishima, Y., Sato, S., Franco, N., Lorenz, K., Kuramata, A., Roqan, I.S., 2014. High optical and structural quality of GaN epilayers grown on (2<sup>-</sup>01)  $\beta$ -Ga<sub>2</sub>O<sub>3</sub>. Appl. Phys. Lett. 105, 042112. <https://doi.org/10.1063/1.4891761>
- Müller, S., Wenckstern, H. von, Schmidt, F., Splith, D., Schein, F.-L., Frenzel, H., Grundmann, M., 2015. Comparison of Schottky contacts on  $\beta$ -gallium oxide thin films and bulk crystals. Appl. Phys. Express 8, 121102. <https://doi.org/10.7567/APEX.8.121102>
- Napari, M., Huq, T.N., Meeth, D.J., Heikkilä M.J., Niang, K.M., Wang, Han, Iivonen, T., Wang, Haiyan, Leskelä M., Ritala, M., Flewitt, A.J., Hoye, R.L.Z., MacManus-Driscoll, J.L., 2021. Role of ALD Al<sub>2</sub>O<sub>3</sub> Surface Passivation on the Performance of p-Type Cu<sub>2</sub>O Thin Film Transistors. ACS Appl. Mater. Interfaces 13, 4156–4164. <https://doi.org/10.1021/acsami.0c18915>
- Navarro-Quezada, A., Alamé S., Esser, N., Furthmüller, J., Bechstedt, F., Galazka, Z., Skuridina, D., Vogt, P., 2015a. Near valence-band electronic properties of semiconducting  $\beta$ -Ga<sub>2</sub>O<sub>3</sub> (100) single crystals. Phys. Rev. B 92, 195306. <https://doi.org/10.1103/PhysRevB.92.195306>
- Navarro-Quezada, A., Galazka, Z., Alamé S., Skuridina, D., Vogt, P., Esser, N., 2015b. Surface properties of annealed semiconducting  $\beta$ -Ga<sub>2</sub>O<sub>3</sub> (100) single crystals for epitaxy. Appl. Surf. Sci. 349, 368–373. <https://doi.org/10.1016/j.apsusc.2015.04.225>
- Neumark, G.F., 1980. Are impurities the cause of "self"-compensation in large-band-gap semiconductors? J. Appl. Phys. 51, 3383–3387. <https://doi.org/10.1063/1.328051>
- Nie, Y., Jiao, S., Li, S., Lu, H., Liu, S., Yang, S., Wang, D., Gao, S., Wang, J., Li, Y., 2022. Modulating the blue and green luminescence in the  $\beta$ -Ga<sub>2</sub>O<sub>3</sub> films. J. Alloys Compd. 900, 163431. <https://doi.org/10.1016/j.jallcom.2021.163431>
- Nistor, M., Gherendi, F., Mandache, N.B., Hebert, C., Perrière, J., Seiler, W., 2009. Metal-semiconductor transition in epitaxial ZnO thin films. J. Appl. Phys. 106, 103710. <https://doi.org/10.1063/1.3259412>
-

- 
- Noun, W., Berini, B., Dumont, Y., Dahoo, P.R., Keller, N., 2007. Correlation between electrical and ellipsometric properties on high-quality epitaxial thin films of the conductive oxide LaNiO<sub>3</sub> on STO (001). *J. Appl. Phys.* 102, 063709. <https://doi.org/10.1063/1.2781517>
- NYCU Instrumentation Webpage, 2023. 球面像差修正掃描穿透式電子顯微鏡 Cs-corrected STEM. 國立陽明交通大學 儀器資源中心 . URL [https://irc.ord.nycu.edu.tw/en/nstc\\_instrument/physics/cs-corrected-stem/](https://irc.ord.nycu.edu.tw/en/nstc_instrument/physics/cs-corrected-stem/) (accessed 5.10.23).
- Oda, M., Tokuda, R., Kambara, H., Tanikawa, T., Sasaki, T., Hitora, T., 2016. Schottky barrier diodes of corundum-structured gallium oxide showing on-resistance of 0.1 mΩ·cm<sup>2</sup> grown by MIST EPITAXY®. *Appl. Phys. Express* 9, 021101. <https://doi.org/10.7567/APEX.9.021101>
- Omata, T., Ueda, N., Ueda, K., Kawazoe, H., 1994. New ultraviolet-transport electroconductive oxide, ZnGa<sub>2</sub>O<sub>4</sub> spinel. *Appl. Phys. Lett.* 64, 1077–1078. <https://doi.org/10.1063/1.110937>
- Onuma, T., Fujioka, S., Yamaguchi, T., Higashiwaki, M., Sasaki, K., Masui, T., Honda, T., 2013. Correlation between blue luminescence intensity and resistivity in β-Ga<sub>2</sub>O<sub>3</sub> single crystals. *Appl. Phys. Lett.* 103, 041910. <https://doi.org/10.1063/1.4816759>
- Onuma, T., Nakata, Y., Sasaki, K., Masui, T., Yamaguchi, T., Honda, T., Kuramata, A., Yamakoshi, S., Higashiwaki, M., 2018. Modeling and interpretation of UV and blue luminescence intensity in β-Ga<sub>2</sub>O<sub>3</sub> by silicon and nitrogen doping. *J. Appl. Phys.* 124, 075103. <https://doi.org/10.1063/1.5030612>
- Oshima, T., Okuno, T., Fujita, S., 2007. Ga<sub>2</sub>O<sub>3</sub> Thin Film Growth on c-Plane Sapphire Substrates by Molecular Beam Epitaxy for Deep-Ultraviolet Photodetectors. *Jpn. J. Appl. Phys.* 46, 7217. <https://doi.org/10.1143/JJAP.46.7217>
- Oshima, T., Wakabayashi, R., Hattori, M., Hashiguchi, A., Kawano, N., Sasaki, K., Masui, T., Kuramata, A., Yamakoshi, S., Yoshimatsu, K., Ohtomo, A., Oishi, T., Kasu, M., 2016. Formation of indium–tin oxide ohmic contacts for β-Ga<sub>2</sub>O<sub>3</sub>. *Jpn. J. Appl. Phys.* 55, 1202B7. <https://doi.org/10.7567/JJAP.55.1202B7>
- Pan, Y., Reeves, G.K., Leech, P.W., Holland, A.S., 2013. Analytical and Finite-Element Modeling of a Two-Contact Circular Test Structure for Specific Contact Resistivity. *IEEE Trans. Electron Devices* 60, 1202–1207. <https://doi.org/10.1109/TED.2013.2242076>
- Pandey, R., Gale, J.D., Sampath, S.K., Recio, J.M., 1999. Atomistic Simulation Study of Spinel Oxides: Zinc Aluminate and Zinc Gallate. *J. Am. Ceram. Soc.* 82, 3337–3341. <https://doi.org/10.1111/j.1151-2916.1999.tb02248.x>
- Pansegrau, C., Jesenovec, J., McCloy, J.S., McCluskey, M.D., 2021. Zinc–hydrogen and zinc–iridium pairs in β-Ga<sub>2</sub>O<sub>3</sub>. *Appl. Phys. Lett.* 119, 102104. <https://doi.org/10.1063/5.0062059>
- Parsons, J.D., Kruaval, G.B., Chaddha, A.K., 1994. Low specific resistance (<6×10<sup>-6</sup> Ω cm<sup>2</sup>) TiC ohmic contacts to n-type β-SiC. *Appl. Phys. Lett.* 65, 2075–2077. <https://doi.org/10.1063/1.112797>
- Paudel, T.R., Lany, S., d’Avezac, M., Zunger, A., Perry, N.H., Nagaraja, A.R., Mason, T.O., Bettinger, J.S., Shi, Y., Toney, M.F., 2011a. Asymmetric cation nonstoichiometry in
-

- 
- spinel: Site occupancy in  $\text{Co}_2\text{ZnO}_4$  and  $\text{Rh}_2\text{ZnO}_4$ . *Phys. Rev. B* 84, 064109. <https://doi.org/10.1103/PhysRevB.84.064109>
- Paudel, T.R., Zakutayev, A., Lany, S., d’Avezac, M., Zunger, A., 2011b. Doping Rules and Doping Prototypes in  $\text{A}_2\text{BO}_4$  Spinel Oxides. *Adv. Funct. Mater.* 21, 4493–4501. <https://doi.org/10.1002/adfm.201101469>
- Pearnton, S.J., Yang, J., Cary, P.H., Ren, F., Kim, J., Tadjer, M.J., Mastro, M.A., 2018. A review of  $\text{Ga}_2\text{O}_3$  materials, processing, and devices. *Appl. Phys. Rev.* 5, 011301. <https://doi.org/10.1063/1.5006941>
- Peelaers, H., Lyons, J.L., Varley, J.B., Van de Walle, C.G., 2019. Deep acceptors and their diffusion in  $\text{Ga}_2\text{O}_3$ . *APL Mater.* 7, 022519. <https://doi.org/10.1063/1.5063807>
- Peelaers, H., Van de Walle, C.G., 2015. Brillouin zone and band structure of  $\beta\text{-Ga}_2\text{O}_3$ . *Phys. Status Solidi B* 252, 828–832. <https://doi.org/10.1002/pssb.201451551>
- Perkins, J.D., Paudel, T.R., Zakutayev, A., Ndione, P.F., Parilla, P.A., Young, D.L., Lany, S., Ginley, D.S., Zunger, A., Perry, N.H., Tang, Y., Grayson, M., Mason, T.O., Bettinger, J.S., Shi, Y., Toney, M.F., 2011. Inverse design approach to hole doping in ternary oxides: Enhancing p-type conductivity in cobalt oxide spinels. *Phys. Rev. B* 84, 205207. <https://doi.org/10.1103/PhysRevB.84.205207>
- Pisani, L., Maitra, T., Valent  $\acute{\text{e}}$  R., 2006. Effects of Fe substitution on the electronic, transport, and magnetic properties of  $\text{ZnGa}_2\text{O}_4$ : A systematic ab initio study. *Phys. Rev. B* 73, 205204. <https://doi.org/10.1103/PhysRevB.73.205204>
- Polyakov, A.Y., Smirnov, N.B., Shchemerov, I.V., Yakimov, E.B., Yang, J., Ren, F., Yang, G., Kim, J., Kuramata, A., Pearnton, S.J., 2018. Point defect induced degradation of electrical properties of  $\text{Ga}_2\text{O}_3$  by 10 MeV proton damage. *Appl. Phys. Lett.* 112, 032107. <https://doi.org/10.1063/1.5012993>
- Portoff, A., Stavola, M., Fowler, W.B., Pearnton, S.J., Glaser, E.R., 2023. Hydrogen centers as a probe of  $\text{VGa}(2)$  defects in  $\beta\text{-Ga}_2\text{O}_3$ . *Appl. Phys. Lett.* 122, 062101. <https://doi.org/10.1063/5.0138904>
- Pozina, G., Hsu, C.-W., Abrikosova, N., Hemmingsson, C., 2021. Doping of  $\beta\text{-Ga}_2\text{O}_3$  Layers by Zn Using Halide Vapor-Phase Epitaxy Process. *Phys. Status Solidi A* 218, 2100486. <https://doi.org/10.1002/pssa.202100486>
- Qian, Y.P., Guo, D.Y., Chu, X.L., Shi, H.Z., Zhu, W.K., Wang, K., Huang, X.K., Wang, H., Wang, S.L., Li, P.G., Zhang, X.H., Tang, W.H., 2017. Mg-doped p-type  $\beta\text{-Ga}_2\text{O}_3$  thin film for solar-blind ultraviolet photodetector. *Mater. Lett.* 209, 558–561. <https://doi.org/10.1016/j.matlet.2017.08.052>
- Qiao, D., Yu, L.S., Lau, S.S., Lin, J.Y., Jiang, H.X., Haynes, T.E., 2000. A study of the Au/Ni ohmic contact on p-GaN. *J. Appl. Phys.* 88, 4196–4200. <https://doi.org/10.1063/1.1311809>
- Qin, Y., Stavola, M., Fowler, W.B., Weiser, P., Pearnton, S.J., 2019. Editors’ Choice—Hydrogen Centers in  $\beta\text{-Ga}_2\text{O}_3$ : Infrared Spectroscopy and Density Functional Theory. *ECS J. Solid State Sci. Technol.* 8, Q3103. <https://doi.org/10.1149/2.0221907jss>
- Quantum Design, 2008. 1070-150 Rev. B5 PQ PPMS Hardware.pdf.

- 
- Rajapitamahuni, A.K., Manjeshwar, A.K., Kumar, A., Datta, A., Ranga, P., Thoutam, L.R., Krishnamoorthy, S., Singiseti, U., Jalan, B., 2022. Plasmon–Phonon Coupling in Electrostatically Gated  $\beta$ -Ga<sub>2</sub>O<sub>3</sub> Films with Mobility Exceeding 200 cm<sup>2</sup> V<sup>-1</sup> s<sup>-1</sup>. *ACS Nano* 16, 8812–8819. <https://doi.org/10.1021/acsnano.1c09535>
- Reeves, G.K., 1980. Specific contact resistance using a circular transmission line model. *Solid-State Electron.* 23, 487–490. [https://doi.org/10.1016/0038-1101\(80\)90086-6](https://doi.org/10.1016/0038-1101(80)90086-6)
- Reeves, G.K., Harrison, H.B., 1982. Obtaining the specific contact resistance from transmission line model measurements. *IEEE Electron Device Lett.* 3, 111–113. <https://doi.org/10.1109/EDL.1982.25502>
- Relvas, M.S., Soares, M.R.N., Pereira, S.O., Girão, A.V., Costa, F.M., Monteiro, T., 2019. Trends in Cr<sup>3+</sup> red emissions from ZnGa<sub>2</sub>O<sub>4</sub> nanostructures produced by pulsed laser ablation in a liquid medium. *J. Phys. Chem. Solids* 129, 413–423. <https://doi.org/10.1016/j.jpcs.2019.01.022>
- Ricci, F., Boschi, F., Baraldi, A., Filippetti, A., Higashiwaki, M., Kuramata, A., Fiorentini, V., Fornari, R., 2016. Theoretical and experimental investigation of optical absorption anisotropy in  $\beta$ -Ga<sub>2</sub>O<sub>3</sub>. *J. Phys. Condens. Matter* 28, 224005. <https://doi.org/10.1088/0953-8984/28/22/224005>
- Rideout, V.L., 1975. A review of the theory and technology for ohmic contacts to group III–V compound semiconductors. *Solid-State Electron.* 18, 541–550. [https://doi.org/10.1016/0038-1101\(75\)90031-3](https://doi.org/10.1016/0038-1101(75)90031-3)
- Rideout, V.L., Crowell, C.R., 1970. Effects of image force and tunneling on current transport in metal-semiconductor (Schottky barrier) contacts. *Solid-State Electron.* 13, 993–1009. [https://doi.org/10.1016/0038-1101\(70\)90097-3](https://doi.org/10.1016/0038-1101(70)90097-3)
- Robbins, D.J., 1980a. Aspects of the Theory of Impact Ionization in Semiconductors (I). *Phys. Status Solidi B* 97, 9–50. <https://doi.org/10.1002/pssb.2220970102>
- Robbins, D.J., 1980b. Aspects of the Theory of Impact Ionization in Semiconductors (II). *Phys. Status Solidi B* 97, 387–406. <https://doi.org/10.1002/pssb.2220970202>
- Sabino, F.P., Cai, X., Wei, S.-H., Janotti, A., 2019. Bismuth-doped Ga<sub>2</sub>O<sub>3</sub> as candidate for p-type transparent conducting material. *ArXiv190600840 Cond-Mat*.
- Sabino, F.P., Chatratin, I., Janotti, A., Dalpian, G.M., 2022. Hole conductivity through a defect band in  $\{\mathrm{ZnGa}\}_2\{\mathrm{O}\}_4$ . *Phys. Rev. Mater.* 6, 064602. <https://doi.org/10.1103/PhysRevMaterials.6.064602>
- Sakata, Y., Matsuda, Y., Yanagida, T., Hirata, K., Imamura, H., Teramura, K., 2008. Effect of metal ion addition in a Ni supported Ga<sub>2</sub>O<sub>3</sub> photocatalyst on the photocatalytic overall splitting of H<sub>2</sub>O. *Catal. Lett.* 125, 22–26. <https://doi.org/10.1007/s10562-008-9557-7>
- Saleh, M., Varley, J.B., Jesenovec, J., Bhattacharyya, A., Krishnamoorthy, S., Swain, S., Lynn, K., 2020. Degenerate doping in  $\beta$ -Ga<sub>2</sub>O<sub>3</sub> single crystals through Hf-doping. *Semicond. Sci. Technol.* 35, 04LT01. <https://doi.org/10.1088/1361-6641/ab75a6>
- Sambandam, B., Michael, R.J.V., Manoharan, P.T., 2015. Oxygen vacancies and intense luminescence in manganese loaded ZnO microflowers for visible light water splitting. *Nanoscale* 7, 13935–13942. <https://doi.org/10.1039/C5NR02666K>
-

- 
- Santia, M.D., Tandon, N., Albrecht, J.D., 2015. Lattice thermal conductivity in  $\beta$ -Ga<sub>2</sub>O<sub>3</sub> from first principles. *Appl. Phys. Lett.* 107, 041907. <https://doi.org/10.1063/1.4927742>
- Sasaki, K., Higashiwaki, M., Kuramata, A., Masui, T., Yamakoshi, S., 2013. MBE grown Ga<sub>2</sub>O<sub>3</sub> and its power device applications. *J. Cryst. Growth* 378, 591–595. <https://doi.org/10.1016/j.jcrysgro.2013.02.015>
- Sasaki, W., de Bruyn Ouboter, R., 1961. Electrical properties of impurity conducting n-type germanium. *Physica* 27, 877–882. [https://doi.org/10.1016/0031-8914\(61\)90086-6](https://doi.org/10.1016/0031-8914(61)90086-6)
- Sato, H., Minami, T., Takata, S., Yamada, T., 1993. Transparent conducting p-type NiO thin films prepared by magnetron sputtering. *Thin Solid Films* 236, 27–31. [https://doi.org/10.1016/0040-6090\(93\)90636-4](https://doi.org/10.1016/0040-6090(93)90636-4)
- Satya Kamal, C., Boddu, S., Vishwanadh, B., Rao, K.R., Sudarsan, V., Vatsa, R.K., 2017. Blue luminescence from ZnGa<sub>2</sub>O<sub>4</sub>: Effect of lattice distortion and particle size. *J. Lumin.* 188, 429–435. <https://doi.org/10.1016/j.jlumin.2017.04.056>
- Satyanarayana, L., Gopal Reddy, C.V., Manorama, S.V., Rao, V.J., 1998. Liquid-petroleum-gas sensor based on a spinel semiconductor, ZnGa<sub>2</sub>O<sub>4</sub>IICT Communication No: 3725.1. *Sens. Actuators B Chem.* 46, 1–7. [https://doi.org/10.1016/S0925-4005\(97\)00313-4](https://doi.org/10.1016/S0925-4005(97)00313-4)
- Seah, M.P., 1980. The quantitative analysis of surfaces by XPS: A review. *Surf. Interface Anal.* 2, 222–239. <https://doi.org/10.1002/sia.740020607>
- Seko, A., Oba, F., Tanaka, I., 2010. Classification of spinel structures based on first-principles cluster expansion analysis. *Phys. Rev. B* 81, 054114. <https://doi.org/10.1103/PhysRevB.81.054114>
- Seryogin, G., Alema, F., Valente, N., Fu, H., Steinbrunner, E., Neal, A.T., Mou, S., Fine, A., Osinsky, A., 2020. MOCVD growth of high purity Ga<sub>2</sub>O<sub>3</sub> epitaxial films using trimethylgallium precursor. *Appl. Phys. Lett.* 117, 262101. <https://doi.org/10.1063/5.0031484>
- Shen, H., Baskaran, K., Yin, Y., Tian, K., Duan, L., Zhao, X., Tiwari, A., 2020. Effect of thickness on the performance of solar blind photodetectors fabricated using PLD grown  $\beta$ -Ga<sub>2</sub>O<sub>3</sub> thin films. *J. Alloys Compd.* 822, 153419. <https://doi.org/10.1016/j.jallcom.2019.153419>
- Shen, Y.-C., Huang, P.-H., Tung, C.-Y., Huang, C.-Y., Tan, C.-S., Huang, Y.-S., Chen, L.-J., He, J.-H., Horng, R.-H., 2020. Power Saving High Performance Deep-Ultraviolet Phototransistors Made of ZnGa<sub>2</sub>O<sub>4</sub> Epilayers. *ACS Appl. Electron. Mater.* 2, 590–596. <https://doi.org/10.1021/acsaelm.9b00820>
- Shen, Y.-C., Tung, C.-Y., Huang, C.-Y., Lin, Y.-C., Lin, Y.-G., Horng, R.-H., 2019. Study on Optoelectronic Characteristics of ZnGa<sub>2</sub>O<sub>4</sub> Thin-Film Phototransistors. *ACS Appl. Electron. Mater.* 1, 783–788. <https://doi.org/10.1021/acsaelm.9b00128>
- Shen, Y.C., Tung, C.Y., Huang, C.Y., Lin, Y.C., Lin, Y.G., Horng, R.H., 2019. Study on optoelectronic characteristic of ZnGa<sub>2</sub>O<sub>4</sub> thin-film phototransistors. *ACS Appl. Electron. Mater.* 1, 783.
- Shen, Y.-S., Wang, W.-K., Horng, R.-H., 2017. Characterizations of Metal-Oxide-Semiconductor Field-Effect Transistors of ZnGaO Grown on Sapphire Substrate. *IEEE J. Electron Devices Soc.* 5, 112–116. <https://doi.org/10.1109/JEDS.2017.2653419>
-

- 
- Sheoran, H., Kumar, V., Singh, R., 2022. A Comprehensive Review on Recent Developments in Ohmic and Schottky Contacts on Ga<sub>2</sub>O<sub>3</sub> for Device Applications. *ACS Appl. Electron. Mater.* 4, 2589–2628. <https://doi.org/10.1021/acsaelm.2c00101>
- Shi, J., Xia, X., Liang, H., Abbas, Q., Liu, J., Zhang, H., Liu, Y., 2019. Low resistivity ohmic contacts on lightly doped n-type  $\beta$ -Ga<sub>2</sub>O<sub>3</sub> using Mg/Au. *J. Mater. Sci. Mater. Electron.* 30, 3860–3864. <https://doi.org/10.1007/s10854-019-00669-7>
- Shi, Q., Wang, Qingru, Zhang, D., Wang, Qinglin, Li, S., Wang, W., Fan, Q., Zhang, J., 2019. Structural, optical and photoluminescence properties of Ga<sub>2</sub>O<sub>3</sub> thin films deposited by vacuum thermal evaporation. *J. Lumin.* 206, 53–58. <https://doi.org/10.1016/j.jlumin.2018.10.005>
- Shi, Y., Ndione, P.F., Lim, L.Y., Sokaras, D., Weng, T.-C., Nagaraja, A.R., Karydas, A.G., Perkins, J.D., Mason, T.O., Ginley, D.S., Zunger, A., Toney, M.F., 2014. Self-Doping and Electrical Conductivity in Spinel Oxides: Experimental Validation of Doping Rules. *Chem. Mater.* 26, 1867–1873. <https://doi.org/10.1021/cm404031k>
- Shimamura, K., V ilora, E.G., Ujiie, T., Aoki, K., 2008. Excitation and photoluminescence of pure and Si-doped  $\beta$ -Ga<sub>2</sub>O<sub>3</sub> single crystals. *Appl. Phys. Lett.* 92, 201914. <https://doi.org/10.1063/1.2910768>
- Shklovskii, B.I., Efros, A.L., 1984. *Electronic Properties of Doped Semiconductors*. Springer Science & Business Media.
- Shockley, W., Scarlett, R.M., Goetzberger, A., 1964. Research and investigation of inverse epitaxial UHF power transistors (No. AI-TOR-64-207). Air Force, Air Force.
- Shrestha, N.K., Lee, K., Kirchgorg, R., Hahn, R., Schmuki, P., 2013. Self-organization and zinc doping of Ga<sub>2</sub>O<sub>3</sub> nanoporous architecture: A potential nano-photogenerator for hydrogen. *Electrochem. Commun.* 35, 112–115. <https://doi.org/10.1016/j.elecom.2013.08.011>
- Siegrist, T., Jost, P., Volker, H., Woda, M., Merkelbach, P., Schlockermann, C., Wuttig, M., 2011. Disorder-induced localization in crystalline phase-change materials. *Nat. Mater.* 10, 202–208. <https://doi.org/10.1038/nmat2934>
- Sood, A., Tarntair, F.-G., Wang, Y.-X., Chang, T.-C., Chen, Y.-H., Liu, P.-L., Horng, R.-H., 2021. Performance enhancement of ZnGa<sub>2</sub>O<sub>4</sub> Schottky type deep-ultraviolet photodetectors by oxygen supercritical fluid treatment. *Results Phys.* 29, 104764. <https://doi.org/10.1016/j.rinp.2021.104764>
- Spaziani, L., Lu, L., 2018. Silicon, GaN and SiC: There's room for all: An application space overview of device considerations, in: 2018 IEEE 30th International Symposium on Power Semiconductor Devices and ICs (ISPSD). Presented at the 2018 IEEE 30th International Symposium on Power Semiconductor Devices and ICs (ISPSD), pp. 8–11. <https://doi.org/10.1109/ISPSD.2018.8393590>
- Speck, J.S., Esmat, F., 2023. Ultrawide Bandgap  $\beta$ -Ga<sub>2</sub>O<sub>3</sub> Semiconductor: Theory and Applications. <https://doi.org/10.1063/9780735425033>
- Srinivas Reddy, G., Sharma, H., Bhaskar, P., Manjunatha, M., 2020. Effect of type of fuel used and calcination temperature on the disorder-order transformation of zinc aluminate spinel during combustion synthesis. *Mater. Chem. Phys.* 253, 123388. <https://doi.org/10.1016/j.matchemphys.2020.123388>
-

- 
- Steimer, P.K., 2010. Enabled by high power electronics - Energy efficiency, renewables and smart grids. Presented at the The 2010 International Power Electronics Conference - ECCE ASIA -, IEEE, pp. 11–15. <https://doi.org/10.1109/IPEC.2010.5542328>.
- Stoica, M., S Lo, C., 2014. P-type zinc oxide spinels: application to transparent conductors and spintronics. *New J. Phys.* 16, 055011. <https://doi.org/10.1088/1367-2630/16/5/055011>
- Su, Y., Guo, D., Ye, J., Zhao, H., Wang, Z., Wang, S., Li, P., Tang, W., 2019. Deep level acceptors of Zn-Mg divalent ions dopants in b-Ga<sub>2</sub>O<sub>3</sub> for the difficulty to p-type conductivity. *J. Alloys Compd.* 5.
- Sun, D., Gao, Y., Xue, J., Zhao, J., 2019. Defect stability and electronic structure of doped  $\beta$ -Ga<sub>2</sub>O<sub>3</sub>: A comprehensive ab initio study. *J. Alloys Compd.* 794, 374–384. <https://doi.org/10.1016/j.jallcom.2019.04.253>
- Sun, H., Torres Castanedo, C.G., Liu, K., Li, K.-H., Guo, W., Lin, R., Liu, X., Li, J., Li, X., 2017. Valence and conduction band offsets of  $\beta$ -Ga<sub>2</sub>O<sub>3</sub>/AlN heterojunction. *Appl. Phys. Lett.* 111, 162105. <https://doi.org/10.1063/1.5003930>
- Sun, R., Ooi, Y.K., Dickens, P.T., Lynn, K.G., Scarpulla, M.A., 2020. On the origin of red luminescence from iron-doped  $\beta$ -Ga<sub>2</sub>O<sub>3</sub> bulk crystals. *Appl. Phys. Lett.* 117, 052101. <https://doi.org/10.1063/5.0012967>
- Sun, Y., Boggs, S.A., Ramprasad, R., 2012. The intrinsic electrical breakdown strength of insulators from first principles. *Appl. Phys. Lett.* 101, 132906. <https://doi.org/10.1063/1.4755841>
- Suzuki, N., Ohira, S., Tanaka, M., Sugawara, T., Nakajima, K., Shishido, T., 2007. Fabrication and characterization of transparent conductive Sn-doped  $\beta$ -Ga<sub>2</sub>O<sub>3</sub> single crystal. *Phys. Status Solidi C* 4, 2310–2313. <https://doi.org/10.1002/pssc.200674884>
- Swallow, J.E.N., Varley, J.B., Jones, L. a. H., Gibbon, J.T., Piper, L.F.J., Dhanak, V.R., Veal, T.D., 2019. Transition from electron accumulation to depletion at  $\beta$ -Ga<sub>2</sub>O<sub>3</sub> surfaces: The role of hydrogen and the charge neutrality level. *APL Mater.* 7, 022528. <https://doi.org/10.1063/1.5054091>
- Tadger, M.J., Alema, F., Osinsky, A., Mastro, M.A., Nepal, N., Woodward, J.M., Myers-Ward, R.L., Glaser, E.R., Freitas, J.A., Jacobs, A.G., Gallagher, J.C., Mock, A.L., Pennachio, D.J., Hajzus, J., Ebrish, M., Anderson, T.J., Hobart, K.D., Hite, J.K., Jr, C.R.E., 2020. Characterization of  $\beta$ -Ga<sub>2</sub>O<sub>3</sub> homoepitaxial films and MOSFETs grown by MOCVD at high growth rates. *J. Phys. Appl. Phys.* 54, 034005. <https://doi.org/10.1088/1361-6463/abbc96>
- Tadger, M.J., Koehler, A.D., Freitas, J.A., Gallagher, J.C., Specht, M.C., Glaser, E.R., Hobart, K.D., Anderson, T.J., Kub, F.J., Thieu, Q.T., Sasaki, K., Wakimoto, D., Goto, K., Watanabe, S., Kuramata, A., 2018. High resistivity halide vapor phase homoepitaxial  $\beta$ -Ga<sub>2</sub>O<sub>3</sub> films co-doped by silicon and nitrogen. *Appl Phys Lett* 6.
- Takiguchi, Y., Miyajima, S., 2017. Effect of post-deposition annealing on low temperature metalorganic chemical vapor deposited gallium oxide related materials. *J. Cryst. Growth* 468, 129–134. <https://doi.org/10.1016/j.jcrysgro.2016.11.005>
- Tang, C., Sun, J., Lin, N., Jia, Z., Mu, W., Tao, X., Zhao, X., 2016. Electronic structure and optical property of metal-doped Ga<sub>2</sub>O<sub>3</sub>: A first principles study. *RSC Adv.* 6, 78322–78334. <https://doi.org/10.1039/c6ra14010f>
-

- 
- Tao, J., Lu, H.-L., Gu, Y., Ma, H.-P., Li, X., Chen, J.-X., Liu, W.-J., Zhang, H., Feng, J.-J., 2019. Investigation of growth characteristics, compositions, and properties of atomic layer deposited amorphous Zn-doped Ga<sub>2</sub>O<sub>3</sub> films. *Appl. Surf. Sci.* 476, 733–740. <https://doi.org/10.1016/j.apsusc.2019.01.177>
- Tippins, H.H., 1965. Optical Absorption and Photoconductivity in the Band Edge of  $\beta\text{-Ga}_2\text{O}_3$ . *Phys. Rev.* 140, A316–A319. <https://doi.org/10.1103/PhysRev.140.A316>
- Tomioka, Y., Ozaki, Y., Inaba, H., Ito, T., 2019. Compensation effects between impurity cations in single crystals of a wide gap semiconductor  $\beta\text{-Ga}_2\text{O}_3$  prepared by the floating zone method. *Jpn. J. Appl. Phys.* 58, 091009. <https://doi.org/10.7567/1347-4065/ab39be>
- Toyozawa, Y., 1962. Theory of localised spin and Negative MR in metallic impurity conduction. *J. Phys. Soc. Jpn.* 17, 986–1004. <https://doi.org/10.1143/JPSJ.17.986>
- Trew, R.J., 1997. Experimental and Simulated Results of SiC Microwave Power MESFETs. *Phys. Status Solidi A* 162, 409–419. [https://doi.org/10.1002/1521-396X\(199707\)162:1<409::AID-PSSA409>3.0.CO;2-O](https://doi.org/10.1002/1521-396X(199707)162:1<409::AID-PSSA409>3.0.CO;2-O)
- Tsai, S.-H., Shen, Y.-C., Huang, C.-Y., Horng, R.-H., 2019. Deep-ultraviolet Schottky photodetectors with high deep-ultraviolet/visible rejection based on a ZnGa<sub>2</sub>O<sub>4</sub> thin film. *Appl. Surf. Sci.* 496, 143670. <https://doi.org/10.1016/j.apsusc.2019.143670>
- Tung, J.-C., Chiang, Y.-H., Wang, D.-Y., Liu, P.-L., 2020. Adsorption of NO<sub>2</sub> and H<sub>2</sub>S on ZnGa<sub>2</sub>O<sub>4</sub>(111) Thin Films: A First-Principles Density Functional Theory Study. *Appl. Sci.* 10, 8822. <https://doi.org/10.3390/app10248822>
- Tuomisto, F., Karjalainen, A., Prozhheeva, V., Makkonen, I., Wagner, G., Baldini, M., 2019. Ga vacancies and electrical compensation in  $\beta\text{-Ga}_2\text{O}_3$  thin films studied with positron annihilation spectroscopy, in: *Oxide-Based Materials and Devices X*. Presented at the Oxide-based Materials and Devices X, International Society for Optics and Photonics, p. 1091910. <https://doi.org/10.1117/12.2518888>
- Ueda, N., Hosono, H., Waseda, R., Kawazoe, H., 1997. Synthesis and control of conductivity of ultraviolet transmitting  $\beta\text{-Ga}_2\text{O}_3$  single crystals. *Appl. Phys. Lett.* 70, 3561–3563. <https://doi.org/10.1063/1.119233>
- Usseinov, A., Koishybayeva, Z., Platonenko, A., Akilbekov, A., Purans, J., Pankratov, V., Suchikova, Y., Popov, A.I., 2021. Calculations of Oxygen Vacancy in GaO Crystals. *Latv. J. Phys. Tech. Sci.* 58, 3–10. <https://doi.org/10.2478/lpts-2021-0007>
- Usseinov, A., Platonenko, A., Koishybayeva, Z., Akilbekov, A., Zdorovets, M., Popov, A.I., 2022. Pair vacancy defects in  $\beta\text{-Ga}_2\text{O}_3$  crystal: Ab initio study. *Opt. Mater.* X 16, 100200. <https://doi.org/10.1016/j.omx.2022.100200>
- Van Der Pauw, L.J., 1958. A method of measuring the resistivity and Hall coefficient on lamellae of arbitrary shape. *Philips Tech. Rev.* 20, 220–224.
- Van der Straten, P.J.M., Metselaar, R., Jonker, H.D., 1978. Flux growth of ZnGa<sub>2</sub>O<sub>4</sub> single crystals. *J. Cryst. Growth* 43, 270–272. [https://doi.org/10.1016/0022-0248\(78\)90179-3](https://doi.org/10.1016/0022-0248(78)90179-3)
- Van Gorkom, G.G.P., Haanstra, J.H., v. d. Boom, H., 1973. Infrared and Raman spectra of the spinel ZnGa<sub>2</sub>O<sub>4</sub>. *J. Raman Spectrosc.* 1, 513–519. <https://doi.org/10.1002/jrs.1250010510>
-

- 
- Varley, J.B., Janotti, A., Franchini, C., Van de Walle, C.G., 2012. Role of self-trapping in luminescence and p -type conductivity of wide-band-gap oxides. *Phys. Rev. B* 85, 081109. <https://doi.org/10.1103/PhysRevB.85.081109>
- Varley, J.B., Peelaers, H., Janotti, A., Walle, C.G.V. de, 2011. Hydrogenated cation vacancies in semiconducting oxides. *J. Phys. Condens. Matter* 23, 334212. <https://doi.org/10.1088/0953-8984/23/33/334212>
- Varley, J.B., Weber, J.R., Janotti, A., Van de Walle, C.G., 2010. Oxygen vacancies and donor impurities in  $\beta$ -Ga<sub>2</sub>O<sub>3</sub>. *Appl. Phys. Lett.* 97, 142106. <https://doi.org/10.1063/1.3499306>
- Vasheghani Farahani, S.K., Veal, T.D., Mudd, J.J., Scanlon, D.O., Watson, G.W., Bierwagen, O., White, M.E., Speck, J.S., McConville, C.F., 2014. Valence-band density of states and surface electron accumulation in epitaxial  $\text{SnO}_2$  films. *Phys. Rev. B* 90, 155413. <https://doi.org/10.1103/PhysRevB.90.155413>
- Vasiltsiv, V.I., Zakharko, Y.M., Rym, Y.I., 1988. On the nature of blue and green luminescence bands of beta-Ga<sub>2</sub>O<sub>3</sub>. *Ukr. Fiz. Zhurnal* 33, 1320–1324.
- V flora, E.G., Shimamura, K., Yoshikawa, Y., Aoki, K., Ichinose, N., 2004. Large-size  $\beta$ -Ga<sub>2</sub>O<sub>3</sub> single crystals and wafers. *J. Cryst. Growth* 270, 420–426. <https://doi.org/10.1016/j.jcrysgro.2004.06.027>
- von Bardeleben, H.J., Zhou, S., Gerstmann, U., Skachkov, D., Lambrecht, W.R.L., Ho, Q.D., Deák, P., 2019. Proton irradiation induced defects in  $\beta$ -Ga<sub>2</sub>O<sub>3</sub>: A combined EPR and theory study. *APL Mater.* 7, 022521. <https://doi.org/10.1063/1.5053158>
- Wahl, U., Correia, J.G., Costa, Â.R.G., David-Bosne, E., Kappers, M.J., da Silva, M.R., Lippertz, G., Lima, T.A.L., Villarreal, R., Vantomme, A., Pereira, L.M.C., 2021. Lattice Location Studies of the Amphoteric Nature of Implanted Mg in GaN. *Adv. Electron. Mater.* 7, 2100345. <https://doi.org/10.1002/aelm.202100345>
- Wahl, U., Correia, J.G., Costa, A.R.G., Lima, T.A.L., Moens, J., Kappers, M.J., da Silva, M.R., Pereira, L.M.C., Vantomme, A., 2022. Direct evidence of Be as an amphoteric dopant in GaN. *Phys. Rev. B* 105, 184112. <https://doi.org/10.1103/PhysRevB.105.184112>
- Walsh, A., Sokol, A.A., Buckeridge, J., Scanlon, D.O., Catlow, C.R.A., 2018. Oxidation states and ionicity. *Nat. Mater.* 17, 958–964. <https://doi.org/10.1038/s41563-018-0165-7>
- Wang, Fuliang, Wang, Feng, He, H., 2016. Parametric Electrochemical Deposition of Controllable Morphology of Copper Micro-Columns. *J. Electrochem. Soc.* 163, E322. <https://doi.org/10.1149/2.1191610jes>
- Wang, M., Mu, S., Van de Walle, C.G., 2021. Adsorption and Diffusion of Aluminum on  $\beta$ -Ga<sub>2</sub>O<sub>3</sub>(010) Surfaces. *ACS Appl. Mater. Interfaces* 13, 10650–10655. <https://doi.org/10.1021/acsami.0c22737>
- Wang, W.-K., Liu, K.-F., Tsai, P.-C., Xu, Y.-J., Huang, S.-Y., 2019a. Influence of Annealing Temperature on the Properties of ZnGa<sub>2</sub>O<sub>4</sub> Thin Films by Magnetron Sputtering. *Coatings* 9, 859. <https://doi.org/10.3390/coatings9120859>
-

- 
- Wang, W.-K., Xu, Y.-J., Huang, Liu, Tsai, 2019b. Structural Characteristics and Photoluminescence Properties of Sputter-Deposition ZnGa<sub>2</sub>O<sub>4</sub> Thin Films on Sapphire and Si(100) Substrates. *Coatings* 9, 469. <https://doi.org/10.3390/coatings9080469>
- Wang, X. H., Zhang, F.B., Saito, K., Tanaka, T., Nishio, M., Guo, Q.X., 2014. Electrical properties and emission mechanisms of Zn-doped  $\beta$ -Ga<sub>2</sub>O<sub>3</sub> films. *J. Phys. Chem. Solids* 75, 1201–1204. <https://doi.org/10.1016/j.jpcs.2014.06.005>
- Wang, X.H., Zhang, F.B., Saito, K., Tanaka, T., Nishio, M., Guo, Q.X., 2014. Electrical properties and emission mechanisms of Zn-doped  $\beta$ -Ga<sub>2</sub>O<sub>3</sub> films. *J. Phys. Chem. Solids* 75, 1201–1204. <https://doi.org/10.1016/j.jpcs.2014.06.005>
- Wang, Y.-P., Zhang, H.-S., Lin, L.-T., Zhou, S.-F., Yao, Y., Yang, X.-B., Zhao, Y.-J., 2019. Role of intrinsic defects on the persistent luminescence of pristine and Mn doped ZnGa<sub>2</sub>O<sub>4</sub>. *J. Appl. Phys.* 125, 095701. <https://doi.org/10.1063/1.5078773>
- Wang, Z., Yu, X., Gong, H., Hu, T., Zhang, Y., Ji, X., Ren, F., Gu, S., Zheng, Y., Zhang, R., Kuznetsov, A.Yu., Ye, J., 2022. Identification and Suppression of Majority Surface States in the Dry-Etched  $\beta$ -Ga<sub>2</sub>O<sub>3</sub>. *J. Phys. Chem. Lett.* 13, 7094–7099. <https://doi.org/10.1021/acs.jpcclett.2c02167>
- Watahiki, T., Yuda, Y., Furukawa, A., Yamamuka, M., Takiguchi, Y., Miyajima, S., 2017. Heterojunction p-Cu<sub>2</sub>O/n-Ga<sub>2</sub>O<sub>3</sub> diode with high breakdown voltage. *Appl. Phys. Lett.* 111, 222104. <https://doi.org/10.1063/1.4998311>
- Wertheim, G.K., Hüfner, S., 1972. X-Ray Photoemission Band Structure of Some Transition-Metal Oxides. *Phys. Rev. Lett.* 28, 1028–1031. <https://doi.org/10.1103/PhysRevLett.28.1028>
- Wolff, P.A., 1954. Theory of Electron Multiplication in Silicon and Germanium. *Phys. Rev.* 95, 1415–1420. <https://doi.org/10.1103/PhysRev.95.1415>
- Wong, M.H., Lin, C.-H., Kuramata, A., Yamakoshi, S., Murakami, H., Kumagai, Y., Higashiwaki, M., 2018. Acceptor doping of  $\beta$ -Ga<sub>2</sub>O<sub>3</sub> by Mg and N ion implantations. *Appl. Phys. Lett.* 113, 102103. <https://doi.org/10.1063/1.5050040>
- Wong, M.H., Sasaki, K., Kuramata, A., Yamakoshi, S., Higashiwaki, M., 2016. Electron channel mobility in silicon-doped Ga<sub>2</sub>O<sub>3</sub> MOSFETs with a resistive buffer layer. *Jpn. J. Appl. Phys.* 55, 1202B9. <https://doi.org/10.7567/JJAP.55.1202B9>
- Wort, C.J.H., Balmer, R.S., 2008. Diamond as an electronic material. *Mater. Today* 11, 22–28. [https://doi.org/10.1016/S1369-7021\(07\)70349-8](https://doi.org/10.1016/S1369-7021(07)70349-8)
- Wu, C., Wu, F., Ma, C., Li, S., Liu, A., Yang, X., Chen, Y., Wang, J., Guo, D., 2022. A general strategy to ultrasensitive Ga<sub>2</sub>O<sub>3</sub> based self-powered solar-blind photodetectors. *Mater. Today Phys.* 23, 100643. <https://doi.org/10.1016/j.mtphys.2022.100643>
- Wu, L.Q., Li, Y.C., Li, S.Q., Li, Z.Z., Tang, G.D., Qi, W.H., Xue, L.C., Ge, X.S., Ding, L.L., 2015. Method for estimating ionicities of oxides using O1s photoelectron spectra. *AIP Adv.* 5, 097210. <https://doi.org/10.1063/1.4931996>
- Wu, Z.Y., Jiang, Z.X., Ma, C.C., Ruan, W., Chen, Y., Zhang, H., Zhang, G.Q., Fang, Z.L., Kang, J.Y., Zhang, T.-Y., 2021. Energy-driven multi-step structural phase transition mechanism to achieve high-quality p-type nitrogen-doped  $\beta$ -Ga<sub>2</sub>O<sub>3</sub> films. *Mater. Today Phys.* 17, 100356. <https://doi.org/10.1016/j.mtphys.2021.100356>
-

- 
- Xia, Y., Wang, T., Zhao, X., Jiao, X., Chen, D., 2018. Theoretical and Experimental Investigations on Effects of Native Point Defects and Nitrogen Doping on the Optical Band Structure of Spinel  $\text{ZnGa}_2\text{O}_4$ . *J. Phys. Chem. C* 122, 5509–5517. <https://doi.org/10.1021/acs.jpcc.7b12326>
- Xu, C., Wang, J., Wang, M., Jin, H., Hao, Y., Wen, C.P., 2006. Reeves's circular transmission line model and its scope of application to extract specific contact resistance. *Solid-State Electron.* 50, 843–847. <https://doi.org/10.1016/j.sse.2006.03.007>
- Xu, J., Teng, Y., Teng, F., 2016. Effect of Surface Defect States on Valence Band and Charge Separation and Transfer Efficiency. *Sci. Rep.* 6, 32457. <https://doi.org/10.1038/srep32457>
- Xue, H., He, Q., Jian, G., Long, S., Pang, T., Liu, M., 2018. An Overview of the Ultrawide Bandgap  $\text{Ga}_2\text{O}_3$  Semiconductor-Based Schottky Barrier Diode for Power Electronics Application. *Nanoscale Res. Lett.* 13, 290. <https://doi.org/10.1186/s11671-018-2712-1>
- Yakimov, E.B., Polyakov, A.Y., Smirnov, N.B., Shchemerov, I.V., Vergeles, P.S., Yakimov, E.E., Chernykh, A.V., Xian, M., Ren, F., Pearton, S.J., 2020. Role of hole trapping by deep acceptors in electron-beam-induced current measurements in  $\beta\text{-Ga}_2\text{O}_3$  vertical rectifiers. *J. Phys. Appl. Phys.* 53, 495108. <https://doi.org/10.1088/1361-6463/abb2bc>
- Yamaga, M., Vflora, E.G., Shimamura, K., Ichinose, N., Honda, M., 2003. Donor structure and electric transport mechanism in  $\beta\text{-Ga}_2\text{O}_3$ . *Phys. Rev. B* 68, 155207. <https://doi.org/10.1103/PhysRevB.68.155207>
- Yamakata, A., Vequizo, J.J.M., Ogawa, T., Kato, K., Tsuboi, S., Furutani, N., Ohtsuka, M., Muto, S., Kuwabara, A., Sakata, Y., 2021. Core–Shell Double Doping of Zn and Ca on  $\beta\text{-Ga}_2\text{O}_3$  Photocatalysts for Remarkable Water Splitting. *ACS Catal.* 11, 1911–1919. <https://doi.org/10.1021/acscatal.0c05104>
- Yan, C., Su, J., Wang, Y., Lin, Z., Zhang, J., Chang, J., Hao, Y., 2021. Reducing the acceptor levels of p-type  $\beta\text{-Ga}_2\text{O}_3$  by (metal, N) co-doping approach. *J. Alloys Compd.* 854, 157247. <https://doi.org/10.1016/j.jallcom.2020.157247>
- Yan, X., Esqueda, I.S., Ma, J., Tice, J., Wang, H., 2018. High breakdown electric field in  $\beta\text{-Ga}_2\text{O}_3$  /graphene vertical barristor heterostructure. *Appl. Phys. Lett.* 112, 032101. <https://doi.org/10.1063/1.5002138>
- Yan, Z., Takei, H., 1997. Flux growth of single crystals of spinel  $\text{ZnGa}_2\text{O}_4$  and  $\text{CdGa}_2\text{O}_4$ . *J. Cryst. Growth* 171, 131–135. [https://doi.org/10.1016/S0022-0248\(96\)00437-X](https://doi.org/10.1016/S0022-0248(96)00437-X)
- Yan, Z., Takei, H., Kawazoe, H., 2005. Electrical Conductivity in Transparent  $\text{ZnGa}_2\text{O}_4$ : Reduction and Surface-Layer Structure Transformation. *J. Am. Ceram. Soc.* 81, 180–186. <https://doi.org/10.1111/j.1151-2916.1998.tb02311.x>
- Yanagi, H., Hase, T., Ibuki, S., Ueda, K., Hosono, H., 2001. Bipolarity in electrical conduction of transparent oxide semiconductor  $\text{CuInO}_2$  with delafossite structure. *Appl. Phys. Lett.* 78, 1583–1585. <https://doi.org/10.1063/1.1355673>
- Yang, T., Zhao, J., Li, X., Gao, X., Xue, C., Wu, Y., Tai, R., 2015. Preparation and characterization of p-type transparent conducting  $\text{SnO}$  thin films. *Mater. Lett.* 139, 39–41. <https://doi.org/10.1016/j.matlet.2014.10.040>

- 
- Yao, Y., Davis, R.F., Porter, L.M., 2017. Investigation of Different Metals as Ohmic Contacts to  $\beta$ -Ga<sub>2</sub>O<sub>3</sub>: Comparison and Analysis of Electrical Behavior, Morphology, and Other Physical Properties. *J. Electron. Mater.* 46, 2053–2060. <https://doi.org/10.1007/s11664-016-5121-1>
- Yao, Y., Sugawara, Y., Ishikawa, Y., 2020. Identification of Burgers vectors of dislocations in monoclinic  $\beta$ -Ga<sub>2</sub>O<sub>3</sub> via synchrotron x-ray topography. *J. Appl. Phys.* 127, 205110. <https://doi.org/10.1063/5.0007229>
- Yi, S.S., Kim, I.W., Park, H.L., Bae, J.S., Moon, B.K., Jeong, J.H., 2003. Luminescence characteristics of pulsed laser deposited ZnGa<sub>2</sub>O<sub>4</sub> thin film phosphors grown on various substrates. *J. Cryst. Growth* 247, 213–218. [https://doi.org/10.1016/S0022-0248\(02\)01915-2](https://doi.org/10.1016/S0022-0248(02)01915-2)
- Ying, T., Gu, Y., Chen, Xiao, Wang, X., Jin, S., Zhao, L., Zhang, W., Chen, Xiaolong, 2016. Anderson localization of electrons in single crystals: Li<sub>x</sub>Fe<sub>7</sub>Se<sub>8</sub>. *Sci. Adv.* 2, e1501283. <https://doi.org/10.1126/sciadv.1501283>
- Yu, Z., Yang, Y., Sun, J., 2021. Electroluminescence from Er-doped ZnGa<sub>2</sub>O<sub>4</sub> spinel nanofilms fabricated by atomic layer deposition on silicon. *Opt. Mater.* 122, 111691. <https://doi.org/10.1016/j.optmat.2021.111691>
- Yue, W., Yan, J., Wu, J., Zhang, L., 2012. Structural and optical properties of Zn-doped  $\beta$ -Ga<sub>2</sub>O<sub>3</sub> films. *J. Semicond.* 33, 073003. <https://doi.org/10.1088/1674-4926/33/7/073003>
- Zacherle, T., Schmidt, P.C., Martin, M., 2013. Ab initio calculations on the defect structure of  $\beta$ -Ga<sub>2</sub>O<sub>3</sub>. *Phys. Rev. B* 87, 235206. <https://doi.org/10.1103/PhysRevB.87.235206>
- Zakutayev, A., Paudel, T.R., Ndione, P.F., Perkins, J.D., Lany, S., Zunger, A., Ginley, D.S., 2012. Cation off-stoichiometry leads to high p-type conductivity and enhanced transparency in Co<sub>2</sub>ZnO<sub>4</sub> and Co<sub>2</sub>NiO<sub>4</sub> thin films. *Phys. Rev. B* 85, 085204. <https://doi.org/10.1103/PhysRevB.85.085204>
- Zerarga, F., Bouhemadou, A., Khenata, R., Bin-Omran, S., 2011. Structural, electronic and optical properties of spinel oxides ZnAl<sub>2</sub>O<sub>4</sub>, ZnGa<sub>2</sub>O<sub>4</sub> and ZnIn<sub>2</sub>O<sub>4</sub>. *Solid State Sci.* 13, 1638–1648. <https://doi.org/10.1016/j.solidstatesciences.2011.06.016>
- Zhang, C., Liao, F., Liang, X., Gong, H., Liu, Q., Li, L., Qin, X., Huang, X., Huang, C., 2019. Electronic transport properties in metal doped beta-Ga<sub>2</sub>O<sub>3</sub>: A first principles study. *Phys. B Condens. Matter* 562, 124–130. <https://doi.org/10.1016/j.physb.2019.03.004>
- Zhang, J., Dong, P., Dang, K., Zhang, Y., Yan, Q., Xiang, H., Su, J., Liu, Z., Si, M., Gao, J., Kong, M., Zhou, H., Hao, Y., 2022. Ultra-wide bandgap semiconductor Ga<sub>2</sub>O<sub>3</sub> power diodes. *Nat. Commun.* 13, 3900. <https://doi.org/10.1038/s41467-022-31664-y>
- Zhang, J., Shi, J., Qi, D.-C., Chen, L., Zhang, K.H.L., 2020. Recent progress on the electronic structure, defect, and doping properties of Ga<sub>2</sub>O<sub>3</sub>. *APL Mater.* 8, 020906. <https://doi.org/10.1063/1.5142999>
- Zhang, K.H.L., Egdell, R.G., Offi, F., Iacobucci, S., Petaccia, L., Gorovikov, S., King, P.D.C., 2013. Microscopic Origin of Electron Accumulation in  $\text{In}_{2}\text{O}_{3}$ . *Phys. Rev. Lett.* 110, 056803. <https://doi.org/10.1103/PhysRevLett.110.056803>
-

- 
- Zhang, L., Ji, G., Zhao, F., Gong, 2011. First-principles study of the structural, mechanical and electronic properties of ZnX<sub>2</sub>O<sub>4</sub> (X=Al, Cr and Ga). *Chin. Phys. B* 20, 047102. <https://doi.org/10.1088/1674-1056/20/4/047102>
- Zhang, L., Yan, J., Zhang, Y., Li, T., Ding, X., 2012a. A comparison of electronic structure and optical properties between N-doped  $\beta$ -Ga<sub>2</sub>O<sub>3</sub> and N-Zn co-doped  $\beta$ -Ga<sub>2</sub>O<sub>3</sub>. *Phys. B Condens. Matter* 407, 1227–1231. <https://doi.org/10.1016/j.physb.2012.01.107>
- Zhang, L., Yan, J., Zhang, Y., Li, T., Ding, X., 2012b. A comparison of electronic structure and optical properties between N-doped  $\beta$ -Ga<sub>2</sub>O<sub>3</sub> and NZn co-doped  $\beta$ -Ga<sub>2</sub>O<sub>3</sub>. *Phys. B Condens. Matter* 407, 1227–1231. <https://doi.org/10.1016/j.physb.2012.01.107>
- Zhang, S.B., Wei, S.-H., 2002. Self-doping of cadmium stannate in the inverse spinel structure. *Appl. Phys. Lett.* 80, 1376–1378. <https://doi.org/10.1063/1.1452789>
- Zhang, T., Lin, J., Zhang, X., Huang, Y., Xu, X., Xue, Y., Zou, J., Tang, C., 2013. Single-crystalline spherical  $\beta$ -Ga<sub>2</sub>O<sub>3</sub> particles: Synthesis, N-doping and photoluminescence properties. *J. Lumin.* 140, 30–37. <https://doi.org/10.1016/j.jlumin.2013.02.031>
- Zhang, X., Zunger, A., 2010. Diagrammatic Separation of Different Crystal Structures of A<sub>2</sub>BX<sub>4</sub> Compounds Without Energy Minimization: A Pseudopotential Orbital Radii Approach. *Adv. Funct. Mater.* 20, 1944–1952. <https://doi.org/10.1002/adfm.200901811>
- Zhang, Y., Alema, F., Mauze, A., Koksaldi, O.S., Miller, R., Osinsky, A., Speck, J.S., 2018. MOCVD grown epitaxial  $\beta$ -Ga<sub>2</sub>O<sub>3</sub> thin film with an electron mobility of 176 cm<sup>2</sup>/Vs at room temperature. *APL Mater.* 7, 022506. <https://doi.org/10.1063/1.5058059>
- Zhang, Z., Yates, J.T.Jr., 2012. Band Bending in Semiconductors: Chemical and Physical Consequences at Surfaces and Interfaces. *Chem. Rev.* 112, 5520–5551. <https://doi.org/10.1021/cr3000626>
- Zhao, X., Wu, Z., Zhi, Y., An, Y., Cui, W., Li, L., Tang, W., 2017. Improvement for the performance of solar-blind photodetector based on  $\beta$ -Ga<sub>2</sub>O<sub>3</sub> thin films by doping Zn. *J. Phys. Appl. Phys.* 50, 085102. <https://doi.org/10.1088/1361-6463/aa5758>
- Zheng, X., Moule, T., Pomeroy, J.W., Higashiwaki, M., Kuball, M., 2022. A trapping tolerant drain current based temperature measurement of  $\beta$ -Ga<sub>2</sub>O<sub>3</sub> MOSFETs. *Appl. Phys. Lett.* 120, 073502. <https://doi.org/10.1063/5.0069655>
- Zhou, H., Si, M., Alghamdi, S., Qiu, G., Yang, L., Ye, P.D., 2017. High-Performance Depletion/Enhancement-mode  $\beta$ -Ga<sub>2</sub>O<sub>3</sub> on Insulator (GOOI) Field-Effect Transistors With Record Drain Currents of 600/450 mA/mm. *IEEE Electron Device Lett.* 38, 103–106. <https://doi.org/10.1109/LED.2016.2635579>
- Zhou, L., Lanford, W., Ping, A.T., Adesida, I., Yang, J.W., Khan, A., 2000. Low resistance Ti/Pt/Au ohmic contacts to p-type GaN. *Appl. Phys. Lett.* 76, 3451–3453. <https://doi.org/10.1063/1.126674>
- Zhou, W., Xia, C., Sai, Q., Zhang, H., 2017. Controlling n-type conductivity of  $\beta$ -Ga<sub>2</sub>O<sub>3</sub> by Nb doping. *Appl. Phys. Lett.* 111, 242103. <https://doi.org/10.1063/1.4994263>
- Zhu, X., Zhang, Y.-W., Zhang, S.-N., Huo, X.-Q., Zhang, X.-H., Li, Z.-Q., 2022. Defect energy levels in monoclinic  $\beta$ -Ga<sub>2</sub>O<sub>3</sub>. *J. Lumin.* 246, 118801. <https://doi.org/10.1016/j.jlumin.2022.118801>
-

---

---

## A. List of Publications and Presentations

### Articles:

- **Z. Chi**, *et al.*, “Oxygen Induced Surface Type Transformation in Spinel ZnGa<sub>2</sub>O<sub>4</sub>”, in preparation.
- **Z. Chi**, C. Sartel, Y. Zheng, G. Sauthier, S. Modak *et al.*, “Native Defect Association in  $\beta$ -Ga<sub>2</sub>O<sub>3</sub> Enabled Room-temperature *p*-type Conductivity”, submitted to *Journal of Alloys and compounds*, under review.
- **Z. Chi**, T. Tchelidze, C. Sartel, T. Gamsakhurdashvili, I. Madaci, *et al.*, “Assessment of Large Critical Electric Fields in Ultra-wide Bandgap *p*-type Spinel ZnGa<sub>2</sub>O<sub>4</sub>”, *Journal of Physics D: Applied Physics* 56, 105102, (2023).
- **Z. Chi**, J.J. Asher, M.R. Jennings, E. Chikoidze, A. Pérez-Tomás. “Ga<sub>2</sub>O<sub>3</sub> and Related Ultra-Wide Bandgap Power Semiconductor Oxides: New Energy Electronics Solutions for CO<sub>2</sub> Emission Mitigation”, *Materials* 15, 1164, (2022).
- **Z. Chi**, F.G. Tarntair, M. Frégnaux, W.Y. Wu, C. Sartel, *et al.*, “Bipolar Self-doping in Ultra-wide Bandgap Spinel ZnGa<sub>2</sub>O<sub>4</sub>”, *Materials Today Physics* 20, 100466, (2021).
- E. Chikoidze, C. Sartel, H. Yamano, **Z. Chi**, G. Bouchez, *et al.*, “Electrical Properties of *p*-type Zn:Ga<sub>2</sub>O<sub>3</sub> Thin Films”, *Journal of Vacuum Science & Technology A* 40, 043401, (2022).
- E. Chikoidze, T. Tchelidze, C. Sartel, **Z. Chi**, R. Kabouche, *et al.*, “Ultra-high critical electric field of 13.2 MV/cm for Zn-doped *p*-type  $\beta$ -Ga<sub>2</sub>O<sub>3</sub>”. *Materials Today Physics* 15, 100263, (2020).

---

## **Presentations:**

- 08/03/2023 – **Oral presentation** – **3rd MOMENTOM International Congress Energy at The Crossroads: Accelerating Innovation in The Age of Disruption, ENS Paris, France** – “Promising Ultra-Wide Band Gap Spinel  $\text{ZnGa}_2\text{O}_4$  for Energy Storage and Conversion”
- 26/01/2023 – **Oral presentation** – **1st National Workshop: Gallium Oxide Ultra-Wide Band Gap Material for Energy Electronics, Meudon, France** – “Zn doping in  $\beta\text{-Ga}_2\text{O}_3$  and beyond”
- 19/10/2022 – **Oral presentation** – **8th TCM-TOEO, Crete, Greece** – “ $\text{ZnGa}_2\text{O}_4$  – Ultra-wide Band Gap *n*-type Transparent Conducting Oxide”
- 21/09/2022 – **Poster** – **E-MRS Fall Meeting 2022, Warsaw, Poland** – “Hole Conductivity in Ultra-wide Bandgap  $\beta\text{-Ga}_2\text{O}_3$  by Zn Doping”
- 19/09/2022 – **Oral presentation** – **E-MRS Fall Meeting 2022, Warsaw, Poland** – “Ultra-wide Bandgap Spinel  $\text{ZnGa}_2\text{O}_4$  Self-doping Capability”
- 04/10/2021 – **Oral presentation (online)** – **IUMRS-ICA 2021, ICC Jeju, Korea** – “Zn-Doped *p*-type  $\beta\text{-Ga}_2\text{O}_3$ : Ultra-High Critical Electric Field”

---

## B. List of Figures

Figure 1-1. Comparison of semiconductor material parameters (Speck and Esmat, 2023).- 2	-
Figure 1-2. Targeted applications of wide bandgap semiconductors (GaN and SiC) and Ga <sub>2</sub> O <sub>3</sub> . Ga <sub>2</sub> O <sub>3</sub> has potential application in both medium and high-voltage range. .... - 3 -	- 3 -
Figure 1-1. Unit cell of $\beta$ -Ga <sub>2</sub> O <sub>3</sub> (Mastro et al., 2020). .... - 8 -	- 8 -
Figure 1-2. Spinel structure of ZnGa <sub>2</sub> O <sub>4</sub> (W.-K. Wang et al., 2019b). .... - 18 -	- 18 -
Figure 1-3. (a) Bulk ZnGa <sub>2</sub> O <sub>4</sub> single crystals synthesized using the VGF/Bridgman method. (b) (100)-oriented wafers prepared from the as-grown and annealed bulk crystals (Galazka et al., 2019). .... - 19 -	- 19 -
Figure 1-4. Illustration of cations inversion in spinel ZnGa <sub>2</sub> O <sub>4</sub> . .... - 20 -	- 20 -
Figure 2-1. MOCVD machine and reactor in GEMaC. .... - 23 -	- 23 -
Figure 2-2. Photograph of X-ray diffractometer Bruker-Siemens D5000, in Bragg-Bretano configuration, in GEMaC. .... - 24 -	- 24 -
Figure 2-3. (a) Photograph of $\beta$ -Ga <sub>2</sub> O <sub>3</sub> samples with 4 handmade metallic silver paste contacts, for the resistivity and Hall effect measurements in a Van der Pauw configuration. (b) picture of shadow mask for RF sputtering of metallic contacts. (c) Photograph of $\beta$ -Ga <sub>2</sub> O <sub>3</sub> samples with sputtered Ti/Au contacts. .... - 30 -	- 30 -
Figure 2-4. (a) Keithley Inc. SCS 4200 Semiconductor Characterization System. (b) Photocurrent test platform with fibered lighting. .... - 31 -	- 31 -
Figure 2-5. (a) Home-built Hall effect set up in Van Der Pauw configuration. (b) Photo of the measurement cell (adapted Linkam Inc. cell). .... - 32 -	- 32 -
Figure 2-6. Van Der Pauw resistivity measurement eight configurations. .... - 33 -	- 33 -
Figure 2-7. The principle of Hall effect for electrons e <sup>-</sup> (right) and for hole h (left) inducing in stationary state opposite Hall electric field E <sub>H</sub> . .... - 34 -	- 34 -
Figure 2-8. Van der Pauw Hall effect measurement eight configurations. .... - 37 -	- 37 -
Figure 2-9. Results of a representative undoped <i>p</i> -type $\beta$ -Ga <sub>2</sub> O <sub>3</sub> thin film: (a) – (b) The current-voltage characteristics at 570 K and 850 K, respectively, and (c) – (d) Hall voltage scanned with the perpendicularly applied magnetic field from -1.6 – +1.6 T at 630 K and 850 K, respectively. .... - 39 -	- 39 -
Figure 2-10. (a) Photo of a sample holder with mounted sample at rotative platform of PPMS-9T (b) 9T PPMS equipment in GEMaC. .... - 39 -	- 39 -
Figure 2-11. Home-built Seebeck Effect in GEMaC. .... - 40 -	- 40 -

- 
- Figure 3-1. XRD and GIXRD scans in sample  $\beta$ -Ga<sub>2</sub>O<sub>3</sub>//*c*-sapphire. (a) Out-of-plane (OP) scan with in the inset the rocking curve of  $\beta$ -Ga<sub>2</sub>O<sub>3</sub> -201 reflection. (b) In-plane (IP) scan along Al<sub>2</sub>O<sub>3</sub> *b*\*-axis azimuth. The rocking curve of  $\beta$ -Ga<sub>2</sub>O<sub>3</sub> 020 reflection is in the inset. Contributions from Cu *K* <sub>$\beta$</sub>  radiation and substrate are marked by \*..... - 43 -
- Figure 3-2. Raman spectra recorded using 514.5 nm excitation for: red trace: (-201)  $\beta$ -Ga<sub>2</sub>O<sub>3</sub> thin film grown on *c*-sapphire substrates; grey trace: bare *c*-sapphire substrate; green trace: (100)  $\beta$ -Ga<sub>2</sub>O<sub>3</sub> single crystal. The phonon modes for  $\beta$ -Ga<sub>2</sub>O<sub>3</sub> are labelled using “#” while the phonon modes for *a*-Al<sub>2</sub>O<sub>3</sub> substrate are labelled using “\*”. ..... - 44 -
- Figure 3-3. (a) Typical  $\beta$ -Ga<sub>2</sub>O<sub>3</sub> Ohmic I–V characteristics at 850 K. (b) Resistivity  $\rho$  versus temperature. (c)  $\ln(\sigma)$  vs.  $1000/T$  plot for the determination of activation energy of conductivity. (d) Temperature dependence of  $\rho_A$  and  $\rho_B$ ..... - 46 -
- Figure 3-4. (a) Hall voltage ( $V_H$ ) versus magnetic field ( $H$ ) at 800 K and 850 K. (b) Ionization energies of the acceptor center ( $E_i$ ) determination from  $\ln(pT^{3/2})$  vs.  $(1000/T)$  plot. (c) Temperature dependence of the Hall free hole concentration in log scale. (d) Hall hole mobility as a function of temperature..... - 48 -
- Figure 3-5. Room-temperature optical transmittance for  $\beta$ -Ga<sub>2</sub>O<sub>3</sub> thin film with the estimation of optical band gap by Tauc plot (inset). Oscillations are interferences associated to the film thickness = 450 nm. .... - 49 -
- Figure 3-6. Photoluminescence spectrum for undoped *p*-type  $\beta$ -Ga<sub>2</sub>O<sub>3</sub> thin layer excited with 266 nm wavelength at 294 K. Right side: enlarged view of the emission located at around 3.7 eV. .... - 50 -
- Figure 3-7. (a) XPS valence band of the  $\beta$ -Ga<sub>2</sub>O<sub>3</sub> valence band for a commercial Si-doped (*n*-type) reference and our *p*-type sample. (b) A zoom of the valence band region (VBM) showing the presence of tail states in the lower part of the bandgap for the *p*-type compounds. .... - 51 -
- Figure 3-8. (a) Temperature dependence of resistivity. (b)  $\ln(\sigma)$  vs.  $1000/T$  plots and linear fits for the determination of the activation energy of conductivity. (c) Hall voltage ( $V_H$ ) versus applied perpendicular magnetic field ( $H$ ). (d) Hall hole concentrations versus temperatures. (e)  $\ln(pT^{3/2})$  vs.  $1000/T$  plots and linear fits for the determination of the activation energies of acceptor centers. .... - 53 -
- Figure 3-9. Phase diagram of  $\beta$ -Zn:Ga<sub>2</sub>O<sub>3</sub> with three thermodynamical regions: native *p*-type, impurity *p*-type and impurity auto-compensation, with boundary curves versus temperature..... - 59 -
- Figure 3-10. (a) XRD patterns for undoped and Zn-doped  $\beta$ -Ga<sub>2</sub>O<sub>3</sub> thin films with different Zn flow (Zn concentration). “\*” refers to XRD peaks of *c*-plane sapphire
-

---

substrates. (b) Enlarged view of five peaks located at $2\theta = 18.94^\circ, 38.38^\circ, 58.98^\circ, 82.14^\circ$ to show that, there's no transition peak. ....	- 61 -
Figure 3-11. SIMS depth profiles for three Zn doped $\beta$ -Ga <sub>2</sub> O <sub>3</sub> samples grown at Zn flows at 1.6, 2.8, 3.9 $\mu\text{mol}/\text{min}$ , respectively. ....	- 62 -
Figure 3-12. Scanning electron microscopy (SEM) top-view images of (a) – (d) undoped, $[\text{Zn}] = 10^{16} \text{ cm}^{-3}$ doped, $[\text{Zn}] = 10^{18} \text{ cm}^{-3}$ doped, and $[\text{Zn}] = 10^{19} \text{ cm}^{-3}$ doped $\beta$ -Ga <sub>2</sub> O <sub>3</sub> grown on <i>c</i> -plane sapphire substrate, respectively. ....	- 63 -
Figure 3-13. (a) Optical transmittance. (b) Tauc plots (for the determination of the optical band gap). (c) Optical band gaps with error bars versus incorporated Zn concentrations. Different oscillations periods are connected to different film thicknesses. ....	- 64 -
Figure 3-14. Hall voltage ( $V_H$ ) versus magnetic field ( $H$ ) for Zn-doped $\beta$ -Ga <sub>2</sub> O <sub>3</sub> with increasing doping levels. Each Hall voltage value and corresponding slope are positive, which is an indication of the <i>p</i> -type conductivity in the samples. ....	- 65 -
Figure 3-15. (a) Temperature dependence of the resistivity. (b) Hole concentration versus temperature. (c) $\ln(pT^{-3/2})$ vs. $1000/T$ plots and linear fits for the determination of the ionization energies. (d) Hall hole mobilities versus temperature. Black squares are for undoped and red disks for Zn-doped Ga <sub>2</sub> O <sub>3</sub> ( $[\text{Zn}] = 10^{16} \text{ cm}^{-3}$ ) thin films. ....	- 67 -
Figure 3-16. (a) Temperature dependence of resistivity. (b) $\ln(\sigma)$ vs. $1000/T$ plot for the determination of the activation energies. (c) Hall hole concentrations versus temperature. (d) Hall hole mobilities versus temperature. Samples: undoped (black) and Zn-doped Ga <sub>2</sub> O <sub>3</sub> ( $[\text{Zn}] = 10^{18} \text{ cm}^{-3}$ (blue), $10^{19} \text{ cm}^{-3}$ (green)) thin films. ....	- 68 -
Figure 3-17. Schematic illustration of the impact ionization process (in the case of electron). ....	- 70 -
Figure 3-18. XRD patterns of undoped (black) and Zn-doped (green, doping level at $10^{19} \text{ cm}^{-3}$ ) $\beta$ -Ga <sub>2</sub> O <sub>3</sub> thin films on conducting Si (111) substrates. “*” refers to the peaks of Si (111) substrates. ....	- 72 -
Figure 3-19. (a) High-resolution TEM cross-section image of $\beta$ -Ga <sub>2</sub> O <sub>3</sub> grown on Si (111) substrate. SAED patterns of (b) the Si(111) substrate, (c) $\beta$ -Zn:Ga <sub>2</sub> O <sub>3</sub> layer, and (d) interface between $\beta$ -Zn:Ga <sub>2</sub> O <sub>3</sub> layer and Si substrate, respectively. (Experiment is done in ICN2, Barcelona Spain). ....	- 73 -
Figure 3-20. (a) Sketch of the vertical heterojunction structures ( $\beta$ -Ga <sub>2</sub> O <sub>3</sub> /Si and $\beta$ -Zn:Ga <sub>2</sub> O <sub>3</sub> //Si) with Ti/Au metal contacts on the top of the Ga <sub>2</sub> O <sub>3</sub> layers. (b) Experimental I–V curves of vertical breakdown voltage measurements through the $\beta$ -Ga <sub>2</sub> O <sub>3</sub> //Si and $\beta$ -Zn:Ga <sub>2</sub> O <sub>3</sub> :Zn//Si structures, indicating a hard breakdown voltage up to 124 V and 540 V at room temperature, respectively. ....	- 74 -

---

---

Figure 3-21. Schematic illustration of Zn doping effect.....	- 75 -
Figure 4-1. (a) XRD patterns for undoped and Zn incorporated $\beta$ -Ga <sub>2</sub> O <sub>3</sub> thin films with different Zn flow (Zn concentration). “*” refers to the peaks of <i>c</i> -plane sapphire substrates. (b) Enlarged views for $2\theta = 17.1 - 19.9^\circ$ , $36.6 - 39.1^\circ$ , $56.0 - 60.5^\circ$ , $78.2 - 83.5^\circ$ , and $103.0 - 114.0^\circ$ to show the double-peak features and the transition of peaks. ....	- 79 -
Figure 4-2. Raman scattering spectra for pure $\beta$ -Ga <sub>2</sub> O <sub>3</sub> , mixed GaO/ZnGaO, and pure ZnGa <sub>2</sub> O <sub>4</sub> .....	- 80 -
Figure 4-3. (a) X-ray diffractograms of as-grown <i>n</i> -type and <i>p</i> -type ZnGa <sub>2</sub> O <sub>4</sub> thin films grown <i>c</i> -sapphire, the peak labelled by “*” indicates the XRD reflection corresponding to the sapphire substrate. ....	- 82 -
Figure 4-4. High-resolution transmission electron microscope (HRTEM) images for (a) <i>n</i> -type ZnGa <sub>2</sub> O <sub>4</sub> thin film and (b) <i>p</i> -type ZnGa <sub>2</sub> O <sub>4</sub> thin film. (c) SAED images of <i>n</i> -ZnGa <sub>2</sub> O <sub>4</sub> and (d) The fast Fourier transform of the image <i>p</i> -ZnGa <sub>2</sub> O <sub>4</sub> . The experiments were carried out in National Chiao Tung University.....	- 83 -
Figure 4-5. XPS spectra of 3 probed places on the surface of <i>n</i> -ZnGa <sub>2</sub> O <sub>4</sub> sample.....	- 84 -
Figure 4-6. Zoom (intensity normalized) of the main XPS peaks for (a) gallium (Ga2 <i>p</i> - Ga2 <i>p</i> <sub>3/2</sub> ), (b) oxygen (O1 <i>s</i> ), (c) zinc (Zn2 <i>p</i> - Zn2 <i>p</i> <sub>3/2</sub> ), (d) adventitious carbon contamination (C1 <i>s</i> , calibration for C-C bonds at 284.8 eV) of <i>n</i> -type ZnGa <sub>2</sub> O <sub>4</sub> , pure $\beta$ -Ga <sub>2</sub> O <sub>3</sub> , pure wurtzite ZnO and <i>p</i> -type ZnGa <sub>2</sub> O <sub>4</sub> for comparison. (e) Deconvolution of the main contributions of the O1 <i>s</i> oxygen peak for spinel ZnGa <sub>2</sub> O <sub>4</sub> .....	- 86 -
Figure 4-7. (a) Experimental XPS high-resolution valence band for the <i>n</i> -type ZnGa <sub>2</sub> O <sub>4</sub> and <i>p</i> -type ZnGa <sub>2</sub> O <sub>4</sub> as a reference. (b) Experimental XPS high-resolution of the first valence band group for <i>n</i> -type ZnGa <sub>2</sub> O <sub>4</sub> , <i>p</i> -type ZnGa <sub>2</sub> O <sub>4</sub> , pure ZnO and pure <i>p</i> -type $\beta$ -Ga <sub>2</sub> O <sub>3</sub> for comparison. (c) Idem, for the first and the second group of valence bands. (d) A zoom of the valence band region (VBM) showing the presence of tail states in the lower part of the bandgap for the <i>p</i> -type compounds (the value of the bandgap is depicted for ZnO, $\beta$ -Ga <sub>2</sub> O <sub>3</sub> and ZnGa <sub>2</sub> O <sub>4</sub> ). ....	- 89 -
Figure 4-8. Room temperature optical transmittance spectra and in inset direct bandgap determination by Tauc’s plot for both <i>n</i> -type (a) and <i>p</i> -type ZnGa <sub>2</sub> O <sub>4</sub> (b) thin films. ....	- 90 -
Figure 4-9. <i>n</i> -ZnGa <sub>2</sub> O <sub>4</sub> thin film (a) electrical resistivity versus temperature dependence from aligned four-probe measurements; (b) electron concentration from Hall effect measurements in Van der Pauw configuration. Pure <i>p</i> -type ZnGa <sub>2</sub> O <sub>4</sub> layer (c) electrical resistivity and (d) hole concentration versus temperature determined from Hall effect measurement.....	- 92 -

---

- 
- Figure 4-10. *n*-type ZnGa<sub>2</sub>O<sub>4</sub> (a)  $\log(\sigma T)$  versus  $1/T$  in the nearest-neighbor hopping regime; (b)  $\ln(\sigma)$  versus  $T^{-1/4}$  showing the variable range hopping regime (VRH); (c) Resistance versus magnetic field at different temperatures (2 – 100 K) in perpendicular to current magnetic field orientation. Measurements were done in four-probe aligned configuration. .... - 94 -
- Figure 4-11. Schematic summary showing the intrinsic conductivity difference between conducting *n*-type and semi-insulating *p*-type ZnGa<sub>2</sub>O<sub>4</sub> thin films, with the corresponding conduction mechanism and origin of the conductivity. .... - 95 -
- Figure 4-12. Cu-K<sub>α</sub> XRD  $\theta$ - $2\theta$  patterns of both ZnGa<sub>2</sub>O<sub>4</sub> thin films, the *c*-plane sapphire substrate is labelled as “\*”. .... - 97 -
- Figure 4-13. (a) TEM cross-section image of ZnGa<sub>2</sub>O<sub>4</sub>-#1 thin film. (b) High resolution TEM image. (c) SAED pattern of the ZnGa<sub>2</sub>O<sub>4</sub>-#1 film, selected part is shown in the red circle in figure (b). The results were provided by collaborators from National Chiao Tung University. .... - 97 -
- Figure 4-14. For ZnGa<sub>2</sub>O<sub>4</sub>-#1 thin film: (a) Current-voltage (*I-V*) characteristics at 300 K; (b) Temperature-dependent resistivity ( $\rho$ ) in the range of 80 – 500 K; (c)  $\ln(\sigma)$  versus  $1000/T$  for the determination of the activation energy of the conductivity. For the ZnGa<sub>2</sub>O<sub>4</sub>-#2 which was cooled in O<sub>2</sub>: (d) *I-V* curve at 750 K; (e) Temperature-dependent resistivity in the range of 550 – 750 K; (f)  $\ln(\sigma)$  versus  $1000/T$ ; (g) Hall voltage ( $V_H$ ) versus magnetic field at 750 K, both the values of the Hall voltage and the slope are positive, indicating the *p*-type conductivity of the ZnGa<sub>2</sub>O<sub>4</sub> sample; (h) Temperature-dependent hole concentration (*p*) in 550 – 750 K. .... - 99 -
- Figure 4-15. Optical transmittance for as grown, O<sub>2</sub> cooled ZnGa<sub>2</sub>O<sub>4</sub> samples, *n*-type ZnGa<sub>2</sub>O<sub>4</sub> thin film discussed in Section 4.2, and only one face polished bare sapphire substrate as reference. .... - 100 -
- Figure 4-16. XPS peaks for (a) gallium (Ga2*p* - Ga2*p*<sub>3/2</sub>), (b) zinc (Zn2*p* - Zn2*p*<sub>3/2</sub>), (c) oxygen (O1*s*), (d) adventitious carbon contamination (C1*s*, calibration for C-C bonds at 284.8 eV) of both ZnGa<sub>2</sub>O<sub>4</sub>-#1 and ZnGa<sub>2</sub>O<sub>4</sub>-#2 samples. .... - 101 -
- Figure 4-17. (a) room-temperature *I-V* curves under dark and illumination. (b) Dynamic photo-response under UV lamp illumination at a 5 V bias of the ZnGa<sub>2</sub>O<sub>4</sub>-#2 thin film. .... - 103 -
- Figure 4-18. Cu-K<sub>α</sub> XRD spectra of ZnGa<sub>2</sub>O<sub>4</sub> thin film grown on Si(111) (black), and Al<sub>2</sub>O<sub>3</sub>(0001) (red). \* and # correspond respectively to Al<sub>2</sub>O<sub>3</sub>(0001) and Si(111) Bragg reflections. .... - 104 -
- Figure 4-19. (a) Ohmic *I-V* characteristics at 700K and 850 K (b) Resistivity versus temperature. (c) Hall voltage ( $V_H$ ) versus magnetic field at different temperatures (700 – 850 K). The Hall voltage is positive and increase with the increasing
-

---

applied magnetic field, indicating the <i>p</i> -type conductivity in ZnGa <sub>2</sub> O <sub>4</sub> layer. (d) Temperature dependence for Hall free hole concentration for ZnGa <sub>2</sub> O <sub>4</sub> thin film. ....	- 106 -
Figure 4-20. (a) Sketch of the vertical heterojunction structure with Ti/Au metal contacts. (b) SEM cross-section image of ZnGa <sub>2</sub> O <sub>4</sub> polycrystalline film deposited on Si(111). The estimated thickness of the film is 600 nm. (c) Experimental <i>I-V</i> curves of vertical breakdown voltage measurements through the ZnGa <sub>2</sub> O <sub>4</sub> //Si structure, indicating a breakdown voltage up to 350 V at room temperature. ....	- 107 -
Figure 5-1. Schematic of band diagram for (a) Au/Ti/ITO and (b) Au/Ti/AZO on GaO.-	111
-	
Figure 5-2. Schematic cross-sectional illustration of equivalent circuit during the current-voltage characterization. ....	- 112 -
Figure 5-3. Schematic illustration of the transfer length method (a) patterns, (b) schema to show the transfer length (Hao Yu et al., 2014), (c) contact resistance and sheet resistance determination by $R_{tot}$ vs. $d_i$ plot. ....	- 114 -
Figure 5-4. (a) Schematic cross-sectional diagram of equivalent circuit in the CTLM measurement technique. The metallization is formed on the inner pad and the areas outside the rings. Where $r$ is the radius of the inner circle (inner metal pad), $r_{out}$ is the outer circle radii, $d_i$ is the gap spacing between inner and the outer circles. Each group of CTLM pattern includes 6 rings with constant inner circle radius ( $r$ ) but different outer circle radii ( $r_{out}$ ). (b) Corresponding schematic top-view of electrodes in a single CTLM pattern. ....	- 114 -
Figure 5-5. (a) spin coater “POLOS SPIN150i” in GEMaC. (b) UV-exposure equipment “Smart Print” in GEMaC. (c) An example of designed pattern for lithography process. Right part is circular transmission line model (CTLM) patterns for the contact resistance study, the diameter of inner circular is 0.25 mm, the ring between two circulars are 40, 60, 80, 100, 120, 140 μm, respectively. ....	- 117 -
Figure 5-6. Microscope image of the CTLM patterns for trail (a) n°1, (b) n°4, (c) n°5 (after development, before metal deposition), (d) n°6 (designed gap $d_i = 120$ μm), (e) n°7 (designed gap $d_i = 46$ μm) with the enlarged view of the gap, (f) n°9. The lithography parameters for each trail are summarized in the Table 5-2. For figure (g), due to the limit of magnification, the whole group of patterns could not be captured together, each concentric circle was captured separately with the same magnification and then merged. ....	- 119 -
Figure 5-7. $R_{tot}$ plotted versus $\ln(r_{out}/r)$ at 700 K. ....	- 122 -
Figure 5-8. <i>I-V</i> curves for sputtered Ag contact at temperatures ranging between 700 – 550 K. ....	- 123 -

---

---

Figure 5-9. $I$ - $V$ curves of Ti/Pt/Au contact at different temperatures (700 – 450 K), and different spacing $d_i$ . .....	- 124 -
Figure 5-10. Total resistance $R_{tot}$ plotted versus gap spacing $d_i$ for Ti/Pt/Au contact between $T = 700$ K and 450 K. ....	- 125 -
Figure 5-11. (a) The calculated sheet resistance ( $R_S$ ) (black) of $\beta$ -Ga <sub>2</sub> O <sub>3</sub> film and the specific contact resistance ( $\rho_C$ ) (red) plotted versus temperature in semi-log shifted scales. (b) The first measurement (black) and the final measurement (dark yellow) after conducting all the $I$ - $V$ tests for the pattern with gap spacing $d_i = 140$ $\mu$ m at 600 K. ....	- 126 -
Figure 5-12. $I$ - $V$ curves of Pt contact at different temperatures (600 – 500 K). ....	- 126 -
Figure 5-13. Schematic illustration for a new version of CTLM patterns, with large outer metallic electrode. ....	- 127 -

---

## C. List of Tables

Table 1-1. Outcome of $\beta$ -Ga <sub>2</sub> O <sub>3</sub> bulk crystal growth methods. Remarks (a) and (b) refer to: a) in diameter, b) in width. ....	- 10 -
Table 1-2. Summary of main parameters and research outcomes for $\beta$ -Ga <sub>2</sub> O <sub>3</sub> and ZnGa <sub>2</sub> O <sub>4</sub> . Remarks (a-e) refer to: a) common value form literature, b) experimental result, c) results will be presented in this manuscript, d) values of epilayers, e) values of bulk crystals. ....	- 22 -
Table 3-1. Lattice parameters of sample $\beta$ -Ga <sub>2</sub> O <sub>3</sub> //c-sapphire inferred with the OP tensile strain of 0.34% and the IP compressive strain of -0.24% measured.....	- 43 -
Table 3-2. Summary of the growth conditions and $\beta$ -Ga <sub>2</sub> O <sub>3</sub> film thicknesses layers.....	- 52 -
Table 3-3. Summary of previously reported Zn-doped $\beta$ -Ga <sub>2</sub> O <sub>3</sub> from the literature, showing Zn related acceptor characteristics. Remarks (a – e) refer to: a) Overall reduction of conductivity/Zn considered as an acceptor; b) determined by photoluminescence; c= determined by cathodoluminescence; d) nanowire; e) determined by Electron paramagnetic resonance (EPR).....	- 56 -
Table 3-4. Summary of the growth conditions.....	- 60 -
Table 4-1. Growth conditions of pure and Zn incorporated $\beta$ -Ga <sub>2</sub> O <sub>3</sub> .....	- 78 -
Table 4-2. Growth conditions of two ZnGa <sub>2</sub> O <sub>4</sub> thin films. ....	- 82 -
Table 4-3. Growth parameters and the thickness of samples. ....	- 96 -
Table 5-1. Adjustment of parameters for lithography process. ....	- 118 -
Table 5-2. Designed and measured $r$ and $d_i$ with uncertainties for Ti/Pt/Au and Pt contact. ....	- 121 -

